EXAMINATION OF METAL OXIDE NANOCRYSTAL FORMATION, GROWTH AND APPLICATIONS USING A CONTINUOUS GROWTH SYNTHESIS

by

TAWNEY ANN KNECHT

A DISSERTATION

Presented to the Department of Chemistry and Biochemistry
and the Division of Graduate Studies of the University of Oregon
in partial fulfillment of the requirements
for the degree of
Doctor of Philosophy

June 2022

DISSERTATION APPROVAL PAGE

Student: Tawney Ann Knecht

Title: Examination of Metal Oxide Nanocrystal Formation, Growth and Applications using a Continuous Growth Synthesis

This dissertation has been accepted and approved in partial fulfillment of the requirements for the Doctor of Philosophy degree in the Department of Chemistry and Biochemistry by:

Dr. Mark Lonergan	Chairperson
Dr. James Hutchison	Advisor
Dr. Shannon Boettcher	Advisor
Dr. Victoria DeRose	Core Member
Dr. Stephanie Majewski	Institutional Representative

and

Krista Chronister	Vice Provost for Graduate Studies

Original approval signatures are on file with the University of Oregon Division of Graduate Studies.

Degree awarded June 2022

DISSERTATION ABSTRACT

Tawney Ann Knecht

Doctor of Philosophy

Department of Chemistry

June 2022

Title: Examination of Metal Oxide Nanocrystal Formation, Growth and Applications using a Continuous Growth Synthesis

Metal oxide nanomaterials can serve as high-performance materials in many applications, but only if their nanoscale structure can be controlled through synthesis. Metal oxide nanocrystals with the necessary structural attributes (size, shape, crystallinity, dopant identity and concentration, defect structure, architecture, etc.) to enhance these applications have been produced, but little is known about growth processes that lead to those structures. Research on the nanocrystal growth process is necessary to gain the level of synthetic control required to predictably engineer the desirable attributes of nanocrystals.

The research described in this dissertation utilizes a continuous addition synthesis that enables fine control over the nanocrystal growth process in examining the influence of precursor oxidation state, reaction atmosphere, precursor ligation, and reagent identity are investigated. In the case of cerium oxide, it was found that precursor oxidation state does not significantly influence the growth of cerium oxide nanocrystals. Instead, we find that reaction atmosphere (N_2 vs air) drastically influences the nanocrystal structure, which in turn influences the growth, with nanoribbons or plates forming under N_2, and nanocubes forming under air. We also found that acetate from the precursor starting material were

responsible for nanoribbon formation. For tin-doped indium oxide (ITO), it was found that changing the primary reagent from oleyl alcohol to oleylamine drastically influenced the nanocrystal growth by influencing the number of nanocrystals formed in the earliest stages of nanocrystal formation and growth.

Towards utilizing ITO nanocrystals in applications, we investigate their use as plasmonic filters and as electrocatalysts. We find that we can sculpt the absorption spectrum of solution-processed ITO nanocrystal films, enabling the fabrication of tunable IR filters. We also find that ITO nanocrystals are unstable and restructure to an indium/tin metal alloy under electrochemically reducing potentials required for CO_2 reduction.

This dissertation includes previously published and unpublished co-authored material.

CURRICULUM VITAE

NAME OF AUTHOR: Tawney Ann Knecht

GRADUATE AND UNDERGRADUATE SCHOOLS ATTENDED:

University of Oregon, Eugene
The Pennsylvania State University, State College

DEGREES AWARDED:

Doctor of Philosophy, Chemistry, 2022, University of Oregon
Master of Science, Chemistry, 2019, University of Oregon
Bachelor of Science, Forensic Science, 2015, The Pennsylvania State University
Bachelor of Science, Criminology, 2015, The Pennsylvania State University

AREAS OF SPECIAL INTEREST:

Materials Science
Nanomaterials Synthesis
Nanomaterials Characterization
    Electron Microscopy
    X-Ray Scattering
    Surface Characterization
Electrocatalysis
    Electrochemical CO_2 Reduction
    Electrochemical Oxygen Reduction
    Electrochemical Oxygen Evolution

PROFESSIONAL EXPERIENCE:

Graduate Research Assistant, Department of Chemistry and Biochemistry, University of Oregon, 2017-2022

Graduate Research Intern, National Renewable Energy Laboratory, 2020-2021

Graduate Teaching Assistant, Department of Chemistry and Biochemistry, University of Oregon, 2016-2017

GRANTS, AWARDS, AND HONORS:

Office of Science Graduate Student Research Award, Department of Energy, 2020

Outstanding Scholarship in Forensic Science, The Pennsylvania State University Department of Forensic Science, 2015

Walt and Lynn Marie Forensic Science Student Research Fund, The Pennsylvania State University, 2013

Bert Elsbach Trustee Scholarship in Science, The Pennsylvania State University, 2013

Daniels Fund Scholarship, Daniels Fund Organization, 2011-2015

PUBLICATIONS:

Knecht, T. A.; Hutchison, J. E. Reaction Atmosphere and Surface Ligation Control Surface Reactivity and Morphology of Cerium Oxide Nanocrystals During Continuous Addition Synthesis. *Inorg. Chem.*, **2022**, *61*, 4690–4704

Levine, J. D.; Rosen, A. Q.; Knecht, T. A.; Johnson, D. W. A Scalable, Eco-Friendly Ultralow-Temperature Approach to Forming Al_2O_3 Water-Repellent Cotton Coatings via UV Photo-Annealing. *Chem. Commun.*, **2022**, *58*, 4536–4539

Knecht, T. A.; Boettcher, S. W.; Hutchison, J. E. Electrochemistry-Induced Restructuring of Tin-Doped Indium Oxide Nanocrystal Films of Relevance to CO_2 Reduction. *J. Electrochem. Soc.*, **2021**, *168*, 126521

Krivina, R. A.; Knecht, T. A.; Crockett, B. M.; Boettcher, S. W.; Hutchison, J. E. Sculpting Optical Properties of Thin Film IR Filters through Nanocrystal Synthesis and Additive, Solution Processing. *Chem. Mater.*, **2020**, *32*, 8683–8693.

ACKNOWLEDGMENTS

My success would not have been possible without the assistance and support of many people. First and foremost, I must thank my advisors Dr. Jim Hutchison and Dr. Shannon Boettcher. Jim, I cannot express enough thanks for your patience and guidance in discussions about research, for teaching me what it means to think critically about science, and for your support of my career goals. You have not only taught me how to be a better scientist, researcher, writer, and speaker, but you also supported my ever-growing love for adventure and the outdoors. Let us not forget the time we coincidentally ran into each other at 4:00 a.m. near the summit of South Sister, chasing the sunrise. Shannon, thank you for mentoring me even before you were my official advisor and allowing me to join your lab late in my graduate career. Thank you also for teaching me to take science as it comes and not fight what nature gives you. I appreciate that you always have an open door and willingness to discuss science.

Thank you to my committee members Dr. Mark Lonergan, Dr. Victoria DeRose, and Dr. Stephanie Majewski for making me feel at ease in committee meetings and for always pushing me towards success. Mark, I want to specifically thank you for your help when things seemed bleak in grad school. I also want to thank my previous mentors Dr. Dan Sykes, Dr. Reena Roy, and Dr. Frank Dorman who were instrumental (pun-intentional) in sparking my love of science and encouraging me to go down this path.

Part of my research was done under the mentorship of Dr. Jack Ferrell III at the National Renewable Energy Laboratory (NREL). Jack, thank you for being such a kind and enthusiastic mentor, and for helping me be successful in a new environment. Thank you also to my friend Dr. Annie Greenaway for helping me both at NREL and UO.

Much of my research was enabled by the support of CAMCOR staff, especially Dr. Stephen Golledge, Josh Razink, Kurt Langworthy, Valerie Brogden, Bobby Fisher, and Steve Wiemholt. Thank you all for your hard work and willingness to help. And Steve (Golledge), thank you for the discussions over wine, they were much appreciated.

None of this work would have been possible without the support of the Department of Chemistry and Biochemistry administrative staff. For this support, I would like to thank Janet Macha-Kneller, Christi Mabinouri, Kathy Noakes, Jim Rasmussen, Gerri Ravjaa, Diane Lachenmeier, and Leah O'Brien.

I would like to thank all of the students who mentored me: Drs. Lisa Enman, Michaela Burke-Stevens, Jaclyn Kellon, Samantha Young, Kira Egelhofer, and Colin Bradley. Thank you to the Boettcher Lab past and present, especially Grace Lindquist, Dr. Jessica Fehrs, and Raina Krivina, for giving me a community and support when I needed it. To Casey Bisted, Makenna Pennel, and Drs. Tatiana Zaikova, Adam Jansons, Sam Young, Susan Cooper, Brandon Crockett, Brantly Fulton, Meredith Sharps, Aurora Ginzburg, Jaclyn Kellon, and Kenyon Plummer: thank you for fostering such a kind, accepting, and healthy culture and making the Hutch Lab feel like family. I am so happy to call all of you my friends. Kenyon, I want to especially thank you for your unending support, both scientifically and personally. You have been crucial to my success and you have made me a better person.

I want to thank my good friends Hazel Fargher for being a wonderful roommate, friend, and adventure buddy (even if she's not a morning person), Jeremy Bard for revenge ice cream and for promising to buy me and Hazel three houses, Gabby Warren and Amber Rolland for the adventures, and Kiana Kawamura for more than I have room to write. Thank you to the staff, fellow volunteers, and feathered friends at the Cascades Raptor Center for cultivating my love of wildlife and teaching me so much about patience, mentoring, working on a team, and public speaking; for this, I am eternally grateful. I was lucky to play cello in two community orchestras: thank you to Dr. Sam Young for introducing me to the Eugene Springfield Community Orchestra and thank you to Dr. Catherine Page for inviting me to play in the Riverside Chamber Symphony. I will of course miss making music with these groups, but I will especially miss the sass coming from my sexagenarian and septuagenarian friends. To my friends outside of chemistry, especially Joe and Ivy Pitts, and Portia Curlee, thank you for being a sobering source of support and perspective, and thank you for all the adventures. Portia, I want to especially thank you for your support, particularly in the last year, and always reminding me that I am loved when I need it most. Finally, thank you to my family for your unwavering love and support, especially to my parents Carol Knecht and Rick Weaver who have supported me through so much. I love you, and I hope I have and will continue to make you proud.

Dedicated to my family and friends, and in loving memory of my aunt Kelly Knecht and Grandma Marlis Weaver.

TABLE OF CONTENTS

Chapter Page

Chapter Page

Chapter Page

LIST OF FIGURES

LIST OF TABLES

LIST OF SCHEMES

CHAPTER I

INTRODUCTION

I am the primary and sole author to the writing of this chapter.

Dissertation Introduction

Nanomaterials have garnered interest over the last several decades as materials that will solve some of the world's most challenging issues, and are used in drug delivery,[1-4] sensing,[5-8] cancer treatment,[1, 4, 9-11] water purification,[12-14] electronics,[15-19] photovoltaics,[7, 17, 20-21] energy storage devices,[7, 22-24] and more. This special class of materials consists of materials that have one dimension below 100 nm in size, and can be any material including carbon-based materials,[25-27] metals,[7, 28-29] and metal chalcogenides,[5, 8, 11, 16, 30] to name a few. These can include one-dimensional wires,[31-33] two-dimensional sheets or films,[8, 11, 28, 34-37] and three-dimensional nanoparticles from simple geometries like spheres[38-39] and cubes,[40-43] to more complex geometries like branched shapes[44] or flowers.[45-46]

The reason nanomaterials are a special class of materials worth studying is because they exhibit size- and shape-dependent properties that are different than their bulk counterparts.[47-48] For example, while bulk gold has a golden yellow color, nanogold can be pink, purple, or red (depending on the particle size and shape) and was used, likely unknowingly, to make red glass since the Middle Ages.[47] Another common example is

quantum dots, which are nanomaterials that exhibit size-dependent photoluminescent properties, appearing as different colors when excited depending on their size.[49-51] Due to these size-dependent optical properties, quantum dots have been adopted into technologies such as LEDs and quantum dot displays,[49, 52-53] solar cells,[54-55] imaging in cell biology,[51] and more.

Because these properties are size- and shape-dependent, there has been a push to develop reliable processes to fabricate or synthesize nanomaterials of predictable compositions, size, and shape. There are two main approaches to nanomaterials fabrication: top-down or bottom up.[56] Top-down approaches start with bulk materials that are further broken down or structured on the nanoscale. Some examples of these processes include mechanical milling and various lithography and selective etching methods.[56] The advantage of mechanical milling is that the process is simple, but it often leads to a range of sizes of material, and the process is not predictable nor controllable. Lithography and etching techniques have been widely used in the electronics industry to fabricate nanoscale electronic circuitry; however, these methods are not broadly applicable to all materials.

Bottom-up approaches are ones in which nanomaterials are synthesized from smaller building blocks such as atoms, molecular precursors, or clusters, and they offer several advantages.[56] These techniques include atomic layer and chemical vapor deposition, as well as solid, liquid, and gas phase syntheses. Each of these techniques has advantages and drawbacks. This dissertation will focus on the liquid phase synthesis of colloidal nanocrystals because such syntheses offer many handles (such as temperature, solvent choice, precursor choice, reagent choice, concentrations, etc.) that can be manipulated to tune nanoscale structure.

The nanoscience community has made strides towards developing liquid phase syntheses, both aqueous and organic, that have enabled access to nearly every material and nanostructure one could think of. Many studies have been published on size- and shape-dependent properties of various nanomaterials. However, size and shape are not the only structural attributes of a nanocrystal that affect properties. Properties can also be influenced by the degree of crystallinity, what crystal phases are present, defects such as twinning[57-58] or oxygen vacancies,[59-61] and in the case of multi-component nanocrystals, phase segregation[62-63] and/or location of dopant within the nanocrystal.[64-65]

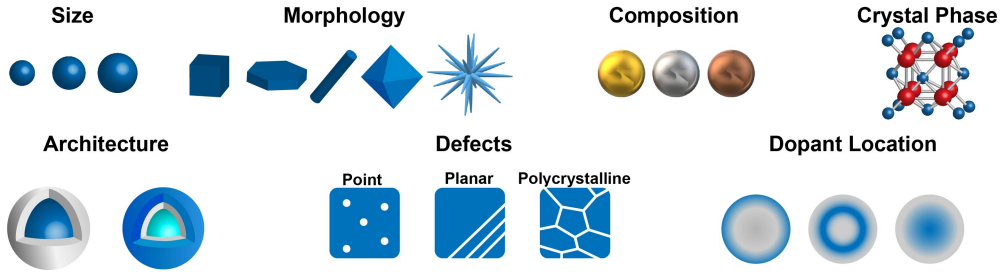

Figure 1.1. Illustration depicting the different nanocrystal structural attributes that can impact nanocrystal properties.

All of these attributes can have profound effects on nanocrystal properties but are often difficult to detect and characterize. Thus, many studies on nanocrystals of similar size, composition, and morphology report a wide variety of properties. For example, Lounis et al. measured the conductivity of two different nanocrystal films made from tin-doped indium oxide (ITO) nanocrystals of the same size and shape, but made from different precursors, and there was an order of magnitude difference in conductivity between the two films.[65] This was due to the location of Sn dopants within the ITO nanocrystals being different between the two sets of nanocrystals.[65] Spinel iron oxide is another commonly used example, where a variety of saturation magnetizations are reported for nanocrystals

of the same size and morphology.[66] This is often due to unintended structural defects and varying thicknesses of a non-magnetic shell within the nanocrystals, both of which are dependent upon the synthetic conditions.[66-67] These discrepancies within the literature make it difficult to establish any accurate structure-property relationships.

All nanocrystal structural attributes are the product of the synthetic conditions used to produce the nanocrystals. Unfortunately, many solution syntheses of nanocrystals are developed through trial and error, often changing multiple synthetic parameters between reports, making it difficult to understand the effect various synthetic conditions are having on nanocrystal properties (this will be discussed in further detail later in this chapter). To better understand how synthetic conditions impact nanocrystal properties, it is imperative that we understand the nanocrystal growth process.

Mechanisms of Nanoparticle Nucleation and Growth in Solution

The formation of nanocrystals in solution is thought to happen in two stages: nucleation and growth.[68-69] Nucleation is the formation of the first nanocrystals,[70] and growth happens when solution monomer continues to react with the nanocrystal surfaces, causing them to grow.[71] There are several theories have been put forth outlining various mechanisms of nanocrystal nucleation and growth. Though none of them are broadly applicable to every nanocrystal synthesis, there are many important and useful concepts that have come from those efforts.

Classical Nucleation and Growth

The theory of classical nucleation and growth stemmed from work by La Mer and coworkers[68-69] and is applicable in many nanoparticle systems. In this theory, molecular precursors convert to reactive monomer species (M). Monomer concentration rapidly increases over a brief period, briefly reaches a concentration above the saturation concentration (M_{Sat}), and then a short burst nucleation occurs with the formation of a finite number of nanoparticles of a critical radius.[68] The critical radius (which happens at $[M]_{Critical}$) is the smallest radius at which a nanoparticle does not redissolve.[68] At this point, growth ensues when solution monomers react with the growing nanoparticles, decreasing the solution monomer concentration below the saturation point, preventing the nucleation of new particles.[68] Growth will continue until the monomer concentration reaches the saturation concentration (M_{Sat}).[68] If monomer concentration falls below the saturation concentration of the solvent, then nanoparticles will redissolve, reforming solution monomer species.[68] Smaller particles will often dissolve first due to their high surface energy, and resulting monomer is then allowed to react with larger particles.[68] This process of smaller nanoparticles dissolving and then monomer regrowing onto larger nanoparticles is called Ostwald ripening and is typically used to describe how nanoparticles can become more uniform and monodisperse over time.[68] A schematic depiction of classical nucleation and growth theory is shown in Figure 1.2 below.

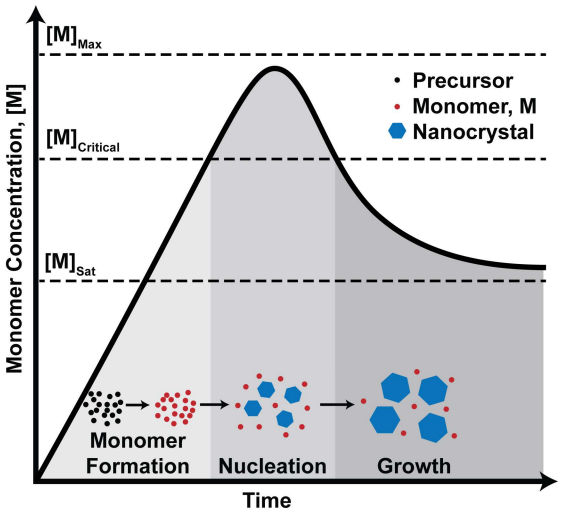

Figure 1.2 Schematic depiction of classical nucleation of growth, showing how the concentration of monomer ([M]) over time impacts nanoparticle formation and growth.

The classical nucleation and growth model has been very useful in describing the formation of nanoparticles and the separation of nucleation and growth, and it is applicable in many nanoparticle systems.[71] However, there are some assumptions that are made that are not appropriate in all systems.[67] For example, one assumption of this theory is that growth is independent of the material properties, but in instances where size influences nanoparticle reactivity, this is not the case.[67] Another assumption is that there is a single surface energy for the growing nanocrystals, but in addition to size, different exposed crystallographic facets have different surface energies, and thus classical nucleation and growth cannot always describe the formation of anisotropic nanoparticles.[72] Further, this theory does not take into account different chemistries that can happen both in solution and at the surface of the nanocrystals. Thus, classical nucleation and growth does not adequately describe all nanoparticle growth and does not allow for the predictability required to be able to intuitively design new nanomaterials.

Continuous Nucleation

Continuous nucleation is another mechanism of nucleation that was first described by Finke and Watzky.[69] This is a two-step mechanism whereby nucleation and growth happen simultaneously. Nucleation happens continuously where monomer forms nanocrystals, and then surface growth happens autocatalytically. This theory is useful in putting forth the notion that both the nature of the monomer as well as the nanoparticles in solution affect each other, though still falls short by not considering the specific chemistries of the monomer or nucleation and surface growth reactions.

Nonclassical Nucleation and Growth

Nonclassical nucleation and growth encompasses other mechanisms that do not fall into the classical or continuous nucleation and growth models.[68-69, 73] These mechanisms can include the formation of clusters, nanoparticle coalescence where nanoparticles react with one another to form larger structures, or intraparticle growth in which diffusion of monomer species along the surface of a nanoparticle leads to a morphology change over time. These processes often driven by high surface energies, which are lowered upon coalescence or rearrangement.

While each of these models put forth useful concepts, they still fail to understand the individual chemistries happening in each system and fail to provide a model that allows for the predictive formation of nanoparticles. Other nucleation models that are seldom discussed take into account the chemistry of the monomer and nanocrystal material. These models describe the reaction of monomer units to form liquid-like phases, amorphous phases, or oligomer units that can polymerize or crosslink, which may then crystallize at

sufficiently high temperatures. While these models are vague and generally poorly understood, they provide a useful framework for thinking about additional pathways to nucleation beyond traditional classical or non-classical nucleation models that account for system-dependent parameters such as the chemical properties of the monomer and intermediates, and material properties of the nanoparticles formed in solution. A depiction of various nucleation pathways[74] is shown in Figure 1.3 below.

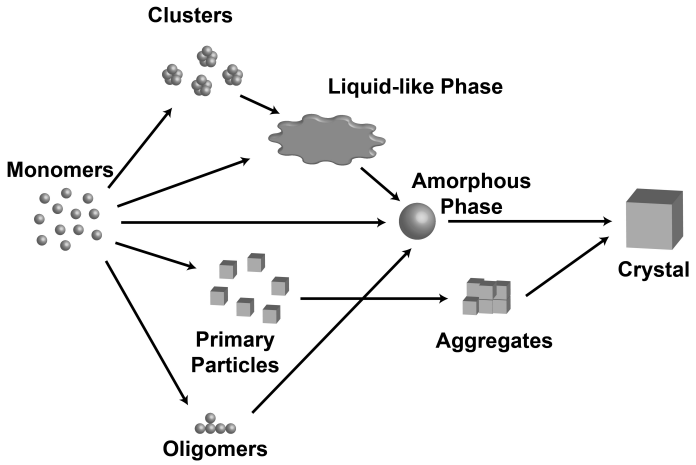

Figure 1.3. Illustration inspired by reference [74] depicting different nucleation pathways from monomer species.

Nanoparticle syntheses are often developed inefficiently through trial and error, and the myriad of different synthetic conditions makes it impossible to understand how each of the synthetic parameters affects nanomaterials properties. To try to understand these, it is important to first understand the common types of reactions that are used to form nanoparticles.

Overview of Solution Phase Syntheses of Metal Oxide Nanoparticles

Metal oxide nanocrystals are a particularly interesting class of nanomaterials due to their ubiquity and unique properties, which have enabled their use in almost every application imaginable, including biomedical applications,[75] sensing,[16, 76-77] energy storage,[7, 22-23] optoelectronics,[64, 78] and beyond. This dissertation focuses on solution methods to synthesize metal oxide nanocrystals due to the level of control afforded by solution-based syntheses, as well as the ease with which one can change various parameters within the syntheses.[67] Solution methods can be divided into two categories: aqueous and nonaqueous routes. The most common aqueous based syntheses are coprecipitation[79-80] and hydrothermal[38, 81-82] syntheses. Both of these form metal oxides through hydrolysis reactions. In coprecipitation syntheses, a precipitating agent, typically an aqueous base, is slowly added to a metal salt solution, either under ambient conditions or at slightly elevated temperatures. Size and morphology are typically controlled by varying the rate of addition of the precipitating agent, concentration of base or metal salt, or by varying the pH of the solution. Hydrothermal syntheses involve mixing metal salts and other additives such as stabilizing ligands in water, sealing the reaction mixture in an autoclave, and heating to high temperatures (and pressures).[38, 41, 81-83] In these syntheses, size and morphology are controlled by varying the temperature, reaction time, metal concentration, or type and concentration of additives used.

Aqueous routes are typically the most straightforward and cost-effective strategies to form metal oxide nanocrystals.[56] However, there are significant drawbacks. The formation of nanoparticles through hydrolysis reactions occurs rapidly, making it nearly impossible to separate nucleation from growth of nanoparticles, which is advantageous for

controlling size and morphology. Rapid hydrolysis also reduces the selectivity of the products formed in the reaction, which often results in polydisperse nanoparticles.[67, 84] Further, some reports have shown that polycrystalline shells can be formed on the surface of nanoparticles using these syntheses,[66-67] further complicating efforts to understand structure-property relationships.

Nonaqueous routes utilize knowledge from organic reactions to more slowly and controllably form nanoparticles. There are two primary nonaqueous reaction routes: thermal decomposition[71] and nonaqueous sol-gel reactions.[85-86] Thermal decomposition involves heating a metal complex (such as a metal carboxylate) to a temperature (often above 300 °C) at which the precursor complex decomposes, forming M• and MO• radical species, which react with each other to form M–O–M bonds, resulting in metal oxide nanocrystals. Nonaqueous sol-gel reactions occur through the formation of M–OH species, that condense with each other to form M–O–M bonds. Each of these two syntheses will be discussed in detail below.

Thermal decomposition syntheses are the most widely studied nonaqueous route to metal oxide nanocrystals and have led to some of the most uniform nanocrystals in the literature.[71, 87] However, because the reaction involves the formation of radical species that quickly and indiscriminately react with each other, it is difficult to control the specific chemistry happening in the reaction. As a result, thermal decomposition syntheses can lead to the formation of defects within the nanocrystals,[66] imparting unintentional and uncontrollable properties. Further, because these syntheses often occur at high temperatures, often under a N_2 atmosphere, this can result in a highly reducing

environment, leading to more reduced phases of metal oxide nanocrystals than may be desired, or even leading to the formation of metal nanocrystals.[84]

Nonaqueous sol-gel routes, on the other hand, allow for higher selectivity of the chemical reactions taking place to form nanocrystals.[85-86] These reactions typically involve mixing a metal precursor (metal halides, acetates, acetylacetonates, carboxylates, etc.) in a solvent (alcohols, amines, ethers, ketones, etc.), which react to form M–OH species, which condense with each other to form M–O–M bonds. Such reactions can occur through alkyl halide elimination, ether elimination, aldol-like condensation, ester elimination, or amide elimination,[85-86] as illustrated in Scheme 1.1.

Scheme 1.1. Depiction of various nonaqueous sol-gel routes to form M–O–M bonds.

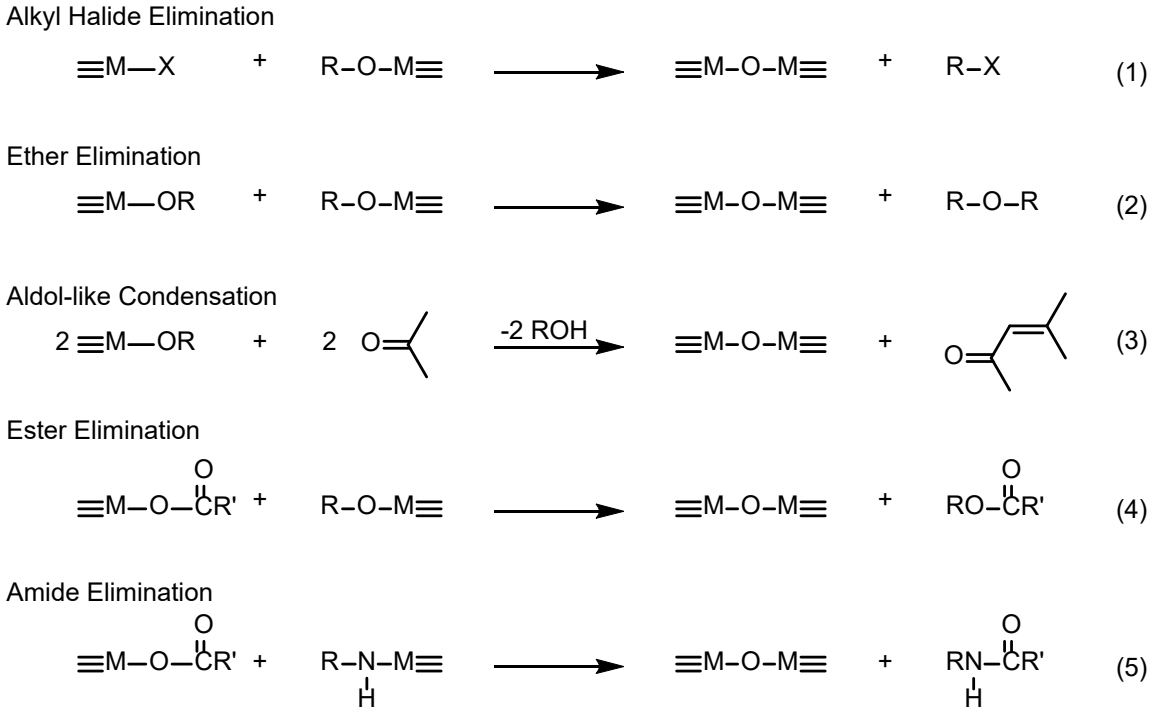

The primary benefit of nonaqueous sol-gel routes is that the reactions can take place at temperatures lower than the thermal decomposition temperature of the precursor

complex,[88] which enables selective control over the reaction chemistry, and therefore more controllable and predictable nanocrystals. It also allows for the exploration of the effect on temperature on nanocrystal syntheses, which may impact whether a synthesis is kinetically vs thermodynamically controlled.[72]

Common Techniques for Nonaqueous Syntheses of Metal Oxide Nanocrystals

There are several different methods with which one could produce metal oxide nanocrystals via either thermal decomposition or nonaqueous sol-gel chemical routes. The most common and simple is the heat-up method, in which a metal precursor, stabilizing ligand, and solvent are simply heated to the desired reaction temperature at a controlled rate, and held at this temperature for a specific amount of time.[71, 89] The size of nanocrystals is determined by the number of nanocrystals formed during nucleation and can be tuned by varying the temperature ramp rate, the temperature, precursor concentration, and stabilizing ligand identity and concentration.[71, 89]

While research has come a long way in the development of these heat-up syntheses, there remain many drawbacks to this method. The synthetic parameters of interest (reaction temperature, precursor concentration, ligand concentration and identity) are often developed through trial and error, without much understanding of how each of the parameters impact nanocrystal growth and resulting properties. Further, nanocrystal growth is highly sensitive to the flux of monomer species (derived from the precursor complex) to the surface of the growing crystals,[90] and this is difficult to control in heat-up syntheses, leading to syntheses that are difficult to reproduce.[91] Monomer flux is often controlled by changing the temperature and precursor concentration. However, once the temperature at which the reaction takes place is reached, the concentration of precursor,

and therefore monomer, rapidly changes, making it difficult to understand how concentration impacts nanocrystal growth. Additionally, changing the reaction temperature might require one to change the reaction solvent. This is especially true of reactions that are carried out under reflux, where the reaction temperature is set by the boiling point of the solvent.[87] Because two parameters (temperature and solvent) must be changed at once, it is impossible to systematically understand the effect of each parameter on the growth process and resulting nanocrystal properties.

Another common synthetic procedure is the hot-injection method.[92-93] The hot-injection method typically involves rapidly injecting a solution by hand containing the metal precursor into a hot solution containing solvent and/or stabilizing ligands. The primary benefit of the hot-injection method is that it introduces a high level of supersaturation from the start of the synthetic procedure, which enables faster nucleation and narrower size dispersities of nanocrystals.[93] Like heat-up methods, hot-injection methods have been developed for many different materials of different sizes and shapes, but still suffer significant drawbacks. Again, the concentration of precursor is difficult to control given that nucleation may begin before all of the precursor is injected, the injection rate is not constant given that it is usually done by hand, and once nucleation starts the concentration of precursor is rapidly and dynamically changing. Further, the rapid injection of a lower temperature precursor into a hot solution drastically and unpredictably changes the reaction temperature, which is known to affect nanocrystal growth processes.

The last method that will be discussed is the slow injection approach, which circumvents many of the drawbacks of heat-up and hot-injection methods.[66, 88, 94-95] This approach involves *slowly* injecting a solution containing precursor into a hot solvent using

a syringe pump. Stabilizing ligands can be in either the precursor solution or in the solvent. The injection rate is easily controlled by the syringe pump, which injects precursor at a slow enough rate such that the temperature change of the reaction solution is negligible. If the formation of monomer species from the precursor complex is sufficiently fast, then the flux of monomer to the nanocrystal surface is controlled by the injection rate. Another primary advantage of slow injection syntheses is that the size of the nanocrystals is not determined by the nucleation event, which is highly sensitive and difficult to control, but by the amount of precursor added, which is far more controllable. Since the reaction happens more slowly, and because the final size of the nanocrystals is determined by the amount of precursor injected, nanocrystal formation can be examined during the course of the reaction by taking aliquots at various time points during the injection.

Slow Injection Esterification Synthesis

The Hutchison lab has developed a nanocrystal synthesis that combines the slow injection approach with ester elimination chemistry that has led to a number of size-tunable, uniform metal oxide nanocrystals.[66, 78, 88, 95-96] In a typical synthesis, a precursor solution is made by heating a metal acetate or metal acetylacetonate in excess oleic acid (stabilizing ligand), which forms a metal oleate and expels acetic acid or acetylacetone. This solution of metal oleate and excess oleic acid is slowly injected via syringe pump into oleyl alcohol, typically between 230 and 290 °C. The metal oleate reacts with the oleyl alcohol, forming an ester (oleyl oleate) and a metal hydroxy species. Oleyl alcohol acts as both a solvent and a reagent, and because it is in high excess it drives the esterification reaction forward. The reactive metal hydroxy species then condense with each other,

forming M–O–M bonds and eliminating water, and eventually nucleating nanocrystals. While the formation of water is typically detrimental to nanocrystal syntheses, because the precursor is slowly injected, water is rapidly removed before it has a chance to build up in solution. The hydroxylated surface of the nanocrystals remains reactive, enabling further reaction between the nanocrystals and solution monomer, allowing for slow, controlled, continuous growth of the nanocrystals. This process is shown in Scheme 1.2.

Scheme 1.2. Depiction of steps involved in the slow injection esterification synthesis developed by the Hutchison lab.

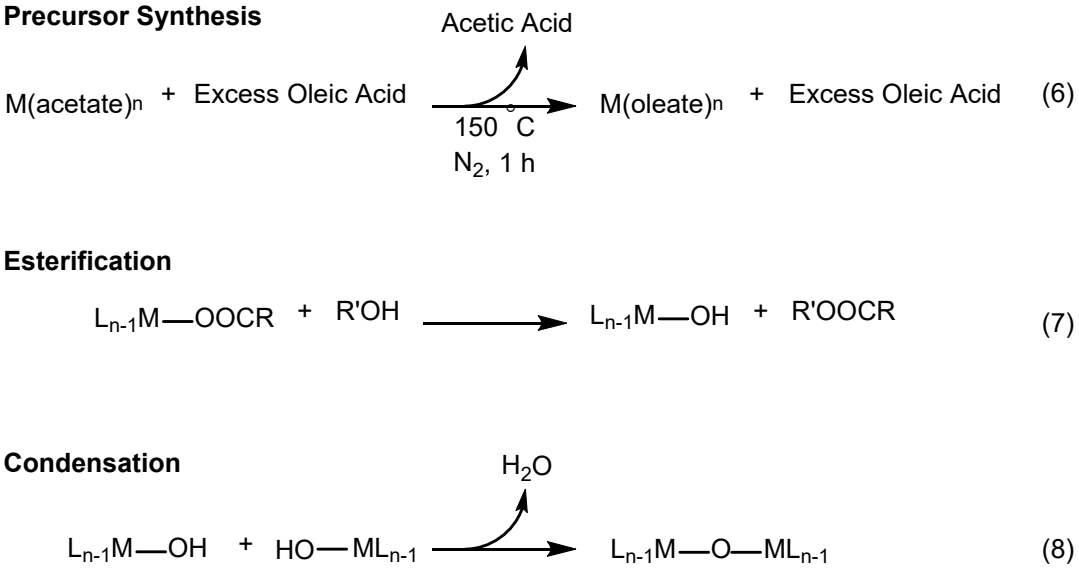

The slow injection synthesis developed by the Hutchison lab has been shown to produce a number of uniform metal oxide nanocrystals, including indium oxide (In_2O_3), cobalt oxide (CoO), manganese oxide (Mn_3O_4), zinc oxide (ZnO), and iron oxide (γ-Fe_2O_3 and Fe_3O_4).[88] Of the metal oxides explored by this synthesis, growth processes of indium oxide[64, 78, 90, 95, 97] and iron oxide[66-67, 84] have been studied the most. For both of these metal

oxides, the volume of precursors increases linearly with the amount of precursor added, which indicates a living growth mechanism and enables sub-nanometer size control of a wide range of sizes (6-22 nm for In_2O_3, 6-18 nm for Fe_3O_4).[96] Indium oxide was found to be able to homogeneously incorporate a number of dopants with high efficacy,[78] and iron oxide was found to have superior magnetic properties compared to most reports in the literature due to the existence of fewer defects (a thinner non-magnetic shell) in the nanocrystals.[66]

An advantage of this slow addition synthesis is that each parameter (temperature, precursor identity and amount injected, and injection rate) can be systematically and independently varied, enabling more controlled studies of the nanocrystal growth process. For example, former members of the Hutchison lab were able to examine the role of injection rate (and thus monomer flux) on the growth of indium oxide nanocrystals at a constant temperature, a study not previously possible with other synthetic methods.[90] In this study, it was determined that higher monomer flux led to increasingly branched nanocrystals as a result of limited surface diffusion that occurs when adsorbed monomer is sterically hindered from diffusing in the presence of high monomer concentration. The effect of reaction temperature independent of injection rate was also examined. From this study, we learned that more uniform nanocrystals were achievable by using a relatively slower injection rate and higher reaction temperature, and that larger nanocrystals form at higher temperatures as the result of initially forming fewer nanocrystals.[90]

Another systematic study that was enabled was the examination of the role of iron precursor oxidation state and ligation on the morphology of iron oxide nanocrystals.[84] In this study, Plummer and Hutchison were able to determine that a deficiency of Fe(II)

species led to twinning crystal defects, leading to triangular and other anisotropic shapes. The Fe(II) deficiency was determined to occur both as a result of the precursor starting material (iron(III) acetylacetonate as opposed to iron(II) acetate), and as a result of remaining acetylacetonate ligands, which limited the amount of Fe(III) species that could be reduced to Fe(II). This study showed that beyond temperature and injection rate, the precursor oxidation state and coordinating ligand were vitally important in determining the resulting nanocrystals.[84]

These studies highlight how the Hutchison lab has been able to utilize the slow injection synthesis. Not only is it a means to uniform, size-tunable metal oxide nanocrystals with few defects, but the unique attributes of the synthesis enable close examination of the growth process itself. This is enabled by the ability to systematically tune one parameter at a time, as well as take aliquots of the reaction mixture throughout the precursor addition, allowing one to examine the growth at specific time points. This dissertation leverages these attributes of the slow injection synthesis to further examine the growth process by varying parameters not previously explored.

Extending the Slow Injection Esterification Synthesis to Other Materials

While the slow injection esterification synthesis has been adapted to several different metal oxides, we have found it challenging to extend it to certain materials. For example, attempts have been made to produce aluminum oxide, titanium dioxide, tin oxide, and zirconium oxide without success. This could be due to a number of different factors. Precursor reactivity, for example, could lead to insufficient esterification or condensation,

inhibiting the formation or growth of nanocrystals. In these cases, it is possible that the use of different reagents or a higher temperature is required.

Despite these initial challenges, it is likely that the slow injection synthesis can be extended to many other materials if the right parameters are used. To be able to predict these parameters, we need to further understand what additional parameters can be tuned beyond temperature and injection rate. This dissertation explores several different aspects of nanocrystal growth for two different metal oxide systems: cerium oxide[98] and Sn-doped indium oxide (ITO). Cerium oxide was chosen as a system to study because the slow injection synthesis had not previously been expanded to cerium oxide, and because cerium can be present as Ce^{3+} and Ce^{4+}, both in molecules and as different oxide materials, allowing us to study the role of precursor oxidation state and reducing vs oxidizing reaction environment on the growth and composition of cerium oxide nanocrystals.[98] ITO was chosen as an additional system to study the role of reagent choice (oleyl alcohol vs oleylamine) on nanocrystal growth. The ITO system was chosen because indium oxide was the most well-studied system regarding metal oxides that could be synthesized by our slow injection synthesis, In^{3+} is redox stable, and because ITO is of technological interest as a plasmonic and electrocatalytic material.

ITO Nanocrystals as Plasmonic Materials

When doped at sufficiently high levels with aliovalent atoms such as Sn, In_2O_3 exhibits interesting plasmonic behavior.[64] Plasmonic nanocrystals are nanocrystals whose electrons interact with incident light of a particular energy, resulting in the absorbance of

light at that energy. This energy is dependent upon the number of free electrons in the crystal lattice, which is directly related to the concentration of dopants within the crystal.[64] Plasmonic nanocrystals have potential applications in sensing,[99-101] telecommunications,[102-103] spectroscopy,[104-105] smart windows,[106-108] and biomedicine,[109-110] if the energy of the localized surface plasmon resonance (LSPR) can be appropriately tuned. Plasmonic metal oxide nanocrystals are especially promising for this since their LSPR can be tuned through composition (i.e. dopant identity, concentration, and radial placement),[64] whereas the LSPR in metal nanocrystals is fixed.

The slow injection esterification synthesis has been used to gain greater synthetic control over doped indium oxide nanocrystals, and have allowed for exquisite control over the concentration of tin introduced into the lattice, which is tuned by altering the ratio of Sn and In oleate in the precursor.[95-96] Further, it has allowed for precise radial placement of tin dopants within the nanocrystal (either surface segregated or core segregated) by alternating between pure a In oleate precursor and mixed In/Sn oleate precursors.[64] This has enabled unprecedented tuning of ITO plasmonic behavior while utilizing a single synthetic procedure, providing predictable control over structure and properties.

Beyond engineering the nanocrystals themselves, the plasmonic response of nanocrystal thin films can be altered based upon the processing method used to fabricate the films.[102] Chapter IV in this dissertation describes in detail how solution processing of different batches of nanocrystals (with varying compositions) is used to sculpt the plasmonic response, which is useful in applications that may need absorption over a broad range of wavelengths or multiple selective wavelengths, as is the case for telecommunications and smart windows applications.

ITO Nanocrystals as Electrocatalysts for the Electrochemical Reduction of CO_2

Indium- and tin-based oxides have been explored as promising electrocatalysts for the electrochemical transformation of CO_2 into formate, which may be a promising way to utilize captured CO_2.[111] This transformation requires highly reducing electrochemical conditions, which is known to reduce the oxides to their metal forms. Despite this reduction of the electrocatalysts, several studies have reported that a metastable oxide persists on the metals under reducing conditions that is thought to be important for the electrocatalytic reduction of CO_2.[112-115]

Since these findings, efforts have been put forth to understand the role of nanoscale structure such as size and morphology on the electrocatalytic performance of these indium- and tin-based oxide catalysts.[114] For example, there have been claims that there is size-dependent reactivity of indium oxide-derived CO_2 reduction electrocatalysts.[116] Due to the level of size and compositional control we have been able to demonstrate for indium oxide and ITO nanocrystals, we explored whether the slow injection synthetic platform could be applied to ITO nanocrystal electrocatalyst films to evaluate the effect of nanoscale structure on the activity and selectivity.[111]

However, a recent study from Pardo et al. showed that tin-doped indium oxide films undergo dynamic structural rearrangement during the electrochemically reducing conditions necessary for CO_2 reduction.[117] This raises questions about the stability of indium- and tin-based catalysts under operating conditions, and how the structures of the catalysts are contributing to the overpotential necessary to drive the reaction, or the observed CO_2 reduction products. While many studies have examined the structural rearrangement of metal-based CO_2 reduction electrocatalysts,[118-119] few reports have

examined the structural evolution of indium- and tin-based electrocatalysts. Chapter V of this dissertation explores the stability and evolution of nanoscale and microscale structure of ITO nanocrystal films under CO_2 reduction electrochemical conditions.

Dissertation Overview

This dissertation will expand the utility of the slow injection nanocrystal synthesis and explore how parameters such as temperature, solvent identity, and reaction atmosphere impact nanocrystal growth. It also examines applicability of ITO nanocrystals in plasmonic and electrocatalytic applications. In Chapter II, the slow injection synthesis is expanded to a new metal oxide, cerium oxide, and the growth process is carefully examined, allowing the understanding of synthetic parameters on nanocrystal growth. Chapter III examines the growth of indium oxide in oleylamine, which occurs through amide-elimination instead of ester-elimination. Chapters IV and V explore the use of solution-processed ITO nanocrystals in band-stop filter and electrocatalytic applications.

Cerium oxide nanocrystals have size- and shape-dependent properties that are potentially useful in a variety of applications if these structural attributes can be controlled through synthesis. Various syntheses have been developed in attempts to access different sizes and shapes, but little is known about selecting reaction conditions to predictably control the growth, and therefore properties, of the nanocrystals. In Chapter II we investigate the role of cerium precursor oxidation state, reaction atmosphere, and acetic acid ligation on the size and shape of cerium oxide nanocrystals. A continuous addition synthesis allowed us to vary individual reaction parameters to better understand how each

affects growth and morphology. Under N_2 the synthesis leads to either irregular shapes or nanoribbons, whereas the same synthesis under air leads to size-tunable nanocubes. To determine whether air might be oxidizing the cerium precursor and changing its reactivity, we synthesized Ce(III) and Ce(IV)-rich oleate precursors and found that the oxidation state of the precursor has little effect on the resulting nanocrystals. In fact, we found that Ce(IV) oleate is readily reduced to Ce(III) at 230 °C in the reaction medium. The significant role of air during synthesis therefore suggests that oxygen is altering the surface reactivity of the nanocrystals, as opposed to the precursor. We investigated the origin of nanoribbon formation and found that the presence of acetate ligands is responsible for nanoribbon formation in syntheses under N_2, with more acetate leading to longer nanoribbons. These insights were used to identify conditions to predictably grow various sizes and shapes of nanocubes and nanoribbons. The findings elucidate the effects that various synthetic parameters can have on cerium oxide nanocrystal synthesis and suggest that redox reactivity may influence growth and properties in other syntheses where changes in oxidation state occur for the precursor or the nanocrystal surface. This chapter was previously published as Knecht, T. A.; Hutchison, J. E. Reaction Atmospheres and Surface Ligation Control Surface Reactivity and Morphology of Cerium Oxide Nanocrystals During Continuous Addition Synthesis. *Inorg. Chem.* **2022**, *61*, (11), 4690–4704. I performed all experiments in this work, and wrote the manuscript with editorial assistance from James Hutchison.

The rate at which precursor is converted to reactive monomer species is an important parameter in nanocrystal synthesis that can have profound effects on the size, shape, and other properties of nanocrystals. Control over the precursor conversion rate is

therefore essential if we are to reliably synthesize nanocrystals with predictable properties. Many researchers have tried to control the precursor conversion rate by varying the reaction temperature, temperature ramp rate, or by modulating the precursor reactivity. However, varying the temperature could also vary the chemical reactions taking place, making it difficult to interpret how precursor conversion rate influences nanocrystal properties. An alternative approach to influencing the precursor conversion rate is to add reagents that either speed up or slow down that conversion rate. Reagent-driven nanocrystal syntheses provide an opportunity to study the impact of precursor conversion rate on nanocrystal formation and growth. The continuous addition synthesis developed by the Hutchison lab is a highly controlled reagent-driven synthesis that allows us to examine the rate of precursor conversion more closely, specifically by altering the primary reagent used: oleyl alcohol or oleylamine. To form reactive monomer species, the oleylamine reacts with the metal carboxylate precursor through amidation, while oleyl alcohol reacts with the metal carboxylate precursor through esterification. We show that the amidation reaction occurs more rapidly than esterification, resulting in faster precursor conversion rate, allowing us to study that effect on ITO nanocrystal formation and growth. We find that the growth rate of ITO nanocrystals can be tuned by controlling the number of nanocrystals that are formed, with increasing oleylamine content (and thus increasing precursor conversion rate) leading to fewer, larger nanocrystals. These results highlight how the earliest nanocrystal formation stages can be tuned, offering yet another handle with which we can tune nanocrystal size. Portions of this chapter may appear in a forthcoming publication coauthored by myself, Brandon M. Crockett, and James E. Hutchison. I performed all

experiments and writing in this work, Brandon M. Crockett provided insightful discussion, and James E. Hutchison provided editorial assistance to the writing of this chapter.

Plasmonic band-stop filters with tunable optical absorbance in the near- and mid-IR are important for wireless communications, bioimaging, and filtering applications. However, their design is constrained by the limited tunability of individual components and complex fabrication techniques. In Chapter IV, we demonstrate a method to overcome these limitations that employs mixtures of nanocrystals to predictably sculpt the combined localized surface plasmon resonance (LSPR) for band-stop filters. The additive nature of the LSPR optical absorbances of tin-doped In_2O_3 (ITO) nanocrystals was used to control the combined absorbance in a nanocrystal thin film. The optical properties of the nanocrystals were modulated via a low-temperature esterification synthesis and an inexpensive solution-processing fabrication method, spin-coating, was used to produce the films. Because of the additive nature of the LSPR absorbance of the nanocrystals, the absorption of the films can be easily predicted and designed by summing the spectra of the individual components over the range of 6,000 – 1,000 cm^{-1}. By design and synthesis of individual nanocrystals with tailored optical properties, and selecting the right combinations of nanocrystals to incorporate into films, both wide and narrow band-stop filters were easily constructed. This chapter was previously published as Krivina, R. A.; Knecht, T. A.; Crockett, B. M.; Boettcher, S. W.; Hutchison, J. E. Sculpting Optical Properties of Thin Film IR Filters Through Nanocrystal Synthesis and Additive, Solution Processing. *Chem. Mater.* **2020**. *32* (19), 8683–8693. Copyright 2020 American Chemical Society. Raina Krivina and I performed all experiments under the guidance of James

Hutchison. Raina Krivina and I wrote the manuscript with editorial assistance from James Hutchison and Shannon Boettcher.

The electrochemical reduction of CO_2 into fuels using renewable electricity presents an opportunity to utilize captured CO_2. Electrocatalyst development has been the primary focus of research in this area. This is especially true at the nanoscale, where researchers have focused on understanding nanostructure-property relationships. However, electrocatalyst structure may evolve during operation. Indium- and tin-based oxides have been widely studied as electrocatalysts for CO_2 reduction to formate, but evolution of these catalysts during operation is not well-characterized. In Chapter V, we report the evolution of nanoscale structure of tin-doped indium oxide nanocrystals under CO_2 reduction conditions. We show that sparse monolayer nanocrystal films desorb from the electrode upon charging, but thicker nanocrystal films remain, likely due to increased number of physical contacts. Upon applying a cathodic voltage of -1.0 V vs RHE or greater, the original 10-nm diameter nanocrystals are no longer visible, and instead form a larger microstructural network. Elemental analysis suggests the network is an oxygen-deficient indium-tin metal alloy. We hypothesize that this morphological evolution is the result of nanocrystal sintering due to oxide reduction. These data provide insights into the morphological evolution tin-doped indium oxide nanocrystal electrocatalysts under reducing conditions and highlight the importance of post-electrochemical structural characterization of electrocatalysts. This chapter was previously published as Knecht, T. A.; Boettcher, S. W.; Hutchison, J. E. Electrochemistry-Induced Restructuring of Tin-Doped Indium Oxide Nanocrystal Films of Relevance to CO_2 Reduction. *J. Electrochem. Soc.* **2021**, *168*, 126521. Copyright 2021 The Electrochemical Society. I performed all

experimental work and writing under the guidance of James Hutchison and Shannon Boettcher.

Chapter VI of this dissertation will detail conclusions and future directions for the work in this dissertation. I am the sole author to the writing of this chapter.

CHAPTER II

REACTION ATMOSPHERE AND SURFACE LIGATION CONTROL SURFACE REACTIVITY AND MORPHOLOGY OF CERIUM OXIDE NANOCRYSTALS DURING CONTINUOUS ADDITION SYNTHESIS

This chapter was previously published as Knecht, T. A.; Hutchison, J. E. Reaction Atmosphere and Surface Ligation Control Surface Reactivity and Morphology of Cerium Oxide Nanocrystals During Continuous Addition Synthesis. *Inorg. Chem.* **2022**, *61*, 4690–4704.

Introduction

Inorganic nanomaterials have been studied widely because of their interesting and useful properties that are influenced by their size, shape and atomic-level surface structure.[1-4] Understanding the interplay between the nanoscale structural dimensions and the surface chemistry is essential to control nanocrystal properties and growth mechanisms.[3, 5-6] Cerium oxide nanocrystals provide a compelling example – their reactivity is dominated by surface oxygen vacancy defects, the presence of which are influenced by size and shape.[2, 7-15] The size and shape are, in turn, significantly influenced by the growth processes.[16-17] It has become clear that atomic structure of the nanocrystal surfaces influence the growth process, too.[3] Further understanding of this interplay between

size, nanocrystal surface chemistry and growth is therefore needed in order to design nanocrystals with the properties of interest. Here, we investigate cerium oxide nanocrystal synthesis under continuous growth conditions as a means to understand the influence of key reaction conditions on the nanocrystal growth process and resulting nanocrystal morphology.

Cerium oxide nanomaterials are attractive catalysts for a number of reactions including alcohol oxidation,[18-22] CO oxidation,[23-26] and CO_2 reduction.[11, 27-30] The enhanced catalytic activity for these materials is influenced by the presence of oxygen vacancies, which are believed to depend upon nanocrystal size and morphology.[31-33] Vacancy formation is often attributed to the facile redox chemistry between Ce^{4+} and Ce^{3+}, particularly at the surface, where reduction of two Ce^{4+} atoms to Ce^{3+} results in the formation of an anionic oxygen vacancy.[12, 14, 34-38] Oxygen vacancy concentration is dependent upon the crystallographic facet exposed.[2, 39] Further, many studies have claimed that surface oxygen vacancy (and thus Ce^{3+}) content increases with decreasing nanocrystal size due to higher surface area and nanoscale strain.[32] Thus, understanding the size- and shape-dependent properties of nanoscale cerium oxide is critical for tailoring these materials towards desired applications.

Interest in harnessing the surface-dependent catalytic properties in cerium oxide nanocrystal materials has spurred development of syntheses with precise control over size and morphology. A number of synthetic techniques have been developed for cerium oxide nanomaterials, leading to the formation of a number of sizes and morphologies (cubes,[16, 40-42] octopods,[43] wires,[44-46] tubes,[35] rods,[8, 40-41, 44, 47-52] and more[53-55]). Although precipitation and hydrothermal methods have been widely used, thermal decomposition

syntheses in organic media are often advantageous compared to aqueous routes because they typically lead to more uniform nanocrystals.[4] Syntheses in organic media typically involve heating a metal precursor in a mix of solvent (often oleylamine and/or 1-octadecene) and stabilizing ligand (such as oleic acid) to reflux.[32, 56-58] Several syntheses in organic media have been developed to access different cerium oxide nanocrystal sizes and morphologies. Yu et al.[55], Lee et al.[32], and Krishnan et al.[59-60] have shown a wide variety of nanocrystal sizes (3-10 nm) and morphologies (nanowires, spheres, tadpoles, butterflies, rods, square plates, and more) via thermal decomposition of various Ce precursors under varying reaction conditions. While these studies have produced a variety of cerium oxide nanostructures, the wide range of synthetic parameters and different reaction pathways and make it difficult to predictably control other sizes and morphologies of cerium oxide nanocrystals. Further, the thermal decomposition of the precursor generates a number of species, including M• and MO• radical species that are known to introduce defects into the nanocrystal structure.[4, 58]

The synthetic conditions influence the concentration of oxygen vacancies, as well as the size and morphology. For instance, Taniguchi et al. found that the choice of cerium precursor influenced both surface oxygen vacancy content and morphology.[16] They proposed that the use of a Ce(III) precursor (compared to starting with a Ce(IV) precursor) led to higher surface Ce(III) content, which induced oriented attachment between nanocrystals due to the higher surface reactivity of the Ce(III). Further, the presence of different counter anions in the precursor starting material has been shown to influence growth and resulting Ce(III) content.[2, 41] The reaction atmosphere can also alter cerium oxide formation. Lin et al. found that an air (oxidizing) atmosphere promoted the growth

of crystalline cerium oxide nanocrystals, whereas performing a synthesis under Ar led to amorphous particles.[50] While these studies showed how different synthetic parameters influence the nanocrystal properties, the influence of the nanocrystal structure itself on the growth process remains largely unknown.

Atomic-scale surface structure has been shown to be an important parameter in controlling the nanocrystal growth process in other inorganic oxides.[3-4] For example, Cooper et al. found that spinel iron oxide nanocrystals had a size-dependent growth rate, with smaller sizes growing faster than larger sizes of nanocrystals.[3] This was attributed to the presence of tetrahedral iron vacancies present in nanocrystals below 6 nm. Given the surface-dependent reactivity in cerium oxide nanocrystals, it is likely that the surface also influences nanocrystal growth, too.

Studying the impact of nanocrystal surfaces on growth is challenging when using thermal decomposition syntheses: growth happens quickly, making it difficult to monitor the reaction over time. Further, it is often the case that multiple parameters must be changed simultaneously to control the size or morphology of particles. Size and shape are also often controlled by altering the precursor starting concentration. However, the precursor concentration fluctuates once growth begins, making it difficult to fully understand or control the nanocrystal growth mechanism. A continuous addition synthesis, wherein a precursor is continuously introduced into the reaction medium, could provide an alternative route that enables more precise control over reaction conditions and makes it easier to study the influence of changes in reaction conditions.[61]

Our group has developed a low-temperature continuous addition strategy to synthesize a number of metal oxide nanocrystals.[5, 62-63] This synthesis is performed at temperatures below thermal decomposition, which has enabled studies of the nanocrystal growth process in ways that are not possible in traditional heat-up methods.[6, 58, 64-65] Reaction parameters such as temperature, solvent, and precursor composition also remain constant throughout the synthesis, and the reaction mixture can be sampled throughout the reaction to easily monitor growth.[4] Combined, these attributes provide an opportunity to study the role of each synthetic parameter individually, as well as monitor the reaction over time to better understand the growth process.

Herein we utilize a continuous addition synthesis to investigate cerium oxide nanocrystal growth under controlled conditions that allow us to understand the influence of reaction atmosphere, precursor oxidation state, and a small molecule additive (acetic acid) on the morphologies. Our findings suggest that these reaction parameters influence the surface reactivity of the nanocrystals, which in turn influences nanocrystal growth. We further use these findings to predictably produce specific cerium oxide morphologies (cubes and ribbons) and sizes.

Experimental

Materials

Cerium(III) acetate sesquihydrate (99.99%), cerium(IV) ammonium nitrate (99.5%), and oleyl alcohol (85%) were purchased from Alfa Aesar. Cerium(III) nitrate hexahydrate (99%), oleic acid (90%), and 1-octadecene (90%) were purchased from

Sigma-Aldrich. Sodium oleate (> 97%) was purchased from TCI America. Hexanes (99.9%), toluene (99.9%), acetone (99.5%), and ethanol (200 proof) were acquired from Fisher Chemical. All chemicals were used as received.

Synthesis of precursors

Initial syntheses of cerium(III) oleate by ligand exchange were conducted using cerium(III) acetate hydrate as the source of cerium. Cerium(III) acetate hydrate and oleic acid were mixed in a glass scintillation vial in a ratio of 2 mL oleic acid per mmol of cerium (~6 equivalents of oleic acid). This mixture was magnetically stirred in an oil bath at 150 °C for 1 h under the flow of N_2. This precursor was used without further purification. Cerium(III) oleate used for thermogravimetric analysis (TGA) was synthesized using the same procedure except a stoichiometric amount of oleic acid (3 mmol oleic acid per mmol cerium(III) acetate hydrate) was used.

Synthesis of cerium(IV) oleate by salt exchange was developed in an analogous manner as a previous literature report for synthesizing Ce(III) oleate.[66] The synthesis was conducted using cerium(IV) ammonium nitrate (CAN) and sodium oleate. 10.97 (10 mmol) of CAN and 24.33 (40 mmol) of sodium oleate were mixed in 100 mL hexanes, 50 mL 18.2 MΩ H_2O, and 50 mL ethanol. This mixture was stirred at room temperature under atmospheric conditions overnight. The hexanes layer was then separated using a separatory funnel and washed with nanopure H_2O three times. The gelatinous cerium(IV) oleate product was then further purified by precipitation with ethanol and centrifuged at 7000 RPM for 5 min. The supernatant was decanted, the product redispersed in a small volume of hexanes, precipitated with acetone, and centrifuged again. This was repeated for a total of three washes in acetone. This procedure was developed with the intent of thoroughly

removing any nitrate contaminants, and to recover a solid final product. The final product was a waxy dark brown solid. Yield of the Ce(IV)-rich oleate was ~ 25%. The low yield was due to the difficulty associated with recovering pure, solid product from the initial gelatinous material. For use in subsequent nanoparticle syntheses, excess oleic acid was added such that the total ratio of oleic acid to cerium was 6:1 (assuming that there were already four oleate ligands per cerium). An equal volume of 1-octadecene was also added so that the solution was not too viscous to pass through an 18-gauge needle. This solution was stirred at 150 °C under flowing N_2 for 1 h prior to nanoparticle syntheses to ensure the solution was sufficiently mixed and free of water.

Synthesis of cerium(III) oleate by salt exchange was conducted using the same procedure as for the Ce(IV)-rich oleate, except 8.68 g (10 mmol) of $Ce(NO_3)_3 \cdot 6H_2O$ and 18.17 g (30 mmol) of sodium oleate were used as the starting materials. Like the Ce(IV)-rich oleate, the initial Ce(III) oleate product made by salt exchange was a gelatinous material. After purification, the final product was a light brown powder. Yield was ~ 26%. For subsequent use in nanoparticle syntheses, excess oleic acid was added such that the total oleic acid/oleate content per cerium was 6:1, and this was calculated assuming there were three oleate ligands per cerium in the purified product. An equal volume of 1-octadecene was added to the precursor so that nanoparticle syntheses using this precursor would be comparable to syntheses conducted using the Ce(IV)-rich oleate.

Synthesis of nanoparticles

In a 50 mL three-neck round-bottom flask, 18 mL of oleyl alcohol was heated to the desired reaction temperature (230, 260, 290, or 315 °C) using a heating mantle and Glas-Col DigiTrol II temperature controller. The three necks were capped with rubber

septa. The desired reaction atmosphere (N_2 or air) was flowed through a desiccant and then through the headspace at a rate of ~120 mL min^{-1} before exiting out of an 18-gauge purge needle. In a separate single-neck 50 mL round-bottom flask, a separate solution of oleyl alcohol (which was to be injected alongside the cerium oleate precursor) was heated to 150 °C under N_2 for 1 h to remove any water. For nanoparticle syntheses conducted under N_2, all oleyl alcohol was sparged with N_2 for 30 min prior to heating to remove dissolved oxygen.

The desired precursor was then loaded into a BD plastic syringe equipped with a 6-inch 18-gauge needle. An equal volume of the oleyl alcohol heated to 150 °C was loaded into a separate identical syringe and needle. These two syringes were then assembled into a KD Scientific syringe pump and the solutions were injected into the three-neck reaction flask at a specific rate. An injection rate of 0.06 mL min^{-1} was used for syntheses conducted using cerium(III) oleate made by acetate ligand exchange. Because 1-octadecene was used to dilute the cerium(III) and cerium(IV) oleate precursors that were made through salt exchange, an injection rate of 0.12 mL min^{-1} was used for nanoparticle syntheses using these precursors in order to keep the overall monomer flux the same. The total injection time for a typical 2 mmol synthesis using Ce(III) oleate is 67 min, with the final reaction volume being 26 mL. After the injection, nanocrystals were purified by centrifugation in acetone three times (7000 RPM for 5 min). Yields were calculated for syntheses with the Ce(III) oleate precursor to be 87% under air, and 60% under N_2.

Characterization of precursors and nanoparticles

Thermogravimetric analysis (TGA) of the cerium oleate precursors was conducted on a TA Instruments Q500 TGA. Temperature was ramped from 25 to 600 °C at a rate of 5 °C min^{-1} under N_2. To prepare the TGA samples of the precursors, the precursors were precipitated with acetone and separated by centrifugation (7000 RPM for 5 min).

Fourier transform infrared (FTIR) characterization of the precursors and nanoparticle reaction aliquots was performed using a Nicolet 6700 FTIR spectrometer with an attenuated total reflectance (ATR) accessory from Thermo Fisher.

X-ray photoelectron spectroscopy (XPS) measurements were performed on a Thermo Scientific ESCALAB 250 spectrometer. Peak binding energies were referenced to the C 1s hydrocarbon peak at 284.8 eV. Samples of the Ce(III) and Ce(IV)-rich oleate precursors were prepared by dispersing the purified solid products in hexanes, drop-casting onto a conductive carbon substrate, and allowing the hexanes to evaporate in air. Nanoparticle samples were prepared by drop-casting solutions of nanoparticles in toluene onto conductive carbon substrates and allowing the toluene to evaporate in air.

For X-ray diffraction (XRD) characterization, samples were prepared by drop-casting a concentrated (~100 mg mL^{-1}) solution of nanoparticles onto a (100) Si wafer. Measurements were conducted with a Rigaku Smartlab diffractometer using Bragg–Brentano geometry and Cu Kα radiation. Data were collected from 20 to 65° 2θ with a 0.01° step size at a rate of 0.15° min^{-1}.

For transmission electron microscopy (TEM) characterization of the nanoparticles, 400 mesh carbon-coated copper grids (Ted Pella) were dipped into dilute (~0.5 mg mL^{-1})

solutions of nanoparticles in toluene. An FEI Tecnai Spirit TEM was used to acquire standard-resolution images, and a Titan 80-300 electron microscope was used to acquire high-resolution images.

Results and Discussion

Design and evaluation of initial synthesis conditions

We have previously shown that the slow injection of a metal oleate precursor to hot (> 200 °C) oleyl alcohol results in monodisperse nanocrystals for a number of metal oxides.[4-5, 62-63] The proposed mechanism for this reaction is detailed in Figure 2.1. In this synthesis, the metal oleate undergoes esterification with the oleyl alcohol, leading to reactive metal-hydroxy monomer species.[62-63] These species then condense with each other to form M–O–M bonds, creating nanocrystals.[62-63] The surface of the nanocrystals remains reactive, allowing solution monomer to be added continually to the surface.[62-63]

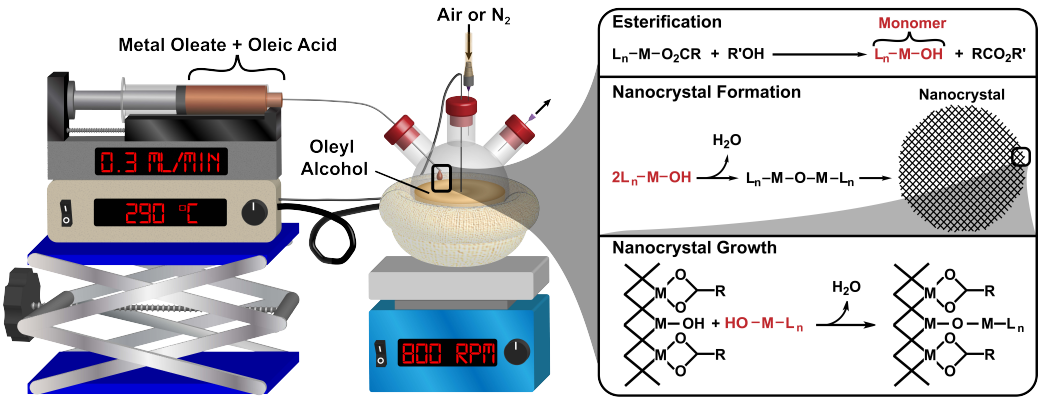

Figure 2.1. Continuous growth synthesis of metal oxide nanoparticles. The illustration shows the reaction setup. The mechanism of nanoparticle formation and growth is depicted next to the illustration.

To establish an initial set of reaction conditions to synthesize cerium oxide nanocrystals, several factors had to be considered. The first is the composition and preparation of the metal precursor. In the preparation of other metal oxides, we prepared precursors by mixing a metal acetate or metal acetylacetonate in 6 equivalents of oleic acid and heating while stirring under flowing N_2 at 150 °C for 1 h. The acetate or acetylacetonate ligands were replaced by oleate ligands, expelling acetic acid and acetylacetone in the process. This produces a mixture of metal oleate and excess oleic acid. This method offers a couple of advantages over traditional salt exchange methods used to produce metal oleates wherein a metal salt is mixed with sodium oleate.[66] One advantage is that acetic acid and acetylacetone are relatively volatile and evaporate out of the precursor mixture upon heating, negating the need for any further purification.[62] Another advantage is that the mixtures are free of contaminating anions that have been shown to impact nanocrystal synthesis.[41]

We decided to use Ce(III) acetate as a starting material because Ce(IV) compounds typically exist as inorganic salts. Upon exchanging 2 mmol of Ce(III) acetate in 12 mmol of oleic acid, Ce(III) acetate (a white solid) dissolved, producing an oily, yellow solution, consistent with other reported Ce(III) oleate syntheses.[66-67] FTIR analysis of the solution (Figure A1) revealed metal–carboxylate bonds around between 1400 and 1600 cm^{-1}, suggesting successful synthesis of Ce(III) oleate.[68-71]

We then needed to determine an appropriate reaction temperature for the synthesis at which thermal decomposition of the precursor is not a competitive reaction pathway. To do this, we took TGA of the metal oleate precursor (Figure A2) to determine at what

temperature thermal decomposition takes place. We removed the excess oleic acid by precipitating the precursor in acetone and separating by centrifugation. This process resulted in a waxy yellow-brown solid. TGA of this precursor is shown in Figure A2 and indicates that thermal decomposition of Ce(III) oleate occurs at temperatures above ~320 °C. Although the TGA experiment was conducted under N_2, the thermal decomposition temperature under air has been reported to be similar.[60, 67, 72] We thus chose to investigate a range of reaction temperatures below 320 °C.

The last parameter we needed to consider was the injection rate for precursor addition. In indium oxide nanocrystal syntheses, it has been shown that a slower injection rate (0.1 mL min^{-1}) leads to more uniform nanocrystals. Further, a slower injection rate reduces the potential for precursor buildup in solution, which could initiate the growth of new nanocrystal populations. We chose to use an injection rate of 0.06 mL min^{-1} for initial syntheses.

Initial Nanocrystal Syntheses

We performed a series of nanocrystal syntheses by injecting 2 mmol of Ce(III) oleate into oleyl alcohol under flowing dry N_2 at 230, 260, 290, and 315 °C. During the course of the reaction, the reaction mixture remained yellow. After cooling to room temperature and exposure to air, the mixture slowly turns purple, and then eventually brown after sitting in ambient conditions for several days. Further discussion of reaction colors will follow in a later section.

The TEM results are shown in Figure 2.2. At 230 °C, round nanoparticles < 2 nm in diameter can be seen. At higher temperatures, anisotropic structures were formed. The

low contrast of the nanoribbons by TEM suggests that the structures are thin along the z-axis (tape-like), similar to 0.5-1 nm two-dimensional CeO_2 nanosheets reported in the literature.[73-75] The nanoribbons appear to increase in both length and width as temperature is increased. Additional syntheses carried out under the same conditions at 315 °C suggested that a variety of shapes are produced at these higher temperatures. TEM images (Figure A3) of the resulting nanoparticles show a mixture of irregular round plates and small (< 2 nm) nanoparticles.

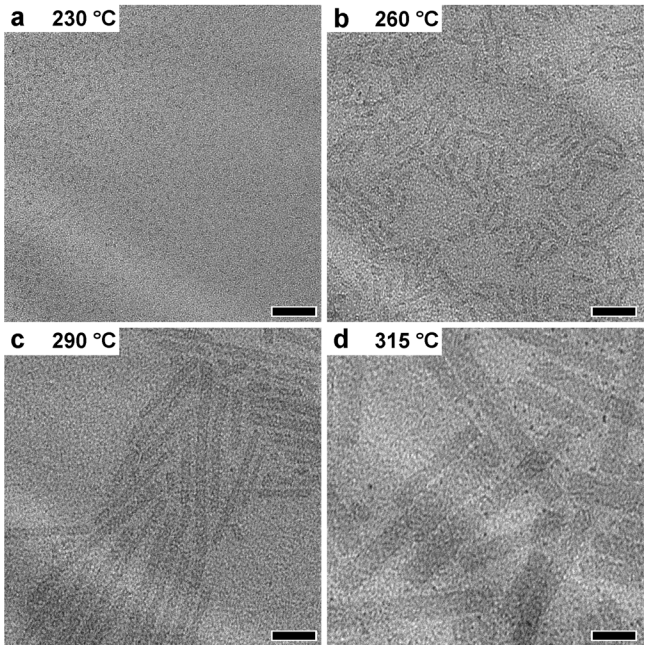

Figure 2.2. TEM images of nanoparticle syntheses conducted under N_2 at an injection rate of 0.06 mL/min at temperatures of (a) 230°C, (b) 260°C, (c) 290°C, and (d) 315°C. Scale bars are 20 nm.

Because the particles did not grow upon the addition of more cerium oleate precursor at 230 °C, it was evident that these were not suitable conditions for a living growth process. In addition, the formation of ribbons and other structures at higher

temperatures was surprising because previous studies of indium oxide and iron oxide showed that nanocrystals produced by the slow injection synthesis produced spherical or cubic shapes.[4, 63] A recent study from our lab on iron oxide nanocrystals demonstrated the importance of the initial precursor oxidation state on the resulting iron oxidation state in the nanocrystals, and resulting morphology.[58] Thus, we decided to investigate the role of oxidation state on the morphologies produced.

Cerium complexes can readily access 3+ and 4+ oxidation states, but solid cerium oxide nanocrystals are typically tetravalent Ce(IV) oxide. In our initial trials, where we started with Ce(III) oleate, an oxidation step is necessary to end up with cerium(IV) oxide. There are several different strategies that have been used to induce oxidation in cerium oxide nanocrystal synthesis. Lee et al. used H_2O_2 as an oxidant additive in a hydrothermal CeO_2 synthesis.[33] Taniguchi et al. started with Ce(IV) ammonium nitrate as a starting material in a hydrothermal synthesis of CeO_2.[16] Finally, Lin et al. conducted syntheses under an air atmosphere, which resulted in more crystalline CeO_2 particles than those formed under an Ar atmosphere.[50] We considered all three of these strategies. We decided against adding an oxidant to the synthesis because additives can introduce unwanted or poorly understood side reactions, making it difficult to determine whether the resulting nanocrystal properties are the result of oxidation state or other effects.[76] We considered using a Ce(IV) salt as a starting material for a Ce(IV) oleate precursor, but this requires the development of a precursor synthesis, as organic Ce(IV) complexes are not readily available,[77] and we did not want to complicate the synthesis by introducing nitrate or sulfate anions (from Ce(IV) ammonium nitrate or Ce(IV) sulfate), which have been shown to influence CeO_2 nanocrystal growth.[2, 41] Thus, we decided to first conduct a nanocrystal

synthesis under a flowing air atmosphere to investigate its influence on nanoparticle formation and growth.

We conducted a synthesis at 290 °C using 2 mmol of the same cerium(III) oleate precursor and an injection rate of 0.06 mL min^{-1}, but instead of flowing N_2 through the reaction flask, we flowed in dry air. Compared to the syntheses conducted under N_2 where the solution remained yellow throughout the course of the reaction, the reaction mixture turned brown upon the addition of the cerium(III) oleate precursor and remained so for the duration of the injection. We took small (~0.3 mL) aliquots of the reaction mixture after the addition of every 0.5 mmol of precursor. Figure 2.3 shows TEM images of the resulting purified nanoparticles.

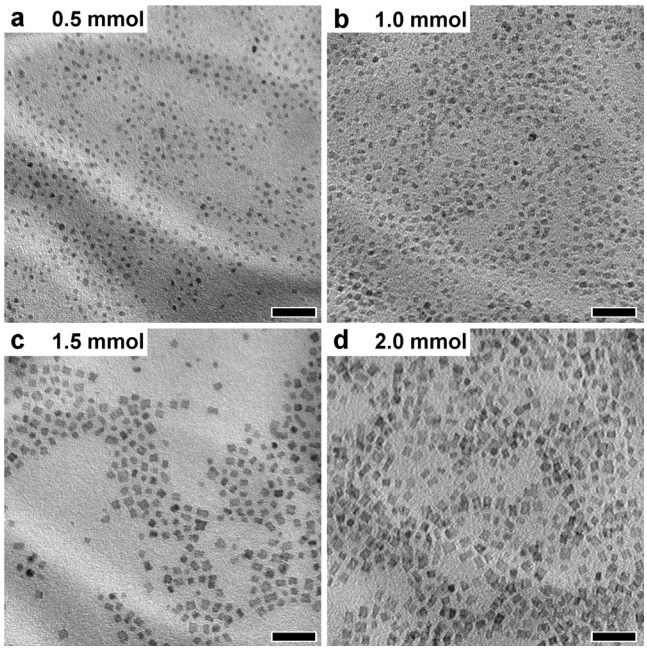

Figure 2.3. TEM images of cerium oxide nanocubes synthesized under air at an injection rate of 0.06 mL/min at a temperature of 290°C. Images show the nanocrystals formed after injecting (a) 0.5 mmol, (b) 1.0 mmol, (c) 1.5 mmol, and (d) 2.0 mmol of precursor. Scale bars are 20 nm.

The introduction of air altered the growth process significantly, producing nanocubes instead of nanoribbons. The production of CeO_2 nanocubes has been seen in several reports where oleic acid is used as the surfactant due to the preferential binding of carboxylates to the (100) surfaces.[2, 16, 78] Furthermore, there was a systematic increase in the nanoparticle diameter upon the addition of precursor, as shown in Figure 2.3. Size analysis of the nanocubes in the TEM images in Figure 2.3 (see Figure A4) reveal that the average diameters are approximately 2.0, 2.5, 3.0, and 3.6 nm after injecting 0.5, 1.0, 1.5, and 2.0 mmol of precursor, respectively. This behavior is more consistent with the behavior previously seen for indium oxide[63] and iron oxide[4] nanocrystals, suggesting that these cerium oxide nanocubes were the result of a continuous growth mechanism.[3-4, 58, 61, 63] These results confirmed that the reaction atmosphere had a significant impact on the resulting nanocrystal morphology.

Investigating the Role of Precursor Oxidation State and Reaction Atmosphere on Nanocrystal Formation

We characterized the nanoribbons produced under N_2 at 290 °C and the nanocubes produced under air at 290 °C by XPS (Figure 2.4a) in order to assess the composition of the nanocrystals. XPS spectra were fit in accordance with previous studies.[79-81] The top trace (nanocubes) and the bottom trace (nanoribbons) look similar, but the differences in peak intensities suggest that the samples have different ratios of Ce(III) and Ce(IV). The peaks associated with Ce(III) at ~882, 889, 900, and 907 eV are much smaller in the case of the nanocubes, indicating a lower concentration of Ce(III) in the nanocubes. Based on

the peak areas, we estimate the Ce(III) content to be ~41% in the nanocubes, and ~56% in the nanoribbons.

We also characterized the nanoribbons and nanocubes by XRD (Figure 2.4b) to assess phase and crystallinity. The patterns for the nanocubes (top trace) are consistent with the fluorite structure of CeO_2 (gray trace for reference). The nanoribbons may be consistent with either the fluorite structure of CeO_2, or the bixbyite structure of Ce_2O_3 (see Figure A5 for reference), however the broadness of the peaks makes this difficult to determine. The pattern for the nanocubes shows more narrow and distinct peaks compared to the nanoribbons, suggesting the nanocubes are more crystalline. Nanocubes were also examined by high resolution TEM (HRTEM) and found to be single crystal with the (100) facets exposed (Figure A6). The nanoribbons were not stable to the electron beam, thus we were not able to gain further crystallographic information about the nanoribbons from HRTEM.

With a better understanding of the nanoparticles produced under the two different atmospheres, we wanted to understand why the reaction atmosphere had such a significant impact particle growth and the resulting nanoparticle morphology. To get at this question, we considered the differences that we observed between the two different reaction conditions. One major observation was the difference in color seen during each of the reactions. Under N_2, the reaction mixture was yellow throughout the synthesis, turned purple upon exposure to air, and turned brown after several days in ambient conditions. Under air, the reaction mixture remained brown throughout and after the synthesis (see S7 for photographs). Reports in the literature suggest a colorless or yellow solution is indicative of a $Ce(OH)_3$ or Ce_2O_3 composition, purple suggests a mixed valence phase, and

brown is consistent with a Ce(III)-rich CeO_{2-x} material.[82-84] Our observations regarding the color changes observed, as well as the XPS and XRD data, are consistent with these literature reports. The XPS data suggest that the nanoribbons are predominantly a Ce(III) phase, likely a mix of bixbyite Ce_2O_3 and fluorite CeO_2 based upon the XRD data. XPS data suggest that the nanocubes are predominantly a Ce(IV) phase. Both nanoribbons and nanocubes are mixed valence. While these findings are useful in determining which phases will be formed under the different atmospheres, we were still interested in understanding the role oxygen was playing in the reaction.

In order to examine the differences in the nanoparticle syntheses under air vs N_2, the reaction mixtures from the two syntheses were characterized using Fourier transform infrared (FTIR) spectroscopy. FTIR can be used to monitor the formation of ester, which is produced in the first step of the nanoparticle synthesis (Figure 2.1), and it can be used to detect the presence of the precursor metal carboxylate species.

The FTIR spectra of the two reaction mixtures (both conducted at 290°C but under the different atmospheres) were identical except for the region shown in Figure 2.4c (see Figure A8 for full spectra). The peaks at 1739 cm^{-1} can be assigned to ester, which is formed in the first step of the synthesis when the metal-oleate precursor reacts with the oleyl alcohol.[62] The peaks at ~1716 cm^{-1} can be assigned to free oleic acid.[58, 62] Peaks in the region between ~1600 – 1500 cm^{-1} can be assigned to the asymmetric vibrations of the metal carboxylate species of the precursor and/or hydroxy monomer species.[58] To enable accurate comparison of the relative concentrations of these species, the spectra were normalized to the peaks from C–H stretching at ~2970 cm^{-1} (see Figure A8).

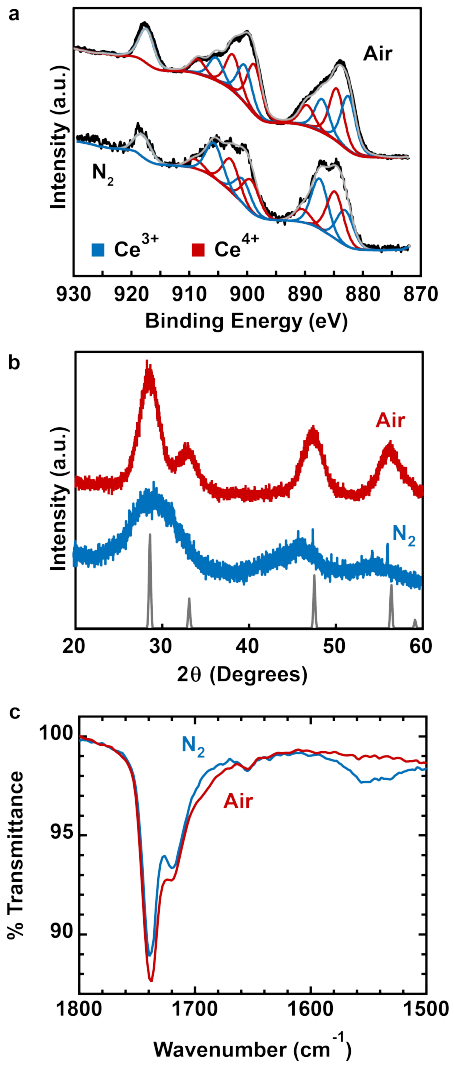

Figure 2.4. (a) XPS Ce 3d spectra and (b) XRD diffractograms of nanocrystals produced from syntheses conducted under air (top) or N_2 (bottom). (c) FTIR spectra of reaction solutions from syntheses conducted under air (red) or N_2 (blue).

The reaction mixture from the synthesis under air contains slightly more ester than the mixture from the synthesis carried out under N_2. More striking, however, is the difference observed in the region between ~1600 – 1500 cm^{-1}, where a broad peak is seen from the synthesis under N_2, while no peak is seen from the synthesis under air. The presence of a peak in this region shows that precursor or monomer is building up under N_2,

suggesting that the consumption of precursor (and nanocrystal growth) is slower under N_2 than under air.

We formed two hypotheses about the possible effect that oxygen could be having on nanocrystal growth. One hypothesis is that the oxygen oxidizes the Ce(III) oleate precursor to Ce(IV) oleate, which then might be a better esterification or condensation catalyst than Ce(III) oleate, resulting in faster reaction kinetics and more crystalline tetravalent CeO_2. Our second hypothesis was that rather than oxidizing the precursor, oxygen was oxidizing the nuclei/nanoparticle surfaces, which then react faster with solution monomer than the reduced nanoparticles.

To test our first hypothesis, we conducted a nanoparticle synthesis using Ce(IV) oleate as the precursor. To synthesize Ce(IV) oleate, we mixed 10 mmol of ceric ammonium nitrate (CAN) with 40 mmol of sodium oleate in 100 mL of a 2:1:1 mixture of hexanes:water:ethanol. Many salt exchange procedures typically bring this mixture to reflux,[58, 66] but we observed that after fewer than five minutes of stirring, the hexanes layer started to turn brown, suggesting the formation of a hydrophobic cerium oleate complex. Given this, we stirred the mixture at room temperature under atmospheric conditions overnight. After the reaction was complete, the hexanes layer was separated using a separatory funnel and washed with water three times to remove contaminant ions. The cerium oleate was then precipitated with ethanol (one time) and acetone (three times) and separated by centrifugation each time. This washing procedure was necessary to obtain a solid product. The resulting product was a waxy powder.

We also synthesized Ce(III) oleate using a salt exchange method using $Ce(NO_3)_3 \cdot 6H_2O$. Because this Ce(III) starting material has the same nitrate counterion as

CAN, the nanoparticles produced using the resulting Ce(III) and Ce(IV) oleate precursors would be more comparable. This precursor made by salt exchange (SE) will be referred to as SE-Ce(III) oleate to distinguish it from the Ce(III) oleate made from the cerium acetate starting material. To make the SE-Ce(III) oleate, we used the same procedure with 10 mmol $Ce(NO_3)_3 \cdot 6H_2O$ and 30 mmol sodium oleate. The initial product was gelatinous and light purple, but after purification with ethanol and acetone, the resulting solid was a white powder.

The SE-Ce(III) and Ce(IV) oleate powders produced by salt exchange were characterized by XPS (Figure A9). The Ce 3d spectrum for SE-Ce(III) oleate only contains peaks that correspond to Ce(III) states, suggesting that it is predominantly trivalent. The Ce(IV) oleate spectrum contains peaks corresponding primarily to Ce(IV) states, suggesting that the synthesis of Ce(IV) oleate was largely successful. There are, however, peaks corresponding to Ce(III) (~30% of the cerium content), thus we will refer to this material as a Ce(IV)-rich oleate precursor. Nitrogen was not detectable in either sample (Figure A9), suggesting that there is no contamination from ammonium and nitrate ions from the CAN and $Ce(NO_3)_3 \cdot 6H_2O$ starting materials. See the supporting information for further discussion on precursor characterization (Figures A10-A12). We added excess oleic acid to each of the SE-Ce(III) and Ce(IV) oleate powders to produce mixtures containing 6 mmol of oleate/oleic acid per mmol of Ce, consistent with prior syntheses. After adding excess oleic acid, the SE-Ce(III) oleate precursor appeared yellow with the same viscosity as the precursor synthesized from Ce(III) acetate. The Ce(IV)-rich oleate was dark brown and was too viscous to pass through an 18-gauge needle. For this reason, we added an equal volume of 1-octadecene to the Ce(IV)-rich oleate mixture, which enabled it to pass through

an 18-gauge needle. 1-octadecene was chosen because it is a liquid at room temperature, which was necessary to get the precursor to pass through the needle for injection. One concern with the use of 1-octadecene is that it has been shown to polymerization during nanocrystal syntheses,[85] however, if polymerization is occurring in our studies, it does not appear to affect nanocrystal morphology as shown later in the comparison of the results for Figure 2.3d and Figure 2.5f. For consistency and comparability, we also added an equal volume of 1-octadecene to the SE-Ce(III) oleate precursor.

With these two precursors in hand, we conducted four nanoparticle syntheses at 290 °C, examining each precursor's reactivity under N_2 and under air using 2 mmol of each precursor. Because we diluted the precursors with 1-octadecene, these syntheses were conducted at injection rates of 0.12 mL min^{-1} to keep the injection rate of the precursor consistent with initial syntheses. For all four of the syntheses with the new precursors, the reaction mixtures turned from yellow to brown as precursors were injected, and remained brown for the duration of the synthesis (see Figure A13 for a schematic of all observations of reaction color changes). This was unexpected for the SE-Ce(III) oleate injection under N_2, since when the Ce(III) oleate made from Ce(III) acetate was used the reaction remained yellow and then turned purple upon exposure to air. This will be discussed further in a later section. We analyzed the final reaction mixtures using FTIR (Figure A14) and the purified nanoparticles using TEM (Figure 2.5a-h), XPS (Figure A15), and XRD (Figure A16).

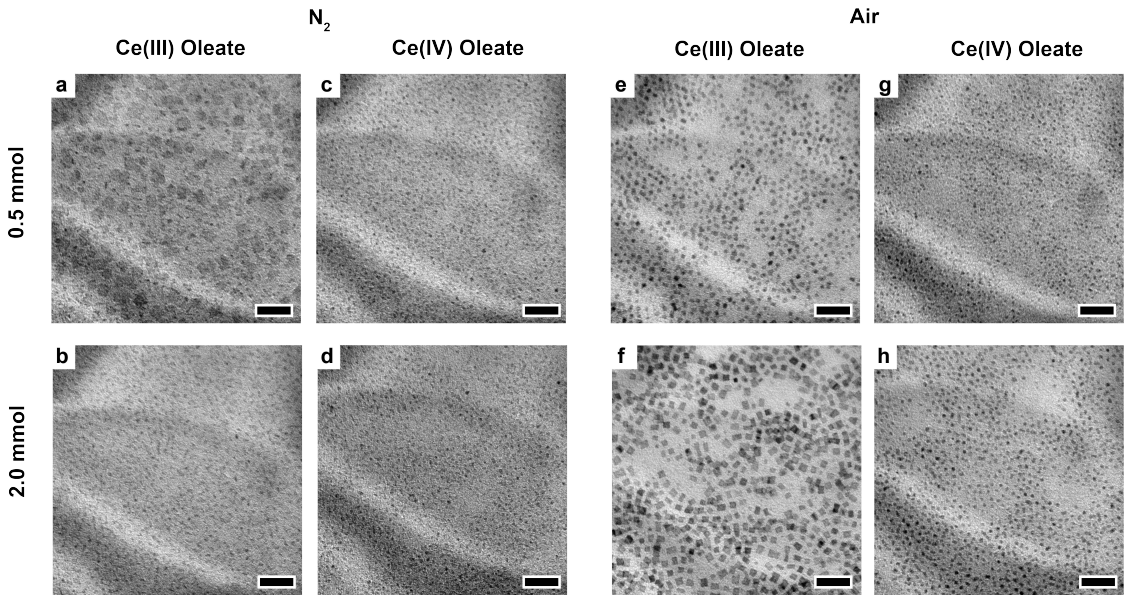

Figure 2.5. TEM images of nanoparticles from syntheses using SE-Ce(III) oleate or Ce(IV)-rich oleate under N_2 or air. The top images show nanoparticles that result from injecting 0.5 mmol of precursor, and the bottom images show the final nanoparticles that result from injecting 2.0 mmol of precursor.

TEM images showed that the reaction atmosphere had a significant influence on morphology, whereas the influence of the precursor oxidation state was more subtle. Under N_2, the SE-Ce(III) oleate resulted in a mix of irregular plates and dots, and the Ce(IV)-rich oleate precursor led to dots, neither of which grew upon the addition of precursor. Under air, the SE-Ce(III) oleate resulted in nanocubes that did grow upon the addition of precursor, consistent with previous results. The Ce(IV)-rich oleate also resulted in nanocubes under air which grew upon the addition of precursor, though these cubes were smaller. The FTIR spectra from the reaction mixtures (Figure A14) show a buildup of precursor in the case of both precursors under N_2, but no buildup from either precursor under air. Given the strong influence of the reaction atmosphere compared to the precursor

oxidation state, we wondered whether either Ce(III) oleate precursor becomes fully oxidized or Ce(IV) oleate becomes fully reduced to Ce(III) under reaction conditions. Such a transformation might explain the limited influence of the initial precursor oxidation state.

We evaluated the thermal stability of the SE-Ce(III) and Ce(IV)-rich oleate precursors. To do this, we annealed the SE-Ce(III) oleate precursor in air at 150 °C for 1 h, and we annealed the Ce(IV)-rich oleate precursor in N_2 at 110 °C for 1 h. We then purified both resulting precursors by centrifuging in acetone three times, resulting in a solid in both cases. XPS of the resulting solids is shown in Figure 2.6.

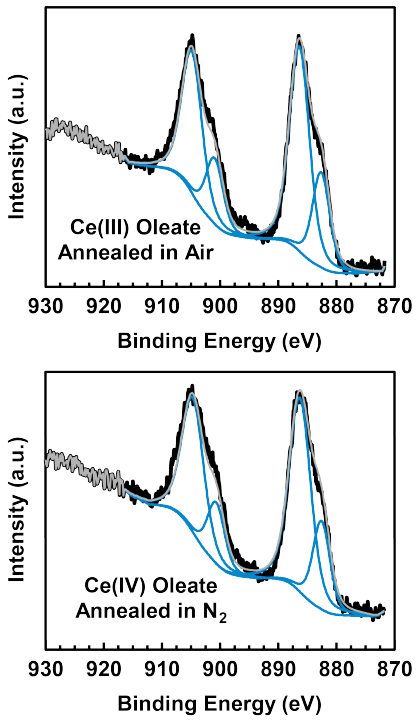

Figure 2.6. XPS Ce 3d spectra of SE-Ce(III) oleate annealed in air at 150 °C (top), and of Ce(IV)-rich oleate annealed in N_2 at 110 °C (bottom) for 1 h. Black traces represent the raw data, blue traces correspond to Ce^{3+} content, and gray traces represent the fits to the raw data.

XPS spectra were analyzed in the same manner as those in Figure 2.4. The Ce 3d XPS spectrum for the SE-Ce(III) oleate (top) showed only Ce(III) content, suggesting it had not been oxidized. Interestingly, the Ce(IV)-rich oleate also only showed Ce(III) content, suggesting it had been fully reduced even at 110 °C. These results suggest that the Ce(IV) oleate is not thermally stable, and is likely reduced to Ce(III) oleate under nanocrystal synthesis conditions. This is supported by other reports that have found Ce(IV) carboxylate complexes thermally unstable.[77, 86-87]

If Ce(IV) is readily reduced to Ce(III), why are the nanocrystals formed from the Ce(IV)-rich oleate were smaller than the ones formed from Ce(III) oleate under air? We first considered that it may be due to the presence of water in the Ce(IV)-rich oleate, which was shown to be present in this precursor by TGA (Figure A12). To test this, we performed a nanocrystal synthesis at 290 °C under air with a Ce(III) oleate precursor that had added water. TEM images of the resulting nanocrystals (Figure A17) suggest that the presence of water does not lead to smaller nanocrystals.

Another possibility is that, during the earliest stages of the reaction, the Ce(IV)-rich oleate precursor initiates growth of significantly more nuclei, leading to more, but smaller, nanocrystals as they growth through addition of Ce(III) monomer. To test this, we conducted a nanocrystal synthesis under air at 290 °C using 1.5 mmol of Ce(IV)-rich oleate, split the resulting reaction mixture in half, and added either Ce(IV)-rich oleate or Ce(III) oleate to each half. The results of these trials are shown in Figure 2.7.

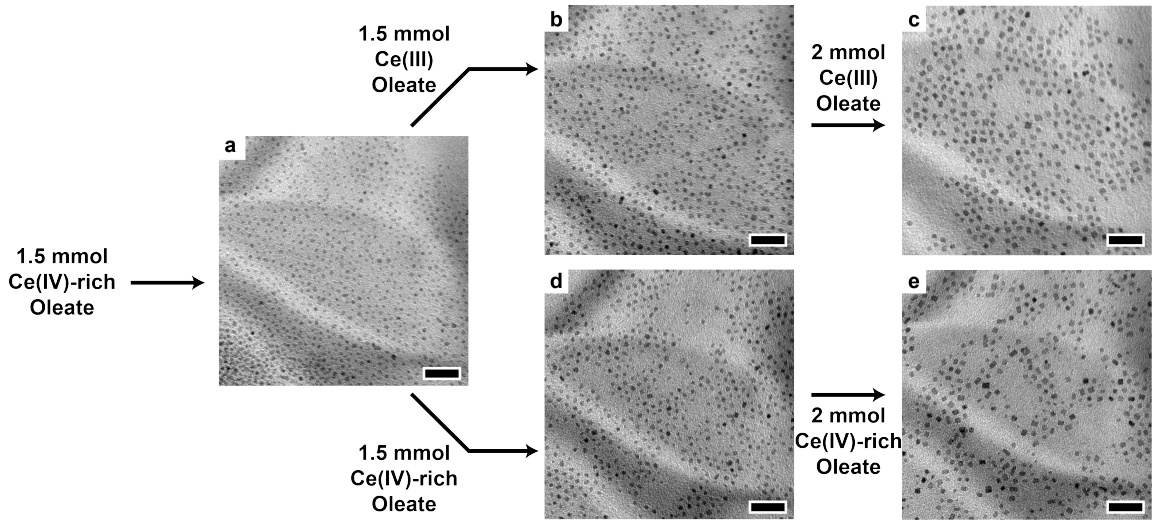

Figure 2.7. TEM images of nanocrystals from two syntheses. (a) Nanocrystals resulting from injecting 1.5 mmol Ce(IV)-rich oleate. This reaction mixture was split in half and used for two separate syntheses where to one half, (b) 1.5 mmol Ce(III) oleate and (c) 2 mmol Ce(III) oleate was added. To the other half, (d) 1.5 mmol Ce(IV)-rich oleate and (e) 2 mmol Ce(IV)-rich oleate was added. Scale bars are 20 nm.

Results show that the Ce(III) and Ce(IV)-rich oleate precursors add to the surface of the nanocrystals in the same manner, resulting in similar sizes and morphologies. The similarity in growth characteristics suggests that the influence of the precursor is manifest only in the earliest stages of the reaction. We propose that the Ce(IV)-rich oleate initially forms more, and therefore smaller, nuclei, but then grow in the same manner as with the Ce(III) precursor. Even though Ce(IV) is reduced under the reaction conditions, we propose that the initial formation of nanocrystals occurs before the initial Ce(IV) oleate is fully reduced to Ce(III) oleate.

From the XPS experiments it was clear that air was not affecting the nanocrystal morphology by oxidizing the precursor, so we hypothesized that oxygen was influencing reactivity by oxidizing the nanoparticle surface. To test this hypothesis, we designed an

experiment in which we switched from N_2 to air halfway through an injection. If air oxidizes the surface of the growing nanocrystals, we would expect to see changes in the amount of precursor buildup after air is introduced and changes to the nanocrystal morphologies as well. We investigated this hypothesis by conducting a 3 mmol synthesis at 290 °C using Ce(III) oleate (made from Ce(III) acetate) in which the first 1.5 mmol of precursor were injected under N_2, and then the atmosphere was switched to air before injecting the remaining 1.5 mmol of precursor. Aliquots of the reaction mixture were analyzed by FTIR, and the purified nanoparticles were characterized by TEM and XPS (Figure 2.8).

The image in Figure 2.8a shows that under N_2, nanoribbons form, as expected. After switching to air (Figure 2.8b), the nanoribbons become kinked. As additional precursor is added, the particles become more isotropic and uniform in morphology, resulting in ~3-5 nm in diameter cubes. These cube-like structures were of similar size (~3-5 nm) as the final nanostructures found in Figure 2.3d.

FTIR analysis was performed on aliquots taken during the reaction to monitor the formation of ester and the presence of precursor. FTIR analysis is shown in Figure 2.8e. The inset shows the metal carboxylate binding region. The presence of a peak in this region for the aliquot taken after injecting 1.5 mmol of precursor under N_2 (blue trace) indicates the buildup of precursor, which then disappears after air is introduced and more precursor is added (red traces). This suggests the precursor reacts faster in the presence of air. XPS of the nanoparticles from each of the aliquots taken during the reaction (Figure 2.8f) indicate that Ce(III) it converted to Ce(IV) upon introduction of air and adding additional precursor.

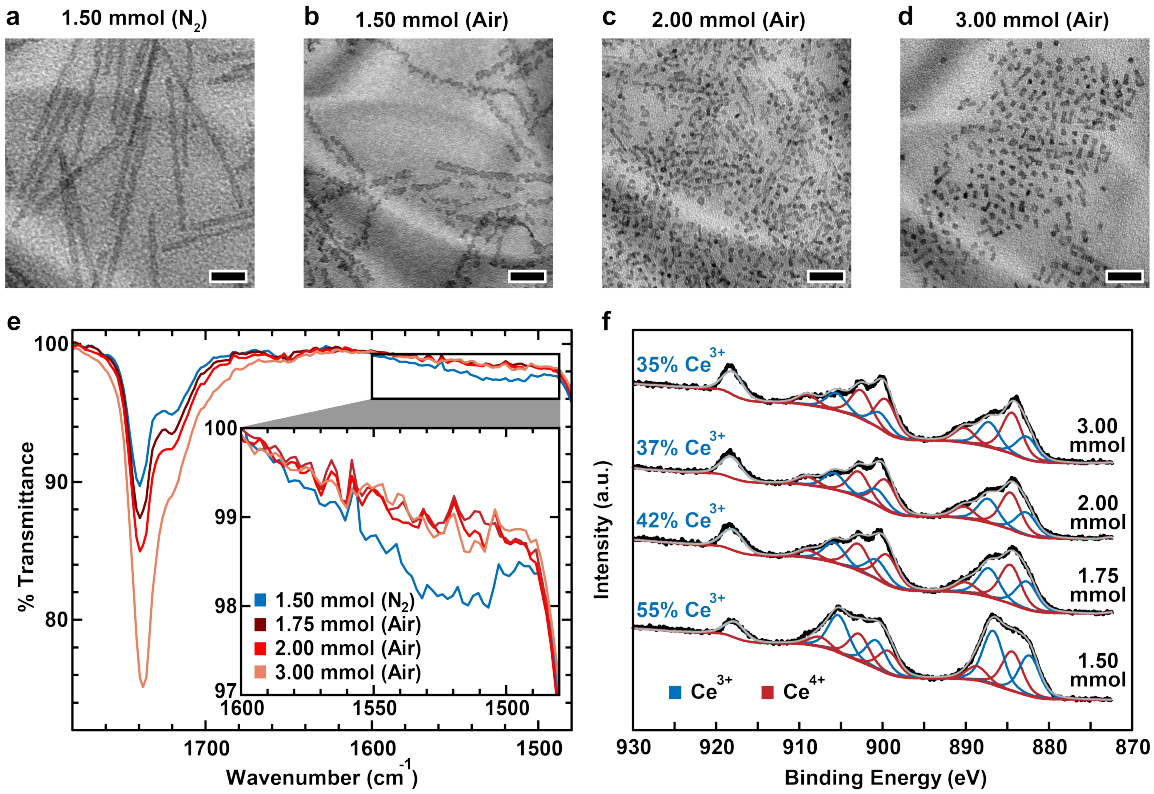

Figure 2.8. Characterization from a 3 mmol nanoparticle synthesis at 290 °C where the first 1.50 mmol of precursor were injected under N_2, and the last 1.50 mmol of precursor were injected under air. (a)-(d) TEM images of nanoparticles formed after injecting (a) 1.50 mmol of precursor under N2, (b) no additional precursor, but we introduced air, (c) 2.00 mmol, and (d) 3.00 mmol of precursor. Scale bars are 20 nm. (e) FTIR spectra of aliquots taken from the reaction mixture after injecting 1.50 mmol (blue), 1.75 mmol (dark red), 2.00 mmol (red), and 3.00 mmol (light red) of precursor. The inset shows the region for metal carboxylate bonds. (f) Ce 3d XPS spectra of nanoparticles formed after the addition 1.50 (bottom trace), 1.75, 2.00, and 3.00 mmol (top trace) of precursor. Black traces show the raw data, gray traces show the fits, blue traces correspond to Ce^{3+} and red traces correspond to Ce^{4+} content. The atomic percentage of Ce^{3+} to total Ce content is shown next to the traces on the left.

The data shown in Figure 2.8 suggest that the consumption of precursor is happening faster under air than N_2 (Figure 2.8e), that air is changing the morphology of

the ribbons (Figure 2.8b), and that air oxidizes Ce(III) to Ce(IV) in the nanocrystals (Figure 2.8f). There are two possibilities regarding the role of air based upon these observations. One possibility is that air reacts with species in solution, which then alter the nanocrystal growth process. We considered that the oleyl alcohol might be oxidizing under air. To assess this, we heated oleyl alcohol to 290 °C for 2 h under air and compared the FTIR spectra before and after heating (Figure A18). After heating, there is an appearance of a peak at ~1740 cm–1 which is associated with a carbonyl, suggesting that some of the alcohol is oxidized to oleic acid, which might be able to etch away nanoribbons under air. However, the TEM images in Figure 2.8 (a-d) showing kinked nanoribbons upon the addition of air, and then by nanocubes upon the addition of more precursor, suggest that air is influencing structure of the nanocrystals themselves. Further, the lower Ce(III) content in the particles heated in air by XPS (Figure 2.8f) suggest that air is oxidizing the nanocrystals. Taken together, these data suggest that nanocrystal oxidation may be responsible for the observed changes in the nanocrystals formed in air vs N_2 rather than the oxidation of the oleyl alcohol, or reactions with other species in solution.

We hypothesize that the initial introduction of air oxidizes the nanorods via one of the following chemical reactions:[88]

$$2Ce_2O_3 + O_2 \rightarrow 4CeO_2 \qquad (1)$$

$$4Ce(OH)_3 + O_2 \rightarrow 4CeO_2 + 6H_2O \qquad (2)$$

It is feasible that undergoing one of these reactions would cause a structural rearrangement, which appear to result in grain boundaries, leading to the kinked appearance of the ribbons. The TEM images from Figure 2.8 also suggest that adding additional precursor causes the ribbons to break at those boundaries. One hypothesis for this is that the nanoparticle growth

continues selectively at the interfaces of those boundaries. Taniguchi et al. described a similar phenomenon in particles that they hypothesized were rich in Ce(III) at grain boundaries, which they described as being more reactive.[16] If this is happening with the nanoparticles in this study, it is possible that sites at the grain boundaries are more reactive, and the addition of precursor causes growth to happen at those boundaries, thus leading to separation of those grains.

Taken together, our results suggest that oxygen impacts the nanocrystal morphology not by oxidizing the cerium oleate precursor, but by altering the reactivity of the nanocrystal surfaces. The morphological changes to nanoribbons upon the introduction of air illustrate how oxygen impacts the surface structure and reactivity. Under all conditions that we tested, Ce(III) is primarily responsible for nanocrystal growth. Even in the presence of air, Ce(IV) oleate is reduced via thermal decomposition reactions to Ce(III) species that contribute to nanocrystal growth in a similar fashion to the Ce(III) oleate precursor. The differences in nanocrystal sizes produced under air starting with Ce(IV) vs. Ce(III) are likely due to differences in nanocrystal formation rates at the earliest stages of the reactions when residual Ce(IV) might still be present.

Investigating the origin of nanoribbon formation

Now that we had a better understanding of the influence of reaction atmosphere on the resulting morphologies, we then wanted to understand the origin of the nanoribbon formation. Under N_2, nanoribbons formed in some cases with the Ce(III) oleate precursor, but poorly defined structures formed in other cases. The TEM images in Figure 2.5 show that the SE-Ce(III) oleate did not lead to nanoribbon formation. Nanoribbons were only seen when Ce(III) oleate made from Ce(III) acetate was used. One hypothesis is that the

difference was due to the presence of nitrate anions in the case of the SE-Ce(III) oleate precursor. However, no nitrogen was detected in the SE-Ce(III) oleate precursor by XPS (Figure A9), suggesting this was not the case. We thus hypothesized that the presence of acetate may be responsible for nanoribbon formation under N_2.

To investigate the possible role of acetate on nanocrystal growth, we performed two experiments: 1) we synthesized nanocrystals made from Ce(III) acetate wherein the ligand exchange between Ce(III) acetate and oleic acid was performed for a longer period of time (5 h vs 1 h) at higher temperature (165 vs 150 °C) in an attempt to remove any trace acetate ligands, and 2) we synthesized nanocrystals using the SE-Ce(III) oleate and deliberately added 2 mmol of acetic acid to the precursor solution prior to injection. The TEM images of the nanocrystals for these two reaction conditions are shown in Figure 2.9. Figure 2.9a shows that irregular plates result from the synthesis conducted using the Ce(III) oleate exchanged in oleic acid for 5 hours. These results are similar to those from Figure 2.5a where the SE-Ce(III) oleate was used, suggesting that the acetic acid had been completely removed. The image of the nanocrystals produced using SE-Ce(III) oleate with added acetic acid (Figure 2.9b) shows predominately nanoribbons. These results suggest that acetate is responsible for anisotropic growth and, thus, nanoribbon formation.

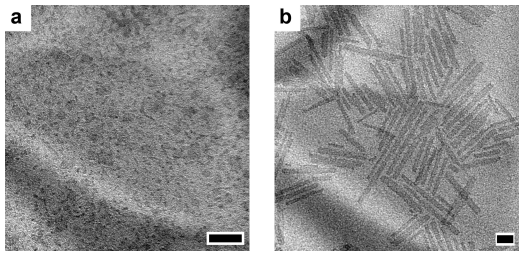

Figure 2.9. TEM images of nanocrystals synthesized with (a) Ce(III) oleate made from a 5 h ligand exchange between $Ce(acetate)_3$ and oleic acid at 165 ºC under N_2, and (b) SE-Ce(III) oleate with added acetic acid. Scale bars are 20 nm.

To try to understand why acetate may be leading to anisotropic growth, we turned to literature studies that investigated the influence of acetate in nanocrystal synthesis.[89-93] These reports suggest that there are several different effects acetate could be having in nanocrystal synthesis, and each will be discussed below. From these, we explored three hypotheses. One hypothesis is that acetate coordinates to the nanocrystal surfaces, which could make those surfaces more sterically accessible, leading to either oriented attachment with other nanocrystals, or leading to additional monomer addition along a crystal facet.[91] Another hypothesis is that the acetate could be coordinating to the precursor complex, altering solubility and changing kinetics of the nanocrystal growth.[90] A final hypothesis we explored was that acetate could be acting as a reductant, which may alter the crystal phase of cerium oxide growing in solution.[93]

Houtepen et al. concluded that the presence of acetate facilitated oriented attachment of nanocrystals.[91] In this study, the authors investigated the role of trace acetate on the growth of PbSe nanocrystals and found that the presence of acetate led to branched nanocrystals, with the degree of branching increasing as the amount of added acetic acid was increased. The authors argued that the branched nanocrystals were the result of oriented attachment due to acetate coordinated to nanocrystal surfaces, which would make the nanocrystal surfaces more sterically accessible.[91]

We considered whether oriented attachment was happening in our syntheses of CeO_2 nanocrystals under N_2. To test this hypothesis that acetate was leading to oriented attachment, we conducted an experiment wherein we annealed nanocrystals synthesized under air using 0.5 mmol Ce(III) oleate (TEM image in Figure 2a) in the presence of acetic acid and oleyl alcohol at 290 °C for 2 h. The TEM images from this experiment (Figure

A19) do not show any elongated structures, suggesting that oriented attachment did not happen in that case. We also annealed particles made by injecting 0.5 mmol Ce(III) oleate into oleyl alcohol under N_2 for 1 h. The TEM images from this experiment (Figure A20) showed that nanocrystal length and width did not change during the annealing period, suggesting that oriented attachment did not occur.

Another explanation for the role of acetate in nanocrystal synthesis is that acetate coordination could be altering the precursor complex solubility, which could alter the kinetics of nanocrystal growth. This was discussed by Riedinger et al. where the authors examined the growth of CdSe quantum dots and found that when a short-chain carboxylate was added, nanoplatelets were formed instead of quantum dots. This was attributed to the short-chain carboxylates coordinating to the precursor, leading to decreased solubility, and therefore phase-separated droplets of the Cd(carboxylate)$_2$ precursor. Due to higher precursor concentration in these droplets, diffusion of material to the nanocrystal surface is fast, and growth is therefore in a "surface-limited regime" (reaction of monomer with the nanocrystal surface is rate-determining), as opposed to a "diffusion-limited regime" (diffusion of material to the nanocrystal is rate-determining). The authors then describe a growth model that suggests being in a surface-limited regime leads to two-dimensional platelets as monomer preferentially reacts with thin facets (edges) rather than large planer surfaces of the nanocrystals.

It is unlikely that the explanation posed by Riedinger et al. regarding precursor solubility explains the role of acetate in our CeO_2 nanocrystal syntheses under N_2. We concluded this based on the FTIR of the reaction mixtures of syntheses under N_2 both with (Figure 2.4c) and without (Figure A21) acetate. The FTIR spectra indicate that there is a

buildup of cerium carboxylate monomer in both cases, more so in the case without acetic acid added, suggesting that these nanocrystals are in a surface-limited, rather than a diffusion-limited, regime regardless of the presence of acetate. However, it is possible that acetate is coordinating with the precursor to form a cerium di-oleate acetate structure, though this is difficult to conclusively determine the presence of such a structure in solution.

Given the importance of surface reactivity and oxidation state at the surface, we wondered whether acetic acid might be influencing the surface oxidation. We noticed that the reaction colors were different between nanocrystal syntheses under N_2 with and without added acetic acid. When acetic acid was added, the colors of the reaction mixture were as previously described, where the mixture was yellow throughout the reaction, then turned purple and eventually brown upon exposure to air. When acetate was not present, the reaction mixture turned from yellow to light brown during the reaction, and eventually a slightly darker brown upon exposure to air (see Figure A13 for schematic depiction of all reaction colors observed). To rule out the possibility that this color change is due to decomposition of the 1-octadecene solvent used to dissolve the SE-Ce(III) oleate precursor, we conducted a control experiment wherein Ce(III) oleate (made from Ce(III) acetate) mixed with 1-octadecene precursor was used in a nanocrystal synthesis under N_2. the reaction mixture remained yellow throughout the synthesis, suggesting that 1-octadecene was not responsible for the observed color changes.

The color changes suggest that in the presence of acetate, the nanocrystals grow as Ce_2O_3 and are then oxidized upon exposure to air, whereas without acetate, the nanocrystals are oxidized continuously throughout the reaction. Zhang et al. found that

more carboxylates on the surface of cerium oxide led to higher Ce(III) content.[93] Thus, in the presence of excess acetate, the higher concentration of carboxylates at the nanocrystal surface may favor a Ce_2O_3 composition at the surface. Ce_2O_3 commonly adopts either a hexagonal crystal structured or a bixbyite structure,[94-95] though our previous XPS and XRD experiments suggest the nanoribbons are a bixbyite structure. There is some evidence to suggest that oxygen diffusion is anisotropic in bixbyite Ce_2O_3, which may also contribute to anisotropic nanocrystal growth.[95] To test whether acetate acts as a reductant, we conducted a nanocrystal synthesis without any acetate but under forming gas (95:5 N_2:H_2). Although nanoribbons were not formed (TEM image in Figure A22) the results don't rule out a reducing role for acetate.

Further studies will be needed to fully elaborate the mechanism by which acetate leads to nanoribbon formation. Our experiments suggest acetate coordination to the nanocrystal surface does not lead to oriented attachment, nor does it change the growth kinetics to a surface-limited regime by changing the precursor solubility in the way discussed by Riedinger et al. The color changes we observed during the reaction suggest that acetate promotes or stabilizes Ce(III), which may, in turn, influence the phase of cerium oxide being grown and influence the resulting morphology. Further, acetate coordination could reduce steric hinderance (relative to oleic acid) between the nanocrystal surface and monomer, serving to passivate a certain crystallographic facet and lead to preferential growth in one direction. Although the coordination chemistry of carboxylates on cerium(III) oxide is not well understood, it seems likely that preferential binding of acetate to the (100) face would lead to preferential growth along the (110) direction and result in the anisotropic ribbons.

Regardless of the mechanism, the use of acetic acid as an additive to the precursor showed promise toward the synthesis of uniform nanoribbons (see Figure A23 for schematic representation of all morphologies observed). The next question was whether the amount of acetic acid had an influence, and whether the morphology could be further tuned by varying the amount of acetic acid added. To investigate this we conducted syntheses using 2 mmol of Ce(III) oleate made from cerium(III) acetate that had been exchanged with oleic acid at 165 °C for 5 h to remove all acetate ligands, and added either 0, 0.4, 1.0, or 2.0 mmol of acetic acid to the precursor. TEM images of resulting nanocrystals are shown in Figure 2.10.

The TEM images in Figure 2.10 show a systematic increase in nanoribbon length with an increase in acetic acid content. Figure 2.10a shows irregular structures, as seen previously. Figure 2.10b shows somewhat more defined nanoplates with an aspect ratio of approximately 1. The nanoribbons in Figure 2.10c (1.0 mmol acetic acid added) are ~16-24 nm long and ~4 nm wide, and nanoribbons in Figure 2.10d (2.0 mmol acetic acid added) are up to ~150 nm long and ~4 nm wide. Interestingly, the nanoribbons in Figure 2.10c and 10d have similar widths, suggesting that acetic acid is primarily influencing growth lengthwise as opposed to widthwise. Overall, using acetic acid as an additive produces monodisperse nanoribbons with predictable lengths, making this synthesis procedure promising for modulating the aspect ratio of cerium oxide nanoplates.

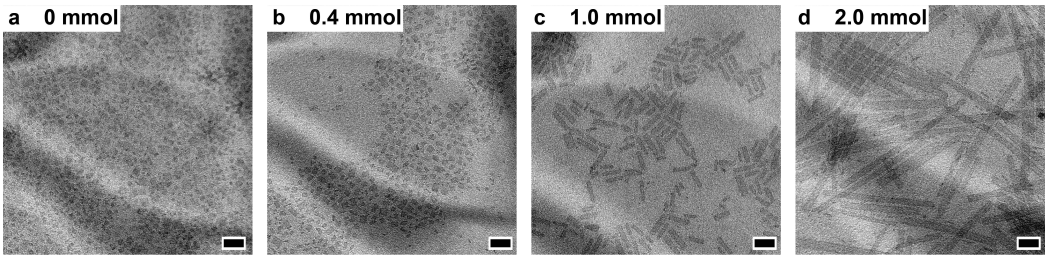

Figure 2.10. TEM images of nanoparticles resulting from syntheses using 2.0 mmol Ce(III) oleate with (a) 0 mmol, (b) 0.4 mmol, (c) 1.0 mmol, and (d) 2.0 mmol of acetic acid added to the precursor. Scale bars are 20 nm.

Conclusions

We investigated the influence of precursor ligation and oxidation state, as well as reaction atmosphere (air vs N_2) on the growth of cerium oxide nanocrystals produced utilizing a slow addition synthesis. We found that the reaction atmosphere and the precursor ligation strongly influenced the morphology of the resulting nanocrystals. When air was used as the reaction atmosphere, growth was faster and nanocubes with controlled sizes could be reliably produced regardless of the precursor used. Reactions carried out under nitrogen, on the other hand, produced ribbons when Ce(III) acetate was used as the starting material, or dots and poorly defined plates when Ce(III) nitrate was used as the starting material. Our results suggest that oxidation of the nanocrystal surface in solution during growth is responsible for the observed differences in morphology during growth under air. The oxidation state of the precursor had little influence on morphology: a comparison of Ce(III) and Ce(IV)-rich oleate precursors showed that the Ce(IV) oleate is thermally unstable and is reduced to Ce(III) even under an air atmosphere, suggesting that Ce(IV) has little influence over morphology during growth under air or nitrogen. Finally,

we discovered that trace amounts of acetate in the Ce(III) oleate precursor leads to ribbon formation for reactions carried out under nitrogen. Deliberate addition of acetic acid resulted in longer (higher aspect ratio) ribbons as the acetic acid concentration increased.

These findings may have broader implications in nanocrystal synthesis. For example, in reports where an air reaction atmosphere is used in the synthesis of cerium oxide nanocrystals, it is clear that the role of oxygen is not to oxidize the precursor, but rather to influence the reactivity of the nanocrystal surface in solution. Further, our results regarding the striking influence of trace amounts of acetic acid under N_2 highlight the importance of choosing an appropriate precursor starting material. Beyond cerium oxide, these findings may be applicable to materials that can have several oxidation states such as cobalt oxide, iron oxide, and copper oxide nanocrystals. Altering the reaction atmosphere (oxidizing or reducing) is a strategy to influence the surface reactivity of nanocrystals. These findings suggest that altering the surface reactivity can significantly impact nanocrystal growth, which may be applicable as a strategy to control nanocrystal morphology in other systems.

Bridge to Chapter III

In Chapter II, the continuous addition nanocrystal synthetic method was extended to a cerium oxide system. Because one variable could be systematically changed at a time, the synthesis enabled the careful study of the role of atmosphere, precursor oxidation state, and ligation on the formation of cerium oxide nanocrystals. Something that was not explored in Chapter II was the role of precursor conversion rate (or rate of activated monomer generation) on the formation of cerium oxide nanocrystals. One way to control the precursor conversion rate is to change the primary reagent used in the synthesis, oleyl alcohol. Chapter III examines the role of precursor conversion rate on the formation of tin-doped indium oxide (ITO) nanocrystals. ITO was chosen because the synthesis of indium oxide using our slow injection esterification approach has been more developed and well-studied, allowing us to further explore parameter space without too many unknown variables. From the data, we learn how using oleylamine vs oleyl alcohol to alter the precursor conversion rate influences the earliest stages of nanocrystal formation, and we use this control over nanocrystal formation to further tune size within indium oxide nanocrystals.

CHAPTER III

MONOMER GENERATION RATE INFLUENCES THE EARLIEST STAGES OF GROWTH FOR TIN-DOPED INDIUM OXIDE NANOCRYSTALS MADE THROUGH A REAGENT-DRIVEN, CONTINUOUS ADDITION SYNTHESIS

This chapter may appear in a forthcoming publication coauthored by Knecht, T. A., Crockett, B. M., and Hutchison, J. E. I performed all experimental work and wrote the chapter. B. M. Crockett helped with the conceptualization of this project. J. E. Hutchison provided guidance on experiments and editorial assistance on the writing of the chapter.

Introduction

Synthesis of inorganic nanocrystals with predictable structures and properties requires control over three processes: conversion of precursor to monomer, nanocrystal formation, and nanocrystal growth.[1-7] It is essential to understand how reaction conditions influence each of these three processes because they influence the size, shape, crystallinity, defects, composition, and dopant placement within the product nanocrystals. Here we investigate how two reagents – oleyl alcohol and oleylamine – impact the conversion of precursor to monomer and, subsequently the formation and growth of tin-doped indium oxide (ITO) nanocrystals.

Nanocrystal formation is thought to be limited by the rate of generation of reactive monomer.[7-8] Thus, many researchers have worked to control the rate of monomer activation by varying the reaction temperature,[9-11] the temperature ramp rate,[12] or precursor reactivity.[7, 13] An alternative approach has been to add reagents that aid in precursor conversion.[8] Increasing the rate of precursor conversion often leads to the formation of a large number of smaller nanocrystals, a finding consistent with the predictions of classical nucleation theory.[12-13] However, there are also reports that increasing the rate of generation of reactive monomers leads to a smaller number of larger nanocrystals.[9-11, 14] That the monomer supply rate appears to influence nanocrystal formation and growth so differently suggests that different nanocrystal formation mechanisms may be responsible for these differences. Our aim in this study is to gain insight into the mechanisms of metal oxide nanocrystal formation by controlling the rate of precursor activation through the use of reactive reagents.

Reagent-driven nanocrystal syntheses provide an opportunity to tune the formation rate of reactive monomer.[2, 15-16] For example, reactive monomers can be readily generated in nonaqueous sol-gel nanocrystal syntheses through halide, ether, ester, or amide elimination reactions.[2, 15-16] These reactions often play a role even in common thermal decomposition syntheses in organic media.[17] Although the simplest thermal decomposition syntheses involve only a metal precursor and a solvent, many thermal decomposition syntheses include additives such as surfactants or additives (such as oleic acid or oleylamine) that can also act as reagents to promote growth.[18-22] While a lot of effort has been put into understanding the various roles of the additives used, thermal decomposition syntheses are inherently difficult to study as these reactions happen on a

short timescale, and radical species are produced that react indiscriminately with each other, the solvent, and any additives. Reagent-driven reactions that take place at temperatures below the thermal decomposition threshold, therefore, provide an opportunity to learn more about the influence of reactive precursor generation on nanocrystal formation.[23-26]

Recently, our group developed a continuous growth synthesis of a series of metal oxide nanocrystals wherein a carboxylate precursor reacts with a large excess of hot oleyl alcohol that serves as both reagent and solvent.[24-25, 27-28] The reactive monomers formed, presumably metal-hydroxy species, condense with each other to form metal oxides.[27] Two key attributes of these syntheses - reaction temperature below thermal decomposition and slow addition of precursor - allow us to systematically control the reaction parameters in order to examine nanocrystal growth processes in detail. For instance, we have been able to study the influence of temperature and monomer flux to the nanocrystal surface on the size and morphology of indium oxide,[26] the influence of nanocrystal size on growth rate in iron oxide,[23] the influence of atmosphere on the growth of cerium oxide nanocrystals,[29] and the influence of incorporating dopants from precursors with various reactivities in indium oxide.[30-31]

In our continuous growth method, ester elimination chemistry, along with a slow, continuous addition method, produces uniform, size-tunable metal oxide nanocrystals. The metal oleate precursor is slowly injected into oleyl alcohol at temperatures between 230-290 °C. The continuous addition approach has advantage over traditional heat up or hot injection syntheses because size is tuned simply by varying the amount of precursor injected, rather than by changing the amount or type of additives used. Further, because

the precursor is injected so slowly (0.05-0.3 mL min^{-1}), the temperature of the reaction does not fluctuate, and because there is continuous supply of precursor, the precursor concentration remains nearly constant throughout the reaction.

Here, we investigate the role of the reagent used (oleylamine vs oleyl alcohol) on the formation and growth of Sn-doped indium oxide (ITO) nanocrystals in our continuous growth synthesis. We show that amidation in oleylamine is faster than esterification in oleyl alcohol and find that the higher monomer conversion rate during amidation leads to the formation of fewer, and therefore larger, nanocrystals. It is possible to tune the number of nanocrystals initially formed by adjusting the oleyl alcohol to oleylamine ratio in the reaction. These findings suggest a more rapid transition from nanocrystal formation to growth in the presence of the more reactive amine. ITO nanocrystals synthesized in oleylamine undergo Sn dopant activation as oxygen is released from the lattice more quickly compared with nanocrystals synthesized in oleyl alcohol, which take several days to finally reach a constant level of oxygen vacancies. These results demonstrate how the choice of reagent not only impacts the formation and growth of metal oxide nanocrystals, but also the properties of the nanocrystals produced.

Experimental

Materials

Indium(III) acetate (99.99%) was purchased from Acros Organics, tin(IV) acetate (99.99%) was purchased from Aldrich Chemistry, oleyl alcohol (85%) was purchased from Alfa Aesar, and oleylamine (70%) was purchased from Aldrich. Hexanes (99.9%), UV-

grade n-hexane (99.9%), toluene (99.9%), and acetone (99.5%) were acquired from Fisher Chemical. All chemicals were used as received.

Synthesis of ITO Nanocrystals

For a typical synthesis of ITO nanocrystals with 10% tin doping, precursor was made by mixing indium acetate and tin acetate in a ratio such that tin acetate was 10 mol% of the total metal acetate content. The metal acetates were mixed in oleic acid in a ratio of 1 mmol of metal for every 2 mL of oleic acid. This mixture was in a glass vial capped with a rubber septum. This vial was suspended in an oil bath at 165 °C and stirred under flowing dry N_2 for 2 h.

In a 100 mL three-neck round-bottom flask, 15 mL of either oleyl alcohol or oleylamine (or mixtures thereof) was heated to 290 °C using a heating mantle and Glas-Col DigiTrol II temperature controller. Each of the three necks of the flask were capped with rubber septa and dry N_2 was flowed in the headspace and out of an 8-gauge purge needle at a rate of ~120 mL min^{-1}.

The precursor was then loaded into a BD plastic syringe equipped with a 6-inch 18-gauge needle, and the syringe was assembled into a KD Scientific syringe pump. The precursor solution was injected into the three-neck reaction flask at the desired reaction rate (0.05 – 0.3 mL min^{-1}). After the injection, nanocrystals were purified by centrifuging in acetone three times at a rate of 7000 RPM for 5 minutes each time. Resulting nanocrystals were then dispersed in either hexanes or toluene.

Characterization of ITO Nanocrystals

Transmission electron microscopy (TEM) characterization of the nanocrystals was performed on an FEI Tecnai Spirit TEM at a voltage of 120 kV. Nanocrystals were deposited onto TEM grids by dipping a 400 mesh carbon-coated copper grid (Ted Pella) into a dilute (~0.5 mg mL^{-1}) solution of nanocrystals in toluene.

Small angle X-ray scattering (SAXS) analysis was performed on an Anton Paar SAXSess mc^2 instrument. SAXS samples were prepared by adding a ~5 mg/mL nanocrystal solution in toluene to borosilicate capillary tubes, which were then sealed with epoxy and left to dry overnight. SAXS patterns were modeled using the Irena software package to determine the nanocrystal diameters, from which the volumes were calculated. For the modeling, a Gaussian distribution and spherical form factor were used.

Fourier transform infrared (FTIR) spectroscopy of the reaction mixture was performed on a Nicolet 6700 FTIR spectrometer equipped with an attenuated total reflectance (ATR) accessory from Thermo Fisher.

Nuclear magnetic resonance (NMR) analysis was performed on a Bruker Advance III-HD 500 MHz NMR spectrometer. NMR solutions were prepared by dispersing the solution to be analyzed in deuterated chloroform.

UV/Vis spectroscopy was performed on a Cary 60 UV/Vis spectrometer from Agilent Technologies. All UV/Vis experiments were performed at room temperature. All solutions analyzed were 5.0 mg mL^{-1} nanocrystals in UV grade n-Hexane.

Results and Discussion

Continuous injection of a metal oleate precursor into oleyl alcohol at temperatures between 230-290 °C results in monodisperse metal oxide nanocrystals and has allowed for in-depth examination of nanocrystal growth processes.[23, 26, 32-33] Under these conditions, esterification results in the formation of ester and metal hydroxy species, the reactive monomers that then condense with each other to form M–O–M bonds (Scheme 3.1a). The rate of esterification limits the rate of production of reactive monomer. Reactive monomers can also be produced by substituting the oleyl alcohol with a primary amine that can react with the metal-carboxylate to form metal hydroxy monomer species through amidation (Scheme 3.1b).[22, 34-41] Although synthesis of metal oxide nanocrystals through amidation,[22, 34-41] and esterification[2, 15-16, 25, 27] are known, there are no reports comparing the effect of amidation vs esterification on resulting metal oxide nanocrystals. Given that amidation is generally faster than esterification, we expected higher rates of reactive monomer production in the amine and aimed to investigate the influence of monomer production on nanocrystal growth in our continuous growth synthesis.

Scheme 3.1. Esterification (a) and amidation (b) reactions to form metal hydroxy species that then condense to form metal oxide nanocrystals

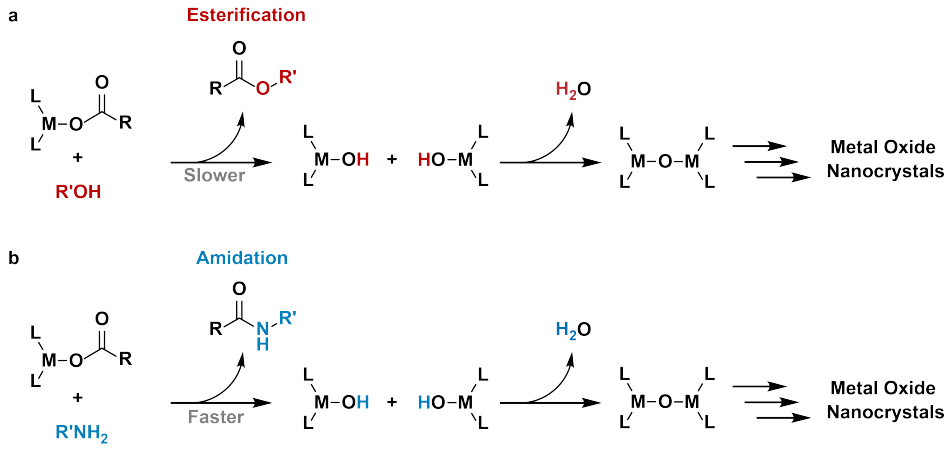

Comparing Rates of Amidation vs Esterification

To confirm that amidation was faster than esterification in this system, we compared the rates of reaction for a mixed In/Sn metal oleate precursor (~10% Sn oleate, ~90% In oleate) when mixed with equal volumes of either oleyl alcohol and oleylamine. The mixtures were heated and the formation of ester and amide monitored by NMR. The precursor was produced by heating 0.1 mmol Sn(IV) acetate and 0.9 mmol In(III) acetate in 2 mL oleic acid at 165 °C for 2 h. Once cooled to room temperature, either 2 mL oleyl alcohol or 2 mL oleylamine was added to the precursor and the reaction mixture was heated to 150 °C and held at that temperature for 30 minutes. 150 °C was chosen because it is below the temperature required to form nanocrystals, thus allowing a direct comparison of the esterification and amidation rates while avoiding complications due to the reactivity of growing nanocrystals.

The amounts of ester and amide formed were determined by proton NMR. For the ester we integrated peaks at 4.0 ppm, which corresponds to the two protons on the carbon adjacent to the ester oxygen in oleyl oleate. For the amide, the peak at 8.1 ppm, which corresponds to the proton on the nitrogen in oleyl oleamide (see Figure B1) was integrated. In each case, we normalized these integrations to the alkene proton peak at 5.3 ppm, which is present in all species containing an oleyl group. We found that more amide was formed (integrated peak of 0.07) than ester (integrated peak of 0.04). We were initially concerned that the acidity of the proton on the amide nitrogen, which can exchange with water, may convolute the integration at 8.1 ppm. However, we used deuterated chloroform dried by molecular sieves to remove water for NMR analysis, which would limit the degree of exchange. Further, if there was exchange between the amide nitrogen proton with residual

water, we would expect that our integration would be artificially low, underestimating rather than overestimating the amount of amide formed. This suggests that amidation is indeed faster than esterification, likely due to the increased nucleophilicity of oleylamine vs oleyl alcohol. This would mean that the precursor is converted to the proposed metal hydroxy monomer species at a more rapid rate in oleylamine vs in oleyl alcohol. Precursor conversion rate has been explored as a factor in nanocrystal growth for a number of systems that fit within the realm of classical nucleation and growth,[7-8, 13] but it has not been explored in depth in reagent-driven growth.

Investigating ITO Nanocrystal Growth in Oleylamine vs Oleyl Alcohol

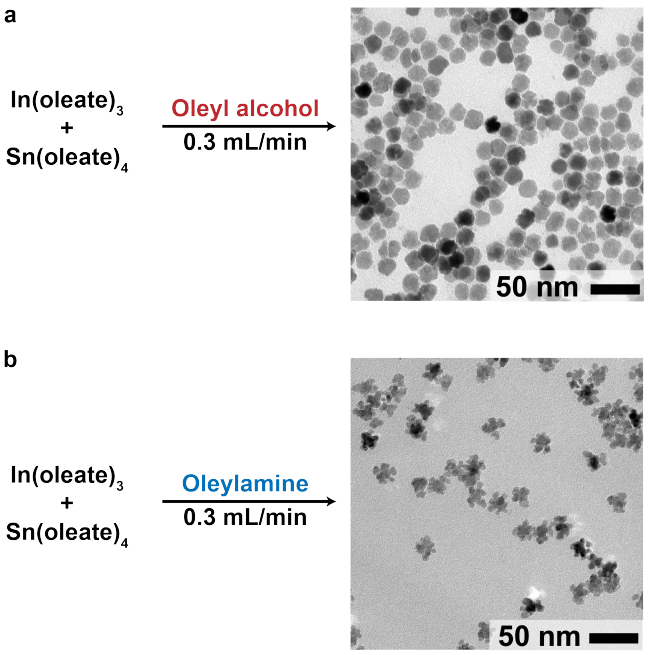

Figure 3.1. TEM images of ITO nanocrystals synthesized by injecting 3 mmol mixed indium/tin oleate precursor at an injection rate of 0.3 mL/min into 290 °C (a) oleyl alcohol, and (b) oleylamine.

Having confirmed the faster rate of amidation, we performed two ITO nanocrystal syntheses to examine the influence on nanocrystal formation and growth., Precursor (3

mmol) was injected at 290 °C at 0.3 mL min^{-1} into both oleyl alcohol and oleylamine. We conducted FTIR analysis of the reaction mixture from the synthesis in oleylamine to confirm the presence of amide (Figure B2). We took TEM images of the resulting purified nanocrystals from each synthesis. The results are shown in Figure 3.1.

The TEM image of the product produced by esterification (Figure 3.1a) shows monodisperse, spherical nanocrystals, consistent with previous studies, whereas the TEM image of the product of amidation (Figure 3.1b) shows highly branched nanocrystal structures. This branched morphology is consistent with what we had previously seen with indium oxide nanocrystals under conditions of high monomer flux to the surface, which happened when high precursor injection rates were used. Based upon this previous study, we hypothesized that the injection rate was too high in the case of oleylamine, and that a slower injection rate would lead to more uniform nanocrystals. To test this hypothesis, we performed a synthesis wherein we injected 3 mmol of the mixed In/Sn oleate precursor into oleylamine at 290 °C at an injection rate of 0.05 mL min^{-1}. The TEM image of the resulting nanocrystals is shown in Figure 3.2.

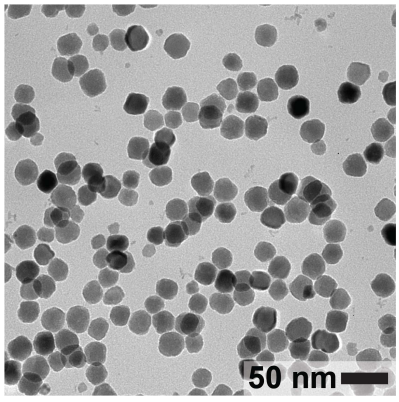

Figure 3.2. TEM image of ITO nanocrystals synthesized by injecting 3 mmol mixed indium/tin oleate precursor at an injection rate of 0.05 mL min^{-1} into 290 °C oleylamine.

The TEM image of the nanocrystals produced by amidation at the slower injection rate (Figure 3.2) shows that when a slower injection rate is used, more spherical and uniform nanocrystals are formed. We were surprised to see that the nanocrystals synthesized in oleylamine in Figure 3.2 are much larger (23.2 ± 3.3 nm in diameter, measured by SAXS) than the nanocrystals synthesized in oleyl alcohol in Figure 3.1a (9.4 ± 1.3 nm in diameter, measured by SAXS). This will be discussed in detail below.

In the case of the nanocrystals synthesized in oleylamine at the higher (0.3 mL min^{-1}) injection rate, we hypothesized that the branched nature of the nanocrystals was due to increased monomer flux to the surface of the nanocrystals. The increased monomer flux to the surface of the nanocrystals synthesized in oleylamine compared to oleyl alcohol could be due to a couple of different reasons. One reason could be that monomer is generated more rapidly, which we know to be the case based upon the previously discussed NMR analysis that showed that more amide formed in oleylamine than ester formed in oleyl alcohol. Another reason could be that fewer nanocrystals were formed, which would lead to larger nanocrystals (as seen in Figure 3.2), and subsequently increased flux to the nanocrystal surfaces.[26] Given the larger nanocrystals in Figure 3.2, we hypothesize that the increased flux is largely due to the formation of larger nanocrystals, though it is also possible that increased flux is also partly due to the more rapid generation of monomer. It is possible that both effects are taking place simultaneously, though it is difficult to definitively conclude this.

We wanted to more closely examine the growth of ITO nanocrystals formed in oleylamine using the continuous growth synthesis, which would enable a closer examination of the growth process. We know from previous studies that the volume of ITO

nanocrystals grown in oleyl alcohol increases linearly with the amount of precursor added.[27, 32] This told us that the nanocrystals grew via a living growth mechanism.[28] We wanted to see if this trend was also observed for nanocrystals grown in oleylamine. To examine this, we performed a 3 mmol synthesis at 290 °C, injecting precursor into oleylamine at 0.05 mL min^{-1}. We took aliquots of the reaction mixture every 0.3 mmol of precursor injected, and purified the nanocrystals in each of those aliquots. We then characterized the nanocrystal size and dispersity by SAXS. For comparison, we also conducted a 12 mmol synthesis wherein precursor was injected into oleyl alcohol at 290 °C at a rate of 0.3 mL min^{-1}. Nanocrystal volume as determined by SAXS is plotted as a function of mmol of precursor added in Figure 3.3 below.

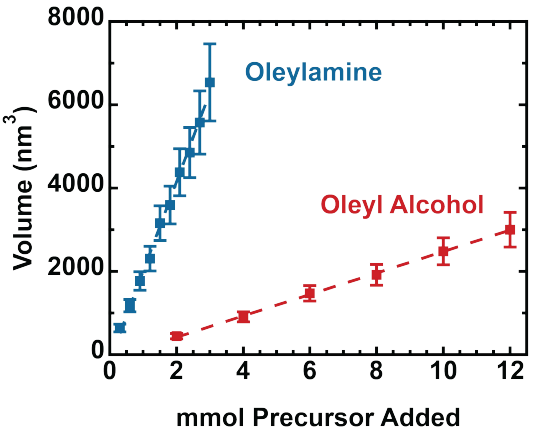

Figure 3.3. Nanocrystal volume obtained by SAXS analysis as a function of mmol precursor added into 290 °C oleylamine at an injection rate of 0.05 mL/min (blue) and oleyl alcohol at an injection rate of 0.3 mL/min (red).

The data in Figure 3.3 show that the nanocrystal volume for nanocrystals synthesized in both oleyl alcohol and oleylamine trend linearly with the amount of precursor added, suggesting in both cases that no new nanocrystals are formed upon addition of precursor, and instead all additional monomer contributes to nanocrystal

growth. The data also show that the growth rate for nanocrystals made in oleylamine is much higher than the growth rate for nanocrystals made in oleyl alcohol. We wondered whether the difference in growth rate was simply due to the number of nanocrystals initially formed. The number of nanocrystals initially formed can be estimated by the slope of the linear trend through the growth curves in Figure 3.3.[26] The equations justifying this estimation are below.

$$y = m * x + b$$

$$\frac{nm^3}{NC} = \frac{1}{NC_{tot}} * \frac{Vol_{tot}}{mmol} * mmol_{inj} + b$$

$$m = \frac{1}{NC_{tot}} * \frac{Vol_{tot}}{mmol}$$

$$NC_{tot} = \frac{2 * 10^{19}}{m}$$

Using the above equations to estimate the number of nanocrystals formed in oleylamine vs oleyl alcohol, we estimate that approximately 1×10^{15} nanocrystals are formed in oleylamine, whereas approximately 8×10^{16} nanocrystals are formed in oleyl alcohol. This suggests the increased growth rate in the case of oleylamine is due to fewer, larger particles forming compared to oleyl alcohol.

To further corroborate the hypothesis that the increased growth rate in oleylamine was simply due to fewer, therefore larger, nanocrystals being formed, we conducted a synthesis wherein we injected 3 mmol of precursor into oleyl alcohol at 290 °C at a rate of 0.3 mL min^{-1}, purified the nanocrystals, redispersed them in oleylamine, heated the mixture

to 290 °C, and injected an additional 2 mmol at 0.05 mL min^{-1}. We took SAXS data of the resulting nanocrystals after injecting 3, 4, and 5 mmol of precursor, and plotted the nanocrystal volume as a function of mmol of precursor added to compare to the growth curves in Figure 3.3. Results are plotted in Figure B3. The data line up exactly with the growth curve using just oleyl alcohol during the synthesis, suggesting that growth occurs in a similar manner at a similar rate in both oleyl alcohol and oleylamine, and the difference in the slopes of the growth curves is just due to the number of nanocrystals initially formed. Taken together, these results suggest that the reagent used in the reaction, oleylamine or oleyl alcohol, alters the earliest stages of nanocrystal formation, changing the number of nanocrystals formed. We will discuss the possible reasons behind this effect in the next section.

In addition to the differences in nanocrystal formation and growth, we noticed a difference in optical properties between nanocrystals synthesized in oleylamine vs oleyl alcohol. For the nanocrystals synthesized in oleyl alcohol, the nanocrystals were initially green upon purification, and then slowly turned blue over the course of ~72 h. For the nanocrystals synthesized in oleylamine, the nanocrystals were blue immediately upon purification. The color of the nanocrystals is associated with the amount of interstitial oxygen within the ITO nanocrystals, with green being indicative of higher interstitial oxygen concentration (more oxidized), and blue being indicative of lower interstitial oxygen concentration (more reduced).[42-43] This phenomenon is the result of the Burstein-Moss effect where an apparent bandgap expansion is observed as electrons populate the conduction band of a material.[42-43] As interstitial oxygen is released from the ITO lattice, an oxygen vacancy is formed and two electrons per oxygen atom get released into the

conduction band, resulting in the bandgap expanding and the color of the nanocrystals changing.[42-43]

The reduction process associated with the release of interstitial oxygen can be monitored by looking at the absorption edge of the ITO nanocrystals in solution by UV/Vis.[42-43] As more oxygen is released and the particles become more reduced, the absorption edge (between 300 – 500 nm) blueshifts. We monitored this process for 24 h post synthesis for nanocrystals synthesized in oleyl alcohol (Figures 3.4a and 3.4b) and oleylamine (Figures 3.4c and 3.4d). UV/Vis spectra were taken once every hour for 24 h in a mixture of 5.0 mg mL^{-1} ITO nanocrystals in UV-grade hexanes. Nanocrystals compared were made by injecting 3 mmol into oleyl alcohol (10.8 ± 1.6 nm by SAXS) or by injecting 0.3 mmol into oleylamine (10.7 ± 1.6 nm by SAXS) so that nanocrystals of the same size could be compared. Results are shown in Figure 3.4.

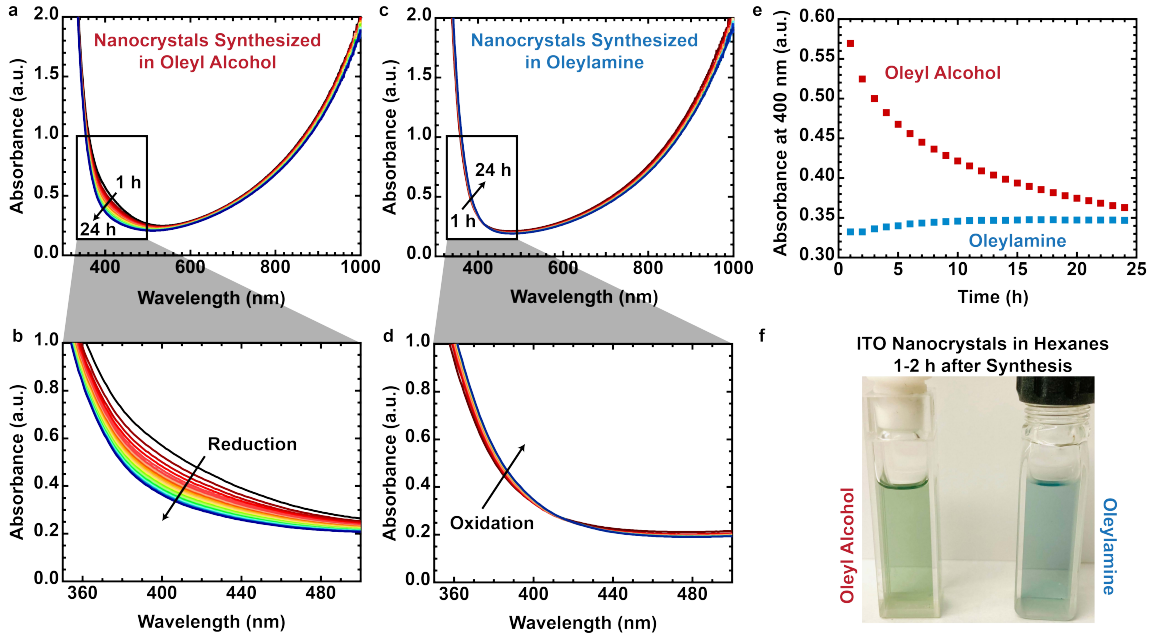

Figure 3.4. (a) UV/Vis spectra of a 5.0 mg mL^{-1} solution of ITO nanocrystals synthesized in oleyl alcohol taken over the course of 24 h. (b) Highlighted region of the spectra in (a)

showing the progressive reduction of the ITO nanocrystals synthesized in oleyl alcohol. (c) UV/Vis spectra of a 5.0 mg mL^{-1} solution of ITO nanocrystals synthesized in oleylamine taken over the course of 24 h. (d) Highlighted region of the spectra in (c) showing the progressive oxidation of the ITO nanocrystals synthesized in oleylamine. (e) Absorbance at 400 nm taken from the spectra in (a)-(d) plotted as a function of time for ITO nanocrystals synthesized in oleyl alcohol (red) and oleylamine (blue). (f) Photograph of 5.0 mg/mL solutions of ITO nanocrystals synthesized in oleyl alcohol (left) and oleylamine (right). The photograph in (f) shows that the ITO nanocrystals synthesized in oleyl alcohol are green upon purification after the synthesis, whereas the ITO nanocrystals synthesized in oleylamine are blue upon purification after the synthesis. In the photograph, the ITO nanocrystals synthesized in oleyl alcohol were 2 h post synthesis, whereas the ITO nanocrystals synthesized in oleylamine were 1 h post synthesis.

Figures 3.4a and 3.4b show the spectra taken over the course of 24 h of the ITO nanocrystals synthesized in oleyl alcohol. Over the course of 24 h, the absorption edge blue shifts as a result of the release of oxygen and the particles become more reduced. Figures 3.4c and 3.4d show the spectra taken over the course of 24 h of the ITO nanocrystals synthesized in oleylamine. Over the first ~10 h, the absorption edge slightly redshifts, eventually leveling out, suggesting that the particles initially undergo a slight oxidation after being exposed to air, before reaching a final absorption. The absorbance at 400 nm for each of the ITO nanocrystal solutions is plotted in Figure 3.4e to further highlight the reduction/oxidation of nanocrystals over 24 h, with lower absorbance at this wavelength corresponding to more reduced nanocrystals. Figure 3.4f shows a photograph of 5.0 mg mL^{-1} ITO nanocrystal solutions in hexanes synthesized in oleyl alcohol (left, green) and oleylamine (right, blue). The photograph was taken 1 h after the synthesis in oleylamine and 2 h after the synthesis in oleyl alcohol to show the color difference observed by eye of the two different nanocrystal solutions.

The results in Figure 3.4 suggest that syntheses in oleylamine result in more reduced nanocrystals. We then wondered whether the basic environment of the oleylamine resulted in more reduced nanocrystals. To test this hypothesis, we synthesized ITO nanocrystals in oleyl alcohol (using 3 mmol of precursor), purified those nanocrystals, redispersed them in oleylamine, and heated the mixture to 290 °C for 5 minutes under flowing N_2. The resulting purified nanocrystals were blue upon purification, suggesting that the reducing environment of the oleylamine facilitates the release of interstitial oxygen, resulting in more reduced nanocrystals.

Investigating the Role of Precursor Conversion on ITO Nanocrystal Growth

Having established the structural and optical properties of the nanocrystals produced in the presence of the two reagents, we return to the question of how the reagent used influences the number of nanocrystals formed. To further establish the links between amidation rate, precursor activation and nanocrystal formation, we examined the synthesis of nanocrystals in mixtures of oleyl alcohol and oleyl amine. We reasoned that it might be possible to tune the number of nanocrystals formed by diluting the more reactive amine with the less reactive alcohol in the reaction flask. Tuning the number of nanocrystals formed at the earliest stages of nanocrystal formation could offer another opportunity to tune size, enabling access to larger nanocrystals.

We performed several nanocrystal syntheses where 6 mmol of precursor was injected into a mixture of either 10%, 25%, or 50% oleylamine in oleyl alcohol (total volume of oleylamine plus oleyl alcohol was always 15 mL). Aliquots of the reaction mixture were taken after every mmol added and the purified nanocrystals from those aliquots were analyzed using SAXS. The resulting nanocrystal volumes are plotted as a

function of mmol precursor added in Figure 3.5a. The original curves for syntheses in solely oleyl alcohol and solely oleylamine from Figure 3.3 are also shown for comparison.

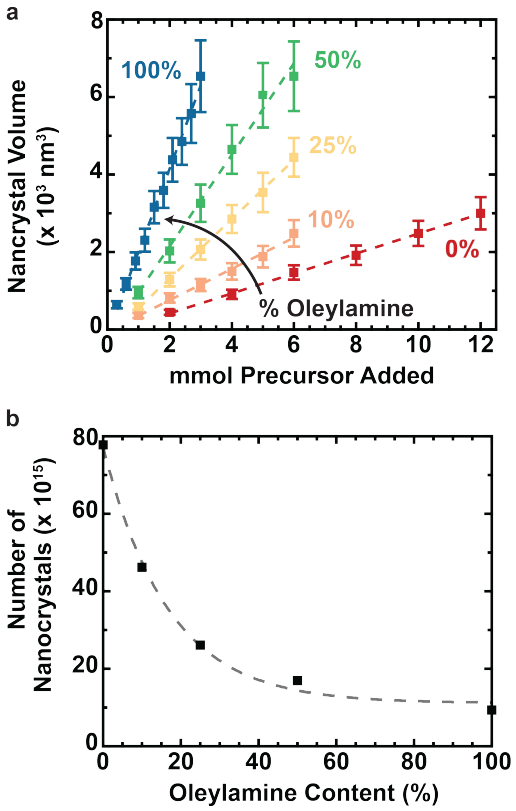

Figure 3.5. (a) Growth curves of nanocrystal volume (obtained by SAXS analysis) as a function of precursor added into varying percentages of oleylamine in oleyl alcohol. As the percentage of oleylamine increases, the nanocrystal growth rate increases. (b) Number of nanocrystals obtained from the slopes of the growth curves in (a) plotted as a function of oleylamine content. The number of nanocrystals formed decreases exponentially (shown by the gray dashed line) as oleylamine concentration increases.

The growth curves in Figure 3.5a show that nanocrystal volume increases linearly with the mmol of precursor added for all mixtures, suggesting that they all undergo a living growth mechanism. The slopes of the curves increase as the content of oleylamine increases, suggesting that the oleyl amine concentration has a direct impact on mechanism of nanocrystal formation. The number of nanocrystals formed can be estimated from the

slopes of the curves in Figure 3.5a, and are plotted in Figure 3.5b. The number of nanocrystals formed seems to decrease exponentially as a function of oleylamine content.

We considered why fewer nanocrystals might form as oleylamine content increases, and how the reaction rate of amidation/esterification influences the earliest stages of nanocrystal formation. It is important to note that amidation and esterification reactions in oleylamine and oleyl alcohol, respectively, occur both with precursor that is injected into solution, as well as on the surfaces of nanocrystals in solution. We know that the nanocrystal surfaces catalyze amidation/esterification and continuously form reactive metal hydroxy species on the surfaces from prior work. In the formation stage, reactions between activated precursor dominate, leading to new nanocrystal formation. After some period, the number of reactive sites on nanocrystals increases to the point where reaction between the surface and the activated precursors outcompetes the reactions between activated precursors, which starts the growth phase.

Oleylamine appears to shorten the duration of the nanocrystal formation phase, leading to fewer nanocrystals that enter the growth phase faster. We hypothesize that this is because the oleylamine increases the rate of formation of reactive hydroxyls on the NC surfaces, effectively increasing the concentration of reactive metal hydroxy species on the surface earlier in the reaction. If the concentration of reactive metal hydroxy species on the nanocrystal surfaces is higher in oleylamine compared to in oleyl alcohol, then these hydroxyls would compete with activated precursor earlier, leading to an earlier transition between nanocrystal formation and growth. This hypothesis is supported by the growth curves in Figure 3.5a and the curve in Figure 3.5b because one would expect that as oleylamine content decreases and is diluted with oleyl alcohol, fewer of the reactive

hydroxyl species would form on the surface, leading to a slightly longer period of nanocrystal formation, therefore leading to more, smaller nanocrystals.

Conclusions

We investigated the growth characteristics and optical properties of ITO nanocrystals grown in oleyl alcohol vs those grown in oleylamine. We find that the amidation reaction that occurs between the metal carboxylate precursor and the oleylamine happens faster than the esterification that occurs between the precursor and oleyl alcohol. This increased reactivity in the case of oleylamine led to fewer, larger nanocrystals. We hypothesized that this is due to increased reaction rates at the surface of the nanocrystals when they are formed, which leads to a higher concentration of reactive hydroxyls on the nanocrystal surfaces in the case of oleylamine, the nanocrystal growth phase starts sooner than it does in oleyl alcohol, leading to fewer nanocrystals. We also investigated the optical properties of ITO nanocrystals produced in oleylamine vs oleyl alcohol. The ITO nanocrystals formed in oleyl alcohol were green upon purification, and turned blue after several days, whereas the nanocrystals formed in oleylamine were blue immediately upon purification. We hypothesized that this was due to the reducing environment of the oleylamine facilitating the faster release of interstitial oxygen, resulting in more reduced nanocrystals immediately after synthesis.

These findings may be more widely applicable in metal oxide nanocrystal syntheses that utilize esterification or amidation reactions to form nanocrystals. For example, size may be further tuned by altering the amount of oleylamine and oleyl alcohol used in the synthesis. The increased reactivity of the oleylamine might also help activate poorly reactive metal carboxylate precursors, such as zinc oleate or zirconium oleate. The use of

oleylamine or mixtures of oleylamine and oleyl alcohol could also extend the utility of the slow addition synthesis to other metal oxides not yet explored.

Bridge to Chapter IV

Chapter III examined the role of precursor conversion kinetics on ITO nanocrystal formation, but has not yet described the potential applications that could benefit from controlling the growth processes of ITO nanocrystals. Chapter IV examines the potential application of precisely engineered ITO nanocrystals for IR plasmonic filters. Such an application comes from the ability to control dopant concentration and radial distribution throughout each nanocrystal. We find that these nanocrystals are amenable to simple, solution processing, which enables a predictably tunable optical response.

CHAPTER IV

SCULPTING OPTICAL PROPERTIES OF THIN FILM IR FILTERS THROUGH NANOCRYSTAL SYNTHESIS AND ADDITIVE, SOLUTION PROCESSING

This chapter was previously published as Krivina, R. A.; Knecht, T. A.; Crockett, B. M.; Boettcher, S. W.; Hutchison, J. E. Sculpting Optical Properties of Thin Film IR Filters Through Nanocrystal Synthesis and Additive, Solution Processing. *Chem. Mater.* **2020**. *32* (19), 8683–8693.

Introduction

Band-pass/band-stop filters with tunable wavelengths and compact structures are desirable for manipulating the optical properties of light sources used in wireless communication, biological imaging, and sensors.[1–4] Traditionally, band-stop filters are composed of several dielectric layers with alternating low and high refractive indices in order to control light absorption in the region of interest.[3,5-15] The materials comprising the filter stack are chosen based on their optical characteristics in the energy range of interest. Such filters typically operate under the multiplication rule of probability, where the amount of light that passes through the filter is determined by the intersection of the passbands.[8] The incident light is absorbed in the regions with no passband overlap and transmitted in the region of an overlap. Thus, resulting spectra are not the sum, but rather the product, of the spectra resulting from each individual layer in the stack. This renders it challenging to create multi-pass band filters with predictable optical spectra from the

preexisting single-pass band filters.[8] Additionally, the stacking of different materials to achieve the desired performance leads to the total thickness of the stack being greater than the target wavelengths.[8] Furthermore, fabrication of the filter geometries often requires processing techniques such as photolithography, sputtering, and pulsed laser ablation, which places practical limits on the scale of application.[16]

Plasmonic nanomaterials can block certain wavelengths of light making them attractive for use in electrochromic windows[17–22] and optical band-pass and band-stop filters.[3,5-15] Optical filters that are based upon plasmonic materials operate under the addition, as opposed to multiplication, rule of probability where the final transmission through the stack is a sum of the individual probabilities and is determined by the bandwidth of each layer.[8] For the localized surface plasmon resonance (LSPR)-facilitated absorbance to be additive, the filter stack must consist of materials with linear optical properties and have a thickness below the target wavelength similar to the traditional filter stacks. In addition, such configurations typically need to be paired with a complex grating composed of plasmonic noble metals such as Au, and require lithographic fabrication techniques.[23,24]

The ability to tune the plasmonic response is an important attribute that, despite much effort to improve, still suffers from several limitations. The most widely studied plasmonic materials are noble metals (e.g. Au, Ag, Cu). The high concentration of the free carriers set by the identity of those metals places the LSPR in the UV and visible range. [25–28] The inability to change the number of free carriers places limits on the potential to tune the LSPR energy and peak shape in metal nanomaterials. Successful strategies include changing the shape and size, or adding “shells” of materials with complementary

properties, however, these structures are not always easy to access through synthesis.[25–28] Even when these structural parameters can be controlled to shift the LSPR, optical absorption typically occurs only from the UV-vis to the onset of the near-infrared (near-IR). Thus, the LSPR energies accessible using noble metals are insufficient for the applications that require tunable optical properties in the near-IR and mid-infrared (mid-IR) ranges of the electromagnetic spectrum, such as electrochromic windows, optical band-stop filters necessary for biological sensing and imaging, and free-space communication.[8,29–31]

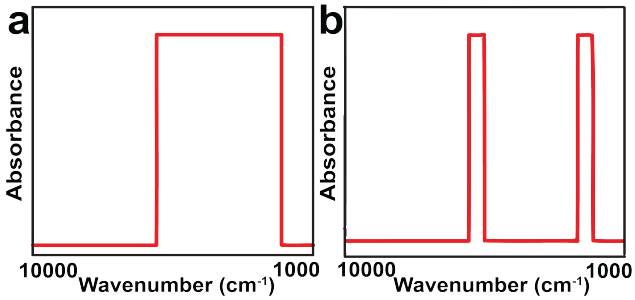

Figure 4.1. Schematic of targeted LSPR responses for (a) a wide band-stop filter that blocks a wide range of wavelengths in the near- and mid-IR regions and (b) a narrow band-stop filter that selectively blocks narrow regions of the near- and mid-IR regions.

Doped metal-oxide nanomaterials are a promising class of materials that have also demonstrated LSPR.[32–34] These materials are more earth-abundant and offer a variety of advantages that complement the attributes of plasmonic noble metals. The LSPR energy of doped metal-oxides is significantly lower than that of the noble metals due to a lower concentration of the charge carriers, which makes it possible to access the energy range from the near-IR into the mid-IR. Given that the carrier concentration is tuned through the dopant concentration, the optical properties of doped metal-oxides can be more easily tuned

than the metals. Varying the doping concentration[17,20,32] and distribution[21] in these materials shifts the LSPR maximum to higher or lower energies and can be used to adjust the LSPR peak width and intensity. The doped metal-oxides are thus promising materials for plasmonic band-stop filters.

Here we present a simple fabrication process to make tunable filters for the energy range between 6,000 and 1,000 cm^{-1} that takes advantage of the additive nature of the absorbance response when employing precisely constructed tin-doped indium oxide (ITO) nanocrystals synthesized through a slow-injection route.[35,36] The LSPR energy of ITO nanocrystals can be shifted from the near-IR to mid-IR range of the spectrum by controlling the size, doping level and dopant placement using the slow-injection synthesis, producing ITO nanocrystals desirable for designing near- or mid-IR filters. Because no single composition of ITO nanocrystal is capable of blocking a wide region (Figure 4.1a) or multiple distinct narrow regions (Figure 4.1b) of the electromagnetic spectrum, construction of a tunable band-stop filter requires a combination of individual optical responses from several nanocrystals. We report the optical properties of layered and homogeneously mixed films of ITO nanocrystals prepared by quick and simple solution processing. We show that the additive nature of the absorbance allows us to sculpt the resulting absorbance spectra to produce wide and narrow band-stop filters in nanocrystal films without the necessity of a thick filter stack, complex grating, and/or restricting processing techniques.

Experimental

Materials and Methods

Indium(III) acetate, tin(IV) acetate, and oleic acid (90% technical grade) were used as received from Sigma-Aldrich. Oleyl alcohol (85% technical grade) was used as received from Alfa Aesar.

Synthesis of ITO and ITO/In_2O_3 Core/Shell Nanocrystals

Syntheses were performed in accordance with previously published results.[34,35] For homogeneously-doped ITO nanocrystals, indium(III) acetate and tin(IV) acetate were mixed in a 20-mL scintillation vial with 4 mL of oleic acid in the desired In/Sn molar ratio to add up to 2 mmol total metal acetate (1.99:0.01, 1.98:0.02, 1.95:0.05, 1.90:0.10, and 1.80:0.20 mmol In:Sn for the 0.6, 1.2, 3.3, 6.8, and 16% doped ITO, respectively). Each precursor solution was heated to 150ºC under N_2 flow with constant stirring for several hours. ITO nanocrystals were then formed by injecting the mixed In/Sn-oleate precursor into 13 mL of oleyl alcohol at 290ºC under flowing N_2 via a syringe pump at a rate of 18 mL hr^{-1}. Nanocrystals were washed in acetone and redispersed in toluene.

ITO/In_2O_3 core/shell nanocrystals were synthesized following a similar procedure as described above. The core and shell precursor solutions were prepared separately. The core precursor solution containing the mixed In/Sn-oleate in the ratios desired for the core doping (0.66:0.01, 0.65:0.02, 0.95:0.05, 0.59:0.07, and 1.67:0.20 mmol In:Sn for the cores of 1.5%, 3%, 5%, 10%, and 16% Sn, respectively) was injected first at a rate of 18 mL hr^{-1} via a syringe pump into 13 mL of oleyl alcohol at 290ºC under flowing N_2. An aliquot of this solution was taken in order to determine the core size and doping concentration. Then In-oleate solution was injected at the same rate in the quantity necessary to bring the total

amount of metal-oleate in the flask to 2 mmol. For the ITO samples used for the narrow band-stop filter we synthesized a 2 mmol doped core (1.80:0.20 and 1.99:0.01 mmol In:Sn for the 12% ITO core and 0.4% ITO core with thin In_2O_3 shells, respectively) and injected 0.3 mmol In-oleate to obtain an ultra-thin shell.

Characterization of ITO and ITO/In_2O_3 Core/Shell Nanocrystals

Elemental compositions of ITO nanocrystals with doping levels above 2% were determined using a Thermo Scientific ESCALAB 250 X-ray photoelectron spectrometer (XPS). Tin:indium content was determined by integrating the tin $3d_{5/2}$ peak and comparing the intensity to that of the indium $3d_{5/2}$ peak. Peak binding energies were referenced to the C1s hydrocarbon peak at 284.8 eV. Samples were prepared by drop-casting solutions of nanocrystals dispersed in toluene onto silicon wafers and allowing them to dry.

Elemental compositions of ITO nanocrystals with doping levels below 2% were determined by inductively coupled plasma optical emission spectrometry (ICP-OES). A Teledyne Leeman Laboratories (Hudson, NH) Prodigy High Dispersion ICP-OES system was used. Samples were prepared by digesting dried nanocrystals in concentrated HCl for 48 h before being diluted with 2% v/v HNO_3 for analysis.

Transmission electron microscopy (TEM) micrographs were acquired on a FEI Tecnai Spirit TEM (Hillsboro, OR) operating at 120 kV. Lacey carbon grids supported on copper from Ted Pella (Redding, CA) were used to image the nanocrystals. TEM grids were prepared by submerging in ~0.5 mg/ml solutions of nanocrystals in toluene.

Size and polydispersity of the nanocrystals were determined using a lab-scale small-angle X-ray scattering (SAXS) instrument (SAXSess, Anton Paar, Austria). The system is equipped with a Cu kα (λ = 0.154 nm) X-ray source that was operated at 40 kV

and 50 mA. A charge-coupled device detector (Roper Scientific, Germany) was used to detect scattered X-rays. An average of 50 individual scattering curves was acquired for various acquisition times (0.1-3 s) to maximize signal to noise. Raw data was processed with SAXSquant software (version 2.0) and curve fitting was done using Irena macros for IGOR (V. 6.3.7.2).[37] A spherical form factor was used for curve fitting, supported by morphology visualized by TEM.

Preparation and Characterization of Thin Films of ITO and ITO/In_2O_3 Core/Shell Nanocrystals

Thin films of ITO nanocrystals were prepared by spin-coating solutions of ~50 mg/mL nanocrystals in toluene onto UV-grade CaF_2 substrates (2.54 cm diameter x 1 mm thick, UQG Optics, Cambridge, England). Substrates were first cleaned by sonication in toluene for 10 min then isopropanol for 10 min. A Laurell WS-400-6NPP-LITE Manual Spin Processor was used at a rotation rate of 3000 RPM for 30 s. Solvent was allowed to evaporate in air before characterization. For multilayered samples, each layer was annealed in air at 150°C for 10 minutes prior to the deposition of the next layer.

UV-vis spectra of thin films were collected on a PerkinElmer (Waltham, MA) Lambda 1050 spectrometer from wavelengths of 250 – 3,300 nm (40,000 – 3,030 cm^{-1}) with a scan resolution of 1 nm. Fourier Transform Infrared (FTIR) spectra were collected on a Thermo Fisher Nicolet 6700 spectrometer from wavelengths of 2,500 – 25,000 nm (4,000 – 400 cm^{-1}). To visualize the LSPR of the thin films with different doping levels in the same plot, we joined the spectra obtained from UV-vis and IR spectrometers at 3,500 cm^{-1}. FWHM was calculated by manually finding the middle of the LSPR peak in OriginPro 9 software.

Scanning electron microscopy (SEM) was performed to characterize the homogeneously-mixed and multilayered films of the homogeneously-doped ITO nanocrystals using an FEI Helios Nanolab 600i FIB-SEM with a Through-Lens detector. The homogeneously mixed film was prepared by first diluting the solutions of 0.7, 1, 3, 7, and 16% Sn-doped indium oxide nanocrystals such that their optical absorbance when spin-coated into a film would be ~0.1. These solutions were then mixed together such that the final concentration was 50 mg/mL, and this solution was then spin-coated onto a silicon substrate. For the multilayered films, the diluted solutions were spin-coated onto a silicon substrate from lowest to highest doping and vice versa, as illustrated in Figure 4.4a and C1, annealing the substrate at 150ºC for 10 minutes in between the layer additions. Oleate ligands in these samples were removed in order to reduce charging during image acquisition. To remove the oleate ligands, the substrates with the films were soaked in a solution of 1 M formic acid in acetonitrile for one hour, and then annealed at 300ºC under air for one hour, following a previously established procedure.[40] Top-down images were acquired using an accelerating voltage of 5 kV and a beam current between 86 – 1,400 pA. To obtain cross section images of the ITO nanocrystal films, a layer of carbon was first deposited. The sample was then milled using a commercial gallium focused ion beam operating at 30 kV using an ion current of 2.5 nA for the initial milling, and then an ion current of 0.79 nA to polish the edge for subsequent imaging. Cross-section images were then acquired using an accelerating voltage of 2 kV and a beam current of 86 pA. SEM images are shown in Figure C1.

Results and Discussion

To investigate tunable optical filters based upon thin films of plasmonic nanocrystals we need access to a variety of nanocrystals with defined optical features from which we can form uniform films. Further, we need to understand how the optical properties of these films depend upon the type and spatial distribution (layered vs. mixed, for example) of the nanocrystal building blocks. Here we describe the synthesis of 12 different compositions of ITO nanocrystals that allow the systematic variation of optical absorption from ~ 6,000 – 1,000 cm^{-1}, report the optical properties of films formed from mixtures of these nanocrystals, and describe how specific mixtures can be used to produce optical filters with desired characteristics.

Synthesis of a Library of Materials

The LSPR response of metal-oxide nanocrystals can be tuned by altering nanocrystal size, the identity and concentration of the dopant(s), where those dopants are localized in the nanocrystal, and defect concentration.[21,34,38] To have a predictable effect on the optical properties of the designed material, each these parameters must be controlled during synthesis. Unfortunately, these parameters have been historically difficult to manage through synthesis. A number of nanocrystal syntheses exist for ITO, but it was difficult to systematically adjust the structural features that influence their properties. The resulting nanocrystals often exhibit significant size dispersity and poorly controlled dopant placement and doping levels. Because of differences in defect levels and radial dopant placement, the properties of ITO nanocrystals of the same size and doping level made by different syntheses differ substantially.[21] The energy, shape, and intensity of the LSPR in

plasmonic nanoparticles are highly sensitive to doping concentration and radial distribution, as well as to the presence of crystal defects, and thus precise control over these properties is necessary in order to predictably shape the optical response.[16,38]

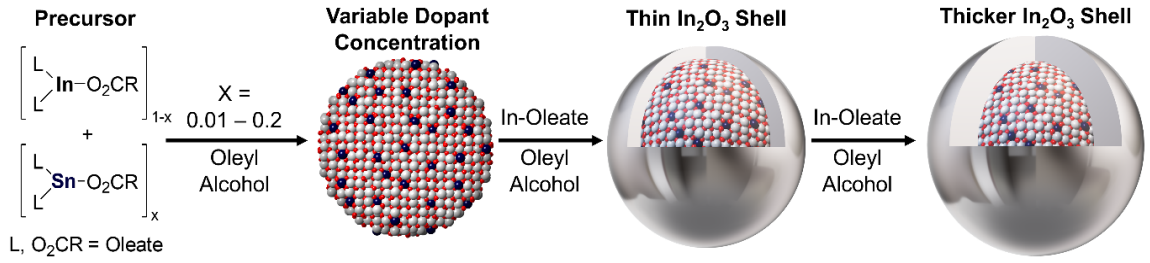

Figure 4.2. Slow-injection synthesis, involving controlled addition of metal oleate precursors into hot oleyl alcohol, allows precise control over nanocrystal size, dopant concentration and placement, and construction of core/shell structures needed to sculpt the optical properties of ITO nanocrystals and resulting thin films.

A low-temperature esterification synthesis previously developed by our group enables unprecedented control over the properties of ITO nanocrystals.[34–36,39] It allows layer-by-layer growth of metal-oxide nanocrystals that leads to superior control of nanocrystal size and dopant concentration and placement. The synthesis grants access to a large library of materials with a wide range of LSPR energies and shapes and has been shown to work for a variety of binary oxides.[34-35] The desired modifications of the optical properties can be easily accomplished by varying parameters such as the amount of precursor added (size), ratio of the metals in the precursor (dopant identity and amount), order of addition of metal precursors (radial dopant distribution), and dopant activation and damping control (core/shell structuring) (Figure 4.2). Ligand-stabilized ITO nanocrystals form dispersions that can be solution-processed to obtain nanocrystal thin films with desired optical and electronic properties.[40]

We started by synthesizing 10 nm ITO nanocrystals with different tin doping levels (0.7, 1, 3, 7, and 16 metal %). Because the nanocrystal size can influence their optical properties,[40] all nanocrystal samples were prepared with the same core diameter so that the effect of size would not need to be considered when comparing optical properties between samples. A predictable shift in the LSPR energy of fabricated ITO thin films towards higher energies was observed as the dopant concentration was increased (Figure 4.3a.). Nanocrystal size was kept constant by using the same amount (2 mmol) of metal-oleate precursor for each synthesis. Doping levels were varied by changing the tin/indium oleate ratio in the precursor. Nanocrystals were first characterized in solution. Small-angle X-ray scattering (SAXS) was performed to characterize size and dispersity (see Figures C2-C3); transmission electron microscopy (TEM) was used to examine the morphology (see Figure C4); and X-ray photoelectron spectroscopy (XPS) and inductively coupled plasma optical emission spectroscopy (ICP-OES) were performed to quantify the Sn content (see Figure C5). Nanoparticles were then spin-coated to form thin films before their optical properties were characterized by UV/Vis and Fourier transform infrared spectroscopy (FTIR) (see Figure C6).

The optical spectrum of the sample containing 0.7 Sn metal % (0.7% ITO) was almost indistinguishable from the undoped indium oxide, thus it formed the lower limit for the doping level. We chose 16% as an upper doping limit because the LSPR-facilitated absorbance of films produced from more heavily doped nanocrystals begins to broaden and red-shift due to increased scattering from the added dopants.[34] The continuous growth of the nanocrystals facilitated by a slow addition of the precursors makes it possible to

increase the doping level up to 20% without phase segregation, but the shift in the LSPR peak induced by the additional dopants is counteracted by increasing scattering.[34]

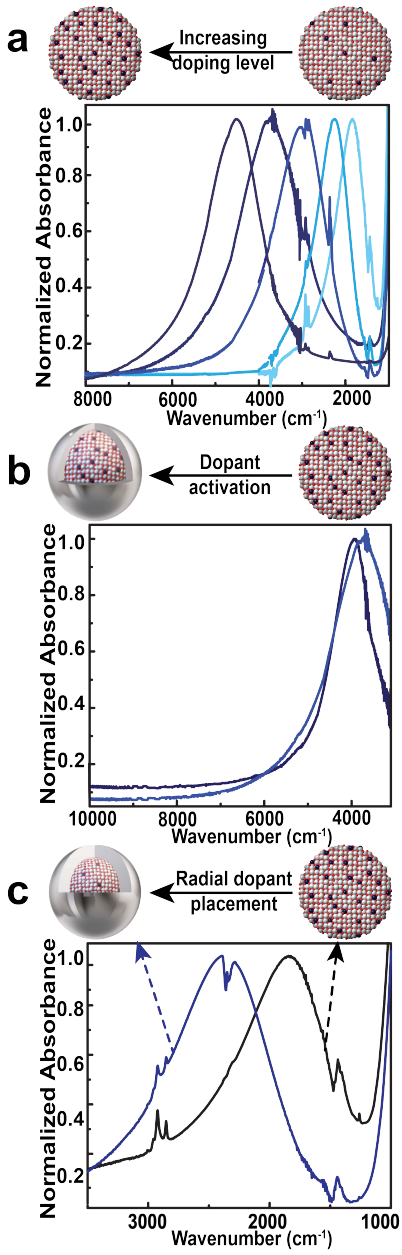

Figure 4.3. The influence of tin dopant concentration and spatial distribution on the energy and shape of the LSPR signal in indium oxide nanocrystal films. (a) Increasing the concentration of dopant, and thus free carriers, shifts the LSPR toward higher energy in homogeneously-doped ITO nanocrystal thin films. Spectra for nanocrystals containing 16%, 7%, 3%, 1%, and 0.7% Sn are displayed from left to right. (b) Adding an undoped

shell increases dopant activation and decreases damping, resulting in narrower LSPR peaks (blue: 7% homogeneously-doped ITO; dark blue: 5% ITO core with an In_2O_3 shell). (c) Manipulating the radial dopant distribution influences the energy of the LSPR peak for nanocrystals. Concentrating dopants in the core instead of uniformly distributing them throughout the nanocrystal results in decreased damping and increased dopant activation. The LSPR of the core/shell nanocrystals is blue-shifted compared to the LSPR of the homogeneously doped ITO despite having the same overall doping concentration (black trace: 0.65 % Sn; blue trace: 0.58 % Sn). The stretches observed at 3,800, 3,000, 2,900, 2,400, and 1,400 cm^{-1} are due to ligands and solvent. The signal interference at 3,200-3,030 cm^{-1} originates from the instrumental noise at the end of the UV/Vis-NIR detector range.

In addition to the overall doping level, the placement of dopant atoms provides an alternative approach to modify the shape and energy of the optical spectrum across the near- and mid-IR ranges.[41] To demonstrate how dopant placement influences the optical properties, we synthesized core/shell ITO/In_2O_3 nanocrystals over the same range of overall dopant concentrations as the homogeneously-doped nanocrystals, but with the tin atoms localized in the core. These core/shell structures have been shown to exhibit narrower LSPR linewidths due to increased surface dopant activation and decreased damping (Figure 4.3b).[34] The core/shell approach can also be utilized to shift the LSPR to higher energy without increasing the overall doping concentration (Figure 4.3c). By manipulating the doping levels and radial placement we obtained a library of ~10 nm ITO nanocrystals (Table 1) that could be easily fabricated into thin films with the absorbance covering a wide range of energies (6,000-1,000 cm^{-1}) and a variety of shapes.

Table 4.1. Library of ITO nanocrystals synthesized through a slow-injection esterification synthesis.

Samples	Diameter[a] (nm, by SAXS)	Doping[b] (by XPS[c] or ICP-OES[d])	LSPR Max (cm^{-1})	FWHM (cm^{-1})
0.7% ITO	10.7 ± 1.3	0.65 ± 0.01[d]	1,844	816
1% ITO	11.3 ± 1.5	1.24 ± 0.01[d]	2,249	895
3% ITO	9.3 ± 0.7	3.3 ± 0.1[c]	2,978	1,375
7% ITO	10.3 ± 1.0	6.8 ± 0.2[c]	3,737	1,793
16% ITO	10.5 ± 1.3	16.0 ± 0.3[c]	4,509	1,534
1.5% ITO core with In_2O_3 shell	Core only: 7.2 ± 1.0 Core/shell: 10.3 ± 1.2	0.58 ± 0.01[d]	2,389	978
3% ITO core with In_2O_3 shell	Core only: 9.0 ± 1.2 Core/shell: 10.3 ± 1.4	1.31 ± 0.01[d]	3,001	1,074
5% ITO core with In_2O_3 shell	10.0 ± 1.1	2.9 ± 0.1[c]	3,937	1,125
10% ITO core with In_2O_3 shell	9.7 ± 0.7	3.8 ± 0.2[c]	4,080	1,140
16% ITO core with In_2O_3 shell	9.9 ± 1.3	13.0 ± 0.1[c]	4,411	1,876
0.4% ITO core with In_2O_3 shell	Core only: 9.7 ± 1.4 Core/shell: 10.3 ± 1.3	0.35 ± 0.01[d]	1,740	872
12% ITO core with In_2O_3 shell	Core only: 9.4 ± 1.1 Core/shell: 9.8 ± 1.2	10.6 ± 0.2[c]	4,509	1,512

[a] SAXS sizes for core/shell nanoparticles were measured twice: after addition of the doped core ("core only" in the table), and after the undoped shell was added ("core/shell" in the table).
[b] Each doping percentage is represented as the Sn-to-In metal percent.
[c] Samples where Sn content was measured by XPS
[d] Samples where Sn content was measured by ICP-OES

Multilayered ITO Films

We next investigated whether we could tap the properties of these nanocrystals to fabricate band-stop filters with tunable absorption across the mid-IR and near-IR. A common practice in the field involves the layering of materials possessing different properties to tune the optical response of a filter.[8] Thus, our first approach was to study the optical properties of filters produced by depositing layers of different doped nanocrystals from the library in Table 1.

For these studies, we utilized several of the homogeneously-doped ITO nanocrystals described in Table 1 with the LSPR energies covering a wide energy range starting in the mid-IR (1000 cm^{-1}) and ending in the near-IR (6,000 cm^{-1}). Each sample was dissolved in toluene and diluted so that a spin-coated layer of that individual nanocrystal had a measured maximum absorbance intensity of approximately 0.1. Solutions of different nanocrystal types were sequentially spin-coated on a CaF_2 substrate starting with the lowest doped sample (0.7% ITO) and increasing the doping level in each consecutive layer, ending with 16% ITO (Figure 4.4a). After each layer was deposited, the substrate was annealed in air at 150°C for 10 minutes. Annealing at 150°C removes solvent and prevents the ITO nanocrystal films from being removed by contact with the organic solvent used in subsequent deposition steps. We also made a film wherein the order of deposition was reversed, starting with the highest doped sample, and finishing with the lowest (Figure 4.4b) to determine if the order of the layers mattered. The changes in the absorbance of the multilayered films were monitored with UV/Vis-NIR (Figure 4.4c and d) after each subsequent layer was deposited.

The spectra in Figure 4.4 (c and d) suggest that the order of deposition of the layers significantly influences the shape and intensities of the optical response of the layered films. The spectra of the film demonstrated in Figure 4.4a show the absorbance maximum shifting to higher energy with each layer along with an increase in the intensity of the absorbance (Figure 4.4c). As layers containing nanocrystals with higher doping levels are added, the contributions to the absorption due to the initially deposited layers containing lower doped nanocrystals seem to diminish completely by the time the 16% ITO layer is deposited. With the addition of the last layer, the shape and energy of the overall absorbance spectrum closely resembles the optical response of a film made of only 16% ITO nanocrystals. For the second film structure (Figure 4.4b) that has the reversed order of layers, the intensity of the combined spectrum (Figure 4.4d) also increases upon the addition of each layer but the absorbance maximum does not shift significantly. Instead, the width of the absorbance increases upon the addition of subsequent layers. Although the spectra reveal contributions from each of the individual spectra, the higher doped layers appear to dominate the spectral response. Still, the second layering approach does produce a filter that absorbs over a broader spectral range, even though the response is not additive.

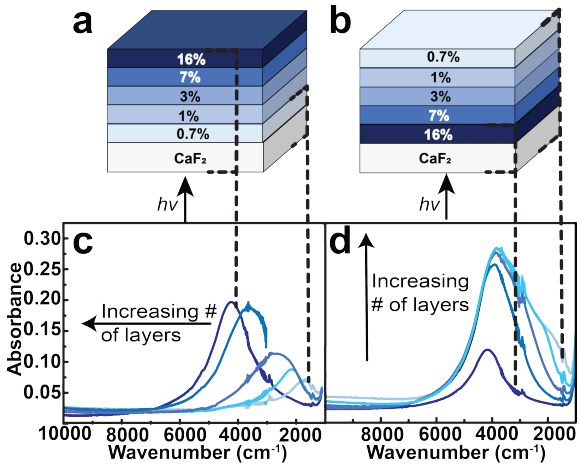

Figure 4.4. Multilayered films fabricated by spin-coating ITO nanocrystal solutions that were diluted to produce films with an absorbance of approximately 0.1. The solutions were spin-coated starting with the lowest doping concentration and proceeding to the highest in (a) and from the highest to lowest in (b). The changes in the optical absorbance were monitored with the UV/Vis-NIR after deposition of each consecutive layer and are shown in the bottom panel. Plot **c)** corresponds to the structure in (a). Plot (d) corresponds to the structure shown in (b). The direction of the beam is shown by the arrows. The absorbance spectra were obtained by measuring the transmittance of the films deposited on CaF_2 and converting transmission to absorbance (2-log(%T)). The collected absorbance was not corrected for the absorbance of the substrate (See Figure C7 for the absorbance of CaF_2), because the substrate did not absorb a significant amount of light in the LSPR region.

We were curious about why the ordering of the layers had such an influence on the optical properties of the films given that composition and the interfaces between the layers within the film are the same. Given the previously stated finding that all the layers remain intact during the deposition process, we reasoned that the two samples in Figure 4.4 might produce a different combined optical spectrum due to differences in reflectivity that arise from the order in which the beam encounters each layer. To test this hypothesis, we took

the UV-vis/NIR spectra of the samples in Figure 4.4, arranging the samples so that the beam entered the sample from the opposite direction. The resulting spectra were identical regardless of the incident beam direction (Figure C8) apart from a small change in the intensity of the signal likely caused by the inhomogeneity of the film thickness. We concluded that the loss of absorbance due to reflectance at each interface cannot be the major cause of the observed differences in the absorbance of the different film structures.

The main difference between the samples with the opposite ordering of the layers is the proximity of the highest and lowest-doped materials to either the substrate or air interfaces. The layer directly in contact with CaF_2 is exposed to a much higher dielectric environment than that provided by the interface with air.[42-43] The shape and energy of LSPR peaks are strongly influenced by the dielectric environment,[16,44-47] shifting to lower energy and broadening when placed in a high dielectric environment. Further, the ITO nanoparticles with higher doping level have been shown to be less affected by the change in the dielectric medium then the lower doped nanoparticles.[16,48-52] Thus, the absorbance contribution of the 0.7% ITO layer in the film shown in Figure 4.4a might be underrepresented in the multilayered films because it is sandwiched between materials with higher dielectric constants than air: the substrate and another ITO film. In the sample shown in Figure 4.4b, the 16% ITO layer is sandwiched between the substrate and the 7% ITO layer that both have relatively high dielectric constants. As more layers are deposited, the environment surrounding the 16% ITO layer remains constant and its contribution is not diminished from being in contact with a high dielectric medium.

To test our hypothesis that the dielectric environment strongly affects the combined optical spectrum of multilayered films, we designed a simpler system that consisted of only

two layers comprised of the 16% and 0.7% ITO nanocrystals. Two films were constructed wherein we changed the order in which we spin-coated the ITO solutions and the optical properties for each were analyzed (Figure 4.5a).

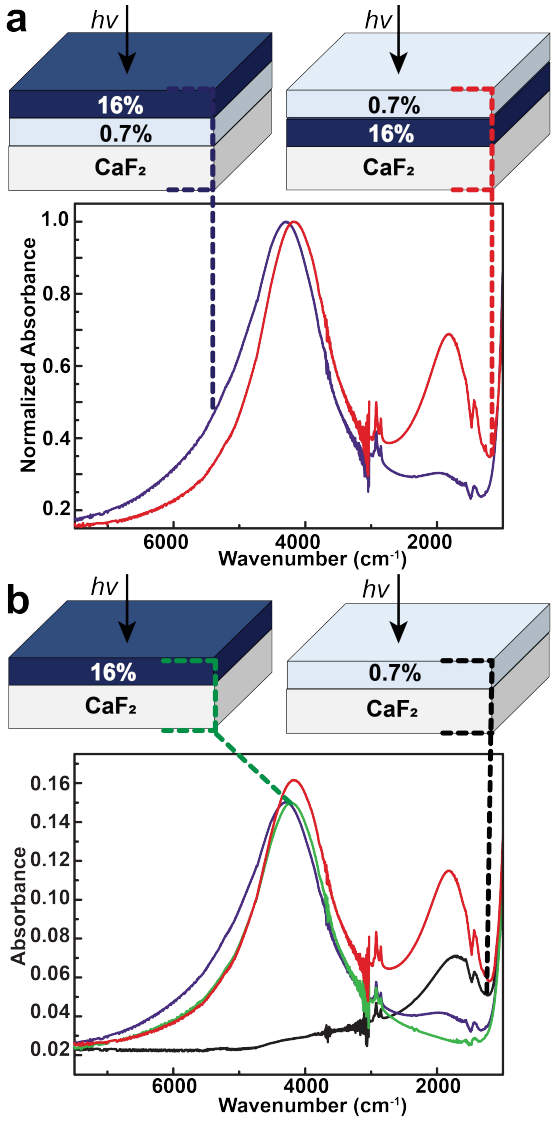

Figure 4.5. (a) Bilayer films fabricated to evaluate the influence of the surrounding dielectric medium on the combined optical responses. The diagrams show the order in which the ITO solutions were spin-coated. The solutions were diluted so that the measured absorbance was approximately equal in intensity. The spectra were normalized to the intensity of the optical absorbance peak at 4,509 cm^{-1} contributed by the 16% Sn-doped

film. (b) Raw (non-normalized) absorbance of the two-layer films (same colors as in (a)) plotted with the individual spectra of the 16% (**green**) and 0.7% (**black**) ITO films. The direction of the beam is shown by the arrows.

When 16% ITO is layered over the 0.7% ITO layer on CaF_2, the spectrum (Figure 4.5a) resembles that of the higher doped film alone. The contribution of the lower-doped layer is underrepresented. The absorbance due to the 0.7% ITO film (at 1,822 cm^{-1}) has lower intensity than was recorded for the lower-doped film alone (Figure 4.5b). When the layering is reversed, absorption due to the 0.7% Sn-doped layer can be clearly identified. The intensities of the layers are not equal but are clearly discernable in the combined optical spectrum. The raw optical spectra of the lower and higher-doped films by themselves compared with the spectra of the two-layer films (Figure 4.5b) clearly show the changes in the absorbance maxima positions and intensities. Layering the 0.7% Sn-doped nanocrystals over the 16% Sn-doped layer intensifies the absorbance of the individual contributions (red trace in Figure 4.5a and b) and red-shifts the 16% Sn-doped layer contribution while blue-shifting the optical contribution of the lower doped layer.

The energy shifts observed in the combined spectra of the two-layer films are consistent with the effects expected from changing the dielectric environment in the vicinity of the film. Further, the attenuation and intensity enhancement of the optical properties in the two-layer films follow the same trend as we found in the multilayered films. The contribution of the 0.7% ITO layer sandwiched between the substrate and the higher doped layer is diminished significantly from being in contact with a high dielectric environment, whereas the reverse ordering does not lessen the optical contribution of the 16% ITO layer to the combined absorbance.

In both the two-layer and multilayered films, the changes in the spectral response appear to be strongly influenced by the local dielectric environment of the layer. Films with a lower doping concentration appear to be affected to a higher extent than the samples with a higher doping level. As a consequence of these effects, spin-coating consecutive layers of ITO films does not result in easily predictable combined absorbance. Given our interests in developing a convenient approach to constructing optical filters from nanocrystal building blocks, we did not investigate other possible reasons for the observed phenomena in the multilayered films, but instead moved on to evaluate the optical properties of homogeneously mixed nanocrystal films. We reasoned that, if the sensitivity of the LSPR to the dielectric environment of the substrate and neighboring layers has a strong influence on the combined optical response, we should be able to fabricate films where the different nanocrystals are homogeneously distributed throughout the film producing a uniform dielectric environment. This approach could potentially lead to a more predictable optical response.

Homogeneously Mixed ITO for Wide Band-Stop Filters

Provided that the ITO nanocrystal films can be solution-processed, a uniform dielectric environment should be achievable through simply combining the nanocrystal solutions of different doping concentrations to attain a combined absorbance that is the sum of the absorbances of the individual nanocrystals. Creating a homogeneous dielectric environment should then allow us to predictably engineer a wide band-stop optical filter covering a range of wavelengths from the mid-IR to the near-IR. Thus, we set out to investigate if mixing the nanocrystal solutions and processing them into a thin film would

enable us to absorb light covering the range of 1,000 and 6,000 cm^{-1} and avoid the unpredictable optical properties observed for the multilayered films.

From the library of nanomaterials in Table 1, we selected the same homogeneously-doped ITO nanocrystals that we used to design the multilayered films and that had individual LSPR absorbance peaks in the range from the mid-IR (1,000 cm^{-1}) to the near-IR (6,000 cm^{-1}). The absorbance spectra of the selected nanocrystals are shown in Figure 4.6a (dashed blue lines). Figure 4.6a shows the predicted absorbance spectrum (solid red line) we obtained by summing the normalized absorbance data for the five homogeneously-doped ITO nanocrystal components. The calculated spectrum predicts a wide band absorbing light between 1,000-6,000 cm^{-1}, encompassing the range of wavelengths covered by the absorbances of the individual nanocrystal components. Note that in the summed spectrum the intensity near 2,000 cm^{-1} is lower than one might intuitively predict from the component spectra. We attribute the decreased absorbance intensity to decreased overlap between neighboring spectra. If mixing the component ITO nanocrystals results in additive absorbance properties, then we would expect a spectrum similar to the predicted spectrum where the absorbance intensity across 1,000 – 6,000 cm^{-1} is equal.

To test the hypothesis that mixing nanocrystals would result in predictable additive optical properties, we mixed the ITO nanocrystal solutions (0.7, 1, 3, 7, and 16% ITO) in concentrations such that the measured absorbance intensity of each nanocrystal doping level would be equal when processed into a thin film. We spin-coated the resulting mixture onto a CaF_2 substrate and measured the optical absorbance by FTIR and UV/Vis spectroscopy. Figure 4.6b depicts the summed spectrum (red) from Figure 4.6a overlaid

with the experimentally measured absorbance spectrum resulting from a mix of nanocrystals of different doping levels processed into a thin film (blue).

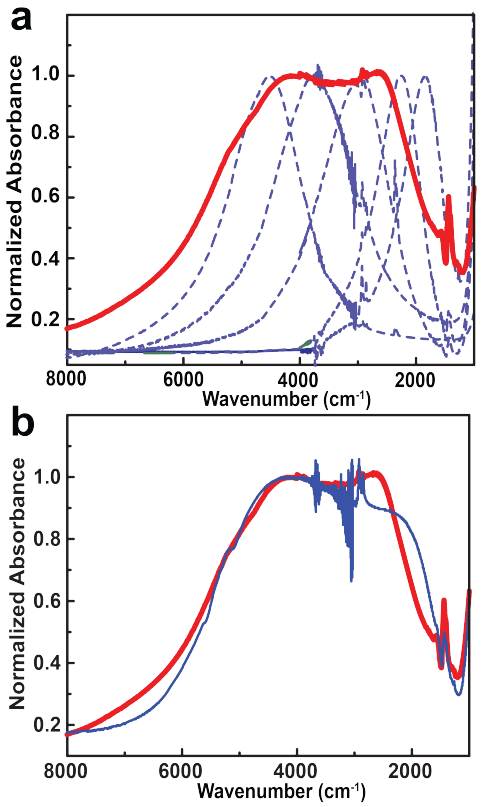

Figure 4.6. Formulation and evaluation of a wide band-pass filter produced by homogeneously mixing nanocrystals in a thin film. (a) Individual spectra (dashed lines) of homogeneously-doped nanocrystals (0.7, 1, 3, 7, and 16% ITO) were summed to obtain the combined normalized spectrum (red) that establishes the predicted optical response of the filter; (b) Comparison of the predicted (red) and measured (blue) absorbance of homogeneously mixed ITO nanocrystal thin film. The interference in the wavelength range of 4,500 to 3,000 cm^{-1} is due to CH stretches and instrumental noise at the end of the detector ranges where the traces from the UV/Vis and FTIR spectrometers were combined.

The experimentally measured spectrum looks remarkably similar to the predicted optical response. The absorbance onset starts at about 7,000 cm^{-1} for both spectra. The combined absorbance extends far into the mid-IR (~1,000 cm^{-1}) accounting for the

individual contributions of each nanocrystal component. Based on the measured experimental spectrum, the optical properties of ITO used in the mixed film are not experiencing an unequal intensity enhancement or attenuation. Given that the same ITO solutions were used to prepare the films with the optical responses shown in Figures 4.4c, 4.4d and Figure 4.6b, the exceptional match between the experimental spectrum and the predicted spectrum in the homogeneously mixed solution films and the loss of the contributions of individual components in the multilayered films clearly demonstrates the superiority of using a solution processing method that renders a uniform dielectric environment.

The close agreement between the measured and predicted spectra supports our hypothesis that a predictable combined optical response is achievable by mixing nanocrystals of different Sn doping concentrations in solution and subsequently spin-coating the mixed solution into a film. The equal contributions of the individual components in the experimental spectrum suggest that ITO nanoparticles of each doping concentration are experiencing a dielectric medium created by a uniform mixture of the other ITO nanocrystals which results in diminishing the effects of the dielectric medium gradient at the air/film and film/substrate interfaces. The absorbance of the film covers a wide energy range desired for a wide band-stop filter or as a coating for low-emissivity windows.[5-15,29–34,57] These results indicate that both the range of absorbance as well as the absorbance intensity are predictable and tunable through selection of different ITO nanocrystals from the library of synthesized materials. The additive nature of the absorbance demonstrated by the solution-processed films, combined with the tunability of the ITO nanocrystal synthesis, enables a superior level of control over the optical properties

of the band-stop filters for the near-IR to the mid-IR region. The final absorbance spectrum is easily predicted by looking at the LSPR energies and shapes of the ITO solutions prior to mixing. This level of tunability is important for a facile design of band-stop filters and has not yet been demonstrated in solution-processed films.[2,8,49-51]

Homogeneously Mixed Core/Shell ITO/In_2O_3 Nanocrystals for Narrow Band-Stop Filters

Having successfully engineered a wide band-stop filter, we turned our attention to the construction of a narrow band-stop filter to emphasize that we can selectively block wavelength ranges while allowing some light to pass in the mid-IR. Our goal was to engineer a band-stop filter schematically illustrated in Figure 4.1b, where two distinct energies of light are blocked, but all other energies of light are allowed to pass. To construct a narrow band-stop filter, we wanted to produce a film from a mixture of two types of nanocrystals that have widely separated peaks and narrow line widths. To do this, we adjusted both dopant level and core/shell architectures to tune the peak positions and widths.

For the narrow band-stop filter, it is desirable to have a set of clearly separated peaks which can be achieved via using a distinctly different doping concentrations and decreased line widths. As a starting point, we considered the nanocrystals that led to the highest and lowest energy peaks shown in Figure 4.3a (16% and 0.7% homogeneously-doped ITO). The two films have a slight overlap in their optical spectra at around 3,000 cm^{-1}. In an attempt to separate the spectra even further, we used the synthesis modification discussed above that leads to the LSPR energy shifts and narrowing of the line width: the core/shell approach. We synthesized ITO nanoparticles with 12% Sn doping concentration

in the core and a thin 0.3 nm In_2O_3 shell so that the overall doping level decreased to 11%. Although these core/shell nanocrystals have a lower doping level (11 %) than the 16% ITO, the dopant activation introduced by an undoped shell shifts the LSPR of the film to the same wavelength (4,509 cm^{-1}). The shell also reduces scattering, thus decreasing the line width from 1,534 to 1,512 cm^{-1} (Figure 4.7a).[34] As we previously mentioned, the lowest doping concentration at which we observed the LSPR in homogeneously-doped nanoparticles was 0.7% (LSPR max at 1,844 cm^{-1}). In order to shift the LSPR to an even lower energy to increase the peak separation from the higher doped peak we aimed to further decrease the doping concentration, but through a core/shell strategy. Using an undoped shell to activate surface dopants and decrease scattering, we synthesized ITO nanoparticles with only 0.4% Sn doping at the core and added an ultrathin 0.2 nm shell of In_2O_3, lowering the overall doping to 0.35% Sn while still supporting the LSPR in the sample. The resulting optical spectrum is shown in Figure 4.7b. An ultrathin shell allowed for a distinguishable LSPR peak at incredibly low doping concentration along with shifting the LSPR energy maximum to 1,740 cm^{-1}.

The top trace in Figure 4.7c shows the sum of the individual, normalized spectra from each of the two individual nanocrystal components. This is the spectrum that one would predict if the absorbances are additive and it shows two energetically separated peaks with absorbance maxima at approximately 4,400 cm^{-1} and 1,800 cm^{-1} of equal absorbance intensity. To construct the filter, we mixed the two nanocrystal solutions in concentrations such that the resulting absorbance intensity from the nanocrystal films would equal approximately 0.1. After having mixed the solutions of the 12% Sn-doped ITO and 0.4% ITO nanocrystals covered with thin In_2O_3 shells in the appropriate

concentrations, the nanocrystals were spin-coated into a thin film. The absorbance was measured using FTIR and UV/Vis spectroscopy. The resulting spectrum is shown in Figure 4.7c (bottom) (see Figure C9 for non-normalized data).

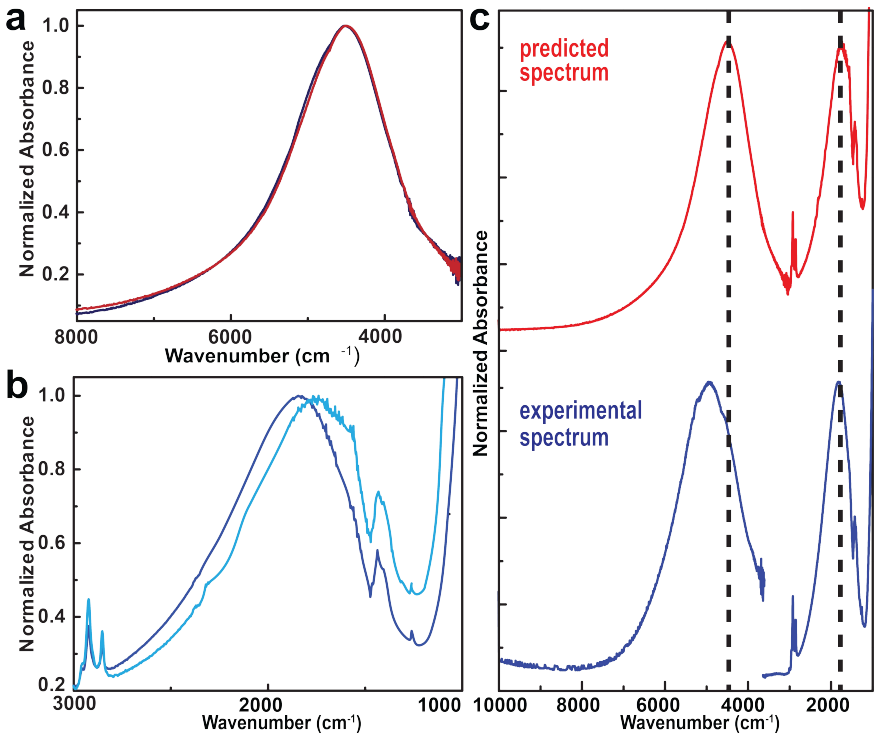

Figure 4.7. Optical properties of ITO nanocrystal building blocks and formulation/evaluation of a narrow band-pass filter. (a) Comparison of the optical spectra for nanocrystals containing 16% homogeneously-doped ITO (dark blue) and ITO core/In_2O_3 shell containing 12% Sn (red trace). The spectra are normalized at the absorption maximum. The ultrathin indium oxide shell (0.3 nm) activates the surface dopants and decreases scattering. The two films have an identical LSPR energy max at 4,509 cm^{-1} but the LSPR line width of the core/shell film is narrower (1,512 compared to 1,534 cm^{-1}); (b) Comparison of the absorbance spectra for 0.7% homogeneously-doped ITO (darker blue) and 0.4% ITO with a thin In_2O_3 shell (light blue). Addition of an ultrathin 0.2 nm undoped shell facilitated surface dopant activation and decreased scattering which resulted in a distinguishable LSPR peak at only 0.4% Sn doping concentration; (c) Predicted (top) and experimental (bottom) spectra of the homogeneously mixed thin film

produced from 0.4% and 12% Sn-doped ITO cores with thin In_2O_3 shells, illustrating the properties of a narrow band-stop filter. The break in the measured spectrum is the result of combining spectra from the FTIR and UV/Vis spectrometers near 3,500 cm^{-1}.

The predicted spectrum, which is the sum of the individual spectra, and the measured absorbance spectra are nearly identical. Both the predicted and measured optical spectra show two distinct absorbance peaks of approximately equal intensity, with one appearing at high energy and one appearing at low energy. Given that using the ITO solutions of similar doping concentrations in the two-layer films (Figure 4.5a) resulted in the attenuation of one of the components, the predictability of the optical response of the narrow band-stop filter shown in Figure 4.7c is truly remarkable. This further supports our hypothesis that homogeneously mixing nanocrystals in solution prior to spin-coating leads to a more homogeneous dielectric environment.

Compared to the predicted absorbance spectrum (Figure 4.7c, top), the high energy band peak is slightly blue-shifted and wider in the measured absorbance spectrum (Figure 4.7c, bottom). We attribute the blue-shift of the high energy LSPR peak to the higher dielectric environment that the 12% ITO with an In_2O_3 shell are embedded in compared to air. ITO with any doping concentration has a higher dielectric constant than air. ITO nanocrystals with high doping concentrations have higher LSPR peak intensities compared to the nanocrystals with low doping level at the same film thicknesses. In order to achieve similar absorbances for the two solutions we chose, we used a larger fraction of the 0.4 % ITO with a thin In_2O_3 shell than of the 12% ITO with an undoped shell (80% of the lower doped nanoparticles and 20% of the higher doped ones). Thus, the highly doped component of the film is affected by the changes in the dielectric medium more than the lower doped

ITO given the film composition. The broadening of the high energy band is attributed to the decreased ability of the 12% ITO with an undoped shell to couple effectively, resulting in increased damping. Thus, when designing a filter consisting of significantly unequal ratios of the components, we must take into consideration the overall dielectric environment in the film and how it affects those components. The combined optical response modulations produced by the created dielectric medium can also be used as a lever to sculp the desired optical filter. These results clearly demonstrate that homogeneously mixed films of specifically tailored ITO nanocrystals can be used to produce a narrow band-stop filter.

Conclusions

A library of 12 ITO nanocrystals with tin doping concentrations ranging from 0.4% to 16% and core/shell architectures with various degrees of dopant activation was constructed using a slow-injection, esterification synthetic strategy. The synthetic method allows one to tune the concentration and spatial distribution of dopant atoms in order to sculpt the LSPR peak shape and energy in the near-IR and mid-IR. We used the library of nanomaterials to produce layered and homogeneously mixed nanocrystal films and studied how the film architecture influenced the optical properties of the films. Wide and narrow band-stop filters were fabricated to evaluate the utility of this approach for applications involving plasmonic band-stop filters.

For nanocrystal films comprised of layers of different nanocrystals, we found that the combined optical properties were not easily predictable. The response was not additive and depended upon the order of deposition of the layers. We attributed the difference

between the layered and the experimental LSPR spectra to the influence of interfaces between the layers of nanocrystals that create dielectric gradients within the final film. The optical response of the ITO nanocrystal layers within the film was either attenuated or enhanced depending on the dielectric environment, which led to unpredictable shifts in energy and broadening of individual absorbances. On the other hand, homogenous mixing of ITO nanocrystals with different doping concentrations in a single film produced optical responses that matched predictions from simple addition of the component optical absorption spectra. These mixed nanocrystal films possess a homogeneous dielectric environment and lack interlayer boundaries that may reflect or scatter light in ways that are not simple to predict. Based upon these findings, it was possible to design and produce nanocrystal ITO films from solution mixtures of precisely doped nanoparticles that function as both wide and narrow band-pass filters in the near- and mid-IR, enabling the use of tunable ITO nanocrystals for band-pass filter applications. To our knowledge, this is the first demonstration of plasmonic wide and narrow band-stop filters that rely on simple solution-processing fabrication scalable to large areas and have predictable properties.

The results suggest that the combination of nanocrystal synthesis, to control the optical properties of the building blocks, and solution processing is a powerful approach to designing thin film optical filters. Although demonstrated here only for ITO nanocrystals, this strategy could also be applied to tuning the LSPR response of other doped metal-oxides, such as cerium- and molybdenum-doped indium oxide,[31,52] In-doped cadmium oxide, or aluminum-doped zinc oxide[31] for a variety of applications beyond optical filters, including electrochromic windows and sensing.[30,31,53]

Bridge to Chapter V

In Chapter IV, the continuous addition synthesis enabled tunability of the plasmonic properties of ITO nanocrystals, which could be solution-processed in such a way that the optical properties of the thin nanocrystal films could be sculpted. Beyond their exciting optical properties, ITO nanocrystals also have interesting electronic properties, and have been investigated as CO_2 reduction electrocatalysts. Some reports have claimed that indium oxide based electrocatalysts exhibit size-dependent activity. With the control afforded by the layer-by-layer growth that was demonstrated in Chapters III and IV, we sought to investigate ITO nanocrystals as CO_2 reduction electrocatalysts, to determine whether there was any size-dependent activity, and to examine the nanoscale structure at electrochemically reducing potentials. This study reveals that the morphology of the ITO nanocrystal films is more dynamic than previously expected, likely as a result of the reduction of ITO to In and Sn metal. This study is the first demonstrating the dynamic morphology of ITO under electrochemically reducing potentials, which impacts results in studies that have examined size- and shape-dependent properties of indium-based electrocatalysts for CO_2 reduction.

CHAPTER V

ELECTROCHEMISTRY-INDUCED RESTRUCTURING OF TIN-DOPED INDIUM OXIDE NANOCRYSTAL FILMS OF RELEVANCE TO CO_2 REDUCTION

This chapter was previously published as Knecht, T. A.; Boettcher, S. W.; Hutchison, J. E. Electrochemistry-Induced Restructuring of Tin-Doped Indium Oxide Nanocrystal Films of Relevance to CO_2 Reduction. *J. Electrochem. Soc.* **2021**, *168*, 126521.

Introduction

The electrochemical reduction of CO_2 into hydrocarbon products utilizing renewable electricity is of technological and economic interest.[1] However, the high overpotentials required to drive the reaction, as well as the propensity to make a number of different products with poor selectivity has hindered commercialization.[2-3] Significant effort has been put into developing and understanding various electrocatalysts for the CO_2 reduction reaction (CO_2RR).[2-7] Nanoscale electrocatalysts, which have higher surface areas and can have different properties from their bulk counterparts, are promising candidates and have been widely studied.[8-17] However, if size- and morphology-dependent properties are not maintained during the electrochemical reaction conditions, the unique catalytic activity of these materials may be lost. Further, elucidating structure-activity relationships

and designing nanoscale structure to influence properties, becomes difficult. Thus, it is important to understand the stability and structural evolution of nanoscale catalysts under operating conditions to help enable rational catalyst design.

Indium- and tin-based oxides, including nanoparticles, have shown promise as selective CO_2RR electrocatalysts for formate.[12, 15, 18-25] Extensive studies of these oxide catalysts has been done by both Bocarsly and Kanan and coworkers. They found that, despite the electrochemical reduction of the oxide to In and Sn metal, a metastable oxide persists under reducing conditions that is thought to be important for selective reduction of CO_2 to formate.[18, 22, 26-29] Huang et al. evaluated the size-dependent reactivity of In_2O_3 nanoparticle catalysts, concluding that catalysts derived from 15 nm In_2O_3 nanocubes exhibited superior formate selectivity compared to catalysts derived from smaller (5 nm) or larger (200 nm) In_2O_3 structures.[15] However, a recent report from Pardo et al. demonstrated that indium-tin-oxide films undergo structural changes during CO_2RR conditions, forming core-shell nanoparticles rich in indium oxide at the surface. Collectively, these studies raise questions about the stability of these catalysts and the properties of the catalyst (i.e. size, morphology) that are contributing to the observed activity or selectivity.[30]

The electrochemical restructuring of nanoscale CO_2RR electrocatalysts under operating conditions has been previously reported using a variety of complementary *operando* techniques such as *in situ* transmission electron microscopy (TEM)[10], *in situ* Raman spectroscopy[31], and more.[8, 10, 17, 31-33] For example, Cu_2O nanocubes were found to become more branched and form dendrites as a result of a dissolution-redeposition process occurring during CO_2 reduction.[10] Similar phenomena were seen with various Cu[17, 31] and

Cu-alloy[8, 33] catalysts. Despite these studies, few reports have examined the evolution of In- and Sn-based CO_2RR electrocatalysts.

There are several mechanisms by which nanoscale catalysts can restructure during the course of electrocatalysis.[34-36] A common form of restructuring is sintering, wherein nanocrystals coalesce through either surface diffusion or a ripening process (i.e. dissolution-redeposition) causing smaller nanocrystals are dissolved and redeposit as larger nanoparticles.[34] The degree of sintering depends upon how the nanocrystal-modified electrode is prepared. For instance, sintering can sometimes be prevented through the use of organic ligand modifiers or engineered supports with strong catalyst-support interactions.[34] Thus, the preparation method is an important consideration when evaluating the stability and structural evolution of nanoscale catalysts.

Herein we report the stability and structural evolution of well-defined tin-doped indium oxide (ITO) nanocrystals under electrochemical CO_2RR conditions. The nanocrystal films were fabricated in two different ways to evaluate the stability of the ITO nanocrystals on the electrode support and the mechanisms associated with the morphological changes. When a sparse monolayer of nanocrystals was deposited on the electrode, the nanocrystals desorbed from the electrode under electrochemically reductive conditions, presumably due to charging that leads to higher solubility. Thicker nanocrystal films (~150 nm), however, were found to adhere to the electrode substantially better allowing for CO_2RR electrolyses conducted for up to 80 min. Chronoamperometry experiments were performed on ITO-nanocrystal-modified electrodes at different potentials for varying amounts of time. Structural characterization of the electrodes was performed before and after electrochemical experiments to investigate how the structure of

the nanocrystals change as a function of potential and the amount of time that potential is applied. We discover that the original size, morphology, and composition of the ITO nanocrystals is not retained, with the initially well-defined ITO nanoparticle assemblies evolving into larger crystallites of an oxide-deficient indium/tin metal alloy. These results are important in the context of using tin/indium-based nanomaterials for CO_2RR catalysis.

Experimental

Materials

Indium(III) acetate (99.99%), tin(IV) acetate (99.95%), oleic acid (90% technical grade), and potassium bicarbonate (99.95%) were acquired from Sigma-Aldrich and used as received. Oleyl alcohol (85% technical grade) was acquired from Alfa Aesar and used as received. The boron-doped diamond (BDD) electrodes were acquired from Element Six.

Nanocrystal Synthesis

ITO nanocrystals were synthesized using a previously reported procedure.[37] Briefly, indium acetate (1.8 mmol) and tin acetate (0.2 mmol) were mixed in 4 mL of oleic acid and stirred under N_2 (g) at 150 °C for 1 h to form the metal-oleate precursor. This mixture was then injected into 13 mL of oleyl alcohol at 290 °C at a rate of 0.3 mL min^{-1}. Oleate-stabilized nanocrystals were washed three times by dispersion in acetone followed by centrifugation (7000 RPM for 5 min) and decanting the solvent.

Electrode Fabrication

To form a thin, sparse monolayer of ITO nanocrystals, BDD electrodes were submerged in a 0.5 mg mL^{-1} solution of ITO nanocrystals in toluene for 2 h. To form thicker ITO nanocrystal films, a 50 mg/mL solution of ITO nanocrystals in toluene was spin coated onto BDD electrodes by flooding the electrode with nanoparticle solution, then rotating at 3000 rpm for 30 s. All electrodes were gently washed with toluene after nanocrystal deposition/assembly to remove any poorly adsorbed nanocrystals. The coated electrodes were then submerged in a 1 M solution of formic acid in acetonitrile for 1 h to remove the oleate ligands, and then gently rinsed with acetonitrile. Afterwards, electrodes were annealed in a tube furnace under forming gas at 300 °C for 4 h to remove any absorbed formate.

Electrochemical Characterization

A single-compartment three-electrode electrochemical cell consisting of the ITO-modified BDD working electrode, a Pt counter electrode, and an Ag/AgCl reference electrode (3 M NaCl), with aq. 0.5 M $KHCO_3$ as the electrolyte was used for measurements. All electrodes were analyzed using cyclic voltammetry (CV) at a scan rate of 100 mV s^{-1}. CV and chronoamperometry (varying potentials and duration) were performed using a BioLogic SP300 potentiostat. All potentials were corrected for uncompensated series resistance, which was between 7.0 to 9.0 Ω for all experiments. Prior to electrochemical experiments, the electrolyte was sparged with either Ar (99.999%) or CO_2 (99.5%) for 30 min at a flow rate of 30 sccm, and then the gas was kept flowing in the headspace of the electrochemical cell for the duration of the experiments.

Physical Characterization

The size and morphology of the synthesized colloidal nanocrystals were characterized using a FEI Tecnai Spirit transmission electron microscope (TEM) operating at 120 kV. Nanocrystals were deposited on lacey-carbon grids supported on 400 mesh copper (Ted Pella) for TEM visualization. The size of the nanocrystals were ascertained using an Anton-Paar SAXSess small angle X-ray scattering (SAXS) instrument. The morphology of the nanocrystal films before and after electrochemical experiments was assessed using a FEI Helios Nanolab 600i scanning-electron microscope[38] equipped with a through-lens detector. Energy-dispersive X-ray spectrometry (EDS) was performed using the same SEM instrument to evaluate the composition of certain films. X-ray photoelectron spectroscopy (XPS) was used to evaluate the composition of the nanocrystals, as well as assess the ITO nanocrystal content on the electrodes (Thermo Scientific ESCALAB 250). A Bruker 500 nuclear magnetic resonance (NMR) spectrometer was used for qualitative liquid product characterization.

Results and Discussion

Evaluation of electrochemical stability of ITO nanocrystal films on a carbon support.

The methods used to prepare the nanocrystal film on the electrode can affect the overall ability of electrocatalysts to catalyze the CO_2 reduction reaction, and several experimental parameters must be considered. When studying fundamental properties of nanocrystal electrocatalysts, an ideal platform consists of a conductive electrocatalyst deposited on a catalytically inactive, electrically conductive support such that the activity

is due to the electrocatalyst alone and each catalyst particle is connected to the electrode with a low-resistance electrical path.[15, 39-41] We chose to investigate the evolution of nanoscale structure in tin-doped indium oxide (ITO) nanocrystals with 10% tin doping because ITO is highly electrically conductive, and the activity and selectivity of In- and Sn-based oxide CO_2RR catalysts are similar.[25] We synthesized the ITO nanocrystals using an established method (Figure 5.1) wherein a mixture of tin oleate and indium oleate in an excess of oleic acid is slowly injected via a syringe pump into oleyl alcohol at 290 °C.[37, 42] This yielded monodisperse ITO nanocrystals ~ 10 nm in diameter (see Figure D1 for size analysis).

We considered several ways to fabricate the nanocrystal-modified electrodes. A boron-doped diamond (BDD) electrode was used as the electrode support due to its chemical stability/inertness and low intrinsic CO_2 reduction activity.[43] To functionalize the electrode, we considered using ionomer such as Nafion or Sustainion as a binder, as has been done in previous reports.[27, 31, 44-46] However, these ionomers have also been shown to alter the activity and selectivity of CO_2RR catalysts,[47] the loadings are often variable,[48] the stability of these ionomers has not been studied, and ionomer/catalyst interactions are complex and poorly understood.[49-50] Taken together, the use of ionomer could make it difficult to attribute the electrode performance to electrocatalyst properties alone. Given these considerations, we aimed here to study ITO nanocrystals directly deposited onto the BDD electrode without ionomer.

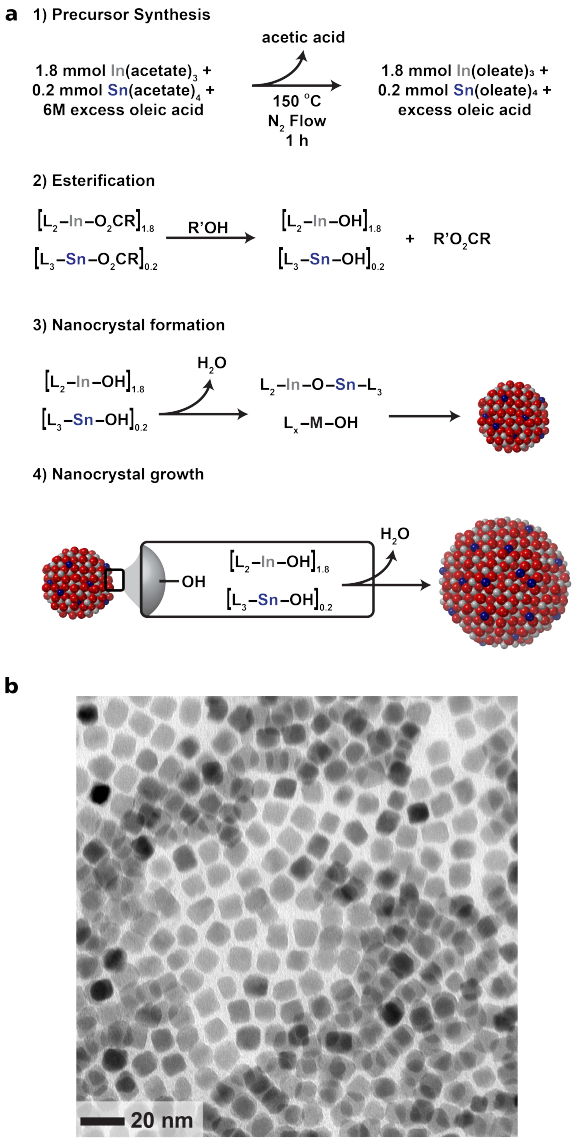

Figure 5.1. (a) Schematic depiction of the mechanism of ITO nanocrystal formation. (b) TEM image of the oleate-stabilized ITO nanocrystals used in this study (prior to annealing).

Nanocrystal-modified electrodes were fabricated by submerging the BDD in a 0.5 mg/mL solution of oleate-stabilized nanocrystals to yield a sparse monolayer of nanocrystals on the surface. The electrode was submerged in 1 M formic acid in acetonitrile to remove the oleate ligands, and then annealed at 300 °C under a 95:5 mix of N_2:H_2 to

remove the formate ligands.[51] This preparation procedure has been previously shown by Fourier transform infrared (FTIR) analysis to successfully remove all ligands.[51] An SEM image of one electrode is shown in Figure 5.2a, illustrating the uniform coverage achieved with well-defined nanoparticles.

Cyclic voltammetry (CV) was used to evaluate these electrodes. The 0.5 M $KHCO_3$ electrolyte was sparged with Ar prior to measurements. The potential was swept from the open circuit voltage to -1.3 V vs. RHE. The first CV cycle (Figure 5.2b) showed a redox feature typical of the reduction and partial re-oxidation of In- and Sn-based oxides.[18, 22] We noticed that by the second CV cycle (Figure 5.2b, inset) this redox feature diminished significantly, completely disappearing by the fourth cycle. The electrode was then characterized by SEM and XPS (Figure 5.2c and 5.2d) without further electrochemical testing in order to evaluate electrode stability. The SEM showed fewer nanocrystals on the electrode, and only carbon and oxygen were detected by XPS.

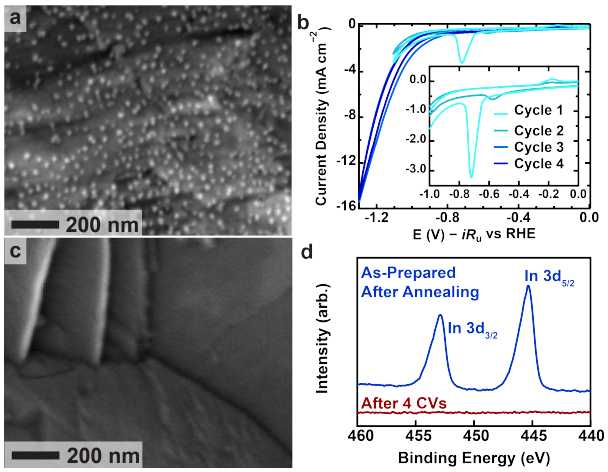

Figure 5.2. (a) SEM image of the as-prepared electrode. (b) Cyclic voltammograms (CVs) of a BDD electrode containing approximately one monolayer of ITO nanocrystals conducted in Ar-saturated 0.5 M $KHCO_3$. (c) SEM image of the BDD electrode after four

CV cycles. (d) XPS analysis of the In 3d region conducted on the as-prepared electrode (blue) and the electrode after performing four CVs in Ar-sparged 0.5 M $KHCO_3$.

To explain the loss of nanocrystals from the electrode surface, we hypothesized that the nanocrystals either dissolved or desorbed. To determine the potential at which this happens, we fabricated a sparse ITO nanoparticle monolayer film (using the same procedure) on a gold-coated quartz crystal and used an electrochemical quartz crystal microbalance (EQCM) to monitor mass as we performed CVs at 100 mV s^{-1} in 0.5 M $KHCO_3$, cycling out to more negative potentials in subsequent cycles. The results are shown in Figure 5.3a. The film mass was stable until approximately -1.0 V vs RHE, at which point nearly all of the mass was lost. This indicates that the loss of the nanocrystal film is dependent upon the applied potential.

It is known that under reducing conditions in near-neutral potassium bicarbonate solutions, the local pH at the electrode surface increases as protons are consumed during the hydrogen evolution reaction,[52-54] so we wanted to determine whether the increased basicity caused loss of nanocrystals through dissolution. The same type of nanocrystal film as described above was prepared on a gold-plated QCM crystal and submerged in 50 mL of water. We then titrated in 10 mL of concentrated KOH, up to pH = 14, while stirring in order to see if mass loss could be due to increasing alkalinity (Figure 5.3b). Over the course of the titration, only 17% mass loss was observed. As a control, we repeated the experiment, instead titrating in concentrated HNO_3, which is known to dissolve ITO nanocrystals, and monitored the mass. We found a mass loss of 91%, as expected. We then soaked nanoparticle-modified electrodes in various pH solutions and

compared the resulting SEM images to those taken of the as-prepared electrode (Figure D2). In all cases, SEM images showed evidence of nanocrystals on the electrode, suggesting nanocrystals are not dissolving as a result of increased alkalinity.

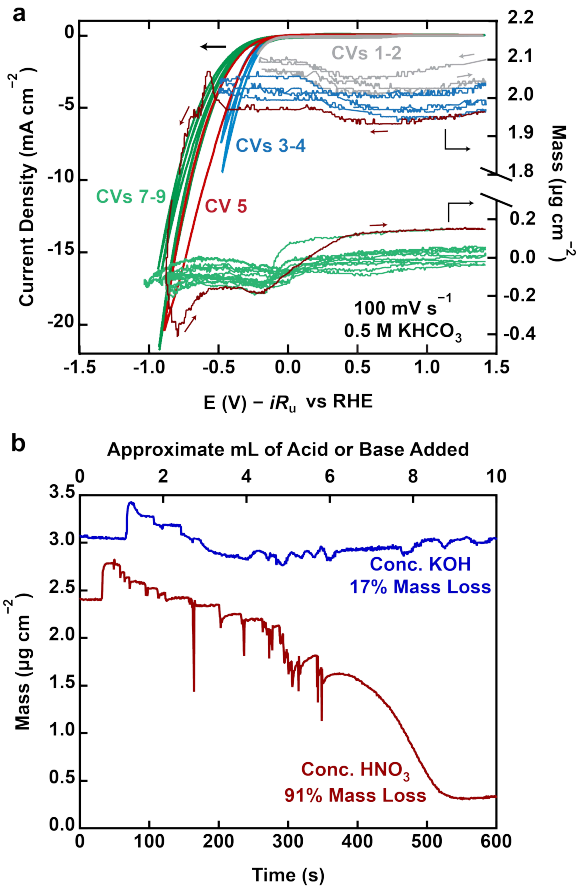

Figure 5.3. QCM data of ITO films under various conditions. (a) Mass loss from an ITO nanocrystal film deposited on a QCM crystal as a function of applied potential. Several CVs were performed in 0.5 M $KHCO_3$ from open circuit voltage (1.48 V vs RHE) to -0.14 V (gray), -0.50 V (blue), and -0.96 V (red and green) vs RHE. Colored arrows show the CV sweep direction. (b) Mass monitored as a function of amount of concentrated HNO_3 (red) or KOH (blue) added to an ultrapure water solution containing the QCM electrode.

Taken together, these results indicate that increasing pH at the electrode surface does not lead to dissolution of the ITO nanocrystals from the electrode. We hypothesized

that other mechanisms for nanocrystal loss could be the electrostatic repulsion of the nanoparticles from the electrode as a negative potential is applied,[55] or cathodic dissolution.[56] We found, however, that when starting with a thicker (~150 nm) nanocrystal film (detailed below), the nanocrystals remain on the electrode, suggesting that cathodic dissolution is unlikely. Thus, our evidence suggests that, for sub-monolayer films, the nanocrystals are desorbing because they become more soluble as they become negatively charged. Charge-induced increases in solubility are common in gold nanoparticles, for example.[57] It has been reported that it is necessary to crosslink gold nanoparticles to prevent their desorption during electrochemical analysis because the non-crosslinked particles became soluble when charged.[57]

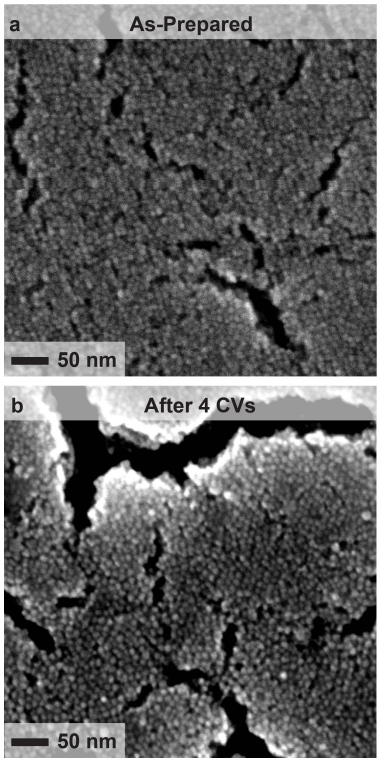

Figure 5.4. SEM images of an ITO nanocrystal film deposited on a BDD electrode from a 50 mg mL^{-1} nanocrystal solution (after annealing) (a) before, and (b) after performing four CVs of the electrode. CVs were performed in Ar-saturated 0.5 M $KHCO_3$.

Evolution of morphology of nanocrystal films

An alternative electrode fabrication procedure resulting in insoluble films was needed to study the structural evolution of ITO nanocrystals under electrochemically reducing conditions. Another way to produce ITO nanocrystal films has been reported[51] wherein a thicker film is made by spin coating a 50 mg/mL solution of ITO nanocrystals in toluene onto a substrate, soaking in a 1 M formic acid solution, and annealing at 300 °C to remove remaining formate ligands. The resulting films were ~ 150 nm thick, with a mass loading of ~ 0.1 mg cm^{-2}. We hypothesized that the higher mass loading of ITO nanocrystals, along with the annealing step, would prevent the desorption by providing more physical/chemical contact points to each individual nanoparticle or by crosslinking between oleate ligands that were not fully removed from the film.[58-60]

We spin coated the nanocrystals onto a BDD substrate using the above procedure, and then conducted four CV cycles from open circuit (~ 1.48 V vs RHE) to -1.1 V vs RHE in Ar-saturated 0.5 M $KHCO_3$ electrolyte (see Figure D3). It appears from Figure D3 that the appearance of the cathodic wave is predicated on a previous sweep to potentials more negative of -1.1 V vs RHE where In^0 is formed, followed by its re-oxidation upon the positive sweep. This is evidenced by the lack of a cathodic wave during the first CV cycle, but a clear cathodic wave on the second and third CV cycles. SEM characterization of the as-deposited nanocrystals (Figure 5.4a) and of the electrode after performing four CV cycles (Figure 5.4b) indicate that the ITO nanocrystal film remains on the electrode.

Cyclic voltammetry and chronoamperometry were used to evaluate the ITO nanocrystal films for CO_2RR. The CVs (Figure D3) were performed in both Ar- and CO_2-sparged electrolyte. The voltammetry did not indicate higher current densities under CO_2,

but previous reports have demonstrated that while total reductive current may be suppressed in some cases, CO_2RR products are often found.[29, 41, 61] Chronoamperometry was then performed at -0.8, -0.9, and -1.1 V vs RHE in CO_2-saturated electrolyte (see Figure D5) for 80 min each on three separate electrodes. NMR spectra taken of the electrolyte showed the presence of formate (Figure D4), which indicated that CO_2 reduction was indeed occurring at these potentials, although this particular study is not focused on the product speciation.

We characterized the electrodes after the chronoamperometry experiments using SEM (Figure 5.5) and found that the ITO nanocrystal films underwent significant morphological change. The 10-nm-diameter nanocrystals in Figure 5.5a were no longer distinguishable on electrodes that had undergone electrochemical analysis, and instead larger agglomerates between ~400 nm to several microns were seen (Figure 5.5b-d).

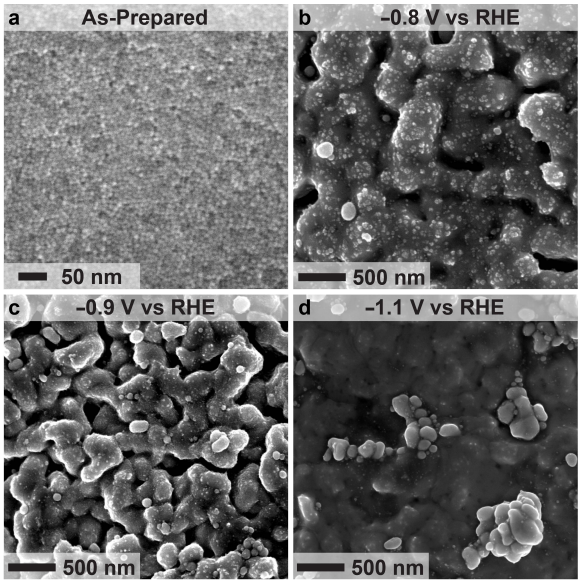

Figure 5.5. SEM images of ITO nanocrystal films (a) as-prepared, and after applying (b) -0.8, (c) -0.9, and (d) -1.1 V vs RHE for 80 min in CO_2-saturated 0.5 M $KHCO_3$. In all the

panels the underlying electrode is not visible and the observed features are ascribed to catalyst agglomerates.

Next, we studied how long a potential must be applied before the morphology of the nanocrystal film changed. We performed chronoamperometry at -1.1 V vs RHE for 5 min and for 25 min in CO_2-sparged 0.5 M $KHCO_3$ (see Figure D6), and evaluated the morphology by SEM. Even after applying a potential for 5 min, larger, micron-sized particles were present on the electrode. Although the sizes and shapes of the particles varied, they were generally larger after 25 min compared to 5 min. These particles were also analyzed by SEM-EDS (Figure D7 and Table D1) and found to have little oxygen content, suggesting that the particles were reduced to an In/Sn metal alloy. Some particles even appeared faceted at the micron scale (Figure 5.6b). We also performed chronoamperometry using a QCM to monitor mass as a function of time in 0.5 M $KHCO_3$ at -1.1 V vs RHE and found that the mass of the In^0/Sn^0 film was stable over the 30 min duration of the experiment (Figure D8).

These results suggest that the nanoparticles are coalescing after reduction to metallic species. It is likely that all of the nanocrystals are getting reduced as nanocrystal film conductivity measurements conducted by Crockett et al. showed that nanocrystals in the films are electrically well-connected to one another.[51] One mechanism that could be occurring is dissolution and redeposition, wherein the In and Sn dissolve, producing In^{3+} and Sn^{4+} species that are subsequently re-deposited as In and Sn metal onto the electrode surface. While this process has been observed with ITO films under acidic conditions,[36] the solubility of In and Sn are low under the neutral-to-basic conditions tested in the present

study. Thus, it is reasonable to conclude that this type of ripening is not likely occurring in this system.

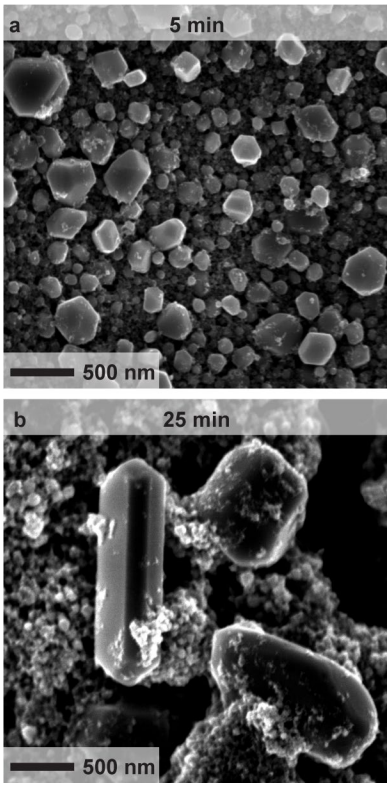

Figure 5.6. SEM images of ITO nanocrystal film after applying -1.1 V vs RHE in CO_2-sparged 0.5 M $KHCO_3$ electrolyte for (a) 5 min and (b) 25 min.

We thus hypothesize that the restructuring is due to diffusion of zero-valent In and Sn adatoms. In the oxide form, ITO has a strong cohesive energy, and thus a high adatom diffusion barrier.[62] On the contrary, both In^0 and Sn^0 have low cohesive energies, enabling facile diffusion of adatoms.[62-64] This is consistent with previous studies investigating the mobility of In and Sn adatoms.[63-67] For example, Wagner et al. found that under reducing conditions, In_2O_3 was partially reduced and In adatoms were formed, which were able to diffuse across the surface.[66] Similarly, Morris et al. studied the surface diffusion of In on a

W surface and found that the activation energy for diffusion decreased as the surface coverage of In increased.[64] Given this information, we conclude that the reduction to In and Sn metal enables surface diffusion of adatoms, which then coalesce to minimize surface energy.

One interesting observation is that at shorter times of an applied potential (Figure 5.6), the generated microparticles appear faceted and crystalline. At longer times, there is a more-agglomerated microscale network. It is possible that as a negative potential is applied for a longer period of time, more and more of the film gets reduced, allowing for more In and Sn adatoms to diffuse along the surface and coalesce with existing structures.

Conclusions

We evaluated how applying cathodic potentials affect the stability and morphology of ITO nanocrystal films. Sparse monolayer nanocrystal films are not stable at highly cathodic potentials (more negative of -1.1 V vs RHE) as the nanocrystals are no longer present on the electrode after a cathodic bias is applied. This phenomenon was found to be potential-dependent and we conclude that it is due to increased solubility of the reductively charged nanoparticles as well as electrostatic repulsion between the ITO nanocrystals and the carbon electrode. Thicker nanocrystal films were found to be more stable and remain on the electrode upon cathodic polarization, but significant morphology and composition changes were observed. The ITO was found to be converted to a reduced In-Sn metal alloy, and the 10 nm nanocrystals were no longer distinguishable as they had formed a larger microscale network. We hypothesize this is due to increased diffusion of In^0 and Sn^0 adatoms, which subsequently coalesce.

These findings have implications in the field of nanoscale electrochemical CO_2 reduction catalysts. For example, White et al. compared the activity of In_2O_3, $In(OH)_3$, and In nanoparticles, and Huang et al. compared the size-dependent activity of various In_2O_3 nanoparticles for CO_2RR; such restructuring may in fact be occurring in those systems as well.[15, 27] As such, this study highlights the necessity of post-electrochemical surface characterization in order to fully understand electrocatalyst structure.

CHAPTER VI

CONCLUSION

I am the primary and sole author to the writing of this chapter.

Concluding Remarks

Nanotechnology is expected to transform a number of fields and solve some of the world's most complex problems, from cancer treatment to waste remediation to energy storage and more. For nanotechnology to make a difference in these fields, we need to be able to precisely engineer nanocrystals at the atomic level, beyond just controlling size and shape. Many of the nanoscale properties that differ from a material's bulk properties are caused by surface-level chemistry, defects, and local structure, all of which are difficult to control and understand. These structural attributes are all controlled by the synthetic procedures used to produce nanocrystals, and thus gaining deep, mechanistic understandings of these syntheses and the nanocrystal growth processes is imperative if we are to manipulate nanoscale structure, and therefore properties, at the atomic level. Unfortunately, most current nanocrystal syntheses are inherently difficult to study, as the nanocrystal growth often proceeds through radical reactions that are too rapid to study using *ex situ* techniques and too poorly selective to control. Further, most nanocrystal syntheses are developed through trial and error, often changing multiple parameters at once to obtain the desired nanocrystal size. Thus, we need nanocrystal syntheses that allow for

the systematic study of one parameter at a time, as well as syntheses that proceed by slower reactions that are easier to study if we are to truly understand nanocrystal growth processes.

The continuous addition synthesis developed by the Hutchison lab has been able to overcome many of these obstacles. Since the reaction proceeds through esterification and subsequent condensation, the syntheses can be conducted at temperatures where thermal decomposition reactions that form radical species can be avoided. Further, performing the reaction at lower temperatures (as opposed to reflux) ensures that we are able to keep the solvent the same, allowing us to change one parameter at a time. Because the nanocrystal surfaces remain reactive after forming, we are able to grow metal oxide nanocrystals in a layer-by-layer, almost atom-by-atom, fashion. Finally, because the reaction is limited by the injection rate of the precursor, which we can control and manipulate, we can sample nanocrystals throughout the course of the reaction, enabling close examination of metal oxide nanocrystal growth processes.

In this dissertation, the growth and properties of different metal oxide nanocrystals were investigated by utilizing the unique attributes of the slow injection esterification synthesis. This synthesis allowed us to explore the growth processes of cerium oxide and tin-doped indium oxide nanocrystals in-depth, taking advantage of the ability to alter a single parameter at a time during the synthesis.

In the case of cerium oxide, we found that atmosphere drastically affects the growth process and resulting morphologies, with syntheses under N_2 leading to nanoribbons or irregular plates, and syntheses under air leading to size-tunable nanocubes. It was found that the role of air was not to oxidize the Ce(III) oleate precursor, as Ce(IV) oleate was found to be thermally unstable. Instead, we used a combination of TEM, XPS, and FTIR

techniques to discover that the role of air was to oxidize the nanocrystal surfaces, which enhanced their reactivity and enabled continuous growth. The origin of the nanoribbons was also investigated and were found to be the result of the presence of acetate in the precursor solution. Thus, the irreproducibility in getting nanoribbons vs irregular plates in initial syntheses when we were using Ce(III) oleate made from Ce(III) acetate was the result of exchanging the acetate for oleate ligands for varying amounts of time, with longer times leading to more complete exchange and therefore less acetate. With this knowledge, we were able to tune the length of the nanoribbons by altering the amount of acetic acid added to the precursor.

In Chapter III we investigated the role of the reagent chosen, oleyl alcohol vs oleylamine, in the growth characteristics of ITO nanocrystals. We found that syntheses in both reagents result in a living growth mechanism based upon esterification (in oleyl alcohol) or amidation (in oleylamine). We found that amidation occurs faster than esterification due to the increased nucleophilicity of the oleylamine compared to the oleyl alcohol. We also found that the number of nanocrystals formed decreases as oleylamine content in oleyl alcohol increases. This was attributed to the growth phase beginning more rapidly in the case of ITO nanocrystals synthesized in oleylamine due to higher concentration of reactive surface hydroxyls, which occurs due to the increased reaction kinetics of amidation compared to esterification. Because the growth phase begins sooner as oleylamine content increases, fewer nanocrystals are formed. The ITO nanocrystals synthesized in oleylamine also exhibit different optical properties immediately after synthesis compared to ITO nanocrystals synthesized in oleyl alcohol. The ITO nanocrystals synthesized in oleyl alcohol were green upon purification and turned blue over the course

of several days, whereas the nanocrystals synthesized in oleylamine were blue immediately upon purification. The blue color is indicative of nanocrystals with lower interstitial oxygen content, and the transition from green to blue is associated with the release of interstitial oxygen atoms, resulting in more reduced nanocrystals. We concluded that the reducing environment of the amine facilitated this transition.

In Chapter IV we explored the use of solution-processed plasmonic ITO nanocrystals as IR optical filters. We found that mixtures, rather than layers, of nanocrystals of different dopant concentrations resulted in predictable optical responses, allowing for the fabrication of both broadband and narrow band IR filters. The homogeneously mixed solutions resulted in more predictable behavior due to a more homogeneous dielectric, as opposed to the layered nanocrystals since the dielectric changes based on the orientation of the nanocrystal film and order of the layers.

Finally, we explored the morphological transformations of ITO nanocrystals that occurred under electrochemically reducing conditions at potentials relevant to electrochemical CO_2 reduction in Chapter V. We found that under highly cathodic potentials, the ITO nanocrystals are reduced to a In^0 and Sn^0 metal alloy, which enables facile adatom diffusion, resulting in larger crystallite structures and eventually nodular networks of the alloy. These results highlighted the importance of post-electrochemical electrode characterization if nanostructure-property relationships are to be made.

Future Directions

The future of the slow injection synthesis could go in several different directions. Its utility, for example, needs to be expanded to other metal oxide systems, each of which

will have its own synthetic parameters and growth characteristics that will need to be explored. For example, we learned in Chapter II that reaction atmosphere can have a profound effect on nanocrystal formation. Exploring the utility of air in more nanocrystal syntheses may allow compositional control in oxides like Fe, Co, Mn, and Cu where multiple oxidation states are possible. We learned in Chapter III that altering the precursor reactivity led to a different number of particles formed, which then dictated the size of the resulting nanocrystals. Using oleylamine could allow access to metal oxides that come from metal carboxylate precursors that have low reactivity, such as zinc or zirconium oleate.

Chapters III and IV explored some of the optical properties of ITO nanocrystals, but these need to be further explored. For syntheses in oleylamine, the localized surface plasmon resonance needs to be compared to that of ITO nanocrystals synthesized in oleylamine. Further, other dopants within indium oxide should be explored to see if IR filters with narrower or broader bands could be obtained.

Finally, the mechanism of structural rearrangement of ITO nanocrystals under electrochemically reducing conditions shown in Chapter V requires further exploration. Specifically, conducting X-ray diffraction of the restructured films could elucidate the crystal structure, and *in situ* atomic force microscopy could shed further light on the mechanism of structural rearrangement.

The entirety of this work focuses on nuances of nanocrystal synthesis and electrocatalysis that are seldom explored in such depth. For example, the role of trace amounts of acetate in the case of cerium oxide had profound effects on the nanocrystal morphology, and may play a larger role in other nanocrystal syntheses than once thought.

In the face of the challenges in studying these processes, the continuous addition synthesis provides some inspiration to the development of future nanomaterials. Expanding this approach to the entirety of metal oxides and studying the growth mechanisms within each system would provide a general framework for the synthesis of superior nanomaterials. This approach should be applied to target technologically relevant nanomaterials, as well as to enhance the fundamental understanding of the chemical processes (monomer identity, precursor reactivity, effect of additives and byproducts, and more) at play. With a greater fundamental understanding of growth, we can intuitively build advanced nanomaterials to tackle the world's most challenging problems.

APPENDIX A

SUPPORTING INFORMATION FOR CHAPTER II: REACTION ATMOSPHERE AND SURFACE LIGATION CONTROL SURFACE REACTIVITY AND MORPHOLOGY OF CERIUM OXIDE NANOCRYSTALS DURING CONTINUOUS ADDITION SYNTHESIS

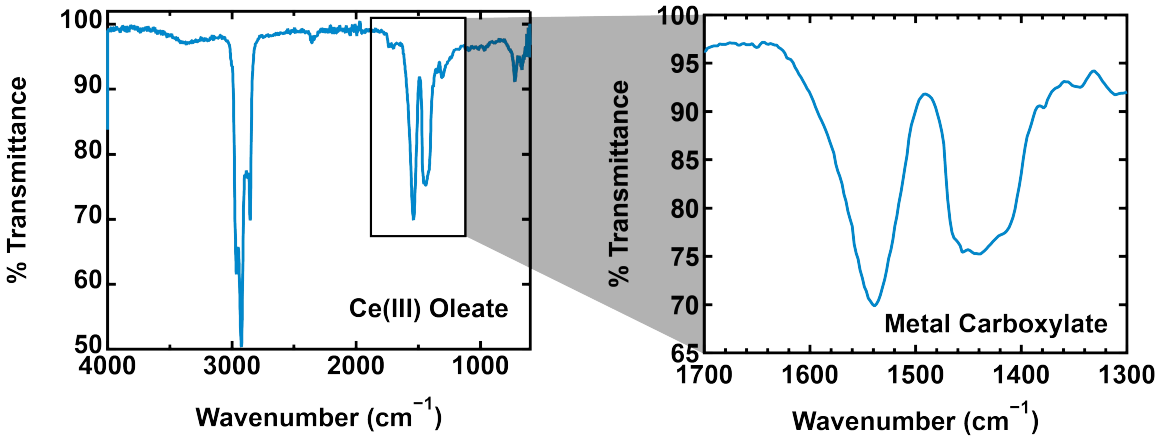

Figure A1. FTIR of Ce(III) oleate made from Ce(III) acetate. The highlighted region shown on the right shows the metal carboxylate binding region. The difference between the symmetric (~1440 cm^{-1}) and asymmetric (~1540 cm^{-1}) metal carboxylate vibrations suggest that the oleate groups bind in a chelating bidentate binding mode.

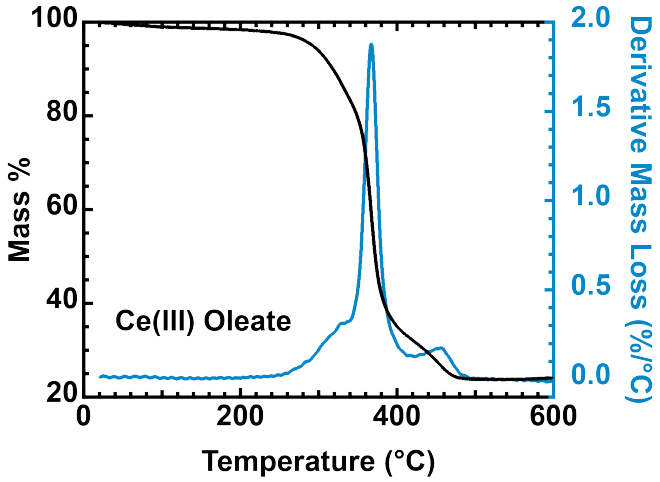

Figure A2. Thermogravimetric analysis of Ce(III) oleate made from Ce(III) acetate. This analysis shows that the primary mass loss event occurring from thermal decomposition of the precursor happens between 320 - 400 °C.

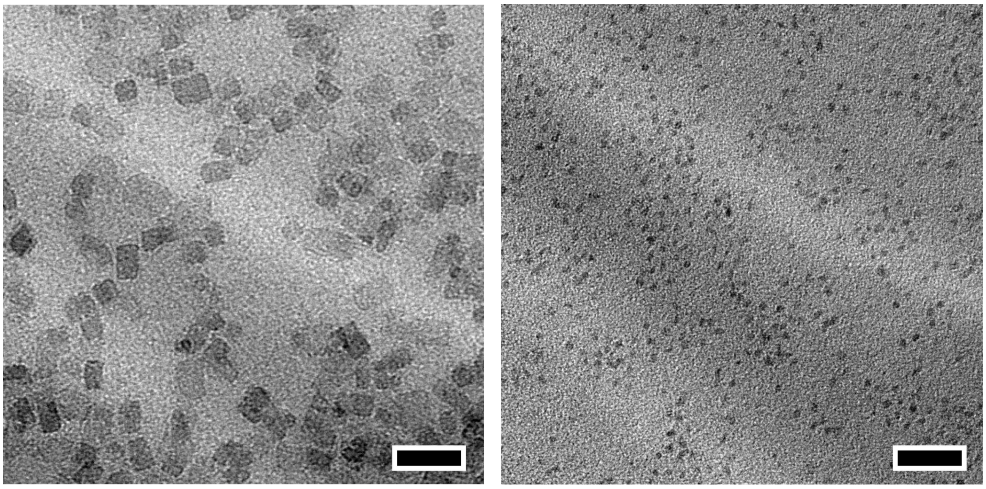

Figure A3. TEM images of nanocrystals resulting from syntheses performed under nitrogen using identical conditions but producing significantly different morphologies. Syntheses were carried out using a Ce(III) oleate precursor under N_2 at 315 °C and an injection rate of 0.06 mL min^{-1}. Scale bars are 20 nm.

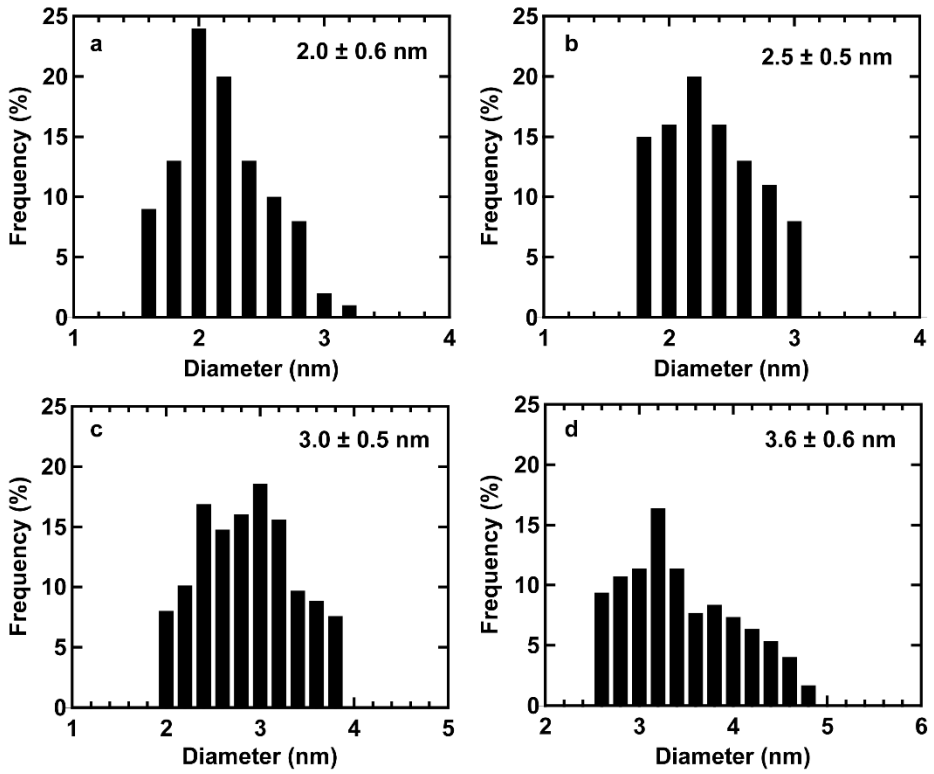

Figure A4. TEM size analysis of nanocubes from Fig. 2 showing the continuous growth of nanocrystals with increasing precursor addition. Nanocubes were formed by injecting (a) 0.5 mmol, (b) 1.0 mmol, (c) 1.5 mmol, and (d) 2.0 mmol of Ce(III) oleate into oleyl alcohol at 290 °C under an air atmosphere.

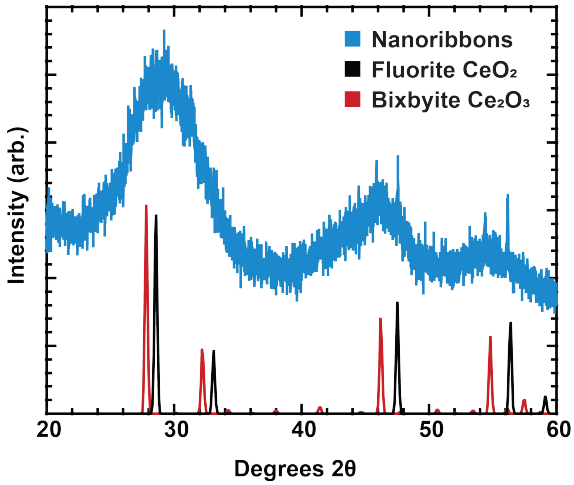

Figure A5. XRD pattern of the nanoribbons produced by injecting 2 mmol of Ce(III) oleate precursor under N_2 (blue). Bixbyite Ce_2O_3 (red) and fluorite CeO_2 (black) reference patterns are shown. Due to the broadness of the peaks, as well as the similarities between the bixbyite and fluorite structures, it is difficult to determine which phase comprises the nanoribbons, however XPS results as well as our observations of color changes (discussed in the manuscript) suggest that the nanoribbons may be a mix of the two phases, which happens once the Ce_2O_3 is partially oxidized to CeO_2 upon exposure to air.

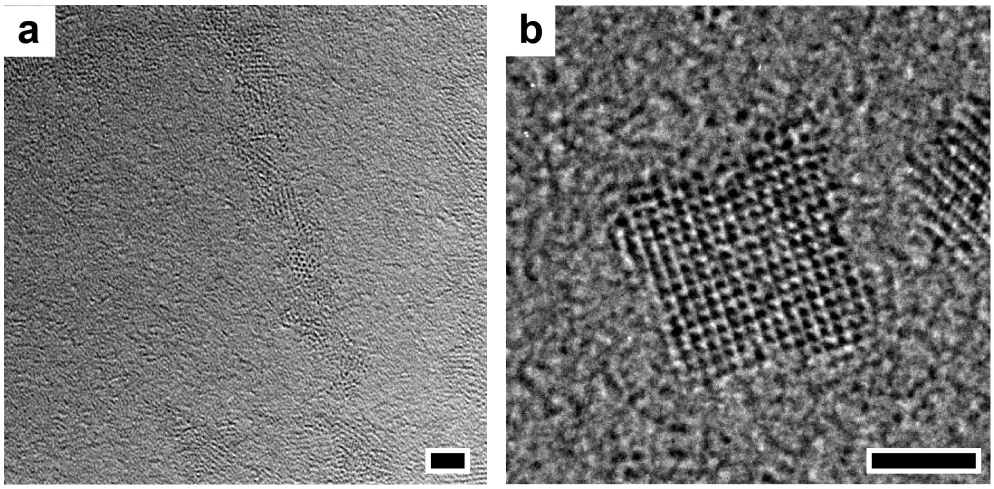

Figure A6. High resolution TEM images of (a) nanoribbons and (b) nanocubes resulting from syntheses using Ce(III) oleate at 290 °C under N_2 and air, respectively. Scale bars are 2 nm.

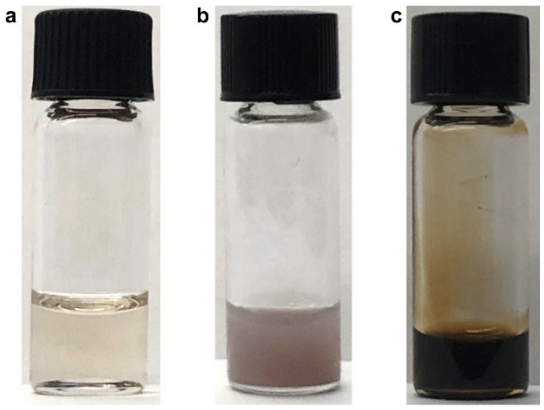

Figure A7. Photograph of reaction mixtures from nanocrystal syntheses performed using Ce(III) oleate. (a) Reaction mixture from synthesis performed under N_2 showing a yellow color. (b) Reaction mixture from synthesis performed under N_2 after being cooled to room temperature and exposed to air for several minutes, showing a purple color. (c) Reaction mixture from synthesis performed under air, showing a brown color.

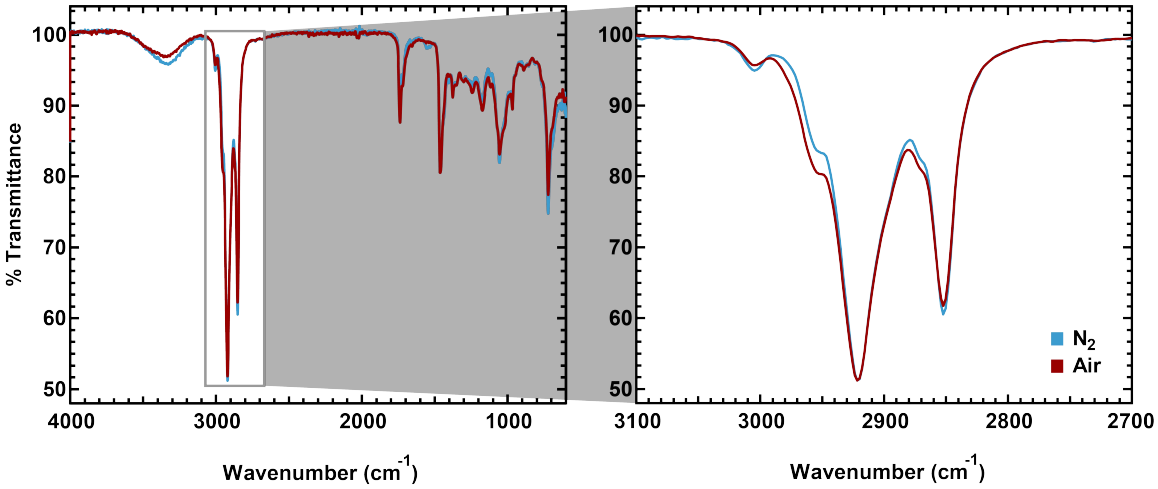

Figure A8. FTIR of reaction mixtures from nanocrystal syntheses performed using Ce(III) oleate under N_2 (blue) and air (red). The full spectra are on the left. The highlighted region shown on the right shows the C–H stretching region, demonstrating that these are equal in intensity, showing the comparability in transmittance intensities between the two samples shown.

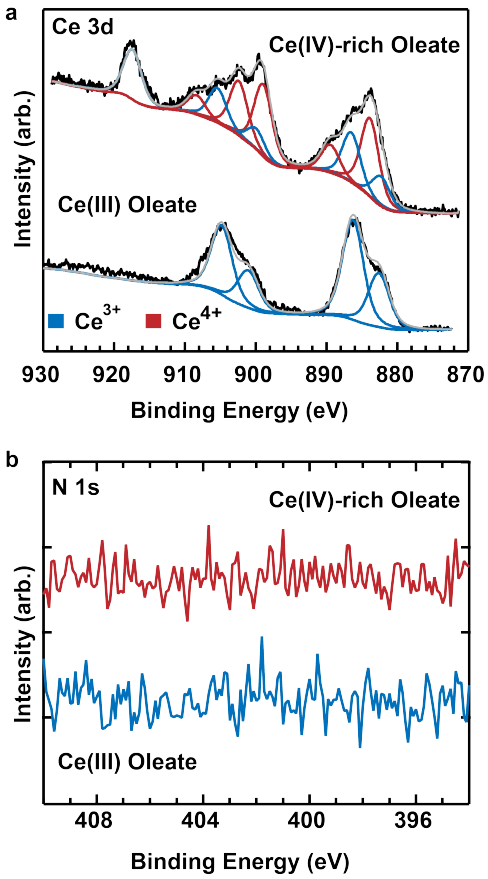

Figure A9. XPS spectra of Ce(III) and Ce(IV)-rich oleate. (a) Ce 3d spectra and (b) N 1s spectra. The Ce 3d spectra show that the Ce(IV)-rich oleate is a mixed valence precursor, while the Ce(III) oleate only contains peaks associated with Ce(III). The N 1s spectra show that nitrogen was not present in either precursor, suggesting that the ammonium and nitrate ions had been successfully removed from the precursors during the washing procedure.

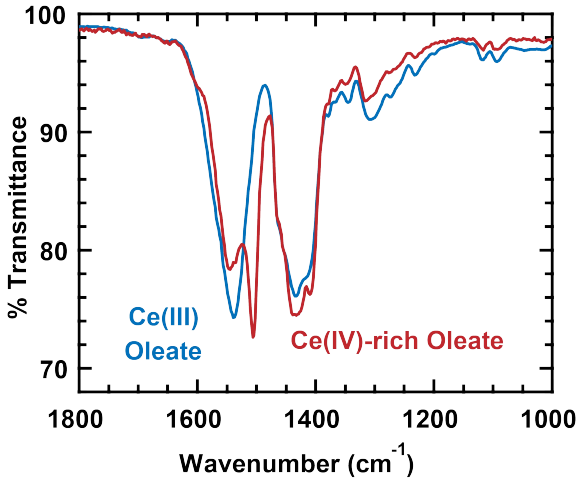

Figure A10. FTIR spectra of SE-Ce(III) oleate (blue) and Ce(IV)-rich oleate (red) showing the metal carboxylate binding region. In both cases, the difference between the symmetric and asymmetric vibrations are less than 110 cm^{-1}, suggesting that the carboxylate ligands in both precursors are bound to the Ce in a chelating bidentate mode. The Ce(IV)-rich oleate trace shows a sharp peak at ~1450 cm^{-1} that is not present in the SE-Ce(III) oleate. This suggests that the binding environment of the carboxylate ligands might be slightly different between the precursors.

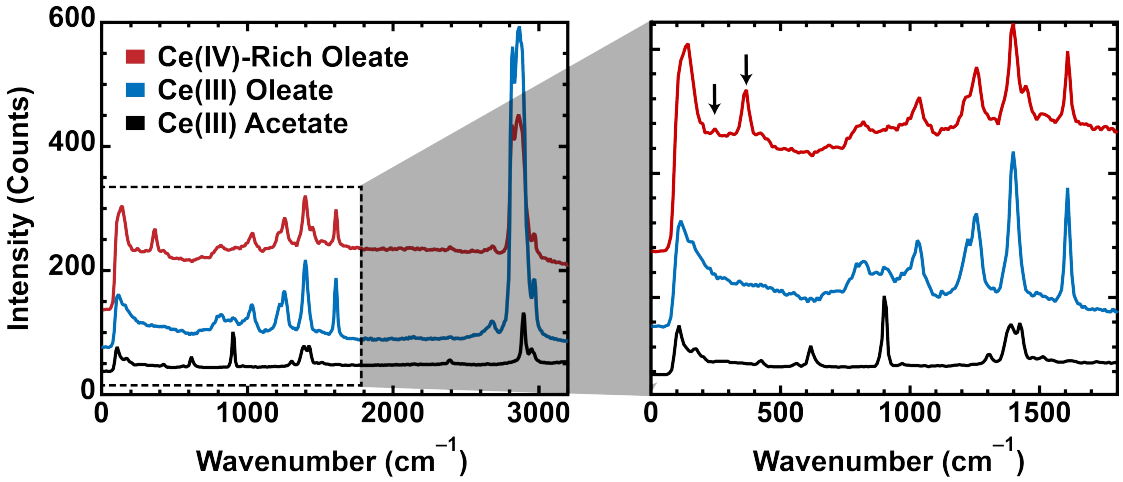

Figure A11. Raman spectra of the Ce(IV)-rich oleate (red), SE-Ce(III) oleate (blue), and Ce(III) acetate (black). The spectra of the Ce(IV)-rich oleate and SE-Ce(III) oleate are nearly identical except for peaks at ~205 cm^{-1} and ~350 cm^{-1} in the Ce(IV)-rich oleate, highlighted in the spectra on the right. The peak at ~205 cm^{-1} may be associated with Ce–O–Ce bonds,[1] while the peak at ~350 cm^{-1} may be associated with a hydrated Ce^{4+} species.[1-2]

1. Demars, T. J.; Bera, M. K.; Seifert, S.; Antonio, M. R.; Ellis, R. J., Revisiting the Solution Structure of Ceric Ammonium Nitrate. *Angew. Chem. Int. Ed.* **2015,** *54* (26), 7534-7538.
2. Miller, J. T.; Irish, D. E., Infrared and Raman Spectra of the Cerium(IV) Ion - Nitrate Ion - Water System. *Can. J. Chem.* **1967,** *45*, 147-155.

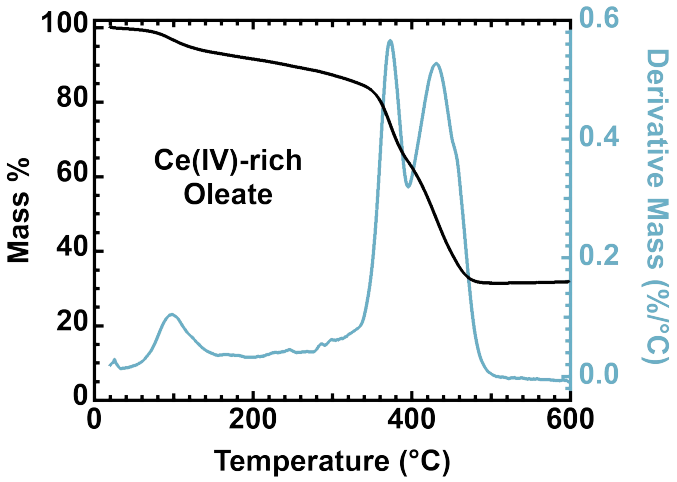

Figure A12. Thermogravimetric analysis of the Ce(IV)-rich oleate precursor. We attribute the mass loss event at 100 °C to the loss of water.

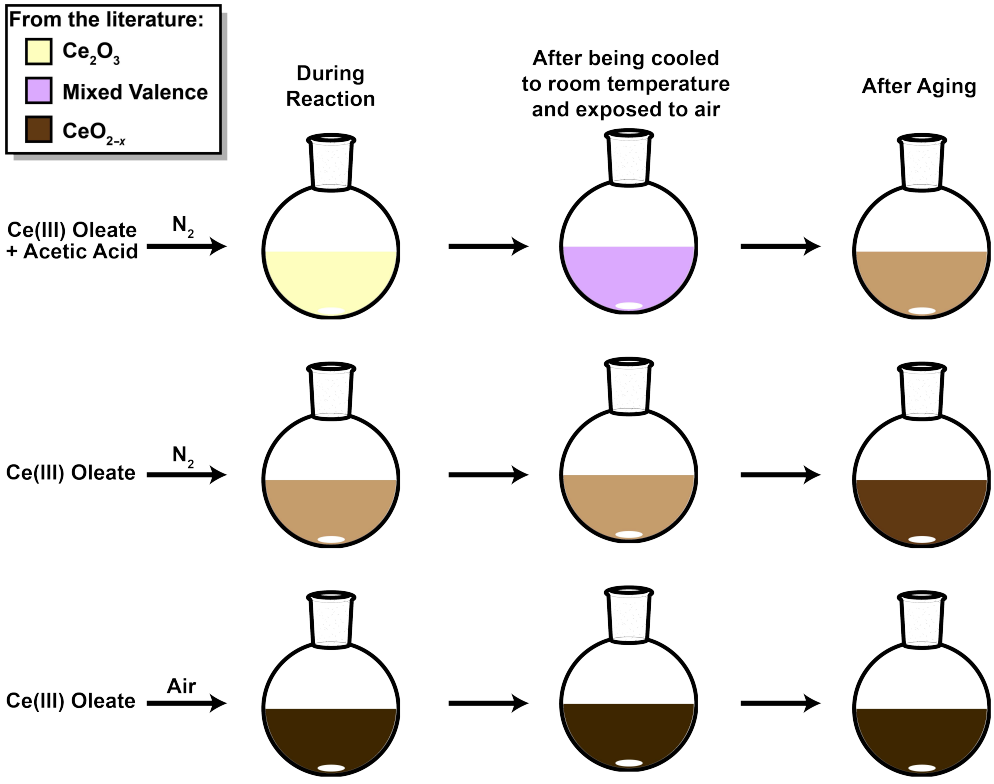

Figure A13. Schematic of all colors observed during reactions using Ce(III) oleate.

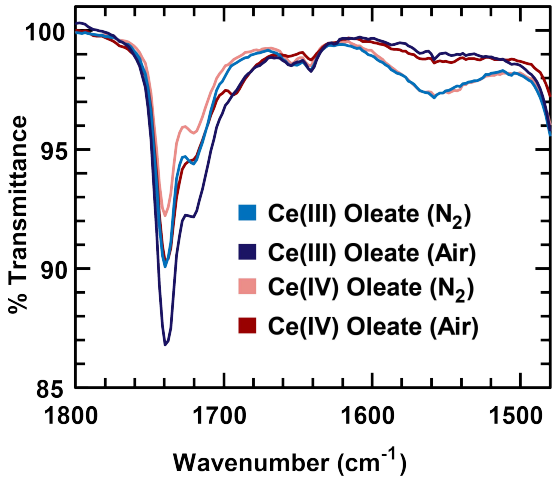

Figure A14. FTIR spectra of reaction mixtures from nanocrystal syntheses using SE-Ce(III) oleate under N_2 (light blue), SE-Ce(III) oleate under air (dark blue), Ce(IV)-rich oleate under N_2 (light red), and Ce(IV)-rich oleate under air (dark red). These data show that ester (~1740 cm^{-1}) is formed in all cases, but more ester is formed from Ce(III) oleate vs Ce(IV)-rich oleate, and more ester is formed under air compared to under N_2. Precursor is also shown to build up in the cases under N_2, as demonstrated by the peaks near ~1550 cm^{-1}, whereas no precursor is built up in cases under air. Collectively these spectra suggest that the reaction proceeds via esterification in all cases, but proceeds faster in cases under air than in cases under N_2. The data also suggest that the Ce(III) and Ce(IV)-rich oleate precursors behave similarly.

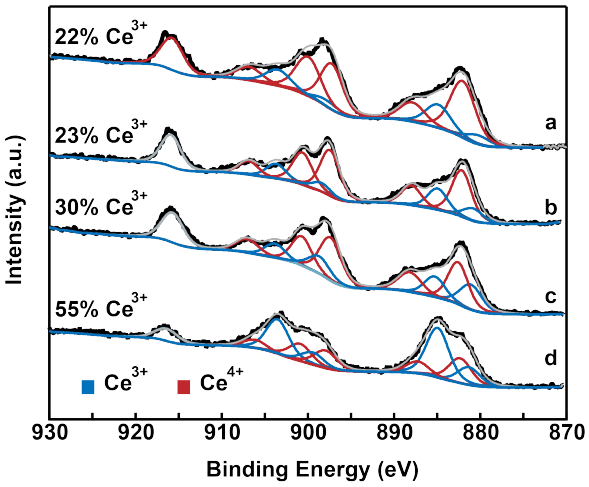

Figure A15. XPS spectra of nanocrystals resulting from using (a) Ce(IV)-rich oleate under air, (b) SE-Ce(III) oleate under air, (c) Ce(IV)-rich oleate under N_2, and (d) SE-Ce(III) oleate under N_2. These results suggest that the nanocrystals are more oxidized in cases where air is used as the reaction atmosphere, whereas nanocrystals produced under N_2 are more reduced. Further, nanocrystals produced under N_2 with the Ce(IV)-rich oleate are more oxidized than those produced from the Ce(III) oleate under N_2.

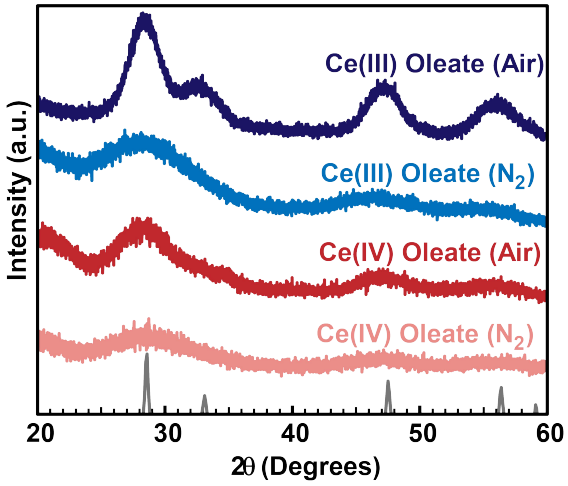

Figure A16. XRD patterns of nanocrystals resulting from syntheses using SE-Ce(III) oleate under air (dark blue), SE-Ce(III) oleate under N_2 (light blue), Ce(IV)-rich oleate under air (dark red), and Ce(IV)-rich oleate under N_2 (light red). These data show a higher degree of crystallinity in samples formed under air than under N_2.

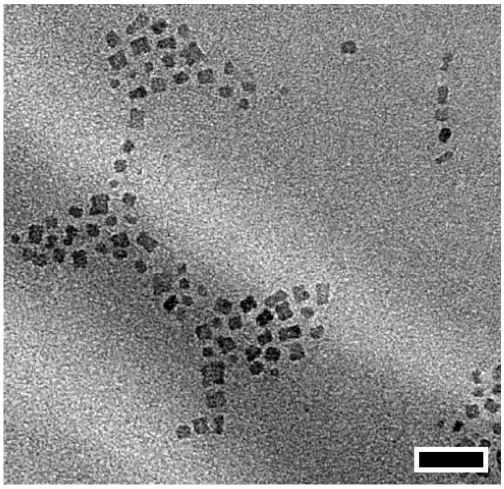

Figure A17. TEM image of nanocrystals resulting from a synthesis using Ce(III) oleate (made from Ce(III) acetate) with water added to the precursor. These results suggest that the presence of residual water is not responsible for smaller nanocube sizes when Ce(IV)-rich oleate is used as the precursor. Scale bar is 20 nm.

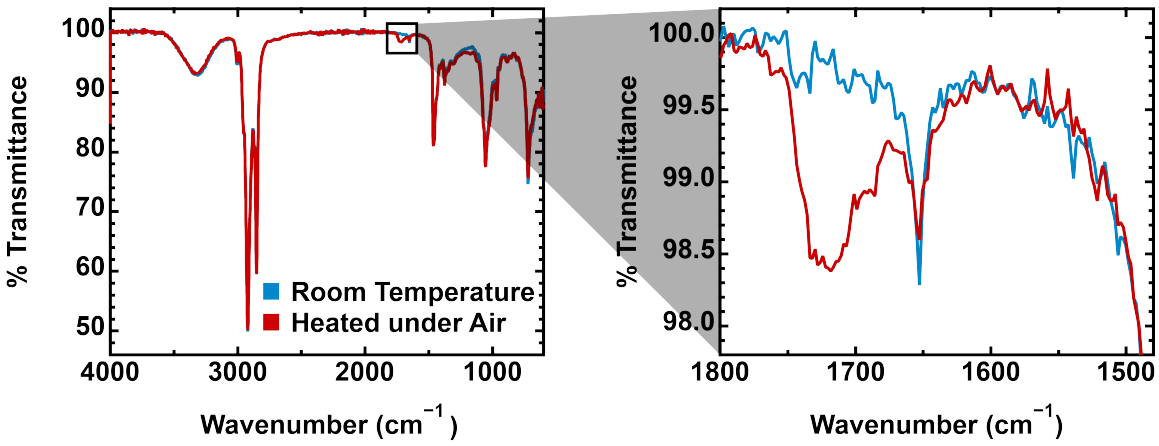

Figure A18. FTIR spectra of oleyl alcohol before (blue) and after (red) heating to 290 °C for 2 h under air.

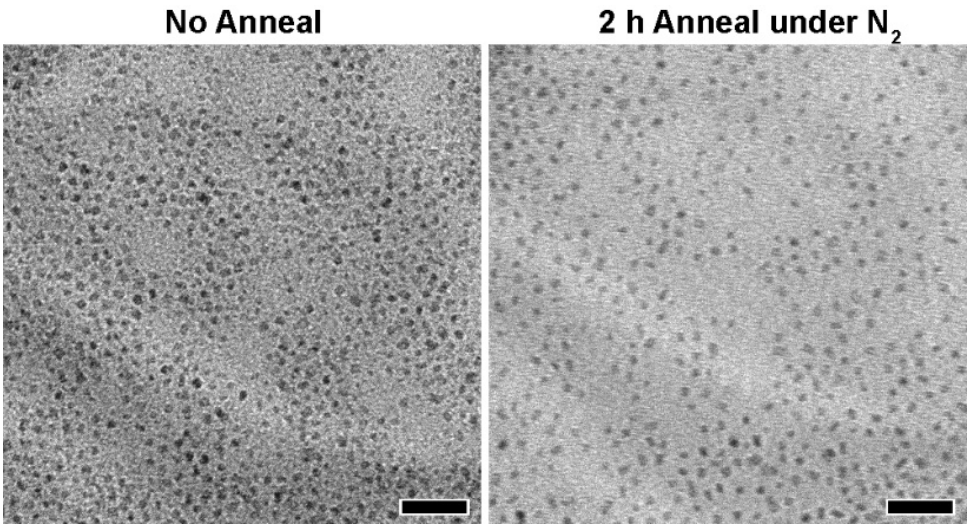

Figure A19. TEM images of small nanocubes made by injecting 0.5 mmol of Ce(III) oleate under air. The left image shows the nanocubes after synthesis, and the right image shows the nanocubes after being annealed for 2 h after 2 mmol of acetic acid had been added to the reaction mixture. These results suggest that acetic acid is not causing oriented attachment. Scale bars are 20 nm.

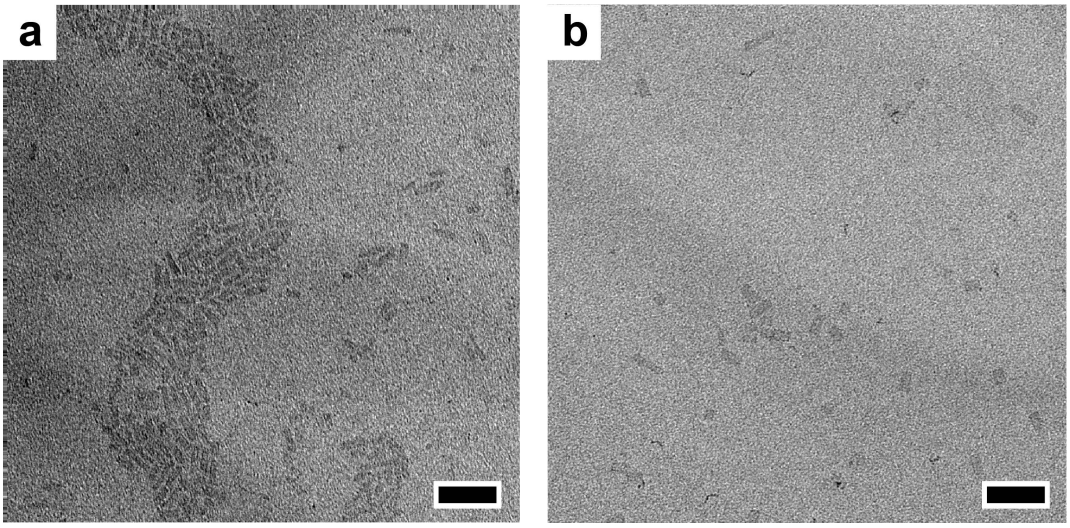

Figure A20. TEM images of nanoribbons (a) immediately after synthesis and (b) after annealing for 2 h under N_2. The similarity in size between the two images suggest that oriented attachment does not occur in this system. Scale bars are 50 nm.

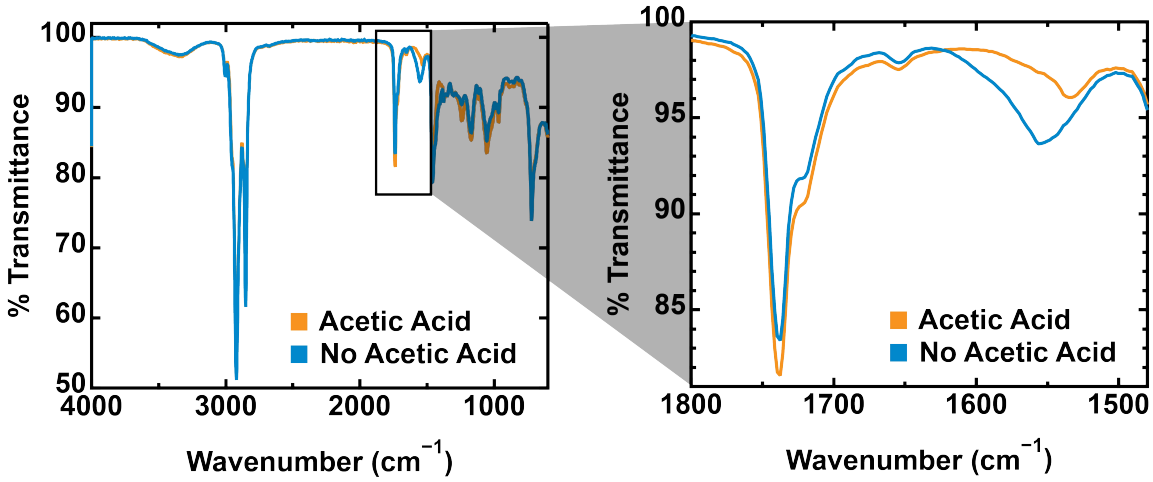

Figure A21. FTIR analysis of reaction mixtures from nanocrystal syntheses performed using Ce(III) oleate with added acetic acid (orange) and without acetic acid (blue). The spectra on the right show the metal carboxylate binding region, suggesting that there is less precursor/monomer buildup in the case with acetic acid compared to the case without acetic acid.

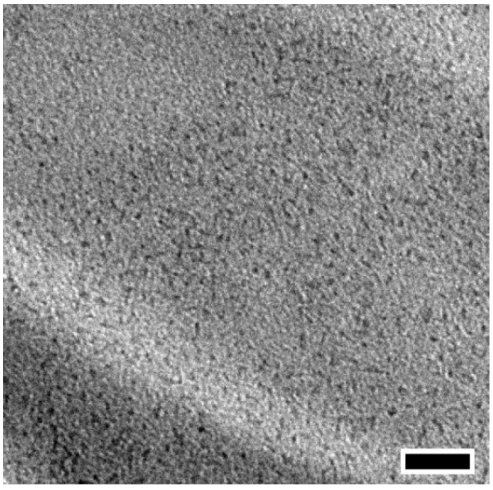

Figure A22. TEM images of nanocrystals resulting from a synthesis conducted using Ce(III) oleate under forming gas (95:5 N_2:H_2), suggesting that a more reducing atmosphere does not lead to nanoribbon formation.

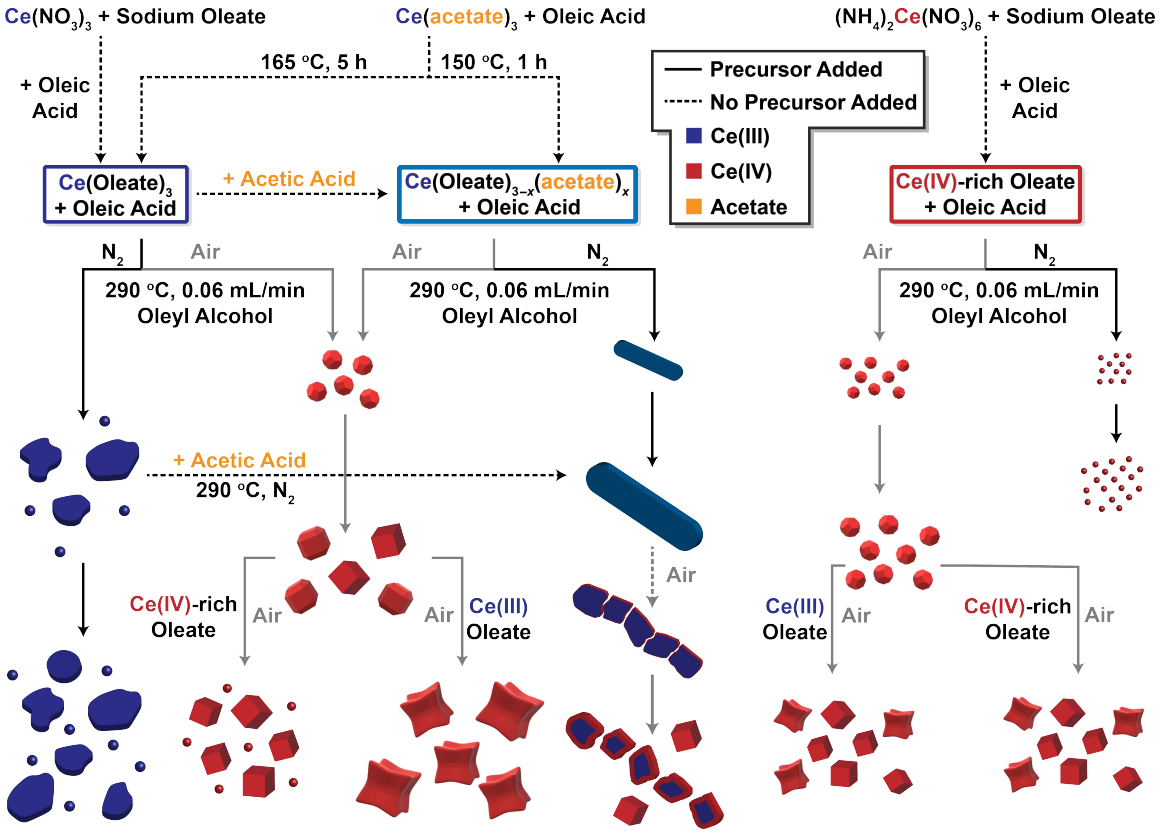

Figure A23. Schematic illustration of nanocrystal morphologies observed under various synthetic conditions.

APPENDIX B

SUPPORTING INFORMATION FOR CHAPTER III: MONOMER GENERATION RATE INFLUENCES THE EARLIEST STAGES OF GROWTH FOR TIN-DOPED INDIUM OXIDE NANOCRYSTALS MADE THROUGH A REAGENT-DRIVEN, CONTINUOUS ADDITION SYNTHESIS

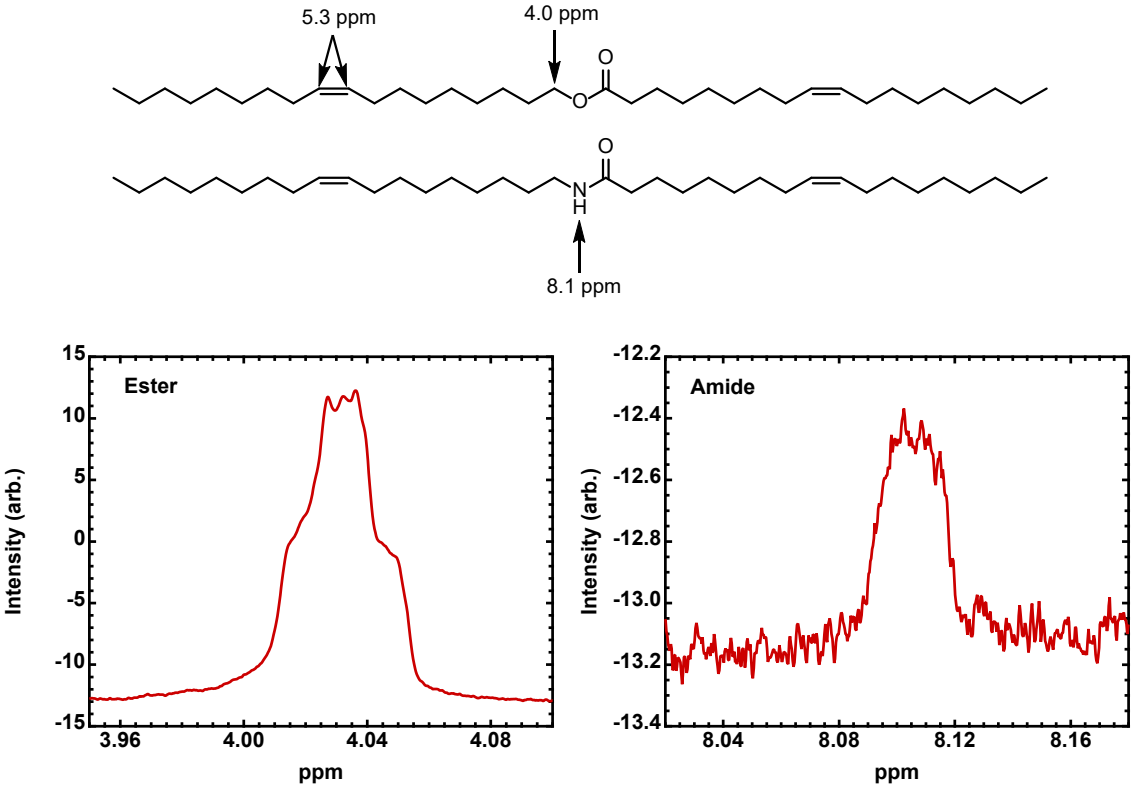

Figure B1. The structures of oleyl oleate (top structure) and oleyl oleamide (bottom structure) are presented with relevant NMR shifts highlighted (discussed in Chapter III). The two graphs show the NMR peaks corresponding to the relevant protons at ~4.0 ppm for the oleyl oleate (left) and the NMR peak corresponding to the relevant protons at ~8.1 ppm for the oleyl oleamide (right).

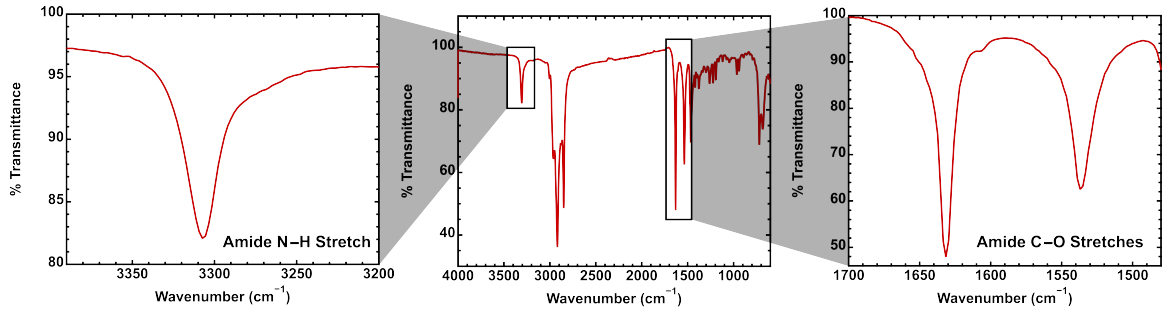

Figure B2. FTIR spectrum of the reaction mixture from a nanocrystal synthesis performed in oleylamine. The center graph shows the full spectrum, and the left and right graphs highlight peaks corresponding to the relevant amide peaks, demonstrating the presence of amide in the reaction mixture.

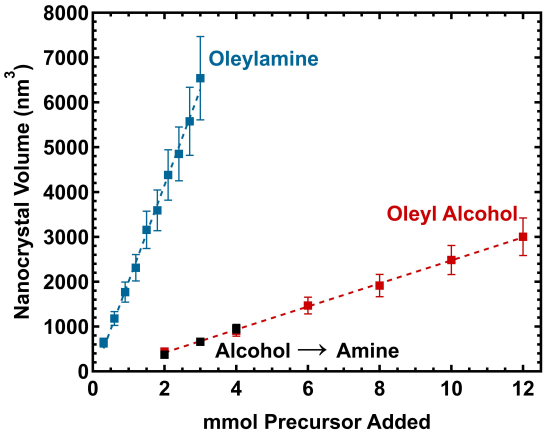

Figure B3. Growth curves of nanocrystal syntheses performed in oleylamine (blue) and oleyl alcohol (red). Overlaid with these results is a growth curve from a nanocrystal synthesis wherein 2 mmol precursor was injected into oleyl alcohol, nanocrystals were purified, redispersed in oleylamine, and 2 additional mmol precursor was injected. This shows that the difference in growth curves between oleyl alcohol and oleylamine is due to the number of nanocrystals formed, not a difference in growth rate.

APPENDIX C

SUPPORTING INFORMATION FOR CHAPTER IV: SCULPTING OPTICAL PROPERTIES OF THIN FILM IR FILTERS THROUGH NANOCRYSTAL SYNTHESIS AND ADDITIVE, SOLUTION PROCESSING

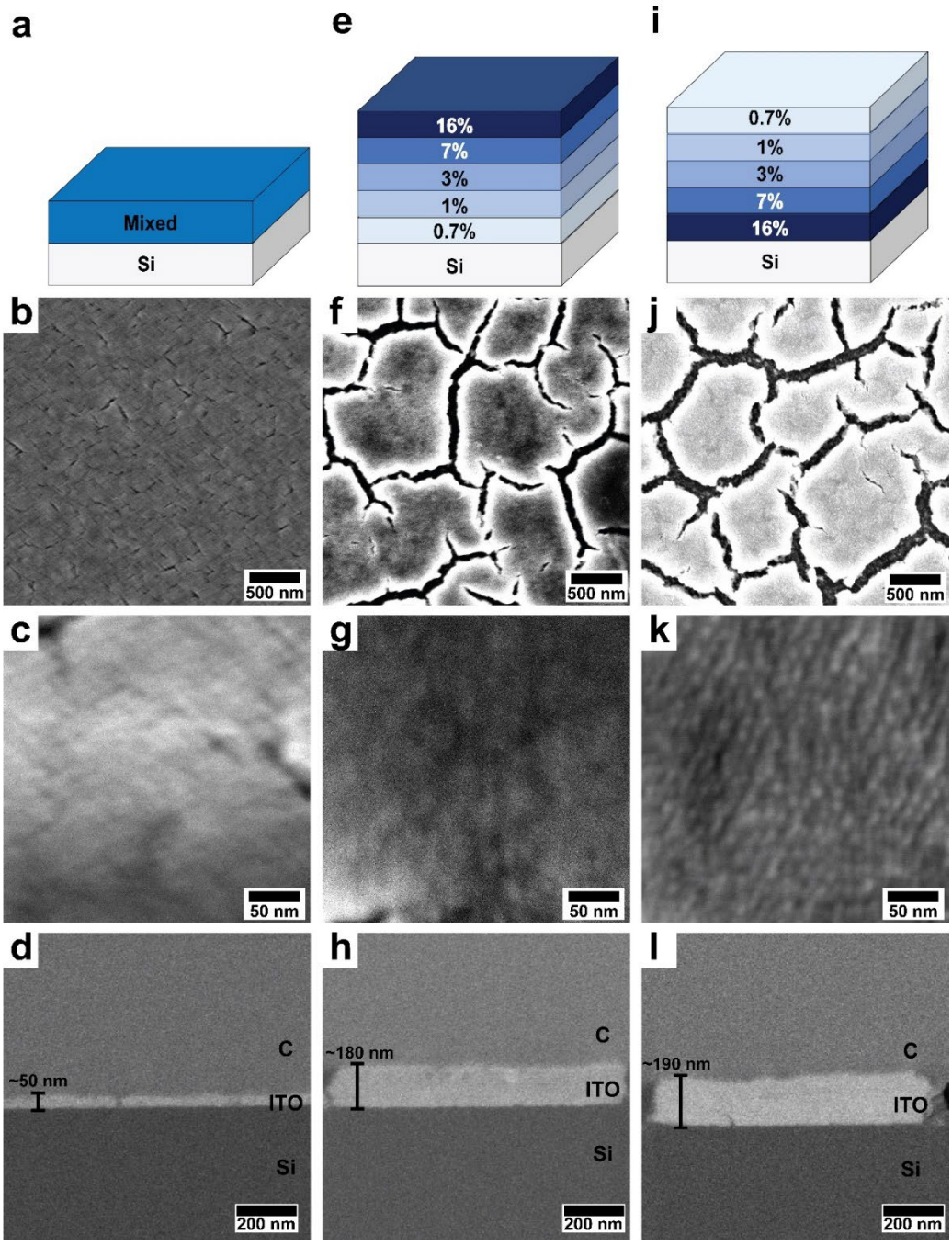

Figure C1. Schematic representations and SEM images of homogeneously mixed and multilayered ITO nanocrystal films containing the 0.7, 1, 3, 7, and 16% homogeneously doped nanocrystals. **a)** Schematic representation of the mixed ITO nanocrystal film imaged in **b)** – **d). b)** and **c)** Top-down images of the film represented in **a)**. **d)** Image of a cross-section of the film represented in **a)** with an estimated film thickness of ~50 nm. **e)** Schematic representation of the mixed ITO nanocrystal film imaged in **f)** – **h). f)** and **h)**

Top-down images of the film represented in **e)**. **h)** Image of a cross-section of the film represented in **e)** with an estimated film thickness of ~180 nm. **i)** Schematic representation of the mixed ITO nanocrystal film imaged in **j)** – **l). j)** and **k)** Top-down images of the film represented in **i)**. **l)** Image of a cross-section of the film represented in **i)** with an estimated film thickness of ~190 nm.

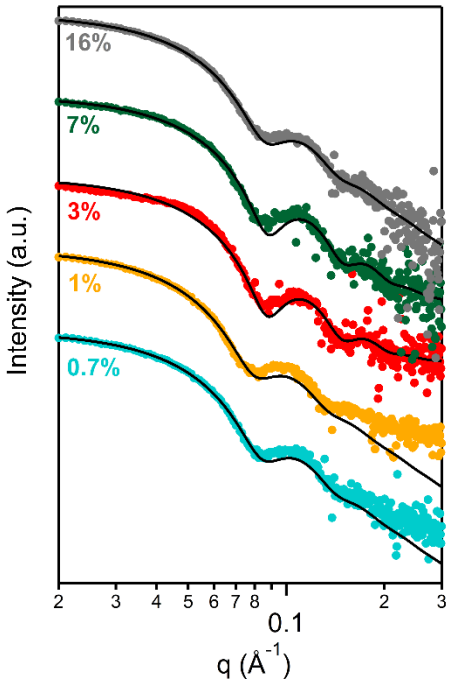

Figure C2. SAXS data for the homogeneously doped ITO nanocrystals used in this study (from top to bottom: 16%, 7%, 3%, 1%, and 0.7% Sn-doping). The colored dots represent the raw SAXS data and the black lines represent fits to those data. Modelled sizes can be found in Table 1.

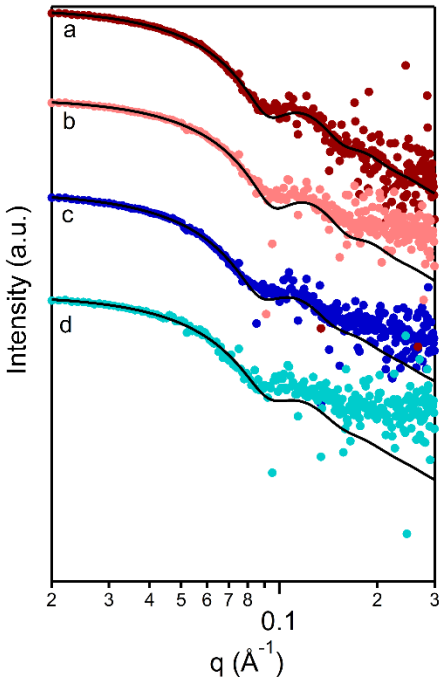

Figure C3. SAXS data for the ITO/In_2O_3 core/shell nanocrystals used in this study. For each of these, we synthesized an ITO core, performed SAXS analysis of the cores, then added a thin In_2O_3 shell and performed SAXS again. This plot shows the scattering patterns for the core/shells nanocrystals **a)** and **c)** compared to the cores alone **b)** and **d)**. **a)** 12% ITO core with a thin In_2O_3 shell, **b)** 12% ITO core with no shell, **c)** 0.4% ITO core with a thin In_2O_3 shell, and **d)** 0.4% ITO core with no shell. The colored dots represent the raw SAXS data and the black lines represent fits to those data. Modelled sizes can be found in Table 1.

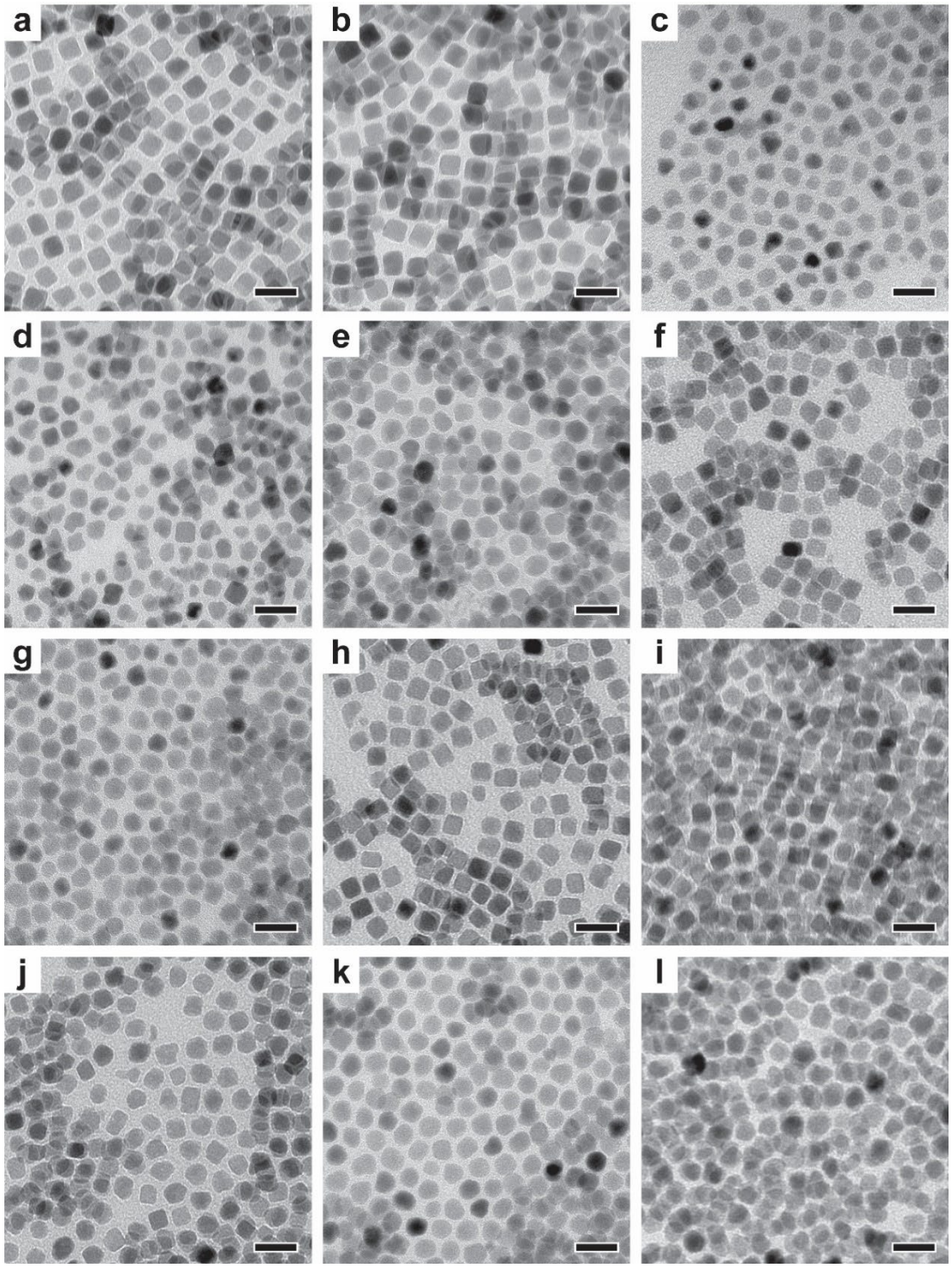

Figure C4. TEM images from all samples listed in Table 1, including homogeneously doped ITO nanocrystals **a)** 0.7%, **b)** 1%, **c)** 3%, **d)** 7%, **e)** 16% Sn metal percent; ITO cores

f) 0.4%, **g)** 12% Sn metal percent with sub-nanometer In_2O_3 shells; and ITO cores with thicker In_2O_3 shells **h)** 1.5%, **i)** 3%, **j)** 5%, **k)** 10%, and **l)** 16% Sn metal percent. All scale bars are 20 nm.

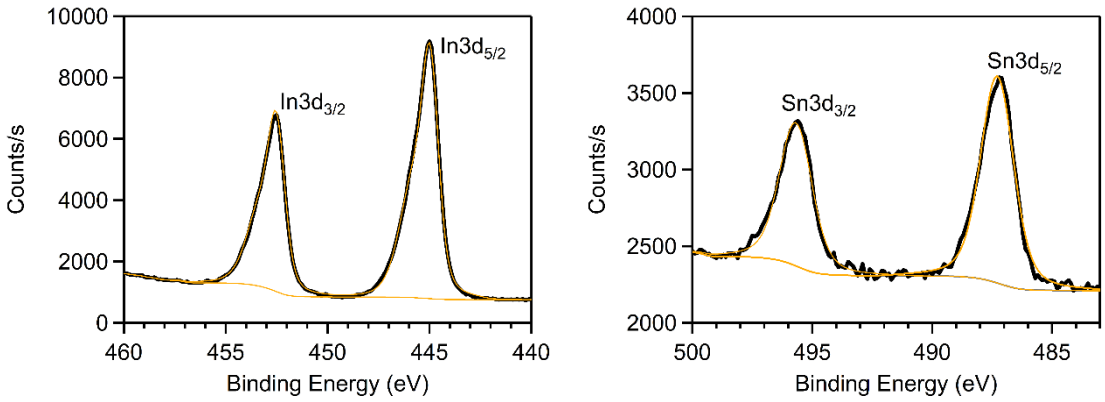

Figure C5. Representative XPS data used to calculate Sn:In content. These spectra show the In and Sn 3d regions for the 16% homogeneously doped ITO nanocrystals as an example. In both spectra, the black lines represent the raw data and the yellow lines represent the overall fits to the data. Sn content can be found in Table 1.

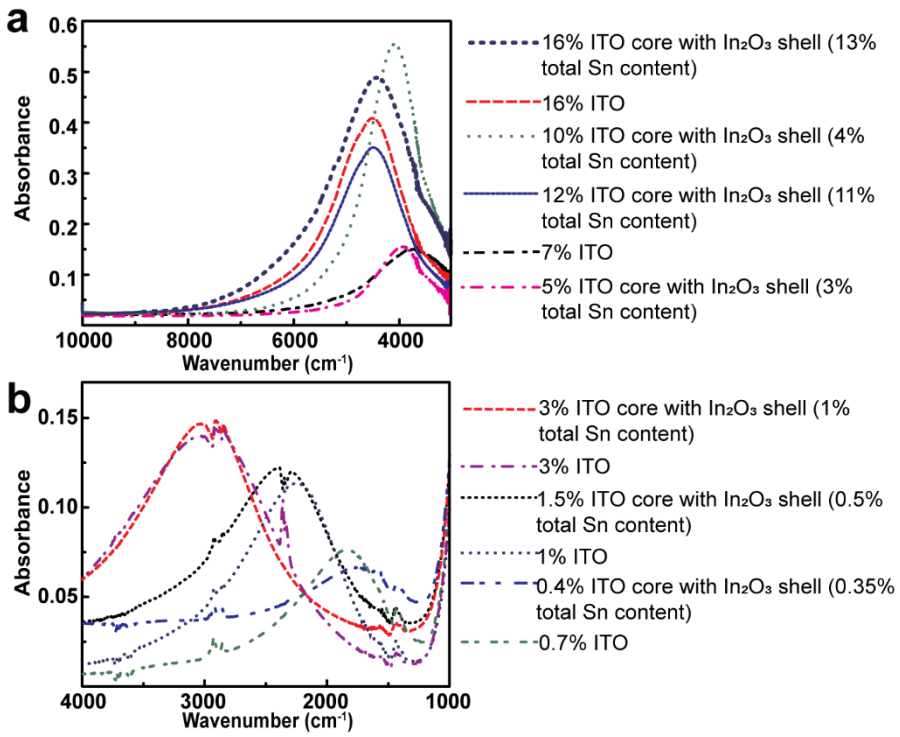

Figure C6. a) Raw non-normalized absorbance data for ITO thin films that possess the LSPR in the wavelength range covered by the UV/Vis-NIR spectrometer; **b)** Raw non-normalized absorbance data for ITO nanocrystal films with low doping level collected using IR spectrometer.

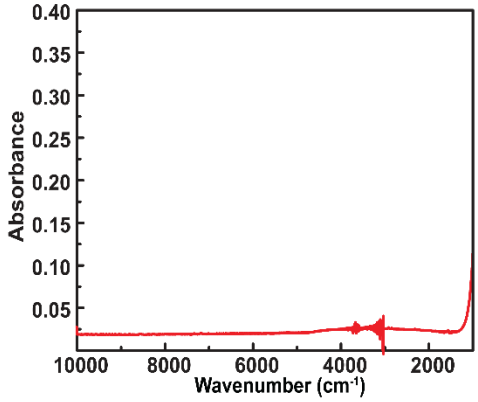

Figure C7. Absorbance of CaF_2 used as a substrate for measuring the absorbance of ITO nanocrystal films.

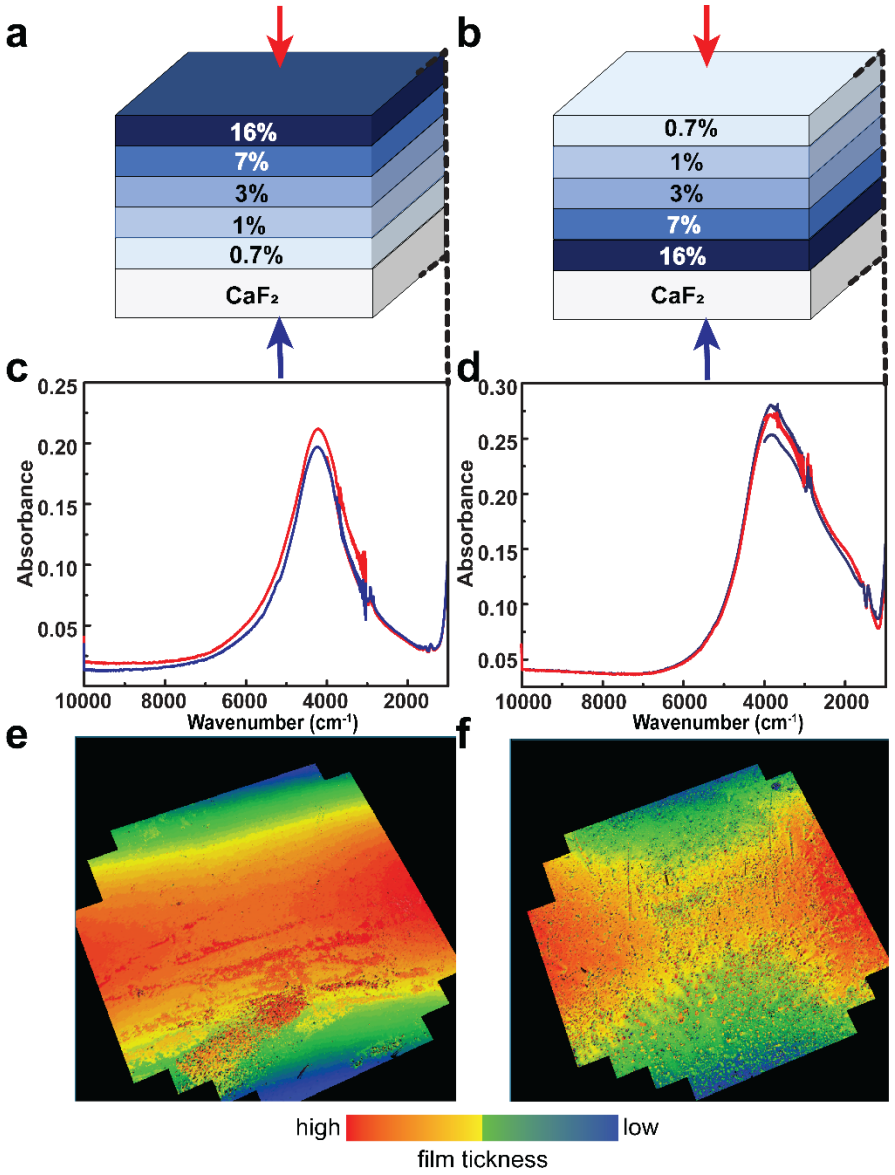

Figure C8. To investigate if the beam direction changed the shape and energy of the combined optical response in the multilayered films, the absorbance spectra for the samples with the geometries **a)** and **b)** were collected from two directions indicated by the arrows. **c)** and **d)** show the corresponding absorbance spectra for the multilayered samples. The colors of the spectra match the colors of the arrows showing from what direction the spectra were collected. **e)** and **f)** show the ellipsometry data collected for each sample. The data were collected on a CaF_2 substrate one-inch diameter. The depicted plots correspond to a 10.82x10.55 mm area in the middle of the substrate.

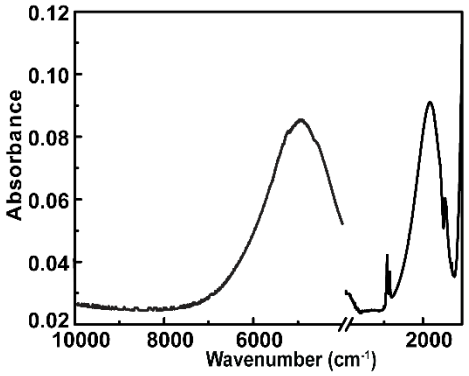

Figure C9. Raw non-normalized absorbance spectrum of the film designed for the narrow band-stop filter. The break in the x-axis (4000-3900 cm^{-1}) is inserted to avoid the instrumental noise at the edge of the detector range. The absorbance data from the FTIR spectrometer was lowered to the same base as the data from the UV/Vis spectrometer to allow intensity comparison.

APPENDIX D

SUPPORTING INFORMATION FOR CHAPTER V: ELECTROCHEMISTRY-INDUCED RESTRUCTURING OF TIN-DOPED INDIUM OXIDE NANOCRYSTAL FILMS OF RELEVANCE TO CO_2 REDUCTION

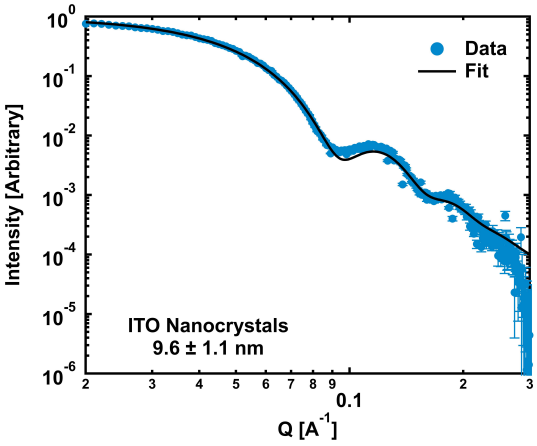

Figure D1. SAXS data for ITO nanocrystals used in this study. The blue trace shows the scattering data and the black line shows the fit to the data. The fit indicates that the ITO nanocrystals are 9.6 ± 1.1 nm in diameter.

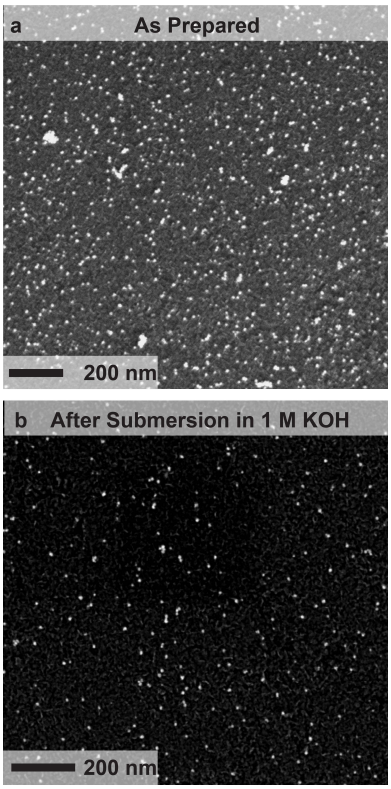

Figure D2. SEM images of (a) as-prepared ITO-functionalized glassy carbon electrode and (b) ITO-functionalized glassy carbon electrode after being submerged in 1 M KOH for 1 h.

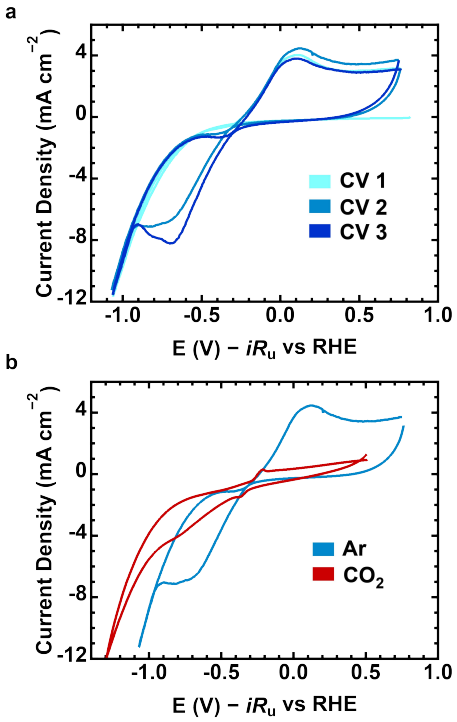

Figure D3. CVs of thick ITO-nanocrystal-functionalized BDD electrode in 0.5 M $KHCO_3$ at 100 mV s^{-1}. (a) Three CV cycles in Ar-sparged electrolyte. (b) CV cycles in Ar-sparged (blue) and CO_2-sparged (red) electrolyte.

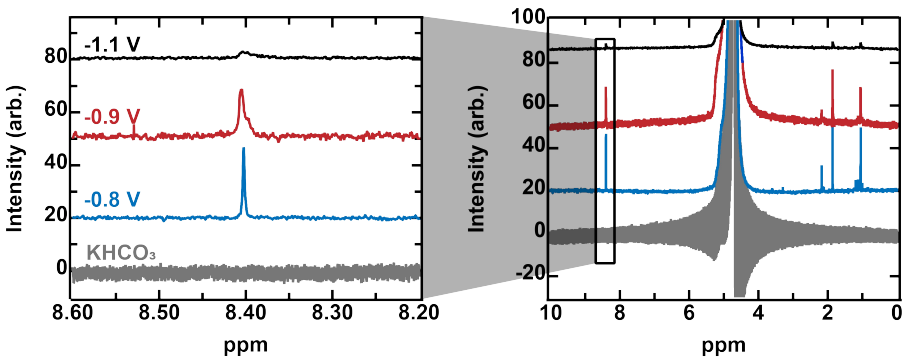

Figure D4. NMR of 0.1 M $KHCO_3$ electrolyte after 30 min electrolyses at potentials of -0.8 V (blue), -0.9 V (red), and -1.1 V (black) vs RHE. The gray trace is of the as-prepared $KHCO_3$ electrolyte. The peaks at ~8.4 ppm are from the production of formate. The large peak in the center is due to water. The peaks between 1.0 and 3.0 ppm are ascribed to other CO_2 reduction products.

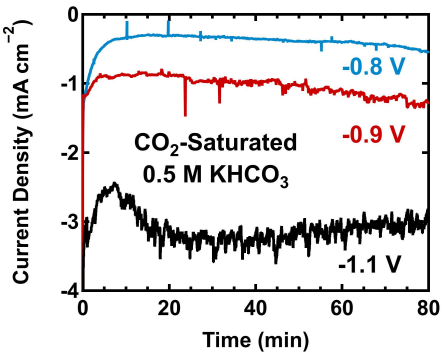

Figure D5. Chronoamperometry data for electrodes in Figure 5 b-c taken in CO_2-sparged 0.5 M $KHCO_3$ for 80 min at -0.8 V (blue), -0.9 V (red), and -1.1 V (black) vs RHE.

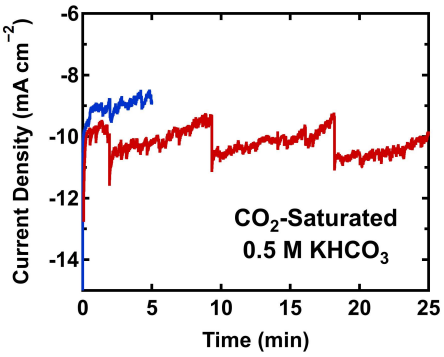

Figure D6. Chronoamperometry data performed on ITO-nanocrystal-functionalized BDD electrodes for 5 min (blue) and 25 min (red).

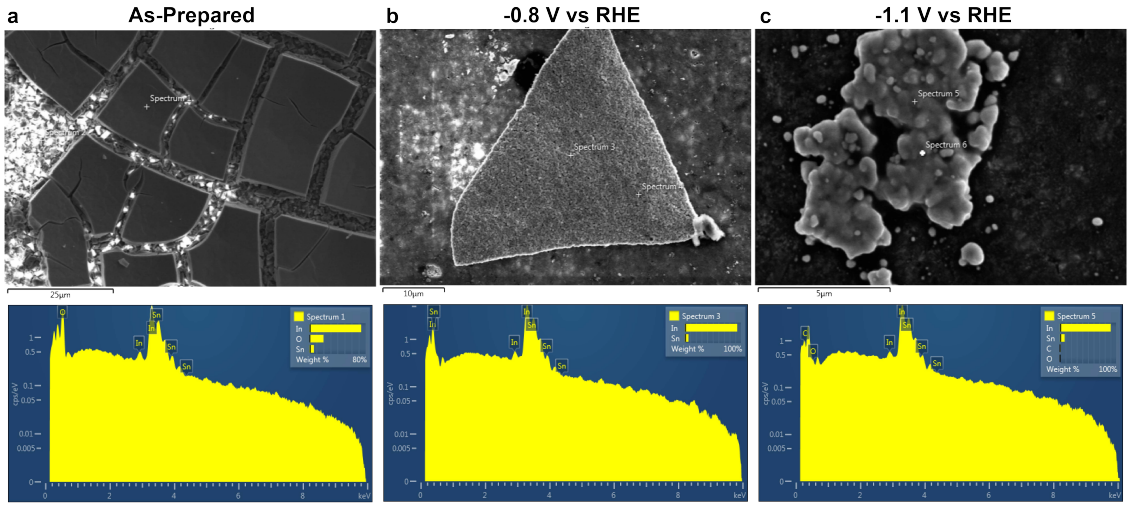

Figure D7. SEM images (top) and corresponding EDS spectra (bottom) for ITO-nanocrystal-functionalized electrodes (a) as-deposited, (b) held at -0.8 V vs RHE for 30 min, and (c) held at -1.1 V vs RHE for 30 min in 0.5 M $KHCO_3$.

Table D1.

Sample (from Fig. S7)	Elemental Composition from EDS (%)			
	In	Sn	O	C
(a) As-Prepared	33.2	2.8	64.0	--
(b) -0.8 V vs RHE	68.7	4.8	5.1	21.4
(c) -1.1 V vs RHE	81.1	5.4	2.4	11.1

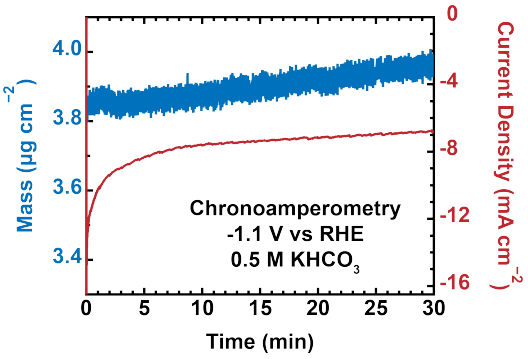

Figure D8. Chronoamperometry data taken using an ITO-functionalized-QCM electrode for 30 min at -1.1 V in 0.5 M $KHCO_3$.

REFERENCES CITED

Chapter I

(1) Dadwal, A.; Baldi, A.; Kumar Narang, R., Nanoparticles as carriers for drug delivery in cancer. *Artificial Cells, Nanomedicine, and Biotechnology* **2018,** *46* (sup2), 295-305.

(2) Napier, M. E.; DeSimone, J. M., Nanoparticle Drug Delivery Platform. *Polymer Reviews* **2007,** *47* (3), 321-327.

(3) Tang, L.; Zheng, Y.; Melo, M. B.; Mabardi, L.; Castaño, A. P.; Xie, Y.-Q.; Li, N.; Kudchodkar, S. B.; Wong, H. C.; Jeng, E. K.; Maus, M. V.; Irvine, D. J., Enhancing T cell therapy through TCR-signaling-responsive nanoparticle drug delivery. *Nat. Biotechnol.* **2018,** *36* (8), 707-716.

(4) Yih, T. C.; Al-Fandi, M., Engineered nanoparticles as precise drug delivery systems. *J. Cell. Biochem.* **2006,** *97* (6), 1184-1190.

(5) Karthick Kannan, P.; Shankar, P.; Blackman, C.; Chung, C.-H., Recent Advances in 2D Inorganic Nanomaterials for SERS Sensing. *Adv. Mater.* **2019,** *31* (34), 1803432.

(6) Lu, C.; Zhou, S.; Gao, F.; Lin, J.; Liu, J.; Zheng, J., DNA-mediated growth of noble metal nanomaterials for biosensing applications. *TrAC, Trends Anal. Chem.* **2022,** *148*, 116533.

(7) Maduraiveeran, G.; Sasidharan, M.; Jin, W., Earth-abundant transition metal and metal oxide nanomaterials: Synthesis and electrochemical applications. *Prog. Mater Sci.* **2019,** *106*, 100574.

(8) Zhou, J.; Yang, T.; Chen, J.; Wang, C.; Zhang, H.; Shao, Y., Two-dimensional nanomaterial-based plasmonic sensing applications: Advances and challenges. *Coord. Chem. Rev.* **2020,** *410*, 213218.

(9) Jose, J.; Kumar, R.; Harilal, S.; Mathew, G. E.; Parambi, D. G. T.; Prabhu, A.; Uddin, M. S.; Aleya, L.; Kim, H.; Mathew, B., Magnetic nanoparticles for hyperthermia in cancer treatment: an emerging tool. *Environmental Science and Pollution Research* **2020,** *27* (16), 19214-19225.

(10) Sztandera, K.; Gorzkiewicz, M.; Klajnert-Maculewicz, B., Gold Nanoparticles in Cancer Treatment. *Molecular Pharmaceutics* **2019,** *16* (1), 1-23.

(11) Wu, J.; Hu, T.; Zhao, G.; Li, A.; Liang, R., Two-dimensional transition metal chalcogenide nanomaterials for cancer diagnosis and treatment. *Chin. Chem. Lett.* **2022**.

(12) Che, W.; Xiao, Z.; Wang, Z.; Li, J.; Wang, H.; Wang, Y.; Xie, Y., Wood-Based Mesoporous Filter Decorated with Silver Nanoparticles for Water Purification. *ACS Sustainable Chemistry & Engineering* **2019,** *7* (5), 5134-5141.

(13) Han, S.; Yang, J.; Li, X.; Li, W.; Zhang, X.; Koratkar, N.; Yu, Z.-Z., Flame Synthesis of Superhydrophilic Carbon Nanotubes/Ni Foam Decorated with Fe2O3 Nanoparticles for Water Purification via Solar Steam Generation. *ACS Applied Materials & Interfaces* **2020,** *12* (11), 13229-13238.

(14) Qin, L.; Huang, D.; Xu, P.; Zeng, G.; Lai, C.; Fu, Y.; Yi, H.; Li, B.; Zhang, C.; Cheng, M.; Zhou, C.; Wen, X., In-situ deposition of gold nanoparticles onto polydopamine-decorated g-C3N4 for highly efficient reduction of nitroaromatics in environmental water purification. *J. Colloid Interface Sci.* **2019,** *534*, 357-369.

(15) Farrell, Z. J.; Thrasher, C. J.; Flynn, A. E.; Tabor, C. E., Silanized Liquid-Metal Nanoparticles for Responsive Electronics. *ACS Applied Nano Materials* **2020,** *3* (7), 6297-6303.

(16) Kim, Y.; Woo, W. J.; Kim, D.; Lee, S.; Chung, S.-m.; Park, J.; Kim, H., Atomic-Layer-Deposition-Based 2D Transition Metal Chalcogenides: Synthesis, Modulation, and Applications. *Adv. Mater.* **2021,** *33* (47), 2005907.

(17) Kulkarni, S. A.; Mhaisalkar, S. G.; Mathews, N.; Boix, P. P., Perovskite Nanoparticles: Synthesis, Properties, and Novel Applications in Photovoltaics and LEDs. *Small Methods* **2019,** *3* (1), 1800231.

(18) Liu, S.; Yuen, M. C.; White, E. L.; Boley, J. W.; Deng, B.; Cheng, G. J.; Kramer-Bottiglio, R., Laser Sintering of Liquid Metal Nanoparticles for Scalable Manufacturing of Soft and Flexible Electronics. *ACS Applied Materials & Interfaces* **2018,** *10* (33), 28232-28241.

(19) Tan, H. W.; An, J.; Chua, C. K.; Tran, T., Metallic Nanoparticle Inks for 3D Printing of Electronics. *Advanced Electronic Materials* **2019,** *5* (5), 1800831.

(20) Das, S.; Hossain, M. J.; Leung, S.-F.; Lenox, A.; Jung, Y.; Davis, K.; He, J.-H.; Roy, T., A leaf-inspired photon management scheme using optically tuned bilayer nanoparticles for ultra-thin and highly efficient photovoltaic devices. *Nano Energy* **2019,** *58*, 47-56.

(21) Wouk de Menezes, L. C.; Renzi, W.; Marchiori, C. F. d. N.; de Oliveira, C. K. B. Q. M.; von Kieseritzky, F.; Duarte, J. L.; Roman, L. S., Nonradiative Energy Transfer between Porphyrin and Copolymer in Films Processed by Organic Solvent and Water-Dispersible Nanoparticles with Photovoltaic Applications. *The Journal of Physical Chemistry C* **2018,** *122* (10), 5796-5804.

(22) Chen, S.; Skordos, A.; Thakur, V. K., Functional nanocomposites for energy storage: chemistry and new horizons. *Materials Today Chemistry* **2020,** *17*, 100304.

(23) Li, H.; Liu, F.; Fan, B.; Ai, D.; Peng, Z.; Wang, Q., Nanostructured Ferroelectric-Polymer Composites for Capacitive Energy Storage. *Small Methods* **2018,** *2* (6), 1700399.

(24) Pham, D. T.; Quan, T.; Mei, S.; Lu, Y., Colloidal metal sulfide nanoparticles for high performance electrochemical energy storage systems. *Current Opinion in Green and Sustainable Chemistry* **2022,** *34*, 100596.

(25) Liu, J.; Li, R.; Yang, B., Carbon Dots: A New Type of Carbon-Based Nanomaterial with Wide Applications. *ACS Central Science* **2020,** *6* (12), 2179-2195.

(26) Serrano-Aroca, Á.; Takayama, K.; Tuñón-Molina, A.; Seyran, M.; Hassan, S. S.; Pal Choudhury, P.; Uversky, V. N.; Lundstrom, K.; Adadi, P.; Palù, G.; Aljabali, A. A. A.; Chauhan, G.; Kandimalla, R.; Tambuwala, M. M.; Lal, A.; Abd El-Aziz, T. M.; Sherchan, S.; Barh, D.; Redwan, E. M.; Bazan, N. G.; Mishra, Y. K.; Uhal, B. D.; Brufsky, A., Carbon-Based Nanomaterials: Promising Antiviral Agents to Combat COVID-19 in the Microbial-Resistant Era. *ACS Nano* **2021,** *15* (5), 8069-8086.

(27) Xin, Q.; Shah, H.; Nawaz, A.; Xie, W.; Akram, M. Z.; Batool, A.; Tian, L.; Jan, S. U.; Boddula, R.; Guo, B.; Liu, Q.; Gong, J. R., Antibacterial Carbon-Based Nanomaterials. *Adv. Mater.* **2019,** *31* (45), 1804838.

(28) Chen, Y.; Fan, Z.; Zhang, Z.; Niu, W.; Li, C.; Yang, N.; Chen, B.; Zhang, H., Two-Dimensional Metal Nanomaterials: Synthesis, Properties, and Applications. *Chem. Rev.* **2018,** *118* (13), 6409-6455.

(29) Cheng, H.; Yang, N.; Lu, Q.; Zhang, Z.; Zhang, H., Syntheses and Properties of Metal Nanomaterials with Novel Crystal Phases. *Adv. Mater.* **2018,** *30* (26), 1707189.

(30) Yadav, S.; Yashas, S. R.; Shivaraju, H. P., Transitional metal chalcogenide nanostructures for remediation and energy: a review. *Environmental Chemistry Letters* **2021,** *19* (5), 3683-3700.

(31) Tang, B.; Zhuo, L.; Ge, J.; Wang, G.; Shi, Z.; Niu, J., A Surfactant-Free Route to Single-Crystalline CeO_2 Nanowires. *Chem. Commun.* **2005,** (28), 3565-3567.

(32) Yada, M.; Sakai, S.; Torikai, T.; Watari, T.; Furuta, S.; Katsuki, H., Cerium Compound Nanowires and Nanorings Templated by Mixed Organic Molecules. *Adv. Mater.* **2004,** *16* (14), 1222-1226.

(33) Yu, T.; Joo, J.; Park, Y. I.; Hyeon, T., Large-Scale Nonhydrolytic Sol-Gel Synthesis of Uniform-Sized Ceria Nanocrystals with Spherical, Wire, and Tadpole Shapes. *Angew. Chem. Int. Ed.* **2005,** *44* (45), 7411-7414.

(34) Jiang, S.; Zhang, R.; Liu, H.; Rao, Y.; Yu, Y.; Chen, S.; Yue, Q.; Zhang, Y.; Kang, Y., Promoting Formation of Oxygen Vacancies in Two-Dimensional Cobalt-Doped Ceria Nanosheets for Efficient Hydrogen Evolution. *J. Am. Chem. Soc.* **2020,** *142* (14), 6461-6466.

(35) Marani, D.; Moraes, L. P. R.; Gualandris, F.; Sanna, S.; de Florio, D. Z.; Esposito, V.; Fonseca, F. C., Nucleation front instability in two-dimensional (2D) nanosheet gadolinium-doped cerium oxide (CGO) formation. *CrystEngComm* **2018,** *20* (10), 1405-1410.

(36) Riedinger, A.; Ott, F. D.; Mule, A.; Mazzotti, S.; Knüsel, P. N.; Kress, S. J. P.; Prins, F.; Erwin, S. C.; Norris, D. J., An Intrinsic Growth Instability in Isotropic Materials Leads to Quasi-Two-Dimensional Nanoplatelets. *Nat. Mater.* **2017,** *16* (7), 743-748.

(37) Zhang, L.; Kang, W.; Ma, Q.; Xie, Y.; Jia, Y.; Deng, N.; Zhang, Y.; Ju, J.; Cheng, B., Two-Dimensional Acetate-Based Light Lanthanide Fluoride Nanomaterials (F–Ln, Ln = La, Ce, Pr, and Nd): Morphology, Structure, Growth Mechanism, and Stability. *J. Am. Chem. Soc.* **2019,** *141* (33), 13134-13142.

(38) Araújo, V. D.; Avansi, W.; De Carvalho, H. B.; Moreira, M. L.; Longo, E.; Ribeiro, C.; Bernardi, M. I. B., CeO_2 Nanoparticles Synthesized by a Microwave-Assisted Hydrothermal Method: Evolution from Nanospheres to Nanorods. *CrystEngComm* **2012,** *14* (3), 1150-1154.

(39) Bokhonov, B. B.; Matvienko, A. A.; Gerasimov, K. B.; Dudina, D. V., Formation of ordered nanocrystalline CeO_2 structures during thermal decomposition of cerium formate $Ce(HCOO)_3$. *Ceram. Int.* **2019,** *45* (16), 19684-19688.

(40) Mai, H. X.; Sun, L. D.; Zhang, Y. W.; Si, R.; Feng, W.; Zhang, H. P.; Liu, H. C.; Yan, C. H., Shape-Selective Synthesis and Oxygen Storage Behavior of Ceria Nanopolyhedra, Nanorods, and Nanocubes. *J. Phys. Chem. B* **2005,** *109* (51), 24380-24385.

(41) Taniguchi, T.; Katsumata, K. I.; Omata, S.; Okada, K.; Matsushita, N., Tuning Growth Modes of Ceria-Based Nanocubes by a Hydrothermal Method. *Cryst. Growth Des.* **2011,** *11* (9), 3754-3760.

(42) Trovarelli, A.; Llorca, J., Ceria Catalysts at Nanoscale: How Do Crystal Shapes Shape Catalysis? *ACS Catal.* **2017,** *7* (7), 4716-4735.

(43) Wu, Q.; Zhang, F.; Xiao, P.; Tao, H.; Wang, X.; Hu, Z.; Lü, Y., Great Influence of Anions for Controllable Synthesis of CeO_2 Nanostructures: From Nanorods to Nanocubes. *J. Phys. Chem. C* **2008,** *112* (44), 17076-17080.

(44) Berestok, T.; Guardia, P.; Blanco, J.; Nafria, R.; Torruella, P.; López-Conesa, L.; Estradé, S.; Ibáñez, M.; De Roo, J.; Luo, Z.; Cadavid, D.; Martins, J. C.; Kovalenko, M. V.; Peiró, F.; Cabot, A., Tuning Branching in Ceria Nanocrystals. *Chem. Mater.* **2017,** *29* (10), 4418-4424.

(45) Yu, R.; Yan, L.; Zheng, P.; Chen, J.; Xing, X., Controlled Synthesis of CeO_2 Flower-like and Well-aligned Nanorod Hierarchical Architectures by a Phosphate-Assisted Hydrothermal Route. *J. Phys. Chem. C* **2008,** *112* (50), 19896-19900.

(46) Zhou, H. P.; Zhang, Y. W.; Mai, H. X.; Sun, X.; Liu, Q.; Song, W. G.; Yan, C. H., Spontaneous Organization of Uniform CeO_2 Nanoflowers by 3D Oriented Attachment in Hot Surfactant Solutions Monitored with an In Situ Electrical Conductance Technique. *Chem. Eur. J.* **2008,** *14* (11), 3380-3390.

(47) Heiligtag, F. J.; Niederberger, M., The fascinating world of nanoparticle research. *Mater. Today* **2013,** *16* (7), 262-271.

(48) Jeevanandam, J.; Barhoum, A.; Chan, Y. S.; Dufresne, A.; Danquah, M. K., Review on nanoparticles and nanostructured materials: history, sources, toxicity and regulations. *Beilstein journal of nanotechnology* **2018,** *9* (1), 1050-1074.

(49) Liu, Z.; Lin, C.-H.; Hyun, B.-R.; Sher, C.-W.; Lv, Z.; Luo, B.; Jiang, F.; Wu, T.; Ho, C.-H.; Kuo, H.-C.; He, J.-H., Micro-light-emitting diodes with quantum dots in display technology. *Light: Science & Applications* **2020,** *9* (1), 83.

(50) Lu, H.; Carroll, G. M.; Neale, N. R.; Beard, M. C., Infrared Quantum Dots: Progress, Challenges, and Opportunities. *ACS Nano* **2019,** *13* (2), 939-953.

(51) Wagner, A. M.; Knipe, J. M.; Orive, G.; Peppas, N. A., Quantum dots in biomedical applications. *Acta Biomaterialia* **2019,** *94*, 44-63.

(52) Moon, H.; Lee, C.; Lee, W.; Kim, J.; Chae, H., Stability of Quantum Dots, Quantum Dot Films, and Quantum Dot Light-Emitting Diodes for Display Applications. *Adv. Mater.* **2019,** *31* (34), 1804294.

(53) Sun, Y.; Jiang, Y.; Sun, X. W.; Zhang, S.; Chen, S., Beyond OLED: Efficient Quantum Dot Light-Emitting Diodes for Display and Lighting Application. *The Chemical Record* **2019,** *19* (8), 1729-1752.

(54) Hu, L.; Zhao, Q.; Huang, S.; Zheng, J.; Guan, X.; Patterson, R.; Kim, J.; Shi, L.; Lin, C.-H.; Lei, Q.; Chu, D.; Tao, W.; Cheong, S.; Tilley, R. D.; Ho-Baillie, A. W. Y.; Luther, J. M.; Yuan, J.; Wu, T., Flexible and efficient perovskite quantum dot solar cells via hybrid interfacial architecture. *Nature Communications* **2021,** *12* (1), 466.

(55) Yuan, J.; Hazarika, A.; Zhao, Q.; Ling, X.; Moot, T.; Ma, W.; Luther, J. M., Metal Halide Perovskites in Quantum Dot Solar Cells: Progress and Prospects. *Joule* **2020,** *4* (6), 1160-1185.

(56) Su, S. S.; Chang, I., Review of Production Routes of Nanomaterials. In *Commercialization of Nanotechnologies–A Case Study Approach*, Brabazon, D.; Pellicer, E.; Zivic, F.; Sort, J.; Dolors Baró, M.; Grujovic, N.; Choy, K.-L., Eds. Springer International Publishing: Cham, 2018; pp 15-29.

(57) Lak, A.; Disch, S.; Bender, P., Embracing Defects and Disorder in Magnetic Nanoparticles. *Advanced Science* **2021,** *8* (7), 2002682.

(58) McDonagh, B. H.; Staudinger, C.; Normile, P. S.; De Toro, J. A.; Bandyopadhyay, S.; Glomm, W. R.; Singh, G., New insights into controlling the twin structure of magnetic iron oxide nanoparticles. *Applied Materials Today* **2021,** *24*, 101084.

(59) Babu, S.; Thanneeru, R.; Inerbaev, T.; Day, R.; Masunov, A. E.; Schulte, A.; Seal, S., Dopant-Mediated Oxygen Vacancy Tuning in Ceria Nanoparticles. *Nanotechnology* **2009,** *20* (8), 085713-085713.

(60) Mehmood, R.; Mofarah, S. S.; Chen, W. F.; Koshy, P.; Sorrell, C. C., Surface, Subsurface, and Bulk Oxygen Vacancies Quantified by Decoupling and Deconvolution of the Defect Structure of Redox-Active Nanoceria. *Inorg. Chem.* **2019,** *58* (9), 6016-6027.

(61) Pacchioni, G., Oxygen Vacancy: The Invisible Agent on Oxide Surfaces. *ChemPhysChem* **2003,** *4* (10), 1041-1047.

(62) Gualdrón-Reyes, A. F.; Yoon, S. J.; Barea, E. M.; Agouram, S.; Muñoz-Sanjosé, V.; Meléndez, Á. M.; Niño-Gómez, M. E.; Mora-Seró, I., Controlling the Phase Segregation in Mixed Halide Perovskites through Nanocrystal Size. *ACS Energy Letters* **2019,** *4* (1), 54-62.

(63) Vinoditha, U.; Sarojini, B. K.; Sandeep, K. M.; Narayana, B.; Balakrishna, K. M., Phase segregation induced third order nonlinear saturable absorption behavior in Erbium doped ZnO nanoparticles synthesized by facile hydrothermal method. *Physica E: Low-dimensional Systems and Nanostructures* **2020,** *124*, 114281.

(64) Crockett, B. M.; Jansons, A. W.; Koskela, K. M.; Johnson, D. W.; Hutchison, J. E., Radial Dopant Placement for Tuning Plasmonic Properties in Metal Oxide Nanocrystals. *ACS Nano* **2017,** *11* (8), 7719-7728.

(65) Lounis, S. D.; Runnerstrom, E. L.; Bergerud, A.; Nordlund, D.; Milliron, D. J., Influence of Dopant Distribution on the Plasmonic Properties of Indium Tin Oxide Nanocrystals. *J. Am. Chem. Soc.* **2014,** *136* (19), 7110-7116.

(66) Cooper, S. R.; Plummer, L. K.; Cosby, A. G.; Lenox, P.; Jander, A.; Dhagat, P.; Hutchison, J. E., Insights into the Magnetic Properties of Sub-10 nm Iron Oxide Nanocrystals through the Use of a Continuous Growth Synthesis. *Chem. Mater.* **2018,** *30* (17), 6053-6062.

(67) Cooper, S. R.; Candler, R. O.; Cosby, A. G.; Johnson, D. W.; Jensen, K. M. Ø.; Hutchison, J. E., Evolution of Atomic-Level Structure in Sub-10 Nanometer Iron Oxide Nanocrystals: Influence on Cation Occupancy and Growth Rates. *ACS Nano* **2020,** *14* (5), 5480-5490.

(68) Jun, Y.-S.; Zhu, Y.; Wang, Y.; Ghim, D.; Wu, X.; Kim, D.; Jung, H., Classical and Nonclassical Nucleation and Growth Mechanisms for Nanoparticle Formation. *Annu. Rev. Phys. Chem.* **2022**.

(69) Thanh, N. T. K.; Maclean, N.; Mahiddine, S., Mechanisms of Nucleation and Growth of Nanoparticles in Solution. *Chem. Rev.* **2014,** *114* (15), 7610-7630.

(70) Bøjesen, E. D.; Iversen, B. B., The chemistry of nucleation. *CrystEngComm* **2016,** *18* (43), 8332-8353.

(71) van Embden, J.; Chesman, A. S. R.; Jasieniak, J. J., The Heat-Up Synthesis of Colloidal Nanocrystals. *Chem. Mater.* **2015,** *27* (7), 2246-2285.

(72) Wang, Y.; He, J.; Liu, C.; Chong, W. H.; Chen, H., Thermodynamics versus Kinetics in Nanosynthesis. *Angew. Chem. Int. Ed.* **2015,** *54* (7), 2022-2051.

(73) Lee, J.; Yang, J.; Kwon, S. G.; Hyeon, T., Nonclassical nucleation and growth of inorganic nanoparticles. *Nature Reviews Materials* **2016,** *1* (8), 16034.

(74) Jin, B.; Liu, Z.; Tang, R., Recent experimental explorations of non-classical nucleation. *CrystEngComm* **2020,** *22* (24), 4057-4073.

(75) Lee, S. S.; Zhu, H.; Contreras, E. Q.; Prakash, A.; Puppala, H. L.; Colvin, V. L., High Temperature Decomposition of Cerium Precursors to Form Ceria Nanocrystal Libraries for Biological Applications. *Chem. Mater.* **2012,** *24* (3), 424-432.

(76) Liu, B.; Ma, L.; Huang, Z.; Hu, H.; Wu, P.; Liu, J., Janus DNA orthogonal adsorption of graphene oxide and metal oxide nanoparticles enabling stable sensing in serum. *Mater. Horiz.* **2018,** *5* (1), 65-69.

(77) Nunes, D.; Pimentel, A.; Gonçalves, A.; Pereira, S.; Branquinho, R.; Barquinha, P.; Fortunato, E.; Martins, R., Metal oxide nanostructures for sensor applications. *Semicond. Sci. Technol.* **2019,** *34* (4), 043001.

(78) Jansons, A. W.; Koskela, K. M.; Crockett, B. M.; Hutchison, J. E., Transition Metal-Doped Metal Oxide Nanocrystals: Efficient Substitutional Doping through a Continuous Growth Process. *Chem. Mater.* **2017,** *29* (19), 8167-8176.

(79) Besenhard, M. O.; LaGrow, A. P.; Hodzic, A.; Kriechbaum, M.; Panariello, L.; Bais, G.; Loizou, K.; Damilos, S.; Margarida Cruz, M.; Thanh, N. T. K.; Gavriilidis, A., Co-precipitation synthesis of stable iron oxide nanoparticles with NaOH: New insights and continuous production via flow chemistry. *Chem. Eng. J.* **2020,** *399*, 125740.

(80) Petcharoen, K.; Sirivat, A., Synthesis and characterization of magnetite nanoparticles via the chemical co-precipitation method. *Materials Science and Engineering: B* **2012,** *177* (5), 421-427.

(81) Darr, J. A.; Zhang, J.; Makwana, N. M.; Weng, X., Continuous Hydrothermal Synthesis of Inorganic Nanoparticles: Applications and Future Directions. *Chem. Rev.* **2017,** *117* (17), 11125-11238.

(82) Hayashi, H.; Hakuta, Y., Hydrothermal Synthesis of Metal Oxide Nanoparticles in Supercritical Water. *Materials* **2010,** *3* (7).

(83) Makinose, Y.; Taniguchi, T.; Katsumata, K. I.; Okada, K.; Matsushita, N., Facet Control of Ceria Nanocrystals Synthesized by an Oleate-Modified Hydrothermal Method. *Adv. Powder Technol.* **2016,** *27* (1), 64-71.

(84) Plummer, L. K.; Hutchison, J. E., Understanding the Effects of Iron Precursor Ligation and Oxidation State Leads to Improved Synthetic Control for Spinel Iron Oxide Nanocrystals. *Inorg. Chem.* **2020,** *59* (20), 15074-15087.

(85) Deshmukh, R.; Niederberger, M., Mechanistic Aspects in the Formation, Growth and Surface Functionalization of Metal Oxide Nanoparticles in Organic Solvents. *Chemistry – A European Journal* **2017,** *23* (36), 8542-8570.

(86) Niederberger, M.; Garnweitner, G., Organic Reaction Pathways in the Nonaqueous Synthesis of Metal Oxide Nanoparticles. *Chemistry – A European Journal* **2006,** *12* (28), 7282-7302.

(87) Gu, H.; Soucek, M. D., Preparation and Characterization of Monodisperse Cerium Oxide Nanoparticles in Hydrocarbon Solvents. *Chem. Mater.* **2007,** *19* (5), 1103-1110.

(88) Ito, D.; Yokoyama, S.; Zaikova, T.; Masuko, K.; Hutchison, J. E., Synthesis of Ligand-Stabilized Metal Oxide Nanocrystals and Epitaxial Core/Shell Nanocrystals via a Lower-Temperature Esterification Process. *ACS Nano* **2014,** *8* (1), 64-75.

(89) Kwon, S. G.; Piao, Y.; Park, J.; Angappane, S.; Jo, Y.; Hwang, N.-M.; Park, J.-G.; Hyeon, T., Kinetics of Monodisperse Iron Oxide Nanocrystal Formation by "Heating-Up" Process. *J. Am. Chem. Soc.* **2007,** *129* (41), 12571-12584.

(90) Plummer, L. K.; Crockett, B. M.; Pennel, M. L.; Jansons, A. W.; Koskela, K. M.; Hutchison, J. E., Influence of Monomer Flux and Temperature on Morphology of Indium Oxide Nanocrystals during a Continuous Growth Synthesis. *Chem. Mater.* **2019,** *31* (18), 7638-7649.

(91) Liz-Marzán, L. M.; Kagan, C. R.; Millstone, J. E., Reproducibility in Nanocrystal Synthesis? Watch out for Impurities! *ACS Nano* **2020,** *14* (6), 6359-6361.

(92) Herman, D. A. J.; Ferguson, P.; Cheong, S.; Hermans, I. F.; Ruck, B. J.; Allan, K. M.; Prabakar, S.; Spencer, J. L.; Lendrum, C. D.; Tilley, R. D., Hot-injection synthesis of iron/iron oxide core/shell nanoparticles for T2 contrast enhancement in magnetic resonance imaging. *Chem. Commun.* **2011,** *47* (32), 9221-9223.

(93) Kwon, S. G.; Hyeon, T., Formation Mechanisms of Uniform Nanocrystals via Hot-Injection and Heat-Up Methods. *Small* **2011,** *7* (19), 2685-2702.

(94) Coropceanu, I.; Rossinelli, A.; Caram, J. R.; Freyria, F. S.; Bawendi, M. G., Slow-Injection Growth of Seeded CdSe/CdS Nanorods with Unity Fluorescence Quantum Yield and Complete Shell to Core Energy Transfer. *ACS Nano* **2016,** *10* (3), 3295-3301.

(95) Jansons, A. W.; Hutchison, J. E., Continuous Growth of Metal Oxide Nanocrystals: Enhanced Control of Nanocrystal Size and Radial Dopant Distribution. *ACS Nano* **2016,** *10* (7), 6942-6951.

(96) Jansons, A. W.; Plummer, L. K.; Hutchison, J. E., Living Nanocrystals. *Chem. Mater.* **2017,** *29* (13), 5415-5425.

(97) Crockett, B. M.; Jansons, A. W.; Koskela, K. M.; Sharps, M. C.; Johnson, D. W.; Hutchison, J. E., Influence of Nanocrystal Size on the Optoelectronic Properties of Thin, Solution-Cast Sn-Doped In_2O_3 Films. *Chem. Mater.* **2019,** *31* (9), 3370-3380.

(98) Knecht, T. A.; Hutchison, J. E., Reaction Atmospheres and Surface Ligation Control Surface Reactivity and Morphology of Cerium Oxide Nanocrystals during Continuous Addition Synthesis. *Inorg. Chem.* **2022,** *61* (11), 4690-4704.

(99) Cobley, C. M.; Skrabalak, S. E.; Campbell, D. J.; Xia, Y., Shape-Controlled Synthesis of Silver Nanoparticles for Plasmonic and Sensing Applications. *Plasmonics* **2009,** *4* (2), 171-179.

(100) Langer, J.; Novikov, S. M.; Liz-Marzán, L. M., Sensing using plasmonic nanostructures and nanoparticles. *Nanotechnology* **2015,** *26* (32), 322001.

(101) Zeng, S.; Baillargeat, D.; Ho, H.-P.; Yong, K.-T., Nanomaterials enhanced surface plasmon resonance for biological and chemical sensing applications. *Chem. Soc. Rev.* **2014,** *43* (10), 3426-3452.

(102) Krivina, R. A.; Knecht, T. A.; Crockett, B. M.; Boettcher, S. W.; Hutchison, J. E., Sculpting Optical Properties of Thin Film IR Filters through Nanocrystal Synthesis and Additive, Solution Processing. *Chem. Mater.* **2020,** *32* (19), 8683-8693.

(103) Wang, Z.; Lin, C.-C.; Ho, Y.-L.; Xiang, R.; Maruyama, S.; Chen, C.-W.; Delaunay, J.-J., Self-Patterned CsPbBr3 Nanocrystal Based Plasmonic Hot-Carrier Photodetector at Telecommunications Wavelengths. *Advanced Optical Materials* **2021,** *9* (24), 2101474.

(104) Metzger, B.; Hentschel, M.; Giessen, H., Ultrafast Nonlinear Plasmonic Spectroscopy: From Dipole Nanoantennas to Complex Hybrid Plasmonic Structures. *ACS Photonics* **2016,** *3* (8), 1336-1350.

(105) Pattanayak, S.; Swarnkar, A.; Priyam, A.; Bhalerao, G. M., Citrate–hydrazine hydrogen-bonding driven single-step synthesis of tunable near-IR plasmonic, anisotropic silver nanocrystals: implications for SERS spectroscopy of inorganic oxoanions. *Dalton Transactions* **2014,** *43* (31), 11826-11833.

(106) Runnerstrom, E. L.; Llordés, A.; Lounis, S. D.; Milliron, D. J., Nanostructured electrochromic smart windows: traditional materials and NIR-selective plasmonic nanocrystals. *Chem. Commun.* **2014,** *50* (73), 10555-10572.

(107) Wang, Y.; Runnerstrom, E. L.; Milliron, D. J., Switchable Materials for Smart Windows. *Annual Review of Chemical and Biomolecular Engineering* **2016,** *7* (1), 283-304.

(108) Zhang, S.; Cao, S.; Zhang, T.; Lee, J. Y., Plasmonic Oxygen-Deficient TiO_{2-x} Nanocrystals for Dual-Band Electrochromic Smart Windows with Efficient Energy Recycling. *Adv. Mater.* **2020,** *32* (43), 2004686.

(109) Liu, Z.; Liu, X.; Du, Y.; Ren, J.; Qu, X., Using Plasmonic Copper Sulfide Nanocrystals as Smart Light-Driven Sterilants. *ACS Nano* **2015,** *9* (10), 10335-10346.

(110) Song, J.; Niu, G.; Chen, X., Amphiphilic-Polymer-Guided Plasmonic Assemblies and Their Biomedical Applications. *Bioconjugate Chem.* **2017,** *28* (1), 105-114.

(111) Knecht, T. A.; Boettcher, S. W.; Hutchison, J. E., Electrochemistry-Induced Restructuring of Tin-Doped Indium Oxide Nanocrystal Films of Relevance to CO_2 Reduction. *J. Electrochem. Soc.* **2021,** *168* (12), 126521.

(112) Baruch, M. F.; Pander, J. E.; White, J. L.; Bocarsly, A. B., Mechanistic Insights into the Reduction of CO_2 on Tin Electrodes using in Situ ATR-IR Spectroscopy. *ACS Catal.* **2015,** *5* (5), 3148-3156.

(113) Pander, J. E.; Baruch, M. F.; Bocarsly, A. B., Probing the Mechanism of Aqueous CO2 Reduction on Post-Transition-Metal Electrodes using ATR-IR Spectroelectrochemistry. *ACS Catal.* **2016,** *6* (11), 7824-7833.

(114) White, J. L.; Bocarsly, A. B., Enhanced Carbon Dioxide Reduction Activity on Indium-Based Nanoparticles. *J. Electrochem. Soc.* **2016,** *163* (6), H410-H416.

(115) Chen, Y.; Kanan, M. W., Tin Oxide Dependence of the CO2 Reduction Efficiency on Tin Electrodes and Enhanced Activity for Tin/Tin Oxide Thin-Film Catalysts. *J. Am. Chem. Soc.* **2012,** *134* (4), 1986-1989.

(116) Huang, Y.; Mao, X.; Yuan, G.; Zhang, D.; Pan, B.; Deng, J.; Shi, Y.; Han, N.; Li, C.; Zhang, L.; Wang, L.; He, L.; Li, Y.; Li, Y., Size-Dependent Selectivity of Electrochemical CO2 Reduction on Converted In_2O_3 Nanocrystals. *Angew. Chem. Int. Ed.* **2021,** *60* (29), 15844-15848.

(117) Pérez, L. C. P.; Teschner, D.; Willinger, E.; Guiet, A.; Driess, M.; Strasser, P.; Fischer, A., In Situ Formed "$Sn_{1-X}In_X$@$In_{1-Y}Sn_YO_Z$" Core@Shell Nanoparticles as Electrocatalysts for CO_2 Reduction to Formate. *Adv. Funct. Mater.* **2021**, 2103601-2103601.

(118) Gregorio, G. L. D.; Burdyny, T.; Loiudice, A.; Iyengar, P.; Smith, W. A.; Buonsanti, R., Facet-Dependent Selectivity of Cu Catalysts in Electrochemical CO_2 Reduction at Commercially Viable Current Densities. *ACS Catal.* **2020,** *10* (9), 4854-4862.

(119) Loiudice, A.; Lobaccaro, P.; Kamali, E. A.; Thao, T.; Huang, B. H.; Ager, J. W.; Buonsanti, R., Tailoring Copper Nanocrystals towards C_2 Products in Electrochemical CO_2 Reduction. *Angew. Chem. Int. Ed.* **2016,** *55* (19), 5789-5792.

Chapter II

(1) Sajanlal, P. R.; Sreeprasad, T. S.; Samal, A. K.; Pradeep, T., Anisotropic Nanomaterials: Structure, Growth, Assembly, and Functions. *Nano Rev.* **2011,** *2* (1), 5883-5883.

(2) Trovarelli, A.; Llorca, J., Ceria Catalysts at Nanoscale: How Do Crystal Shapes Shape Catalysis? *ACS Catal.* **2017,** *7* (7), 4716-4735.

(3) Cooper, S. R.; Candler, R. O.; Cosby, A. G.; Johnson, D. W.; Jensen, K. M. Ø.; Hutchison, J. E., Evolution of Atomic-Level Structure in Sub-10 Nanometer Iron Oxide Nanocrystals: Influence on Cation Occupancy and Growth Rates. *ACS Nano* **2020,** *14* (5), 5480-5490.

(4) Cooper, S. R.; Plummer, L. K.; Cosby, A. G.; Lenox, P.; Jander, A.; Dhagat, P.; Hutchison, J. E., Insights into the Magnetic Properties of Sub-10 nm Iron Oxide Nanocrystals through the Use of a Continuous Growth Synthesis. *Chem. Mater.* **2018,** *30* (17), 6053-6062.

(5) Jansons, A. W.; Koskela, K. M.; Crockett, B. M.; Hutchison, J. E., Transition Metal-Doped Metal Oxide Nanocrystals: Efficient Substitutional Doping through a Continuous Growth Process. *Chem. Mater.* **2017,** *29* (19), 8167-8176.

(6) Crockett, B. M.; Jansons, A. W.; Koskela, K. M.; Johnson, D. W.; Hutchison, J. E., Radial Dopant Placement for Tuning Plasmonic Properties in Metal Oxide Nanocrystals. *ACS Nano* **2017,** *11* (8), 7719-7728.

(7) Pacchioni, G., Oxygen Vacancy: The Invisible Agent on Oxide Surfaces. *ChemPhysChem* **2003,** *4* (10), 1041-1047.

(8) Liu, X.; Zhou, K.; Wang, L.; Wang, B.; Li, Y., Oxygen Vacancy Clusters Promoting Reducibility and Activity of Ceria Nanorods. *J. Am. Chem. Soc.* **2009,** *131* (9), 3140-3141.

(9) Babu, S.; Thanneeru, R.; Inerbaev, T.; Day, R.; Masunov, A. E.; Schulte, A.; Seal, S., Dopant-Mediated Oxygen Vacancy Tuning in Ceria Nanoparticles. *Nanotechnology* **2009,** *20* (8), 085713-085713.

(10) Migani, A.; Vayssilov, G. N.; Bromley, S. T.; Illas, F.; Neyman, K. M., Dramatic Reduction of the Oxygen Vacancy Formation Energy in Ceria Particles: A Possible Key to their Remarkable Reactivity at the Nanoscale. *J. Mater. Chem.* **2010,** *20* (46), 10535-10546.

(11) Yang, S. C.; Su, W. N.; Rick, J.; Lin, S. D.; Liu, J. Y.; Pan, C. J.; Lee, J. F.; Hwang, B. J., Oxygen Vacancy Engineering of Cerium Oxides for Carbon Dioxide Capture and Reduction. *ChemSusChem* **2013,** *6* (8), 1326-1329.

(12) Della Mea, G. B.; Matte, L. P.; Thill, A. S.; Lobato, F. O.; Benvenutti, E. V.; Arenas, L. T.; Jürgensen, A.; Hergenröder, R.; Poletto, F.; Bernardi, F., Tuning the Oxygen Vacancy Population of Cerium Oxide (CeO_{2-x}, $0 < x < 0.5$) Nanoparticles. *Appl. Surf. Sci.* **2017,** *422*, 1102-1112.

(13) Ma, Y.; Gao, W.; Zhang, Z.; Zhang, S.; Tian, Z.; Liu, Y.; Ho, J. C.; Qu, Y., Regulating the Surface of Nanoceria and its Applications in Heterogeneous Catalysis. *Surf. Sci. Rep.* **2018,** *73* (1), 1-36.

(14) Gunawan, C.; Lord, M. S.; Lovell, E.; Wong, R. J.; Jung, M. S.; Oscar, D.; Mann, R.; Amal, R., Oxygen-Vacancy Engineering of Cerium-Oxide Nanoparticles for Antioxidant Activity. *ACS Omega* **2019,** *4* (5), 9473-9479.

(15) Mehmood, R.; Mofarah, S. S.; Chen, W. F.; Koshy, P.; Sorrell, C. C., Surface, Subsurface, and Bulk Oxygen Vacancies Quantified by Decoupling and Deconvolution of the Defect Structure of Redox-Active Nanoceria. *Inorg. Chem.* **2019,** *58* (9), 6016-6027.

(16) Taniguchi, T.; Katsumata, K. I.; Omata, S.; Okada, K.; Matsushita, N., Tuning Growth Modes of Ceria-Based Nanocubes by a Hydrothermal Method. *Cryst. Growth Des.* **2011,** *11* (9), 3754-3760.

(17) Makinose, Y.; Taniguchi, T.; Katsumata, K. I.; Okada, K.; Matsushita, N., Facet Control of Ceria Nanocrystals Synthesized by an Oleate-Modified Hydrothermal Method. *Adv. Powder Technol.* **2016,** *27* (1), 64-71.

(18) Zhang, L.; Shen, Y., One-Pot Synthesis of Platinum-Ceria/Graphene Nanosheet as Advanced Electrocatalysts for Alcohol Oxidation. *ChemElectroChem* **2015,** *2* (6), 887-895.

(19) Laga, S. M.; Townsend, T. M.; O'Connor, A. R.; Mayer, J. M., Cooperation of Cerium Oxide Nanoparticles and Soluble Molecular Catalysts for Alcohol Oxidation. *Inorg. Chem. Front.* **2020,** *7* (6), 1386-1393.

(20) He, Q.; Mukerjee, S.; Shyam, B.; Ramaker, D.; Parres-Esclapez, S.; Illán-Gómez, M. J.; Bueno-López, A., Promoting Effect of CeO_2 in the Electrocatalytic Activity of Rhodium for Ethanol Electro-Oxidation. *J. Power Sources* **2009,** *193* (2), 408-415.

(21) Zhao, J.; Chen, W.; Zheng, Y., Effect of Ceria on Carbon Supported Platinum Catalysts for Methanol Electrooxidation. *Mater. Chem. Phys.* **2009,** *113* (2-3), 591-595.

(22) Uhm, S.; Yi, Y.; Lee, J., Electrocatalytic Activity of Pd-CeO_2 Nanobundle in an Alkaline Ethanol Oxidation. *Catal. Lett.* **2010,** *138* (1-2), 46-49.

(23) Guzman, J.; Carrettin, S.; Corma, A., Spectroscopic Evidence for the Supply of Reactive Oxygen During CO Oxidation Catalyzed by Gold Supported on Nanocrystalline CeO_2. *J. Am. Chem. Soc.* **2005,** *127* (10), 3286-3287.

(24) Wu, K.; Sun, L. D.; Yan, C. H., Recent Progress in Well-Controlled Synthesis of Ceria-Based Nanocatalysts towards Enhanced Catalytic Performance. *Advanced Energy Materials* **2016,** *6* (17), 1600501-1600501.

(25) Lykaki, M.; Pachatouridou, E.; Iliopoulou, E.; Carabineiro, S. A. C.; Konsolakis, M., Impact of the Synthesis Parameters on the Solid State Properties and the CO Oxidation Performance of Ceria Nanoparticles. *RSC Adv.* **2017,** *7* (10), 6160-6169.

(26) Elias, J. S.; Stoerzinger, K. A.; Hong, W. T.; Risch, M.; Giordano, L.; Mansour, A. N.; Shao-Horn, Y., In Situ Spectroscopy and Mechanistic Insights into CO Oxidation on Transition-Metal-Substituted Ceria Nanoparticles. *ACS Catal.* **2017,** *7* (10), 6843-6857.

(27) Kumari, N.; Haider, M. A.; Agarwal, M.; Sinha, N.; Basu, S., Role of Reduced CeO_2(110) Surface for CO_2 Reduction to CO and Methanol. *J. Phys. Chem. C* **2016,** *120* (30), 16626-16635.

(28) Gao, D.; Zhang, Y.; Zhou, Z.; Cai, F.; Zhao, X.; Huang, W.; Li, Y.; Zhu, J.; Liu, P.; Yang, F.; Wang, G.; Bao, X., Enhancing CO_2 Electroreduction with the Metal-Oxide Interface. *J. Am. Chem. Soc.* **2017,** *139* (16), 5652-5655.

(29) Wang, Y.; Chen, Z.; Han, P.; Du, Y.; Gu, Z.; Xu, X.; Zheng, G., Single-Atomic Cu with Multiple Oxygen Vacancies on Ceria for Electrocatalytic CO_2 Reduction to CH_4. *ACS Catal.* **2018,** *8* (8), 7113-7119.

(30) Verlato, E.; Barison, S.; Einaga, Y.; Fasolin, S.; Musiani, M.; Nasi, L.; Natsui, K.; Paolucci, F.; Valenti, G., CO_2 Reduction to Formic Acid at Low Overpotential on BDD Electrodes Modified with Nanostructured CeO_2. *J. Mater. Chem. A.* **2019,** *7* (30), 17896-17905.

(31) Özkan, E.; Cop, P.; Benfer, F.; Hofmann, A.; Votsmeier, M.; Guerra, J. M.; Giar, M.; Heiliger, C.; Over, H.; Smarsly, B. M., Rational Synthesis Concept for Cerium Oxide Nanoparticles: On the Impact of Particle Size on the Oxygen Storage Capacity. *J. Phys. Chem. C* **2020,** *124* (16), 8736-8748.

(32) Lee, S. S.; Zhu, H.; Contreras, E. Q.; Prakash, A.; Puppala, H. L.; Colvin, V. L., High Temperature Decomposition of Cerium Precursors to Form Ceria Nanocrystal Libraries for Biological Applications. *Chem. Mater.* **2012,** *24* (3), 424-432.

(33) Lee, S. S.; Song, W.; Cho, M.; Puppala, H. L.; Nguyen, P.; Zhu, H.; Segatori, L.; Colvin, V. L., Antioxidant Properties of Cerium Oxide Nanocrystals as a Function of Nanocrystal Diameter and Surface Coating. *ACS Nano* **2013,** *7* (11), 9693-9703.

(34) Tsurugi, H.; Mashima, K., Renaissance of Homogeneous Cerium Catalysts with Unique Ce(IV/III) Couple: Redox-Mediated Organic Transformations Involving Homolysis of Ce(IV)−Ligand Covalent Bonds.

(35) Zhou, K.; Yang, Z.; Yang, S., Highly Reducible CeO_2 Nanotubes. *Chem. Mater.* **2007,** *19* (6), 1215-1217.

(36) Sreeremya, T. S.; Krishnan, A.; Remani, K. C.; Patil, K. R.; Brougham, D. F.; Ghosh, S., Shape-Selective Oriented Cerium Oxide Nanocrystals Permit Assessment of the Effect of the Exposed Facets on Catalytic Activity and Oxygen Storage Capacity. *ACS Appl. Mater. Interfaces* **2015,** *7* (16), 8545-8555.

(37) Yu, Y.; Wang, X.; Gao, W.; Li, P.; Yan, W.; Wu, S.; Cui, Q.; Song, W.; Ding, K., Trivalent Cerium-Preponderant CeO_2/Graphene Sandwich-Structured Nanocomposite with Greatly Enhanced Catalytic Activity for the Oxygen Reduction Reaction. *J. Mater. Chem. A.* **2017,** *5* (14), 6656-6663.

(38) Dvor, F.; Szabova, L.; Joha, V.; Farnesi Camellone, M.; Stetsovych, V.; Vorokhta, M.; Tovt, A.; Matolínova, I.; Tateyama, Y.; Myslivec, J.; Fabris, S.; Matolín, V., Bulk Hydroxylation and Effective Water Splitting by Highly Reduced Cerium Oxide: The Role of O Vacancy Coordination. *ACS Catal.* **2018,** *8* (5), 4354-4363.

(39) Wu, Z.; Mann, A. K. P.; Li, M.; Overbury, S. H., Spectroscopic Investigation of Surface Dependent Acid Base Property of Ceria Nanoshapes. *J. Phys. Chem. C* **2015,** *119* (13), 7340-7350.

(40) Mai, H. X.; Sun, L. D.; Zhang, Y. W.; Si, R.; Feng, W.; Zhang, H. P.; Liu, H. C.; Yan, C. H., Shape-Selective Synthesis and Oxygen Storage Behavior of Ceria Nanopolyhedra, Nanorods, and Nanocubes. *J. Phys. Chem. B* **2005,** *109* (51), 24380-24385.

(41) Wu, Q.; Zhang, F.; Xiao, P.; Tao, H.; Wang, X.; Hu, Z.; Lü, Y., Great Influence of Anions for Controllable Synthesis of CeO_2 Nanostructures: From Nanorods to Nanocubes. *J. Phys. Chem. C* **2008,** *112* (44), 17076-17080.

(42) Sakthivel, T.; Das, S.; Kumar, A.; Reid, D. L.; Gupta, A.; Sayle, D. C.; Seal, S., Morphological Phase Diagram of Biocatalytically Active Ceria Nanostructures as a Function of Processing Variables and their Properties. *ChemPlusChem* **2013,** *78* (12), 1446-1455.

(43) Berestok, T.; Guardia, P.; Blanco, J.; Nafria, R.; Torruella, P.; López-Conesa, L.; Estradé, S.; Ibáñez, M.; De Roo, J.; Luo, Z.; Cadavid, D.; Martins, J. C.; Kovalenko, M. V.; Peiró, F.; Cabot, A., Tuning Branching in Ceria Nanocrystals. *Chem. Mater.* **2017,** *29* (10), 4418-4424.

(44) Wang, W.; Howe, J. Y.; Li, Y.; Qiu, X.; Joy, D. C.; Parans Paranthaman, M.; Doktycz de, M. J.; Gu, B., A Surfactant and Template-Free Route for Synthesizing Ceria Nanocrystals with Tunable Morphologies. *J. Mater. Chem.* **2010,** *20* (36), 7776-7781.

(45) Yada, M.; Sakai, S.; Torikai, T.; Watari, T.; Furuta, S.; Katsuki, H., Cerium Compound Nanowires and Nanorings Templated by Mixed Organic Molecules. *Adv. Mater.* **2004,** *16* (14), 1222-1226.

(46) Tang, B.; Zhuo, L.; Ge, J.; Wang, G.; Shi, Z.; Niu, J., A Surfactant-Free Route to Single-Crystalline CeO_2 Nanowires. *Chem. Commun.* **2005,** (28), 3565-3567.

(47) Ho, C.; Yu, J. C.; Kwong, T.; Mak, A. C.; Lai, S., Morphology-Controllable Synthesis of Mesoporous CeO_2 Nano- and Microstructures. *Chem. Mater.* **2005,** *17* (17), 4514-4522.

(48) Du, N.; Zhang, H.; Chen, B.; Ma, X.; Yang, D., Ligand-Free Self-Assembly of Ceria Nanocrystals into Nanorods by Oriented Attachment at Low Temperature. *J. Phys. Chem. C* **2007,** *111* (34), 12677-12680.

(49) Yang, Y.; Jin, Y.; He, H.; Ye, Z., Facile Synthesis and Characterization of Ultrathin Cerium Oxide Nanorods. *CrystEngComm* **2010,** *12* (10), 2663-2665.

(50) Lin, H. L.; Wu, C. Y.; Chiang, R. K., Facile Synthesis of CeO_2 Nanoplates and Nanorods by [100] Oriented Growth. *J. Colloid Interface Sci.* **2010,** *341* (1), 12-17.

(51) Lu, X.; Zhai, T.; Cui, H.; Shi, J.; Xie, S.; Huang, Y.; Liang, C.; Tong, Y., Redox Cycles Promoting Photocatalytic Hydrogen Evolution of CeO_2 Nanorods. *J. Mater. Chem.* **2011,** *21* (15), 5569-5572.

(52) Araújo, V. D.; Avansi, W.; De Carvalho, H. B.; Moreira, M. L.; Longo, E.; Ribeiro, C.; Bernardi, M. I. B., CeO_2 Nanoparticles Synthesized by a Microwave-Assisted Hydrothermal Method: Evolution from Nanospheres to Nanorods. *CrystEngComm* **2012,** *14* (3), 1150-1154.

(53) Zhou, H. P.; Zhang, Y. W.; Mai, H. X.; Sun, X.; Liu, Q.; Song, W. G.; Yan, C. H., Spontaneous Organization of Uniform CeO_2 Nanoflowers by 3D Oriented Attachment in Hot Surfactant Solutions Monitored with an In Situ Electrical Conductance Technique. *Chem. Eur. J.* **2008,** *14* (11), 3380-3390.

(54) Yu, R.; Yan, L.; Zheng, P.; Chen, J.; Xing, X., Controlled Synthesis of CeO_2 Flower-like and Well-aligned Nanorod Hierarchical Architectures by a Phosphate-Assisted Hydrothermal Route. *J. Phys. Chem. C* **2008,** *112* (50), 19896-19900.

(55) Yu, T.; Joo, J.; Park, Y. I.; Hyeon, T., Large-Scale Nonhydrolytic Sol-Gel Synthesis of Uniform-Sized Ceria Nanocrystals with Spherical, Wire, and Tadpole Shapes. *Angew. Chem. Int. Ed.* **2005,** *44* (45), 7411-7414.

(56) Kamruddin, M.; Ajikumar, P. K.; Nithya, R.; Tyagi, A. K.; Raj, B., Synthesis of Nanocrystalline Ceria by Thermal Decomposition and Soft-Chemistry Methods. *Scripta Mater.* **2004,** *50* (4), 417-422.

(57) Chen, S. Y.; Lu, Y. H.; Huang, T. W.; Yan, D. C.; Dong, C. L., Oxygen Vacancy Dependent Magnetism of CeO_2 Nanoparticles Prepared by Thermal Decomposition Method. *J. Phys. Chem. C* **2010,** *114* (46), 19576-19581.

(58) Plummer, L. K.; Hutchison, J. E., Understanding the Effects of Iron Precursor Ligation and Oxidation State Leads to Improved Synthetic Control for Spinel Iron Oxide Nanocrystals. *Inorg. Chem.* **2020,** *59* (20), 15074-15087.

(59) Krishnan, A.; Sreeremya, T. S.; Murray, E.; Ghosh, S., One-Pot Synthesis of Ultra-Small Cerium Oxide Nanodots Exhibiting Multi-Colored Fluorescence. *J. Colloid Interface Sci.* **2013,** *389* (1), 16-22.

(60) Krishnan, A.; Sreeremya, T. S.; Ghosh, S., Morphological Evolution and Growth of Cerium Oxide Nanostructures by Virtue of Organic Ligands as Well as Monomer Concentration. *CrystEngComm* **2015,** *17* (37), 7094-7106.

(61) Jansons, A. W.; Plummer, L. K.; Hutchison, J. E., Living Nanocrystals. *Chem. Mater.* **2017,** *29* (13), 5415-5425.

(62) Ito, D.; Yokoyama, S.; Zaikova, T.; Masuko, K.; Hutchison, J. E., Synthesis of Ligand-Stabilized Metal Oxide Nanocrystals and Epitaxial Core/Shell Nanocrystals via a Lower-Temperature Esterification Process. *ACS Nano* **2014,** *8* (1), 64-75.

(63) Jansons, A. W.; Hutchison, J. E., Continuous Growth of Metal Oxide Nanocrystals: Enhanced Control of Nanocrystal Size and Radial Dopant Distribution. *ACS Nano* **2016,** *10* (7), 6942-6951.

(64) Crockett, B. M.; Jansons, A. W.; Koskela, K. M.; Sharps, M. C.; Johnson, D. W.; Hutchison, J. E., Influence of Nanocrystal Size on the Optoelectronic Properties of Thin, Solution-Cast Sn-Doped In_2O_3 Films. *Chem. Mater.* **2019,** *31* (9), 3370-3380.

(65) Plummer, L. K.; Crockett, B. M.; Pennel, M. L.; Jansons, A. W.; Koskela, K. M.; Hutchison, J. E., Influence of Monomer Flux and Temperature on Morphology of Indium Oxide Nanocrystals during a Continuous Growth Synthesis. *Chem. Mater.* **2019,** *31* (18), 7638-7649.

(66) Gu, H.; Soucek, M. D., Preparation and Characterization of Monodisperse Cerium Oxide Nanoparticles in Hydrocarbon Solvents. *Chem. Mater.* **2007,** *19* (5), 1103-1110.

(67) Álvarez-Asencio, R.; Corkery, R. W.; Ahniyaz, A., Solventless Synthesis of Cerium Oxide Nanoparticles and their Application in UV Protective Clear Coatings. *RSC Adv.* **2020,** *10* (25), 14818-14825.

(68) Marques, E. F.; Burrows, H. D.; Miguel, M. D. G., The Structure and Thermal Behaviour of Some Long Chain Cerium(III) Carboxylates. *J. Chem. Soc., Faraday Trans.* **1998,** *94* (12), 1729-1736.

(69) Otero, V.; Sanches, D.; Montagner, C.; Vilarigues, M.; Carlyle, L.; Lopes, J. A.; Melo, M. J., Characterization of Metal Carboxylates by Raman and Infrared Spectroscopy in Works of Art. *J. Raman Spectrosc.* **2014,** *45* (11-12), 1197-1206.

(70) Palacios, E. G.; Juárez-López, G.; Monhemius, A. J., Infrared Spectroscopy of Metal Carboxylates: II. Analysis of Fe(III), Ni and Zn Carboxylate Solutions. *Hydrometallurgy* **2004,** *72* (1-2), 139-148.

(71) Sutton, C. C. R.; Da Silva, G.; Franks, G. V., Modeling the IR Spectra of Aqueous Metal Carboxylate Complexes: Correlation Between Bonding Geometry and Stretching Mode Wavenumber Shifts. *Chem. Eur. J.* **2015,** *21* (18), 6801-6805.

(72) Bokhonov, B. B.; Matvienko, A. A.; Gerasimov, K. B.; Dudina, D. V., Formation of ordered nanocrystalline CeO_2 structures during thermal decomposition of cerium formate $Ce(HCOO)_3$. *Ceram. Int.* **2019,** *45* (16), 19684-19688.

(73) Yan, G.; Wang, Y.; Zhang, Z.; Li, J.; Carlos, C.; German, L. N.; Zhang, C.; Wang, J.; Voyles, P. M.; Wang, X., Enhanced Ferromagnetism from Organic–Cerium Oxide Hybrid Ultrathin Nanosheets. *ACS Applied Materials & Interfaces* **2019,** *11* (47), 44601-44608.

(74) Jiang, S.; Zhang, R.; Liu, H.; Rao, Y.; Yu, Y.; Chen, S.; Yue, Q.; Zhang, Y.; Kang, Y., Promoting Formation of Oxygen Vacancies in Two-Dimensional Cobalt-Doped Ceria Nanosheets for Efficient Hydrogen Evolution. *J. Am. Chem. Soc.* **2020,** *142* (14), 6461-6466.

(75) Marani, D.; Moraes, L. P. R.; Gualandris, F.; Sanna, S.; de Florio, D. Z.; Esposito, V.; Fonseca, F. C., Nucleation front instability in two-dimensional (2D) nanosheet gadolinium-doped cerium oxide (CGO) formation. *CrystEngComm* **2018,** *20* (10), 1405-1410.

(76) Liz-Marzán, L. M.; Kagan, C. R.; Millstone, J. E., Reproducibility in Nanocrystal Synthesis? Watch out for Impurities! *ACS Nano* **2020,** *14* (6), 6359-6361.

(77) Anwander, R.; Dolg, M.; Edelmann, F. T., The Difficult Search for Organocerium(IV) Compounds. *Chem. Soc. Rev.* **2017,** *46* (22), 6697-6709.

(78) Xu, Y.; Mofarah, S. S.; Mehmood, R.; Cazorla, C.; Koshy, P.; Sorrell, C. C., Design Sstrategies for Ceria Nanomaterials: Untangling Key Mechanistic Concepts. *Mater. Horiz.* **2020**.

(79) Eloirdi, R.; Cakir, P.; Huber, F.; Seibert, A.; Konings, R.; Gouder, T., X-ray Photoelectron Spectroscopy Study of the Reduction and Oxidation of Uranium and Cerium Single Oxide Compared to (U-Ce) Mixed Oxide Films. *Appl. Surf. Sci.* **2018,** *457*, 566-571.

(80) Zhu, Y.; Jain, N.; Hudait, M. K.; Maurya, D.; Varghese, R.; Priya, S., X-ray Photoelectron Spectroscopy Analysis and Band Offset Determination of CeO_2 Deposited on Epitaxial (100), (110), and (111) Ge. *J. Vac. Sci. Technol., B* **2014,** *32* (1), 011217.

(81) Paparazzo, E., Use and Mis-use of X-ray Photoemission Spectroscopy Ce3d Spectra of Ce_2O_3 and CeO_2. *J. Phys.: Condens. Matter* **2018,** *30* (34), 343003.

(82) Terribile, D.; Trovarelli, A.; Llorca, J.; De Leitenburg, C.; Dolcetti, G., The Synthesis and Characterization of Mesoporous High-Surface Area Ceria Prepared using a Hybrid Organic/Inorganic Route. *J. Catal.* **1998,** *178* (1), 299-308.

(83) Kurian, M.; Joys, M., Properties of Nanoceria Particles: Comparison Among Thermal and Microwave Mediated Synthesis. *AIP Conf Proc* **2020,** *2263*, 50009-50009.

(84) Liu, Z.; Li, X.; Mayyas, M.; Koshy, P.; Hart, J. N.; Sorrell, C. C., Growth Mechanism of Ceria Nanorods by Precipitation at Room Temperature and Morphology-Dependent Photocatalytic Performance. *CrystEngComm* **2017,** *19* (32), 4766-4776.

(85) Dhaene, E.; Billet, J.; Bennett, E.; Van Driessche, I.; De Roo, J., The Trouble with ODE: Polymerization during Nanocrystal Synthesis. *Nano Lett.* **2019,** *19* (10), 7411-7417.

(86) Hay, N. E.; Kochi, J. K., Cerium(IV) Acetate. *J. Inorg. Nucl. Chem.* **1968,** *30*, 884-886.

(87) Shirase, S.; Tamaki, S.; Shinohara, K.; Hirosawa, K.; Tsurugi, H.; Satoh, T.; Mashima, K., Cerium(IV) Carboxylate Photocatalyst for Catalytic Radical Formation from Carboxylic Acids: Decarboxylative Oxygenation of Aliphatic Carboxylic Acids and Lactonization of Aromatic Carboxylic Acids. *J. Am. Chem. Soc.* **2020,** *142* (12), 5668-5675.

(88) Huntelaar, M. E.; Booij, A. S.; Cordfunke, E. H. P.; van der Laan, R. R.; van Genderen, A. C. G.; van Miltenburg, J. C., The Thermodynamic Properties of Ce_2O_3(s) from T→ 0 K to 1500 K. *J. Chem. Thermodyn.* **2000,** *32* (4), 465-482.

(89) Hudry, D.; Abeykoon, A. M. M.; Hoy, J.; Sfeir, M. Y.; Stach, E. A.; Dickerson, J. H., Ultrathin Europium Oxide Nanoplatelets: Hidden Parameters and Controlled Synthesis, Unusual Crystal Structure, and Photoluminescence Properties. *Chem. Mater.* **2015,** *27* (3), 965-974.

(90) Riedinger, A.; Ott, F. D.; Mule, A.; Mazzotti, S.; Knüsel, P. N.; Kress, S. J. P.; Prins, F.; Erwin, S. C.; Norris, D. J., An Intrinsic Growth Instability in Isotropic Materials Leads to Quasi-Two-Dimensional Nanoplatelets. *Nat. Mater.* **2017,** *16* (7), 743-748.

(91) Houtepen, A. J.; Koole, R.; Vanmaekelbergh, D.; Meeldijk, J.; Hickey, S. G., The Hidden Role of Acetate in the PbSe Nanocrystal Synthesis. *J. Am. Chem. Soc.* **2006,** *128* (21), 6792-6793.

(92) Zhang, L.; Kang, W.; Ma, Q.; Xie, Y.; Jia, Y.; Deng, N.; Zhang, Y.; Ju, J.; Cheng, B., Two-Dimensional Acetate-Based Light Lanthanide Fluoride Nanomaterials (F–Ln, Ln = La, Ce, Pr, and Nd): Morphology, Structure, Growth Mechanism, and Stability. *J. Am. Chem. Soc.* **2019,** *141* (33), 13134-13142.

(93) Zhang, J.; Naka, T.; Ohara, S.; Kaneko, K.; Trevethan, T.; Shluger, A.; Adschiri, T., Surface Ligand Assisted Valence Change in Ceria Nanocrystals. *Physical Review B* **2011,** *84* (4), 45411-45411.

(94) Tandra Ghoshal; G. Fleming, P.; D. Holmes, J.; A. Morris, M., The Stability of "Ce_2O_3" Nanodots in Ambient Conditions: a Study Using Block Copolymer Templated Structures. *J. Mater. Chem.* **2012,** *22* (43), 22949-22957.

(95) Zhu, L.; Jin, X.; Zhang, Y.-Y.; Du, S.; Liu, L.; Rajh, T.; Xu, Z.; Wang, W.; Bai, X.; Wen, J.; Wang, L., Visualizing Anisotropic Oxygen Diffusion in Ceria under Activated Conditions. *Phys. Rev. Lett.* **2020,** *124* (5), 056002.

Chapter III

(1) Bøjesen, E. D.; Iversen, B. B., The chemistry of nucleation. *CrystEngComm* **2016,** *18* (43), 8332-8353.

(2) Deshmukh, R.; Niederberger, M., Mechanistic Aspects in the Formation, Growth and Surface Functionalization of Metal Oxide Nanoparticles in Organic Solvents. *Chemistry – A European Journal* **2017,** *23* (36), 8542-8570.

(3) Jin, B.; Liu, Z.; Tang, R., Recent experimental explorations of non-classical nucleation. *CrystEngComm* **2020,** *22* (24), 4057-4073.

(4) Jun, Y.-S.; Zhu, Y.; Wang, Y.; Ghim, D.; Wu, X.; Kim, D.; Jung, H., Classical and Nonclassical Nucleation and Growth Mechanisms for Nanoparticle Formation. *Annu. Rev. Phys. Chem.* **2022**.

(5) Kwon, S. G.; Hyeon, T., Formation Mechanisms of Uniform Nanocrystals via Hot-Injection and Heat-Up Methods. *Small* **2011,** *7* (19), 2685-2702.

(6) Lee, J.; Yang, J.; Kwon, S. G.; Hyeon, T., Nonclassical nucleation and growth of inorganic nanoparticles. *Nature Reviews Materials* **2016,** *1* (8), 16034.

(7) Owen, J. S.; Chan, E. M.; Liu, H.; Alivisatos, A. P., Precursor Conversion Kinetics and the Nucleation of Cadmium Selenide Nanocrystals. *J. Am. Chem. Soc.* **2010,** *132* (51), 18206-18213.

(8) Hendricks, M. P.; Cossairt, B. M.; Owen, J. S., The Importance of Nanocrystal Precursor Conversion Kinetics: Mechanism of the Reaction between Cadmium Carboxylate and Cadmium Bis(diphenyldithiophosphinate). *ACS Nano* **2012,** *6* (11), 10054-10062.

(9) Lester, E.; Aksomaityte, G.; Li, J.; Gomez, S.; Gonzalez-Gonzalez, J.; Poliakoff, M., Controlled continuous hydrothermal synthesis of cobalt oxide (Co3O4) nanoparticles. *Prog. Cryst. Growth Charact. Mater.* **2012,** *58* (1), 3-13.

(10) Sasani Ghamsari, M.; Mehranpour, H.; Askari, M., Temperature effect on the nucleation and growth of TiO2 colloidal nanoparticles. *Nanochemistry Research* **2017,** *2* (1), 132-139.

(11) Abécassis, B.; Testard, F.; Kong, Q.; Francois, B.; Spalla, O., Influence of Monomer Feeding on a Fast Gold Nanoparticles Synthesis: Time-Resolved XANES and SAXS Experiments. *Langmuir* **2010,** *26* (17), 13847-13854.

(12) Sharifi Dehsari, H.; Heidari, M.; Halda Ribeiro, A.; Tremel, W.; Jakob, G.; Donadio, D.; Potestio, R.; Asadi, K., Combined Experimental and Theoretical Investigation of Heating Rate on Growth of Iron Oxide Nanoparticles. *Chem. Mater.* **2017,** *29* (22), 9648-9656.

(13) Franke, D.; Harris, D. K.; Xie, L.; Jensen, K. F.; Bawendi, M. G., The Unexpected Influence of Precursor Conversion Rate in the Synthesis of III–V Quantum Dots. *Angew. Chem. Int. Ed.* **2015,** *54* (48), 14299-14303.

(14) Chen, X.; Schröder, J.; Hauschild, S.; Rosenfeldt, S.; Dulle, M.; Förster, S., Simultaneous SAXS/WAXS/UV–Vis Study of the Nucleation and Growth of Nanoparticles: A Test of Classical Nucleation Theory. *Langmuir* **2015,** *31* (42), 11678-11691.

(15) Niederberger, M.; Garnweitner, G., Organic Reaction Pathways in the Nonaqueous Synthesis of Metal Oxide Nanoparticles. *Chemistry – A European Journal* **2006,** *12* (28), 7282-7302.

(16) Pinna, N.; Garnweitner, G.; Antonietti, M.; Niederberger, M., A general nonaqueous route to binary metal oxide nanocrystals involving a C-C bond cleavage. *J. Am. Chem. Soc.* **2005,** *127* (15), 5608-5612.

(17) Wainer, P.; Kendall, O.; Lamb, A.; Barrow, S. J.; Tricoli, A.; Gómez, D. E.; van Embden, J.; Della Gaspera, E., Continuous Growth Synthesis of Zinc Oxide Nanocrystals with Tunable Size and Doping. *Chem. Mater.* **2019,** *31* (23), 9604-9613.

(18) Dinh, C. T.; Nguyen, T. D.; Kleitz, F.; Do, T. O., Shape-controlled synthesis of highly crystalline titania nanocrystals. *ACS Nano* **2009,** *3* (11), 3737-3743.

(19) Mourdikoudis, S.; Liz-Marzán, L. M., Oleylamine in Nanoparticle Synthesis. *Chem. Mater.* **2013,** *25* (9), 1465-1476.

(20) Wu, H.; Yang, Y.; Charles Cao, Y., Synthesis of Colloidal Uranium−Dioxide Nanocrystals. *J. Am. Chem. Soc.* **2006,** *128* (51), 16522-16523.

(21) Krishnan, A.; Sreeremya, T. S.; Murray, E.; Ghosh, S., One-Pot Synthesis of Ultra-Small Cerium Oxide Nanodots Exhibiting Multi-Colored Fluorescence. *J. Colloid Interface Sci.* **2013,** *389* (1), 16-22.

(22) Zhang, Z.; Zhong, X.; Liu, S.; Li, D.; Han, M., Aminolysis route to monodisperse titania nanorods with tunable aspect ratio. *Angewandte Chemie - International Edition* **2005,** *44* (22), 3466-3470.

(23) Cooper, S. R.; Candler, R. O.; Cosby, A. G.; Johnson, D. W.; Jensen, K. M. Ø.; Hutchison, J. E., Evolution of Atomic-Level Structure in Sub-10 Nanometer Iron Oxide Nanocrystals: Influence on Cation Occupancy and Growth Rates. *ACS Nano* **2020,** *14* (5), 5480-5490.

(24) Cooper, S. R.; Plummer, L. K.; Cosby, A. G.; Lenox, P.; Jander, A.; Dhagat, P.; Hutchison, J. E., Insights into the Magnetic Properties of Sub-10 nm Iron Oxide Nanocrystals through the Use of a Continuous Growth Synthesis. *Chem. Mater.* **2018,** *30* (17), 6053-6062.

(25) Ito, D.; Yokoyama, S.; Zaikova, T.; Masuko, K.; Hutchison, J. E., Synthesis of Ligand-Stabilized Metal Oxide Nanocrystals and Epitaxial Core/Shell Nanocrystals via a Lower-Temperature Esterification Process. *ACS Nano* **2014,** *8* (1), 64-75.

(26) Plummer, L. K.; Crockett, B. M.; Pennel, M. L.; Jansons, A. W.; Koskela, K. M.; Hutchison, J. E., Influence of Monomer Flux and Temperature on Morphology of Indium Oxide Nanocrystals during a Continuous Growth Synthesis. *Chem. Mater.* **2019,** *31* (18), 7638-7649.

(27) Jansons, A. W.; Hutchison, J. E., Continuous Growth of Metal Oxide Nanocrystals: Enhanced Control of Nanocrystal Size and Radial Dopant Distribution. *ACS Nano* **2016,** *10* (7), 6942-6951.

(28) Jansons, A. W.; Plummer, L. K.; Hutchison, J. E., Living Nanocrystals. *Chem. Mater.* **2017,** *29* (13), 5415-5425.

(29) Knecht, T. A.; Hutchison, J. E., Reaction Atmospheres and Surface Ligation Control Surface Reactivity and Morphology of Cerium Oxide Nanocrystals during Continuous Addition Synthesis. *Inorg. Chem.* **2022,** *61* (11), 4690-4704.

(30) Crockett, B. M.; Jansons, A. W.; Koskela, K. M.; Johnson, D. W.; Hutchison, J. E., Radial Dopant Placement for Tuning Plasmonic Properties in Metal Oxide Nanocrystals. *ACS Nano* **2017,** *11* (8), 7719-7728.

(31) Jansons, A. W.; Koskela, K. M.; Crockett, B. M.; Hutchison, J. E., Transition Metal-Doped Metal Oxide Nanocrystals: Efficient Substitutional Doping through a Continuous Growth Process. *Chem. Mater.* **2017,** *29* (19), 8167-8176.

(32) Crockett, B. M.; Jansons, A. W.; Koskela, K. M.; Sharps, M. C.; Johnson, D. W.; Hutchison, J. E., Influence of Nanocrystal Size on the Optoelectronic Properties of Thin, Solution-Cast Sn-Doped In_2O_3 Films. *Chem. Mater.* **2019,** *31* (9), 3370-3380.

(33) Plummer, L. K.; Hutchison, J. E., Understanding the Effects of Iron Precursor Ligation and Oxidation State Leads to Improved Synthetic Control for Spinel Iron Oxide Nanocrystals. *Inorg. Chem.* **2020,** *59* (20), 15074-15087.

(34) Bergerud, A.; Buonsanti, R.; Jordan-Sweet, J. L.; Milliron, D. J., Synthesis and phase stability of metastable bixbyite V2O 3 colloidal nanocrystals. *Chem. Mater.* **2013,** *25* (15), 3172-3179.

(35) Buonsanti, R.; Carlino, E.; Giannini, C.; Altamura, D.; De Marco, L.; Giannuzzi, R.; Manca, M.; Gigli, G.; Cozzoli, P. D., Hyperbranched anatase TiO2 nanocrystals: Nonaqueous synthesis, growth mechanism, and exploitation in dye-sensitized solar cells. *J. Am. Chem. Soc.* **2011,** *133* (47), 19216-19239.

(36) Buonsanti, R.; Grillo, V.; Carlino, E.; Giannini, C.; Kipp, T.; Cingolani, R.; Cozzoli, P. D., Nonhydrolytic synthesis of high-quality anisotropically shaped brookite TiO2 nanocrystals. *J. Am. Chem. Soc.* **2008,** *130* (33), 11223-11233.

(37) Chang, J.; Waclawik, E. R., Facet-controlled self-assembly of ZnO nanocrystals by non-hydrolytic aminolysis and their photodegradation activities. *CrystEngComm* **2012,** *14* (11), 4041-4048.

(38) Jin, Y.; Yi, Q.; Ren, Y.; Wang, X.; Ye, Z., Molecular mechanism of monodisperse colloidal tin-doped indium oxide nanocrystals by a hot-injection approach. *Nanoscale Research Letters* **2013,** *8* (1), 1-10.

(39) Jin, Y.; Yi, Q.; Zhou, L.; Chen, D.; He, H.; Ye, Z.; Hong, J.; Jin, C., Synthesis and characterization of ultrathin tin-doped zinc oxide nanowires. *Eur. J. Inorg. Chem.* **2012,** (27), 4268-4272.

(40) Manera, M. G.; Taurino, A.; Catalano, M.; Rella, R.; Caricato, A. P.; Buonsanti, R.; Cozzoli, P. D.; Martino, M., Enhancement of the optically activated NO2 gas sensing response of brookite TiO2 nanorods/nanoparticles thin films deposited by matrix-assisted pulsed-laser evaporation. *Sensors and Actuators B: Chemical* **2012,** *161* (1), 869-879.

(41) Ong, G. K.; Saez Cabezas, C. A.; Dominguez, M. N.; Skjærvø, S. L.; Heo, S.; Milliron, D. J., Electrochromic Niobium Oxide Nanorods. *Chem. Mater.* **2020,** *32* (1), 468-475.

(42) Gilstrap, R. A.; Capozzi, C. J.; Carson, C. G.; Gerhardt, R. A.; Summers, C. J., Synthesis of a nonagglomerated indium tin oxide nanoparticle dispersion. *Adv. Mater.* **2008,** *20* (21), 4163-4166.

(43) Gilstrap, R. A.; Summers, C. J., Synthesis and analysis of an indium tin oxide nanoparticle dispersion. *Thin Solid Films* **2009,** *518* (4), 1136-1139.

Chapter IV

(1) Cai, L.; Xu, H.; Chu, D. Compact Liquid Crystal Based Tunable Band-Stop Filter with an Ultra-Wide Stopband by Using Wave Interference Technique. *Int. J. Antennas Propag*. **2017**, *2017*, 1-11.

(2) Chen, Z.; Li, H.; Li, B.; He, Z.; Xu, H.; Zheng, M.; Zhao, M. Tunable Ultra-Wide Band-Stop Filter Based on Single-Stub Plasmonic-Waveguide System. *Appl. Phys. Express* **2016**, *9*, 1-4.

(3) Li, H. J.; Zhai, X.; Wujiaihemaiti, R.; Wang, L. L.; Li, X. F. Tunable Optical Filters and Multichannel Switches Based on MIM Plasmonic Nanodisk Resonators Inset a Silver Bar. *Phys. Scr.* **2015**, *90*, 1-6.

(4) Zhang, Z.; Yang, J.; He, X.; Han, Y.; Zhang, J.; Huang, J.; Chen, D. Plasmonic Filter and Demultiplexer Based on Square Ring Resonator. *Appl. Sci.* **2018**, *8*, 1-10.

(5) Wang, G.; Lu, H.; Liu, X.; Mao, D.; Duan, L. Tunable Multi-Channel Wavelength Demultiplexer Based on MIM Plasmonic Nanodisk Resonators at Telecommunication Regime. *Opt. Express* **2011**, *19*, 3513-3518.

(6) Nguyen-Huu, N.; Lo, Y. L. Tailoring the Optical Transmission Spectra of Double-Layered Compound Metallic Gratings. *IEEE Photonics J.* **2013**, *5*, 2700108, 1-9.

(7) Fleischman, D.; Sweatlock, L. A.; Murakami, H.; Atwater, H. Hyper-Selective Plasmonic Color Filters. *Opt. Express* **2017**, *25*, 27386-27395.

(8) Kyoung, J.; Hwang, S. W. Configurable Plasmonic Band-Pass Filters Operating under the Addition Rule. *ACS Photonics* **2016**, *3*, 819–827.

(9) Cheng, C.; Chen, J.; Wu, Q. Y.; Ren, F. F.; Xu, J.; Fan, Y. X.; Wang, H. T. Controllable Electromagnetic Transmission Based on Dual-Metallic Grating Structures Composed of Subwavelength Slits. *Appl. Phys. Lett.* **2007**, *91*, 1-3.

(10) Tanzid, M.; Sobhani, A.; DeSantis, C. J.; Cui, Y.; Hogan, N. J.; Samaniego, A.; Veeraraghavan, A.; Halas, N. J. Imaging through Plasmonic Nanoparticles. *Proc. Natl. Acad. Sci. U.S.A.* **2016**, *113*, 5558–5563.

(11) Noginov, M. A.; Gu, L.; Livenere, J.; Zhu, G.; Pradhan, A. K.; Mundle, R.; Bahoura, M.; Barnakov, Y. A.; Podolskiy, V. A. Transparent Conductive Oxides: Plasmonic Materials for Telecom Wavelengths. *Appl. Phys. Lett.* **2011**, *99*, 1-3.

(12) Lu, H.; Liu, X.; Mao, D.; Wang, L.; Gong, Y. Tunable Band-Pass Plasmonic Waveguide Filters with Nanodisk Resonators. *Opt. Express* **2010**, *18*, 17922-17927.

(13) Lu, H.; Liu, X.; Wang, G.; Mao, D. Tunable High-Channel-Count Bandpass Plasmonic Filters Based on an Analogue of Electromagnetically Induced Transparency. *Nanotechnology* **2012**, *23*, 1-6.

(14) Guo, Q.; Yao, Y.; Luo, Z. C.; Qin, Z.; Xie, G.; Liu, M.; Kang, J.; Zhang, S.; Bi, G.; Liu, X.; et al. Universal Near-Infrared and Mid-Infrared Optical Modulation for Ultrafast Pulse Generation Enabled by Colloidal Plasmonic Semiconductor Nanocrystals. *ACS Nano* **2016**, *10*, 9463–9469.

(15) Kriegel, I.; Scotognella, F. Tunable Light Filtering by a Bragg Mirror/Heavily Doped Semiconducting Nanocrystal Composite. *Beilstein J. Nanotechnol.* **2015**, *6*, 193–200.

(16) Lounis, S. D.; Runnerstrom, E. L.; Llordés, A.; Milliron, D. J. Defect Chemistry and Plasmon Physics of Colloidal Metal Oxide Nanocrystals. *J. Phys. Chem. Lett*. **2014**, *5*, 1564–1574.

(17) Agrawal, A.; Johns, R. W.; Milliron, D. J. Control of Localized Surface Plasmon Resonances in Metal Oxide Nanocrystals Keynote Topic. *Annu. Rev. Mater. Res.* **2017**, *47*, 1-31.

(18) Tandon, B.; Ghosh, S.; Milliron, D. J. Dopant Selection Strategy for High-Quality Factor Localized Surface Plasmon Resonance from Doped Metal Oxide Nanocrystals. *Chem. Mater.* **2019**, *31*, 7752–7760.

(19) Mortimer, R. J., Rosseinsky, D. R., Monk, P. M. S., *Electrochromic Materials and Devices*; Wiley-VCH Verlag GmbH & Co. KGaA: Weinheim, Germany, **2015**, 3-33.

(20) Kanehara, M.; Koike, H.; Yoshinaga, T.; Teranishi, T. Indium Tin Oxide Nanoparticles with Compositionally Tunable Surface Plasmon Resonance Frequencies in the Near-IR Region. *J. Am. Chem. Soc.* **2009**, *131*, 17736–17737.

(21) Lounis, S. D.; Runnerstrom, E. L.; Bergerud, A.; Nordlund, D.; Milliron, D. J. Influence of Dopant Distribution on the Plasmonic Properties of Indium Tin Oxide Nanocrystals. *J. Am. Chem. Soc.* **2014**, *136*, 7110–7116.

(22) Wang, Y.; Runnerstrom, E. L.; Milliron, D. J. Switchable Materials for Smart Windows. *Annu. Rev. Chem. Biomol. Eng.* **2016**, *7*, 283–304.

(23) Kasani, S.; Curtin, K.; Wu, N. A Review of 2D and 3D Plasmonic Nanostructure Array Patterns: Fabrication, Light Management and Sensing Applications. *Nanophotonics* **2019**, *8*, 2065-2089.

(24) Ghobadi, A.; Hajian, H.; Soydan, M. C.; Butun, B.; Ozbay, E. Lithography-Free Planar Band-Pass Reflective Color Filter Using A Series Connection of Cavities. *Sci. Rep.* **2019**, *9*, 1-11.

(25) Freeman, R. G.; Hommer, M. B.; Grabar, K. C.; Jackson, M. A.; Natan, M. J. Ag-Clad Au Nanoparticles: Novel Aggregation, Optical, and Surface-Enhanced Raman Scattering Properties. *J. Phys. Chem.* **1996**, *100*, 718–724.

(26) Navarro Ab, J. R. G.; Werts, M. H. V. Resonant Light Scattering Spectroscopy of Gold, Silver and Gold-Silver Alloy Nanoparticles and Optical Detection in Microfluidic Channels. *Analyst* **2013**, *138*, 583-592.

(27) Liao, H.; Lu, W.; Yu, S.; Wen, W.; Wong, G. K. L. Optical Characteristics of Gold Nanoparticle-Doped Multilayer Thin Film. *J. Opt. Soc. Am. B* **2005**, *22*, 1923-1926.

(28) Jun Liu, Y.; Bing Zheng, Y.; Liou, J.; Chiang, I.-K.; Choon Khoo, I.; Jun Huang, T. All-Optical Modulation of Localized Surface Plasmon Coupling in a Hybrid System Composed of Photoswitchable Gratings and Au Nanodisk Arrays. *J. Phys. Chem. C* **2011**, *115*, 7717–7722.

(29) Stanley, R. Plasmonics in the Mid-Infrared. *Nat. Photonics* **2012**, 6, 409–411.

(30) Hartland, G. Designing Plasmon Resonances. *J. Phys. Chem. Lett.* **2014**, *5*, 1583–1584.

(31) Kovalenko, M. V.; Manna, L.; Cabot, A.; Hens, Z.; Talapin, D. V.; Kagan, C. R.; Klimov, V. I.; Rogach, A. L.; Reiss, P.; Milliron, D. J.; et al. Prospects of Nanoscience with Nanocrystals. *ACS Nano* **2015**, *9*, 1012–1057.

(32) Zhao, Y.; Pan, H.; Lou, Y.; Qiu, X.; Zhu, J.; Burda, C. Plasmonic $Cu_{2-x}S$ Nanocrystals: Optical and Structural Properties of Copper-Deficient Copper(I) Sulfides. *J. Am. Chem. Soc.* **2009**, *131*, 4253–4261.

(33) Tandon, B.; Yadav, A.; Khurana, D.; Reddy, P.; Santra, P. K.; Nag, A. Size-Induced Enhancement of Carrier Density, LSPR Quality Factor, and Carrier Mobility in Cr−Sn Doped In_2O_3 Nanocrystals. *Chem. Mater.* **2017**, *29*, 9360-9368.

(34) Crockett, B. M.; Jansons, A. W.; Koskela, K. M.; Johnson, D. W.; Hutchison, J. E. Radial Dopant Placement for Tuning Plasmonic Properties in Metal Oxide Nanocrystals. *ACS Nano* **2017**, *11*, 7719–7728.

(35) Jansons, A. W.; Koskela, K. M.; Crockett, B. M.; Hutchison, J. E. Transition Metal-Doped Metal Oxide Nanocrystals: Efficient Substitutional Doping through a Continuous Growth Process. *Chem. Mater.* **2017**, *29*, 8167–8176.

(36) Jansons, A. W.; Hutchison, J. E. Continuous Growth of Metal Oxide Nanocrystals: Enhanced Control of Nanocrystal Size and Radial Dopant Distribution. *ACS Nano* **2016**, *10*, 6942–6951.

(37) Ilavsky, J.; Jemian, P. R. Irena: Tool Suite for Modeling and Analysis of Small-Angle Scattering. *J. Appl. Crystallogr.* **2009**, *42*, 347–353.

(38) Runnerstrom, E. L.; Bergerud, A.; Agrawal, A.; Johns, R. W.; Dahlman, C. J.; Singh, A.; Selbach, S. M.; Milliron, D. J. Defect Engineering in Plasmonic Metal Oxide Nanocrystals. *Nano Lett.* **2016**, *16*, 3390–3398.

(39) Ito, D.; Yokoyama, S.; Zaikova, T.; Masuko, K.; Hutchison, J. E. Synthesis of Ligand-Stabilized Metal Oxide Nanocrystals and Epitaxial Core/Shell Nanocrystals via a Lower- Temperature Esterification Process. *ACS Nano* **2014**, *8,* 64–75.

(40) Crockett, B. M.; Jansons, A. W.; Koskela, K. M.; Sharps, M. C.; Johnson, D. W.; Hutchison, J. E. Influence of Nanocrystal Size on the Optoelectronic Properties of Thin, Solution-Cast Sn-Doped In_2O_3 Films. *Chem. Mater.* **2019**, *31*, 3370–3380.

(41) Fang, H.; Hegde, M.; Yin, P.; Radovanovic, P. V. Tuning Plasmon Resonance of In_2O_3 Nanocrystals throughout the Mid-Infrared Region by Competition between Electron Activation and Trapping. *Chem. Mater.* **2017**, *29*, 4970–4979.

(42) Malitson, I. H. A Redetermination of Some Optical Properties of Calcium Fluoride. *Appl. Opt.* **1963**, *2*, 1103-1107.

(43) König, T. A. F.; Ledin, P. A.; Kerszulis, J.; Mahmoud, M. A.; El-Sayed, M. A.; Reynolds, J. R.; Tsukruk, V. V. Electrically Tunable Plasmonic Behavior of Nanocube-Polymer Nanomaterials Induced by a Redox-Active Electrochromic Polymer. *ACS Nano* **2014**, *8*, 6182–6192.

(44) Rycenga, M.; Camargo, P. H. C.; Li, W.; Moran, C. H.; Xia, Y. Understanding the SERS Effects of Single Silver Nanoparticles and Their Dimers, One at a Time. *J. Phys. Chem. Lett.* **2010**, *1*, 696–703.

(45) Jiang, C.; Markutsya, S.; Tsukruk, V. V. Collective and Individual Plasmon Resonances in Nanoparticle Films Obtained by Spin-Assisted Layer-by-Layer Assembly. *Langmuir* **2004**, *20*, 882–890.

(46) Mahmoud, M. A.; Chamanzar, M.; Adibi, A.; El-Sayed, M. A. Effect of the Dielectric Constant of the Surrounding Medium and the Substrate on the Surface Plasmon Resonance Spectrum and Sensitivity Factors of Highly Symmetric Systems: Silver Nanocubes. *J. Am. Chem. Soc.* **2012**, *134*, 6434–6442.

(47) R. Daniel, J.; McCarthy, L. A.; Ringe, E.; Boudreau, D. Enhanced Control of Plasmonic Properties of Silver-Gold Hollow Nanoparticles via a Reduction-Assisted Galvanic Replacement Approach. *RSC Adv.* **2019**, *9*, 389–396.

(48) Lu, H.; Liu, X.; Wang, L.; Gong, Y.; Mao, D. Ultrafast All-Optical Switching in Nanoplasmonic Waveguide with Kerr Nonlinear Resonator. *Opt. Express* **2011**, *19*, 2910-2915.

(49) Hendrickson, J. R.; Vangala, S.; Dass, C.; Gibson, R.; Goldsmith, J.; Leedy, K.; Walker, D. E.; Cleary, J. W.; Kim, W.; Guo, J. Coupling of Epsilon-Near-Zero Mode to Gap Plasmon Mode for Flat-Top Wideband Perfect Light Absorption. *ACS Photonics* **2018**, *5*, 776–781.

(50) Yang, L.; Zhou, Y. J.; Zhang, C.; Xiao, Q. X. Compact Wideband Plasmonic Filter with Flat-Top Transmission Response Based on Corrugated Metal-Insulator-Metal Ring Resonator. *Sci. Rep.* **2017**, *7*, 1–10.

(51) Hu, X. L.; Sun, L. B.; Wu, Q. J.; Wang, L. S.; Bai, S. A.; Li, Q.; Yang, S. M.; Tai, R. Z.; Mohr, M.; Fecht, H. J.; et al. Broad Band Optical Band-Reject Filters in Near-Infrared Regime Utilizing Bilayer Ag Metasurface. *J. Appl. Phys.* **2017**, *121*, 1-6.

(52) Bhachu, D. S.; Scanlon, D. O.; Sankar, G.; Veal, T. D.; Egdell, R. G.; Cibin, G.; Dent, A. J.; Knapp, C. E.; Carmalt, C. J.; Parkin, I. P. Origin of High Mobility in Molybdenum-Doped Indium Oxide. *Chem. Mater.* **2015**, *27*, 2788–2796.

(53) Zandi, O.; Agrawal, A.; Shearer, A. B.; Reimnitz, L. C.; Dahlman, C. J.; Staller, C. M.; Milliron, D. J. Impacts of Surface Depletion on the Plasmonic Properties of Doped Semiconductor Nanocrystals. *Nat. Mater.* **2018**, *17*, 710-717.

Chapter V

(1) Lee, M.-Y.; Park, K. T.; Lee, W.; Lim, H.; Kwon, Y.; Kang, S., Current achievements and the future direction of electrochemical CO_2 reduction: A short review. *Angew. Chem. Int. Ed.* **2019,** *50* (8), 769-815.

(2) Ting, L. R. L.; Yeo, B. S., Recent advances in understanding mechanisms for the electrochemical reduction of carbon dioxide. *Curr. Opin. Electrochem.* **2018,** *8*, 126-134.

(3) Zhang, W.; Hu, Y.; Ma, L.; Zhu, G.; Wang, Y.; Xue, X.; Chen, R.; Yang, S.; Jin, Z., Progress and Perspective of Electrocatalytic CO_2 Reduction for Renewable Carbonaceous Fuels and Chemicals. *Adv. Sci.* **2018,** *5* (1).

(4) Gunasekar, G. H.; Park, K.; Jung, K. D.; Yoon, S., Recent developments in the catalytic hydrogenation of CO_2 to formic acid/formate using heterogeneous catalysts. *Inorg. Chem. Front.* **2016,** *3* (7), 882-895.

(5) Sun, Z.; Ma, T.; Tao, H.; Fan, Q.; Han, B., Fundamentals and Challenges of Electrochemical CO_2 Reduction Using Two-Dimensional Materials. *Chem* **2017,** *3* (4), 560-587.

(6) Zheng, T.; Jiang, K.; Wang, H., Recent Advances in Electrochemical CO_2-to-CO Conversion on Heterogeneous Catalysts. *Adv.* **2018,** *30* (48).

(7) Zhu, D. D.; Liu, J. L.; Qiao, S. Z., Recent Advances in Inorganic Heterogeneous Electrocatalysts for Reduction of Carbon Dioxide. *Adv.* **2016,** *28* (18), 3423-3452.

(8) Longfei Wu; E. Kolmeijer, K.; Yue Zhang; Hongyu An; Sven Arnouts; Sara Bals; Thomas Altantzis; P. Hofmann, J.; Figueiredo, Marta C.; M. Hensen, E. J.; M. Weckhuysen, B.; Stam, Ward v. d., Stabilization effects in binary colloidal Cu and Ag nanoparticle electrodes under electrochemical CO_2 reduction conditions. *Nanoscale* **2021,** *13* (9), 4835-4844.

(9) Zhang, S.; Kang, P.; Meyer, T. J., Nanostructured tin catalysts for selective electrochemical reduction of carbon dioxide to formate. *J. Am. Chem. Soc.* **2014,** *136* (5), 1734-1737.

(10) Arán-Ais, R. M.; Rizo, R.; Grosse, P.; Algara-Siller, G.; Dembélé, K.; Plodinec, M.; Lunkenbein, T.; Chee, S. W.; Cuenya, B. R., Imaging electrochemically synthesized Cu_2O cubes and their morphological evolution under conditions relevant to CO_2 electroreduction. *Nat. Commun. 2020 11:1* **2020,** *11* (1), 1-8.

(11) Daiyan, R.; Lu, X.; Saputera, W. H.; Ng, Y. H.; Amal, R., Highly Selective Reduction of CO_2 to Formate at Low Overpotentials Achieved by a Mesoporous Tin Oxide Electrocatalyst. *ACS Sustain. Chem. Eng.* **2018,** *6* (2), 1670-1679.

(12) Ding, C.; Li, A.; Lu, S. M.; Zhang, H.; Li, C., In Situ Electrodeposited Indium Nanocrystals for Efficient CO_2 Reduction to CO with Low Overpotential. *ACS Catal.* **2016,** *6* (10), 6438-6443.

(13) Fu, W.; Liu, Z.; Wang, T.; Liang, J.; Duan, S.; Xie, L.; Han, J.; Li, Q., Promoting C_{2+} Production from Electrochemical CO_2 Reduction on Shape-Controlled Cuprous Oxide Nanocrystals with High-Index Facets. *ACS Sustain. Chem. Eng.* **2020,** *8* (40), 15223-15229.

(14) Gao, D.; Zhou, H.; Wang, J.; Miao, S.; Yang, F.; Wang, G.; Wang, J.; Bao, X., Size-Dependent Electrocatalytic Reduction of CO_2 over Pd Nanoparticles. *J. Am. Chem. Soc.* **2015,** *137* (13), 4288-4291.

(15) Huang, Y.; Mao, X.; Yuan, G.; Zhang, D.; Pan, B.; Deng, J.; Shi, Y.; Han, N.; Li, C.; Zhang, L.; Wang, L.; He, L.; Li, Y.; Li, Y., Size-Dependent Selectivity of Electrochemical CO_2 Reduction on Converted In_2O_3 Nanocrystals. *Angew. Chem. Int. Ed.* **2021,** *60* (29), 15844-15848.

(16) Kumar, B.; Atla, V.; Brian, J. P.; Kumari, S.; Nguyen, T. Q.; Sunkara, M.; Spurgeon, J. M., Reduced SnO_2 Porous Nanowires with a High Density of Grain Boundaries as Catalysts for Efficient Electrochemical CO_2-into-HCOOH Conversion. *Angew. Chem. Int. Ed.* **2017,** *56* (13), 3645-3649.

(17) Loiudice, A.; Lobaccaro, P.; Kamali, E. A.; Thao, T.; Huang, B. H.; Ager, J. W.; Buonsanti, R., Tailoring Copper Nanocrystals towards C2 Products in Electrochemical CO_2 Reduction. *Angew. Chem. Int. Ed.* **2016,** *55* (19), 5789-5792.

(18) Baruch, M. F.; Pander, J. E.; White, J. L.; Bocarsly, A. B., Mechanistic Insights into the Reduction of CO_2 on Tin Electrodes using in Situ ATR-IR Spectroscopy. *ACS Catal.* **2015,** *5* (5), 3148-3156.

(19) Cui, C.; Han, J.; Zhu, X.; Liu, X.; Wang, H.; Mei, D.; Ge, Q., Promotional effect of surface hydroxyls on electrochemical reduction of CO_2 over SnOx/Sn electrode. *J. Catal.* **2016,** *343*, 257-265.

(20) Gu, J.; Héroguel, F.; Luterbacher, J.; Hu, X., Densely Packed, Ultra Small SnO Nanoparticles for Enhanced Activity and Selectivity in Electrochemical CO_2 Reduction. *Angew. Chem. Int. Ed.* **2018,** *57* (11), 2943-2947.

(21) Han, N.; Ding, P.; He, L.; Li, Y.; Li, Y., Promises of Main Group Metal–Based Nanostructured Materials for Electrochemical CO_2 Reduction to Formate. *Adv. Energy Mater.* **2020,** *10* (11), 1902338-1902338.

(22) Detweiler, Z. M.; White, J. L.; Bernasek, S. L.; Bocarsly, A. B., Anodized indium metal electrodes for enhanced carbon dioxide reduction in aqueous electrolyte. *Langmuir* **2014,** *30* (25), 7593-7600.

(23) Ghuman, K. K.; Wood, T. E.; Hoch, L. B.; Mims, C. A.; Ozin, G. A.; Singh, C. V., Illuminating CO_2 reduction on frustrated Lewis pair surfaces: Investigating the role of surface hydroxides and oxygen vacancies on nanocrystalline $In_2O_{3-x}(OH)_y$. *Phys. Chem. Chem. Phys.* **2015,** *17* (22), 14623-14635.

(24) Hegner, R.; Rosa, L. F. M.; Harnisch, F., Electrochemical CO_2 reduction to formate at indium electrodes with high efficiency and selectivity in pH neutral electrolytes. *Appl. Catal. B.* **2018,** *238*, 546-556.

(25) Lai, Q.; Yang, N.; Yuan, G., Highly efficient In–Sn alloy catalysts for electrochemical reduction of CO_2 to formate. *Electrochem. Commun.* **2017,** *83*, 24-27.

(26) Detweiler, Z. M.; Wulfsberg, S. M.; Frith, M. G.; Bocarsly, A. B.; Bernasek, S. L., The oxidation and surface speciation of indium and indium oxides exposed to atmospheric oxidants. *Surf. Sci.* **2016,** *648*, 188-195.

(27) White, J. L.; Bocarsly, A. B., Enhanced Carbon Dioxide Reduction Activity on Indium-Based Nanoparticles. *J. Electrochem. Soc.* **2016,** *163* (6), H410-H416.

(28) Chen, Y.; Kanan, M. W., Tin oxide dependence of the CO_2 reduction efficiency on tin electrodes and enhanced activity for tin/tin oxide thin-film catalysts. *J. Am. Chem. Soc.* **2012,** *134* (4), 1986-1989.

(29) Pander, J. E.; Ren, D.; Huang, Y.; Loo, N. W. X.; Hong, S. H. L.; Yeo, B. S., Understanding the Heterogeneous Electrocatalytic Reduction of Carbon Dioxide on Oxide-Derived Catalysts. *ChemElectroChem* **2018,** *5* (2), 219-237.

(30) Pérez, L. C. P.; Teschner, D.; Willinger, E.; Guiet, A.; Driess, M.; Strasser, P.; Fischer, A., In Situ Formed "$Sn_{1-X}In_X$@$In_{1-Y}Sn_YO_Z$" Core@Shell Nanoparticles as Electrocatalysts for CO_2 Reduction to Formate. *Adv. Funct. Mater.* **2021**, 2103601-2103601.

(31) Xu, Z.; Wu, T.; Cao, Y.; Chen, C.; Zeng, X.; Lin, P.; Zhao, W. W., Dynamic restructuring induced Cu nanoparticles with ideal nanostructure for selective multi-carbon compounds production via carbon dioxide electroreduction. *J. Catal.* **2020,** *383*, 42-50.

(32) Wu, Z.; Huang, L.; Liu, H.; Wang, H., Element-Specific Restructuring of Anion- and Cation-Substituted Cobalt Phosphide Nanoparticles under Electrochemical Water-Splitting Conditions. *ACS Catal.* **2019,** *9* (4), 2956-2961.

(33) Weng, Z.; Zhang, X.; Wu, Y.; Huo, S.; Jiang, J.; Liu, W.; He, G.; Liang, Y.; Wang, H., Self-Cleaning Catalyst Electrodes for Stabilized CO_2 Reduction to Hydrocarbons. *Angew. Chem. Int. Ed.* **2017,** *56* (42), 13135-13139.

(34) Goodman, E. D.; Schwalbe, J. A.; Cargnello, M., Mechanistic Understanding and the Rational Design of Sinter-Resistant Heterogeneous Catalysts. *ACS Catal.* **2017,** *7* (10), 7156-7173.

(35) Geiger, S.; Kasian, O.; Mingers, A. M.; Mayrhofer, K. J. J.; Cherevko, S., Stability limits of tin-based electrocatalyst supports. *Sci. Rep.* **2017,** *7* (1).

(36) Huang, C. A.; Li, K. C.; Tu, G. C.; Wang, W. S., The electrochemical behavior of tin-doped indium oxide during reduction in 0.3 M hydrochloric acid. *Electrochim. Acta* **2003,** *48* (24), 3599-3605.

(37) Jansons, A. W.; Hutchison, J. E., Continuous Growth of Metal Oxide Nanocrystals: Enhanced Control of Nanocrystal Size and Radial Dopant Distribution. *ACS Nano* **2016,** *10* (7), 6942-6951.

(38) Sweeney, S. W.; Roseman, G.; Deming, C. P.; Wang, N.; Nguyen, T. A.; Millhauser, G. L.; Chen, S., Impacts of oxygen vacancies on the electrocatalytic activity of AuTiO2 nanocomposites towards oxygen reduction. *Int. J. Hydrog.* **2016,** *41* (40), 18005-18014.

(39) Korotcenkov, G.; Brinzari, V.; Ivanov, M.; Cerneavschi, A.; Rodriguez, J.; Cirera, A.; Cornet, A.; Morante, J., Structural stability of indium oxide films deposited by spray pyrolysis during thermal annealing. *Thin Solid Films* **2005,** *479* (1-2), 38-51.

(40) Köstlin, H.; Jost, R.; Lems, W., Optical and electrical properties of doped In_2O_3 films. *Phys. Status Solidi* **1975,** *29* (1), 87-93.

(41) Larrazábal, G. O.; Martín, A. J.; Mitchell, S.; Hauert, R.; Pérez-Ramírez, J., Synergistic effects in silver–indium electrocatalysts for carbon dioxide reduction. *J. Catal.* **2016,** *343*, 266-277.

(42) Jansons, A. W.; Koskela, K. M.; Crockett, B. M.; Hutchison, J. E., Transition Metal-Doped Metal Oxide Nanocrystals: Efficient Substitutional Doping through a Continuous Growth Process. *Chem. Mater.* **2017,** *29* (19), 8167-8176.

(43) Verlato, E.; Barison, S.; Einaga, Y.; Fasolin, S.; Musiani, M.; Nasi, L.; Natsui, K.; Paolucci, F.; Valenti, G., CO_2 reduction to formic acid at low overpotential on BDD electrodes modified with nanostructured CeO_2. *J. Mater. Chem.* **2019,** *7* (30), 17896-17905.

(44) Wu, Y.; Cao, S.; Hou, J.; Li, Z.; Zhang, B.; Zhai, P.; Zhang, Y.; Sun, L., Rational Design of Nanocatalysts with Nonmetal Species Modification for Electrochemical CO_2 Reduction. *Adv. Energy Mater.* **2020,** *10* (29), 2000588-2000588.

(45) Yuan, J.; Zhang, J. J.; Yang, M. P.; Meng, W. J.; Wang, H.; Lu, J. X., CuO nanoparticles supported on TiO_2 with high efficiency for CO_2 electrochemical reduction to ethanol. *Catalysts* **2018,** *8* (4), 171-171.

(46) Yuan, J.; Liu, L.; Guo, R. R.; Zeng, S.; Wang, H.; Lu, J. X., Electroreduction of CO_2 into ethanol over an active catalyst: Copper supported on Titania. *Catalysts* **2017,** *7* (7), 220-220.

(47) Koshy, D. M.; Akhade, S. A.; Shugar, A.; Abiose, K.; Shi, J.; Liang, S.; Oakdale, J. S.; Weitzner, S. E.; Varley, J. B.; Duoss, E. B.; Baker, S. E.; Hahn, C.; Bao, Z.; Jaramillo, T. F., Chemical Modifications of Ag Catalyst Surfaces with Imidazolium Ionomers Modulate H_2 Evolution Rates during Electrochemical CO_2 Reduction. *J. Am. Chem. Soc.* **2021**.

(48) Yang, Z.; Fujigaya, T.; Nakashima, N., Homogeneous coating of ionomer on electrocatalyst assisted by polybenzimidazole as an adhesive layer and its effect on fuel cell performance. *J. Power Sources* **2015,** *300*, 175-181.

(49) Artyushkova, K.; Workman, M. J.; Matanovic, I.; Dzara, M. J.; Ngo, C.; Pylypenko, S.; Serov, A.; Atanassov, P., Role of Surface Chemistry on Catalyst/Ionomer Interactions for Transition Metal–Nitrogen–Carbon Electrocatalysts. *ACS Appl. Energy Mater.* **2018,** *1* (1), 68-77.

(50) Berlinger, S. A.; McCloskey, B. D.; Weber, A. Z., Probing Ionomer Interactions with Electrocatalyst Particles in Solution. *ACS Energy Lett.* **2021,** *6* (6), 2275-2282.

(51) Crockett, B. M.; Jansons, A. W.; Koskela, K. M.; Sharps, M. C.; Johnson, D. W.; Hutchison, J. E., Influence of Nanocrystal Size on the Optoelectronic Properties of Thin, Solution-Cast Sn-Doped In_2O_3 Films. *Chem. Mater.* **2019,** *31* (9), 3370-3380.

(52) Burdyny, T.; Smith, W. A., CO_2 reduction on gas-diffusion electrodes and why catalytic performance must be assessed at commercially-relevant conditions. *Energy Environ. Sci.* **2019,** *12* (5), 1442-1453.

(53) Zhang, F.; Co, A. C., Direct Evidence of Local pH Change and the Role of Alkali Cation during CO_2 Electroreduction in Aqueous Media. *Angew. Chem. Int. Ed.* **2020,** *59* (4), 1674-1681.

(54) Singh, M. R.; Kwon, Y.; Lum, Y.; Ager, J. W.; Bell, A. T., Hydrolysis of Electrolyte Cations Enhances the Electrochemical Reduction of CO_2 over Ag and Cu. *J. Am. Chem. Soc.* **2016,** *138* (39), 13006-13012.

(55) Barsotti, R. J.; Vahey, M. D.; Wartena, R.; Chiang, Y. M.; Voldman, J.; Stellacci, F., Assembly of metal nanoparticles into nanogaps. *Small* **2007,** *3* (3), 488-499.

(56) Arulmozhi, N.; P Hersbach, T. J.; M Koper, M. T., Nanoscale morphological evolution of monocrystalline Pt surfaces during cathodic corrosion. *PNAS* **2017,** *117* (51), 32267-32277.

(57) Boettcher, S. W.; Strandwitz, N. C.; Schierhorn, M.; Lock, N.; Lonergan, M. C.; Stucky, G. D., Tunable electronic interfaces between bulk semiconductors and ligand-stabilized nanoparticle assemblies. *Nat. Mater.* **2007,** *6* (8), 592-596.

(58) Chuang, C.-H. M.; Brown, P. R.; Bulović, V.; Bawendi, M. G., Improved performance and stability in quantum dot solar cells through band alignment engineering. *Nat. Mater.* **2014,** *13* (8), 796-801.

(59) Kramer, I. J.; Sargent, E. H., The Architecture of Colloidal Quantum Dot Solar Cells: Materials to Devices. *Chem. Rev.* **2013,** *114* (1), 863-882.

(60) Bernechea, M.; Miller, N. C.; Xercavins, G.; So, D.; Stavrinadis, A.; Konstantatos, G., Solution-processed solar cells based on environmentally friendly $AgBiS_2$ nanocrystals. *Nat. Photonics* **2016,** *10* (8), 521-525.

(61) Pander, J. E.; Ren, D.; Yeo, B. S., Practices for the collection and reporting of electrocatalytic performance and mechanistic information for the CO_2 reduction reaction. *Catal. Sci. Technol.* **2017,** *7* (24), 5820-5832.

(62) Kittel, C., Chapter 3 - Crystal Binding and Elastic Constants. *Introduction to Solid State Physics* **2004**, 453-486.

(63) King, D. A., Surface Diffusion of Adsorbed Species: A Review. *J. Vac. Sci. Technol.* **1979,** *17* (1), 241-247.

(64) Morris, M. A.; Barnes, C. J.; King, D. A., Monolayer and multilayer surface diffusion, growth mode and thermal stability of indium on W {100}. *Surf. Sci.* **1986,** *173* (2-3), 618-638.

(65) King, D. A., Surface diffusion of adsorbed species: A review. *J. Vac. Sci. Technol.* **1998,** *17* (1), 241-241.

(66) Wagner, M.; Seiler, S.; Meyer, B.; Boatner, L. A.; Schmid, M.; Diebold, U., Reducing the In_2O_3(111) Surface Results in Ordered Indium Adatoms. *Adv. Interfaces* **2014,** *1* (8), 1400289-1400289.

(67) Wei, H. L.; Zhang, L.; Liu, Z.; Huang, H.; Zhang, X., Spontaneous growth of indium nanostructures. *J. Cryst. Growth* **2006,** *297* (2), 300-305.